
# PLASMAS AND MAGNETIC FIELDS IN PROPULSION AND POWER RESEARCH



A conference held at
LEWIS RESEARCH CENTER
Cleveland, Ohio
October 16, 1969



NATIONAL AERONAUTICS AND SPACE ADMINISTRATION

NASA SP-226

# PLASMAS AND MAGNETIC FIELDS IN PROPULSION AND POWER RESEARCH

The proceedings of a conference held at
the NASA Lewis Research Center on
October 16, 1969


*Scientific and Technical Information Division*
OFFICE OF TECHNOLOGY UTILIZATION 1970
NATIONAL AERONAUTICS AND SPACE ADMINISTRATION
*Washington, D.C.*

For sale by the Clearinghouse for Federal Scientific and Technical Information
Springfield, Virginia 22151 – Price $3.00

# FOREWORD

In keeping with its mission of research on propulsion and power systems, the Lewis Research Center has been engaged in studies of electric thrusters and the key scientific topics related to their development. The purpose of this Conference is to present recent results from this body of work, specifically, research on plasmas and magnetic fields, and to examine their importance to aerospace propulsion and power generation. We hope that this review will prove useful to those working in the field.

Abe Silverstein
Director

# CONTENTS

# INTRODUCTION

W. E. Moeckel

The primary roll of the Lewis Research Center in the NASA organization is to conduct research and development on propulsion and power systems for aircraft and spacecraft. This roll predates the formation of NASA by many years. In fact, it dates back to 1941 when a group from the Langley Laboratory was moved to Cleveland to establish the Aircraft Engine Research Laboratory of the National Advisory Committee for Aeronautics, the direct predecessor of NASA. With this historical background, it is not surprising that we view most of our research from the standpoint of application to new or improved propulsion and power concepts and systems. This is the viewpoint which led to most of the research and technology that we are discussing at this conference. Some of the propulsion and power concepts toward which this research is directed are still quite remote from application, and some may prove to be infeasible. But we can not find out about the real problems and limitations of these concepts unless some work is done on them. A determination of the feasibility of propulsion concepts is really the main responsibility at Lewis.

During the 1940's and early 1950's, most of the activity at this Center involved aircraft engines, primarily turbojets and their associated components. Their missions were studied for all speed ranges. The results of these system, component, and mission studies were presented periodically in the form of conferences for the aircraft industry, interested universities, and the armed services. Such conferences have continued intermittently during the past decade. This conference is one of a new series which will present in condensed and summarized form our viewpoints and research results in several areas of Lewis activity.

During the NACA period, research at Lewis was proceeding on other propulsion concepts (in addition to turbojets), such as ramjets, high-energy chemical rockets, and nuclear-powered aircraft engines, together with mission and application studies. Some of the evaluation studies on the uses of nuclear energy for turbojets, ramjets, and rockets date back to 1946. With the increased emphasis on missiles in the mid-1950's, the work at Lewis on chemical rocket propulsion increased, and further studies of nuclear rockets were pursued. At present, work is continuing on all of these propulsion systems.

Of more direct interest as background for this conference, however, is the origin of the work related to electric rockets, space power, and the possibilities for thermonuclear fusion for propulsion. Our active studies in each of these areas date back to 1956. That year marked the intensification of Lewis studies in space missions and space propulsion in general. These studies showed, among other things, the potential importance of electric rockets and low-mass electric power systems for space propulsion. The research and development programs in electric propulsion and space power systems were initiated shortly thereafter. The plasma physics aspects of electric rockets are presented in the first paper Two space power system concepts that involve plasma physics to a substantial degree - magnetogasdynamic and thermionic systems -- are also discussed. These papers represent, of course, only a small portion of Lewis programs in these areas, since some types of electric rockets and space power systems are now in the development stage.

In studying electric rockets, Lewis has acquired experimental facilities which are uniquely suited to studying certain subjects not directly related to propulsion and power. One of these studies, the simulation of solar-wind magnetosphere interaction, is described in the paper by Donald Chubb. In another research paper John Dugan describes some studies of plasma chemistry and ion-molecule interactions that are related to all of the plasma programs, but which have much more basic and general interest.

Lewis interest in fusion research also started in 1956 when the Atomic Energy Commission released some results of studies of means to achieve controlled thermonuclear fusion power. At that time, a preliminary study was made here at Lewis of possible propulsion applications of controlled fusion. This study concluded that controlled fusion, if achieved, could have significant aerospace propulsion and power applications, provided that sufficiently lightweight magnetic containment and ignition systems could be developed. This low mass requirement is not significant for terrestrial applications. It represents one of several differences between terrestrial and aerospace fusion applications. This was the beginning of the Lewis exploratory program to develop high-intensity, large-volume electromagnets with the lowest possible mass. The program is still in progress, and the results are described in the fifth paper of this conference. Since that beginning, other potential aerospace uses for such low-mass magnets have become evident. These include magnetogasdynamic power generation, some types of electric thrusters, and possibly shielding from high-energy charged particles. Some of the electromagnets that we have developed are unique facilities for basic research on the effects of intense magnetic fields. The solid-state research that is being carried out in these magnets is described in the paper by John Woollam. In addition, the technology developed in this area can be expected to benefit the many terrestrial applications of magnetic fields and high current densities.

In 1958 we initiated a small program on plasma heating to go with the studies to produce bigger and stronger magnetic fields. The most appropriate heating method appeared to be ion cyclotron resonance heating. A program was set up to study this process in the steady state, in contrast to the programs at Princeton and elsewhere that were using pulsed radiofrequency power. Our reasons for going to a steady-state heating method rather than pulsed methods were that it seemed more suitable for eventual propulsion applications and that it simplified the problems of diagnostics to determine what was going on. The results on this and related plasma heating studies are presented in the third paper.

The plasma physics and plasma engineering programs described herein cover a very broad range of plasma parameters -- broader, I believe, than that being studied at any other single laboratory. This range of plasma parameters is shown in figure 1 where plasma regimes are indicated on a density-temperature field. For MHD and thermionic power generation, the concern is with high density, but relatively low temperature -- with a high neutral background in MHD case, and a low neutral background in the thermionic plasma. In thrusters there are higher energies, but somewhat lower densities, particularly for ion thrusters. The exhaust plasma beam from thrusters is much lower in density, and such exhausts are being used to try to simulate the solar wind impinging on the Earth's magnetosphere. In fusion-related plasma experiments we try to achieve both high temperature and higher density, with the lowest possible neutral or impurity background. This broad scope of plasma research is very useful to us, and leads to some profitable cross-fertilization.

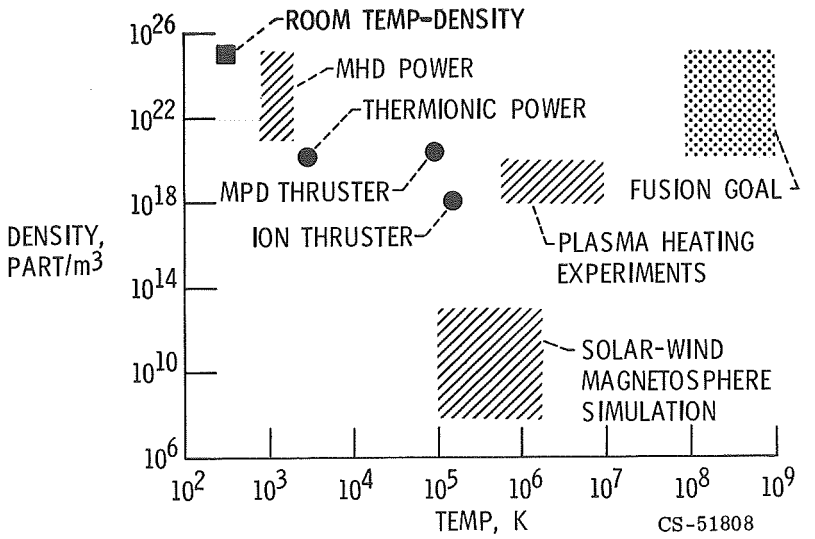


Figure 1. - Plasma regimes studied at Lewis Research Center.

Now that the origin of the work described in this conference has been presented, I will illustrate the main reason for our interest in these subjects. The fact is that we are still rather poorly prepared, from the propulsion standpoint, to undertake exploration of space. Man has reached the Moon, and there is some talk about going on to the stars. But we are still quite inadequately endowed, even conceptually, with propulsion systems suitable for exploration of our own solar system. The trip times are excessive, even to the near planets, if we are limited to propulsion systems now in use or in the development stage.

To illustrate the extent of the inadequacy, I will show some results of a recent mission study[1] which indicates the propulsion system performance that is needed as function of the round-trip time to reach various planets of our solar system. For the purpose of illustration, the space propulsion systems are divided into two types. Type I consists of high-thrust systems whose performance is limited by the specific impulse (or exhaust jet velocity) that they can attain. Typical examples are chemical rockets, solid-core nuclear rockets, and probably also gas-core nuclear rockets, if they become feasible. These systems can produce thrust with nearly impulsive bursts so that the vehicle travels almost entirely along free fall conic-section trajectories.

Type II systems can achieve high specific impulse, but they are limited primarily by the specific mass - that is, the mass per kilowatt of jet power produced. Electric rockets and fusion rockets (if they become a reality) fall into this category. These systems produce low thrust relative to the mass of the vehicle, so they must keep pushing for a major part of the trajectory. In this respect, they are more like our terrestrial transportation systems than are the type I rockets. The trajectories are more complicated and must be calculated by numerical integration procedures.

Figure 2 shows the specific impulse needed for type I propulsion systems for round trips to Mars as function of trip times. These curves are for the interplanetary part of the mission only and for single- or two-stage vehicles. These vehicles are assumed to have been launched to escape velocity from Earth by a suitable high-thrust chemical or nuclear launching rocket. The vehicle then travels to Mars and returns to Earth with only a short stopover time. This mission can be thought of as a resupply mission for a Martian base, in which a payload is unloaded at Mars and one of about equal mass is loaded on and returned to Earth. It represents the shortest round-trip time possible with a fixed payload mass as function of the attainable specific impulse of the propulsion system.

---

[1]Moeckel, Wolfgang E.: Propulsion Systems for Manned Exploration of the Solar System. Astronautics and Aeronautics, vol. 7, no. 8, Aug. 1969, pp. 66-77.

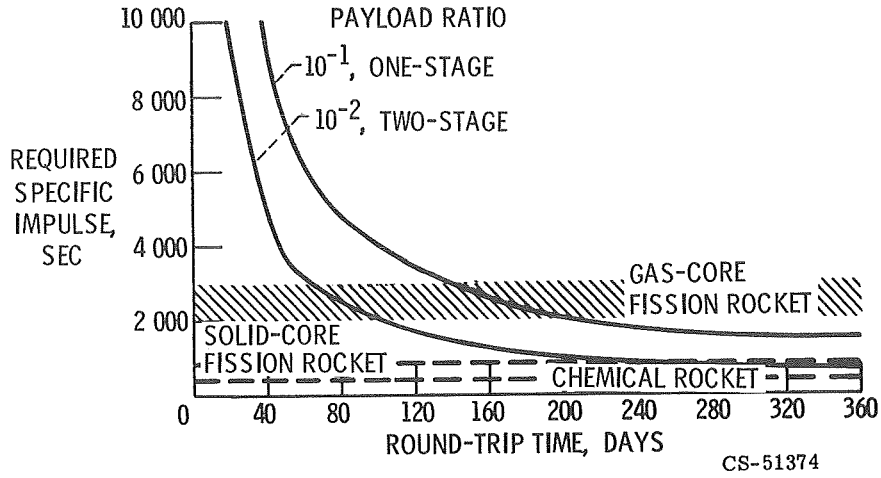


Figure 2. - Mars "quick trip" requirements. Type I propulsion; Earth orbit to Mars orbit and back.

The single-stage vehicle with $10^{-1}$ payload ratio represents a reasonable size for assembling and launching on such a mission. A typical payload may be of the order of 50 000 kilograms, so that the entire vehicle would have a mass of 500 000 kilograms. This mass, together with a nuclear rocket for launch to escape velocity, could be assembled in low Earth orbit with five or six Saturn V launch vehicles. The two-stage vehicle, with $10^{-2}$ payload ratio, represents an upper extreme mass ratio that might be contemplated if mission costs were not a factor, or if payloads were much smaller.

This figure shows that solid-core nuclear fission rockets with a specific impulse of 850 seconds would require about 300 days for the two-stage vehicles, and they would be incapable of performing the single-stage mission. If a gas-core nuclear fission rocket could be developed with specific impulse of 2500 seconds, this mission could be done in 3 to 6 months. This is still a long voyage for resupply and maintenance of a remote base. For that application, a round-trip time of a month would be desirable, but this would require specific impulses far beyond those attainable with any known type I propulsion concept.

Figure 3 shows what we can do for the same mission with type II propulsion systems. With an electric rocket with a specific mass of about 7 kilograms per kilowatt, which may be achievable in the not too distant future, this mission can be accomplished with the single-stage in about a year. With a specific mass of about 1 kilogram per kilowatt, which may be possible with fusion rockets, the trip time

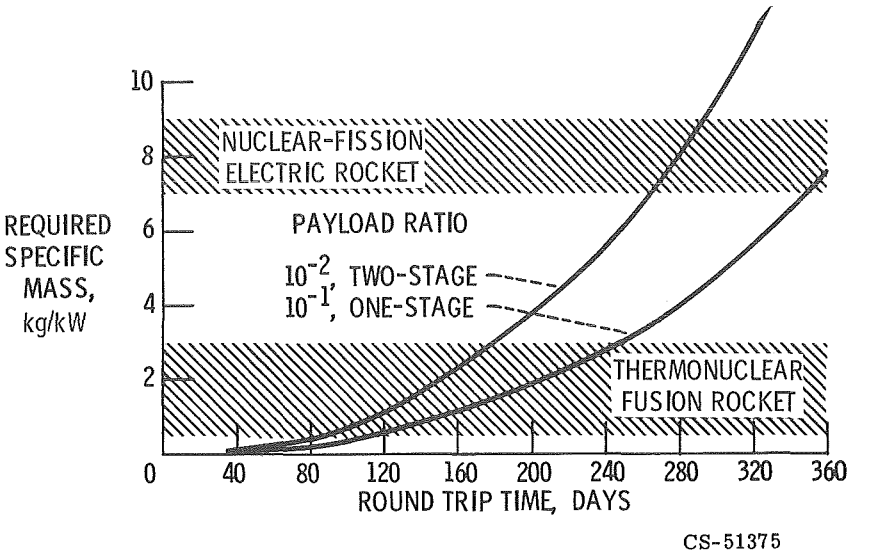


Figure 3. - Mars "quick trip" requirements. Type II propulsion; Earth orbit to Mars orbit and back.

is reduced to about 5 months for the single-stage vehicle. Again, the reduction is well worth achieving, but it still does not get us to the 30-day range. We can foresee no propulsion concept that approaches the 0.1 kilogram per kilowatt level or lower that would be needed. The nearest might be a fusion rocket operating without external magnetic containment, perhaps with high pinch currents through the plasma. But such plasma heating and containment schemes have been shown to be highly unstable and incapable of net fusion power output.

Mass annihilation as a potential lightweight energy source and a photon rocket for high specific impulse have frequently been suggested. However, the energy released per unit fuel mass is not the limiting factor once we have progressed from chemical to nuclear power. The problem is really one of containment of the power and its conversion to directed jet power. This containment and conversion problem is what determines the maximum specific impulse of a type I system and the minimum specific mass of a type II system.

Figure 4 shows what is required to reach the more distant planets with type I systems. The same out-and-back mission is assumed. If a 3-year voyage is assumed as the maximum a crew can be expected to tolerate, we can just about make it to Jupiter with the specific impulse of solid-core nuclear rockets (850 sec). With gas-core fission rockets ($I_{sp}$ = 2500 sec), the Jupiter trip is reduced to $1\frac{1}{2}$ years and Saturn would be attainable in a 3-year trip.

For type II systems, figure 5 shows that a voyage can be made to Saturn in 3 years with the specific mass expected for nuclear-electric rockets. If fusion

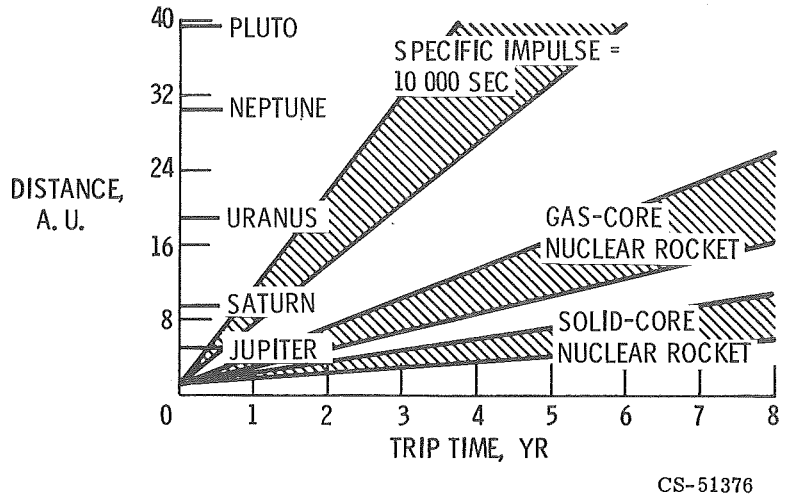


Figure 4. - Round-trip time to planets. Type I propulsion; payload ratio, $10^{-1}$ to $10^{-2}$ after launch to Earth escape velocity.

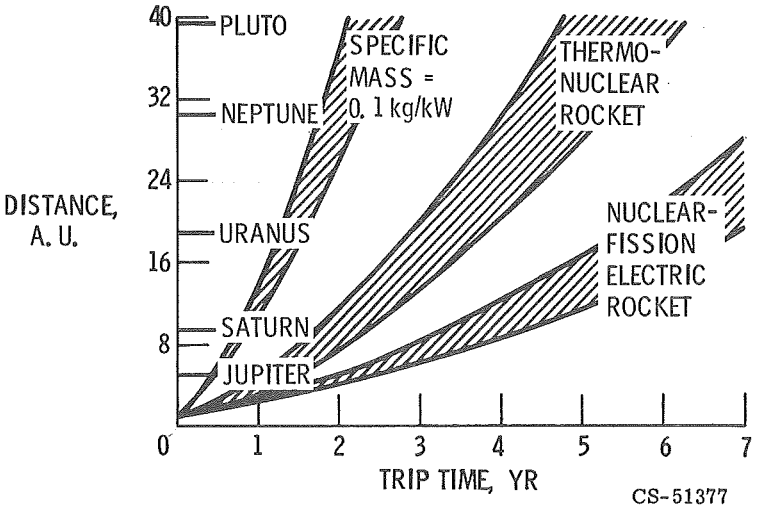


Figure 5. - Round-trip time to planets. Type II propulsion; payload ratio, $10^{-1}$ to $10^{-2}$ after launch to Earth escape velocity.

becomes a reality and the anticipated specific mass of 1 kilogram per kilowatt can be achieved, a trip out to Uranus and back could be made in 3 years. Again, to get to Neptune or Pluto and back in 3 years requires propulsion capabilities far beyond anything now anticipated. However, with some gravitational assists from Jupiter or Saturn, we might be able to reach all planets occasionally with 3-year trips.

In dwelling on the inadequacy of the existing and anticipated propulsion systems for quick trips to Mars and 3-year trips to the outer planets, my intention was to illustrate that the propulsion capability is ultimately the primary factor which will determine the extent and frequency of manned space voyages. This is true not only for the outer planets, but also to the near planets and to the Moon. Research should continue to determine the feasibility and limitations of advanced propulsion concepts. Plasmas and magnetic fields play dominant rolls in many of these advanced concepts.

# I. PLASMA PHYSICS OF ELECTRIC ROCKETS

George R. Seikel, Denis J. Connolly, Charles J. Michels, Edward A. Richley, J. Marlin Smith, and Ronald J. Sovie

Most electric thrusters make use of plasma. This paper attempts to focus on the major plasma processes of two basically different type thrusters, which are being investigated over a wide range of power levels (figs. I-1 and I-2). They are the electron bombardment ion thruster and the magnetoplasmadynamic (MPD) arc thruster. Discussions of alternative types of electric thrusters are included in references 1 to 4.

NASA Lewis Research Center has been doing research on both electron bombardment ion thrusters and MPD arc thrusters for a number of years. In both, a plasma is created by a dc discharge between a central cathode and a cylindrical anode in a diverging axial magnetic field, and ultimately a high velocity plasma exhaust is produced.

The ion and arc thrusters, however, employ completely different concepts to accelerate the propellant. The ion thrusters use strong electric fields applied by an accelerator grid to extract and accelerate the propellant ions produced in the discharge. The MPD arc thruster uses forces produced by the interaction of currents and magnetic fields to accelerate the plasma.

This paper will mention the current status and performance of both of these thrusters. But, the approach will be to primarily examine how they work and what limits their performance. The major inefficiencies in both are shown to result from the same plasma processes.

## ELECTRON BOMBARDMENT ION THRUSTER

### Concept

The electron bombardment thruster is a member of a broader family of thrusters known as electrostatic thrusters. These thrusters differ mainly in the manner in which they create ions. They are basically the same in terms of the method of accelerating the ions and it is from that process that they get their name. Fig-

ure I-3 illustrates the electrostatic acceleration process. An ion source is shown followed by an accelerator electrode system. An electric field is established between the set of electrodes in such a manner that it causes, in this case, positively charged ions to be accelerated to the right and leave the spacecraft. For each ion that leaves the spacecraft, though, an electron remains that must be removed so that the spacecraft will maintain charge neutrality. These electrons are shown being introduced into the beam downstream of the thruster. The lower portion of the figure shows a potential field diagram of the potentials as they would exist in the electrode system and downstream of the thruster. Thrust per unit area is proportional to the square of the field strength, which is labeled $E_a$ in the figure. At Lewis we have worked mainly with electron bombardment thrusters. This thruster was invented by Harold Kaufman, a research scientist at Lewis (ref. 5).

## Bombardment Thruster Configuration

Figure I-4 is a schematic diagram of a 15-centimeter-diameter SERT II thruster (SERT stands for Space Electric Rocket Test). In 1964, Lewis managed the SERT I flight test. This test was a ballistic flight launched from Wallops Island which served to demonstrate that electron bombardment thrusters would work in space. Lewis is presently preparing for the SERT II flight test which will be a 6-month duration test of an electron bombardment thruster.

This SERT II thruster operates as follows. Liquid mercury propellant is brought in from the left and contacts the vaporizer which is a heated porous plug. There it is vaporized and the mercury vapor passes to the right into a plenum chamber where it then passes (see the small arrows in the fig. I-4) into the main body or discharge chamber. A small portion of the propellant enters the discharge chamber through the hollow cathode. In the chamber a mercury plasma is created as a result of electrons which are emitted from the hollow cathode and keeper arrangement. The electrons pass into the chamber, ionize the propellant, and eventually arrive at the anode. The entire chamber including the screen electrode is maintained at high positive potential. The accelerator electrode is maintained at a negative potential and an appropriate electric field is established between these two electrodes so that ions from the discharge are extracted, accelerated, and exhausted to the right. The neutralizer cathode and keeper arrangement is used to introduce electrons into the exhaust beam. The thruster is surrounded by a grounded screen that would be maintained at spacecraft potential. To enhance the ionization process, a weak magnetic field is imposed on the discharge chamber by means of bar magnets located around the periphery of the chamber and which are in contact with soft iron pole pieces. As

illustrated in figure I-5, magnetic flux emanates from the tips of the so-called pole pieces and gives rise to a divergent magnetic field in the discharge chamber.

## Bombardment Thruster Performance

Bombardment thrusters have been tested at Lewis in sizes ranging from a few centimeters to 150 centimeters in diameter at power levels ranging from a few watts up to 150 kilowatts and at thrust levels ranging from a fraction of a millipound up to 1/2 pound. Figure I-6 summarizes present day performance in terms of the variation in overall efficiency as a function of specific impulse. As a point of reference, the SERT II performance point is shown at about 4500 seconds specific impulse and about 72-percent overall efficiency. The SERT II thruster has been tested in vacuum facilities for more than 3000 hours. Current research is concentrating on the specific impulse range of 2000 to 3000 seconds where, as a result of some recent improvements in thruster performance, efficiencies in the range of 50 to 60 percent are being obtained. This range of specific impulse has been shown from mission analysis studies to be one of great interest for a number of possible applications for electron bombardment thrusters.

For our research investigations, table I-1 shows a summary of a typical thruster performance point for a 30-centimeter-diameter research thruster. From this table it can be seen that the discharge chamber power is a significant portion of the total power and one which we would like to minimize. If the discharge chamber power is divided by the beam current, in this case $1\frac{1}{2}$ amperes, the resulting parameter is the amount of energy required to create an ion in the beam. This parameter is called "eV per ion" and is used to evaluate the effects of various thruster modifications. This parameter is plotted in a number of different ways. For example, figure I-7 is a plot of the discharge energy against propellant utilization efficiency. The propellant utilization efficiency is the beam current divided by the flow into the thruster expressed as an equivalent current. Here we see that the eV per ion stays at about 200 up to a value of utilization efficiency of about 80 percent. It is interesting to note that when Lewis started research on the electron bombardment thrusters (about 10 years ago) values of eV per ion at 80 percent propellant utilization efficiency were about 1250. So there has been more than a factor of six improvement over this 10-year time period. This improvement has been primarily the result of experimental efforts in the laboratory rather than the development of theories that predict the behavior of the plasma in the discharge chamber. The empirical approach was followed because the plasma of the discharge chamber is very complex as is illustrated by figure I-8.

In figure I-8, the discharge energy loss is plotted against magnetic field strength where, for the purposes of these investigations, the permanent magnets of the thruster are replaced by electromagnets so that the magnetic field can be varied. According to a classical electron diffusion theory, the eV per ion should drop as the magnetic field increases. This is found to be the case in practice up to a point (labeled $B_{critical}$ in this plot). Beyond this magnetic field value it is found that the eV per ion does not decrease in accordance with classical diffusion considerations but in fact may increase and exhibit an anomalous behavior. We have investigated a number of magnetic field configurations to determine their effect on performance. In one case, for example, a magnetic field was configured to be similar to the "minimum B" configurations used in some fusion experimental research programs. This configuration was found to be effective in moving the critical magnetic field value to the right somewhat (fig. I-8) and in suppressing plasma noise in the exhaust beam; however, it was not particularly effective in reducing the eV per ion. Another approach was to use the previously described diverging magnetic field (fig. I-5). This configuration was found to be the most effective in reducing the eV per ion.

## Ion Extraction System

The greatest reductions in discharge chamber power, however, have been associated with modifications of the ion extraction system. At Lewis, analog and computer techniques for investigating various ion extraction designs have been developed. For example, figure I-9 shows a single hole of the SERT II grid system as it would be set up for modeling on the digital computer program. On the left the shaded portion represents the plasma of the discharge chamber, and the sheath is shown as the parting line between the plasma and the accelerating field region of the grid system. The screen electrode is depicted by the small rectangular blocks and the accelerator electrode by the larger ones. These blocks represent the web of the grids. With this model the digital computer program yields the ion trajectories as they leave the plasma sheath and pass through the grid system as well as the distribution of equipotentials in the grid region.

One startling improvement in performance associated with the grid system resulted from increasing the screen electrode percent open area. In the past the screen electrode holes were similar in size to the accelerator electrode holes (about a 50-percent open area). It was found that increasing the screen electrode percent open area to about 70 percent reduced the discharge chamber losses by a factor of two. We believe this is primarily a result of exposing more of the plasma sheath

area to the extraction field of the grid system. We have been pursuing approaches which we believe can take further advantage of this idea.

Figure I-10 is a comparison of the conventional grid system just described with a newer one - a glass-coated or composite grid. In the new approach a coating of glass is bonded to the accelerator grid. We believe the plasma attaches to the upstream surface of this glass in such a way that an electric field is established along the surface of the glass. Thus, ions are extracted in much the same manner as with the conventional system. With this newer glass-coated grid, high performance at low specific impulses has been achieved. For example, at 2000 seconds specific impulse values of eV per ion of 200 have been obtained with the glass-coated grid as compared with values of 400 or greater with the conventional grids. Of course, the structural advantages of the single glass-coated grid concept are apparent. It eliminates both the need to maintain close spacing between the screen and accelerator grid and alinement between the screen and accelerator grid. These are two important advantages of this new very attractive grid concept.

## Present Research Aims

In summary, electron bombardment thrusters appear to have good efficiency at the higher specific impulse levels, and they recently have been making strong gains in performance in the lower specific impulse regions. In our research programs we are focusing on this lower specific impulse region because of its potential application to a number of missions. Work with the coated optics is continuing, and we are now beginning to examine the possibility of coating other components of the thruster which we believe may result in better performance. Of course, we still need a better understanding of the discharge chamber plasma, and in that respect we have recently initiated a spectrographic experiment which we hope will shed some light on the plasma characteristics.

# ION SOURCE POWER BALANCE

As discussed in the preceding section, the major inefficiency in a bombardment ion thruster is the plasma discharge energy expended per beam ion produced. This eV per ion is a gross parameter that characterizes the performance of the ion source. An understanding of the plasma processes that limit a dc ion source performance can be obtained by examining a power balance.

If only unavoidable discharge losses are considered, then the limiting per-

formance can be determined. The two major unavoidable losses in a dc discharge are the power lost to the anode and the power consumed in ionization.

The average electron arriving at the anode brings with it at least twice its kinetic temperature $kT_e$. It also deposits in the anode the energy it gains falling through the anode work function $\Phi_A$. Since the electron current to the anode will be greater than or approximately equal to the total anode current $I_A$, the power lost to the anode $P_A$ can be written

$$P_A \gtrsim \left( 2 \frac{kT_e}{e} + \Phi_A \right) I_A \tag{1}$$

The discharge power consumed in ionization $P_I$ is

$$P_I \gtrsim I_B \Phi_{EFF} \tag{2}$$

where $I_B$ is the beam ion current and $\Phi_{EFF}$ the energy required to produce an ion in the plasma discharge. The greater than sign results from the fact that only in the most advantageous limit would all the ions produced in the discharge be usefully exhausted as beam current.

## Volume Ion Production Cost

The volume ion production cost $\Phi_{EFF}$ has been evaluated for the sustained tenuous plasmas generated in low pressure discharges by considering the collisional and radiative losses in the plasma volume. Results have been obtained for specific gases (refs. 6 to 8) and an approximate general theory (ref. 9) has also been developed that is applicable to all gases. Jack Dugan discusses the atomic models used in this general calculation in his presentation Plasma Chemistry and Ion-Molecule Interactions. Typical results for the volume ion production cost for mercury are shown in figure I-11. The volume ion production cost in eV per ion is presented as a function of electron kinetic temperature in this figure. The number of ions produced per unit volume can also be predicted as a function of electron kinetic temperature. Of course, the product of the ion production rate and volume ion production cost is the power consumed in ionization and excitation processes per unit volume.

## Limiting Ion Source Performance

If only the minimum anode power and ionization power losses are considered, then the limiting performance of a dc ion source can be evaluated. The analysis uses only conservation of energy and current. If the discharge has a constant electron kinetic temperature $kT_e$ (eV), then for a given propellant, discharge voltage V, and anode work function $\Phi_A$, the discharge energy per beam ion is only a function of electron temperature:

$$\text{Energy per beam ion (eV/ion)} = \frac{2\frac{kT_e}{e} + \Phi_A + \Phi_{EFF}}{1 - \frac{2\frac{kT_e}{e} + \Phi_A}{V}} \tag{3}$$

Results for mercury are shown in figure I-12 for $\Phi_A = 4.5$ volts, which is the value for tungsten. The eV per ion curves are shown as a function of $kT_e$ for V = 25, 36, and 150 volts. For each V there is an optimum $kT_e$. Their locus is shown by the dashed curve.

The eV per ion becomes large at low temperatures because as shown in figure I-11 the volume ion production cost is becoming unbounded. The eV per ion also becomes unbounded as

$$\frac{kT_e}{e} \to \frac{1}{2}(V - \Phi_A)$$

because at this temperature all the power is being lost to the anode. When the discharge is operating near the optimum temperature, approximately half the discharge power is lost to the anode and the outer half is consumed in the inelastic atomic processes in the plasma volume.

These minimum values of eV per ion indicate that the performance of present ion sources (under 200 eV/ion at 36 V) may be approaching a fundamental limit. Such a conclusion is however not warranted since a number of simplifying assumptions have been made in evaluating this power balance. Thus these values should be viewed only as a first approximation to the performance limit of such sources.

These results, however, do demonstrate both the importance of examining the power balances for ion sources, and they do indicate the potential performance gains

possible through raising the discharge voltage. Also, similar calculations for propellants other than mercury showed that cesium and possibly xenon ion thrusters might outperform mercury thrusters at least from the point of view of an energy efficiency.

## MPD ARC CONCEPT

A typical MPD arc thruster is shown schematically in figure I-13. Its major components are a cathode, anode, insulator, and magnet. Although MPD arc thrusters are not as highly developed and have not achieved as high a performance as the electron bombardment ion thrusters, they do possess a number of relative advantages. The MPD thrusters are physically and electrically simpler, they have an order of magnitude higher thrust density, and a given thruster can operate over a wide range of specific impulse. An MPD arc thruster system may potentially, also, be substantially lighter than an equivalent ion thruster system.

NASA-Lewis has tested steady-state radiation cooled MPD thrusters at power levels from 100 watts to 40 kilowatts. In the higher power radiation cooled thrusters the magnet must be located as shown in figure I-13 upstream of the anode because of the high heat flux from the radiation cooled anode. If adequate insulation is provided, a permanent magnetic can be used. In the lower power devices one has the option of using a magnet coil surrounding the anode or a combination of both. Water cooled dc MPD arcs have been operated to power levels of over 200 kilowatts and we are also operating a pulsed MPD arc of this same geometry at powers up to 4 megawatts for a fraction of a millisecond.

In the particular category of MPD arc thrusters on which we have been doing research, most of the thrust results from the interaction of an induced azimuthal current and the radial component of the applied diverging magnetic field, the magnetic nozzle. There are, however, also simultaneously present two other thrust mechanisms.

But before discussing the various acceleration mechanisms in an MPD arc, it would be well to examine briefly the general interactions of currents and magnetic fields and electric fields associated with these in a plasma.

### Plasma Ohm's Law

Figure I-14 shows a vector diagram of plasma current, magnetic field, and electric field. The figure illustrates first that if you pass a current through a

plasma or any other conductor in the presence of a magnetic field you get a Lorentz force or electromagnetic force, which is the vector product $\vec{j} \times \vec{B}$ and is perpendicular to both the current density $\vec{j}$ and the magnetic field $\vec{B}$. In a plasma you get some other effects that are not so common in ordinary conductors. The electric fields that are associated with this current are comprised of the normal resistive component $j/\sigma$ that is parallel to the current ($\sigma$ being the conductivity) plus a component of electric field perpendicular to the current flow direction. This is termed the Hall field, and it is given by the quantity $(\omega\tau/\sigma)\left[\left(\vec{j}\times\vec{B}\right)/B\right]$. The parameter $\omega\tau$ is defined as the electron Hall parameter where $\omega$ is the electron cyclotron frequency (i.e., the frequency with which electrons spin around the magnetic field lines), and $\tau$ is the mean time for an electron to lose its momentum by collision. As a result, the equivalent electric field $E^*$ in figure I-14 is comprised of two components and is not parallel to the current. The angle between the equivalent electric field and current is denoted here as $\theta$. The arc tangent of $\theta$ is equal to the Hall parameter times the sine of the angle between the magnetic field and the current:

$$\tan^{-1}\theta = \omega\tau \sin\varphi$$

The corresponding Ohm's law is

$$\vec{E}^* = \frac{1}{\sigma}\left[\vec{j} + \omega\tau\left(\frac{\vec{j}\times\vec{B}}{B}\right)\right] \tag{4}$$

where the equivalent electric field is defined

$$\vec{E}^* = \vec{E} + \vec{v}\times\vec{B} + \frac{\nabla p_e}{en_e} \tag{5}$$

which is the sum of the applied field plus a $\vec{v}\times\vec{B}$ field plus a term due to the electron pressure gradient divided by the electron charge density.

## Instabilities and Turbulence

In addition to the Hall effect on Ohm's law there are effects due to oscillations or turbulence. Since plasmas are rarely quiescent, oscillations are nearly always present. In some cases these fluctuations are of sufficiently small amplitude that

they can be ignored. However, under some circumstances (generally termed instability) these oscillations grow to such large amplitudes that they totally govern the phenomena being observed. Here are some examples of these circumstances:

First is the anomalous or Bohm diffusion - that is, the enhanced diffusion of charged particles across magnetic field lines. This diffusion is important in the nuclear fusion field since here the endeavor is to contain charged particles within magnetic field configurations. This is discussed in greater detail in the paper by Rayle et al. As already mentioned, anomalous diffusion also is the cause of an increased energy to produce an electron-ion pair in the ion thruster and hence leads to a decrease in the efficiency of the device.

Second, fluctuations also play an important role in the performance of MHD power generators as is discussed in the paper by Lester Nichols. In this case fluctuations lead to a saturation of the Hall parameter at a value of the order of one even though the magnetic field is continually increased. This is an undesirable result since the performance of these devices is a strongly increasing function of the effective Hall parameter.

Third, in MPD accelerators the phenomenon appears to manifest itself by concentrating the current in the form of a rotating current spoke rather than allowing it to have azimuthal symmetry about the cathode.

To illustrate the influence of oscillations on plasma devices, consider their effect on Ohm's law. From a theoretical standpoint, the problem is one of providing a theory which agrees with what is observed experimentally. This can best be understood by recognizing that while Ohm's law as presented (eq. (4)) may well be valid within the little black box which is the experiment, we are in general observing that experiment from the outside by way of ammeters and voltmeters which cannot resolve in time or space the high frequency oscillations in the plasma. So in effect average values are measured. Therefore, the theory need only predict these average values.

To better understand this statement, consider the effect of electron density fluctuations on Ohm's law. For simplicity assume the following: (1) the pressure gradients are negligible, (2) only Coulomb collisions are important so that the electrical conductivity $\sigma$ is independent of the electron density, and (3) the induced magnetic field is negligible relative to the constant applied external field so that the cyclotron frequency $\omega$ and the magnetic field $\vec{B}$ are also independent of time. Therefore, $\sigma$, $\omega$, and B are independent of time as denoted by the subscript o.

It is convenient for theoretical development to separate the current into two parts:

$$\vec{j} = \vec{j}_o + \vec{\tilde{j}} \tag{6}$$

so that the measured or average value is

$$\langle \vec{j} \rangle = \vec{j}_o \tag{7}$$

Therefore in order to obtain correspondence between theory and experiment an expression must be established for $\vec{j}_o$. To do this, the quantities $\vec{j}$, $\vec{E}$, and $\tau$ are written as in equation (6) (i.e., the sum of an average plus fluctuating part) and substituted into Ohm's law (eq. (4)) which is then averaged to yield

$$E_o = \frac{1}{\sigma_o}\left( \vec{j}_o + \omega_o \tau_o \frac{\vec{j}_o \times \vec{B}_o}{B_o} + \omega_o \tau_o \left\langle \frac{\tilde{n}_e}{n_{eo}} \tilde{\vec{j}} \right\rangle \times \frac{\vec{B}_o}{B_o} \right) \tag{8}$$

where we have used the fact that $\tau$ is inversely proportional to $n_e$ for Coulomb collisions and have assumed that the fluctuation quantities are sufficiently small so that we need only retain terms which are quadratics - that is, to order of the product of fluctuating quantities.

Equation (8) has the same form as equation (4) except it contains the extra term $\omega_o \tau_o \left\langle (\tilde{n}_e/n_{eo}) \tilde{\vec{j}} \right\rangle \times (\vec{B}_o/B_o)$ which can be put in a more conventional form by multiplying equation (4) by $\tilde{n}_e/n_{eo}$ and again averaging using the additional relations $\nabla \times \vec{E} = 0$ and $\nabla \cdot \vec{j} = 0$ to obtain

$$\vec{E}_o = \frac{1}{\sigma_{EFF}} \left[ \vec{j}_o + (\omega\tau)_{EFF} \frac{\vec{j}_o \times \vec{B}_o}{B_o} \right] \tag{9}$$

which has exactly the same form as the original Ohm's law but $\sigma$ and $\omega\tau$ are effective values given by

$$\sigma_{EFF} = \frac{\sigma_o}{1 + \left\langle \frac{\tilde{n}_e^2}{n_{eo}^2} \right\rangle (\omega_o \tau_o)^2} \tag{10}$$

$$(\omega\tau)_{EFF} = \frac{\omega_o \tau_o}{1 + \left\langle \frac{\tilde{n}_e^2}{n_{eo}} \right\rangle (\omega_o \tau_o)^2} \tag{11}$$

Obviously transport coefficients are grossly modified from their steady state or usual gas kinetic values (i.e., $\tau_o$ and $\omega_o\tau_o$) in the presence of fluctuations as $\omega_o\tau_o$ becomes large.

In order to establish the magnitude of the fluctuation $\left\langle n_e^2/n_{eo}^2 \right\rangle$, one must evaluate in the presence of the electron density fluctuation all other pertinent equations (i.e., electron density, etc.). In the case of MHD generators, for example, it can be shown (ref. 10) that

$$\left\langle \frac{\tilde{n}_e^2}{n_{eo}^2} \right\rangle \propto \frac{1}{\omega_o\tau_o}$$

so that $(\omega\tau)_{EFF} \rightarrow$ constant as $\omega_o\tau_o \rightarrow \infty$; that is, the effective Hall parameter saturates.

Later in this discussion results are presented of some calculations performed in the supersonic expansion region of a MPD thruster where reasonable agreement with experiment is obtained assumming $(\omega\tau)_{EFF}$ = constant.

## MPD Acceleration Mechanisms

Figure I-15 illustrates the current and magnet field distribution in a typical MPD arc thruster. Current is shown with solid lines and magnetic field by dashed lines. The applied arc current between the anode and cathode flows radially with some pluming into the exhaust. The applied magnetic field diverges to form what can be termed a magnetic nozzle. In addition to the applied magnetic field there is an azimuthal magnetic field which is caused by the applied arc current itself. In addition to the applied arc current there is, as already indicated, an induced azimuthal current. Why it is there will be explained shortly.

With this geometry and these currents and fields there are three basically different thrust mechanisms simultaneously present:

1. Pressure on the physical nozzle
2. Direct magnetic pumping, $j_r B_\theta$
3. Magnetic nozzle processes, $j_\theta B_r$
   - (a) Expansion
     - (1) Recovery of thermal energy, $j_\theta \propto \partial p/\partial r$
     - (2) Recovery of swirl energy, $v_\theta \propto j_r B_z$
   - (b) Drift current, $j_\theta \propto \vec{E} \times \vec{B}$

The first is simply the ordinary gas dynamic pressure on the physical anode nozzle. The second is the direct plasma acceleration which is termed magnetic pumping (sometimes also termed blowing) and is the result of the interaction of the radial current and the azimuthal magnetic field. The third category is the magnetic nozzle plasma acceleration process which results from the interaction of the azimuthal current with the radial field of the magnetic nozzle.

As indicated, there are two major subcategories of magnetic nozzle processes. The first subcategory, the processes termed "expansion" in a magnetic nozzle, is analogous to expansion processes in an ordinary physical nozzle. In the conversion of thermal energy into directed energy in a magnetic nozzle, the radial plasma pressure gradient gives rise to a diamagnetic azimuthal current. With regard to the second subcategory of expansion processes, the interaction of the applied arc current and applied magnetic field causes rotational or swirl energy to be added to the plasma. In the subsequent expansion in the magnetic nozzle, energy and angular momentum are conserved, and the swirl energy is converted into directed energy. Associated with this conversion is an azimuthal current driven by the $\vec{v} \times \vec{B}$ electric field. Thus associated with expansion processes in a magnetic nozzle are two mechanisms that cause azimuthal current to be induced in the magnetic nozzle. A third alternative mechanism is the drift current which may result from the interaction of the applied electric and magnetic fields.

For any given MPD arc experiment the thruster mass flow, current, and magnetic field can be adjusted so as to make any one of the mechanisms discussed important. Conversely, to determine how a given MPD arc thruster is producing thrust requires an assessment of the relative importance of the various possible thrust mechanisms. As indicated earlier, research at Lewis has been aimed at attempting to utilize primarily the magnetic nozzle thrust mechanisms. One can then view the magnetic nozzle MPD arc thrusters as an arc jet in which the physical nozzle has been replaced by a magnetic nozzle so that the gas dynamic heat-transfer losses of the physical nozzle are avoided.

## MPD ARC THRUSTERS

NASA-Lewis is investigating MPD thrusters at both the subkilowatt and multikilowatt power levels. Figures I-2 and I-16 are cutaway drawings of the 30- and 1/2-kilowatt thrusters. Both operate on low voltage dc and have radiation cooled anodes. The two thrusters differ in mass flow rate, power, and thrust level, but have comparable size, efficiency, and specific impulse.

The multikilowatt MPD thruster (fig. I-2) operates with an arc power near 30 kilowatts and produces thrust of about 1/2 newton (1/10 lb). Generally $NH_3$ is used as propellant. Ionization of the plasma exhaust of this thruster is between about 10 and 100 percent. The thrust is developed primarily through magnetic nozzle effects since data show that most of the ion acceleration occurs out in the magnetic nozzle. The ions also apparently drag many neutral particles along with them. Some thrust, of course, is also due to gas-dynamic effects.

The 1/2-kilowatt MPD thruster shown in figure I-16 operates with an arc power of a few hundred watts. The thrust produced is a few millipounds. Xenon propellant has yielded the highest efficiency. It has a lower density discharge that ionizes almost all the propellant atoms. The acceleration in this case also takes place out in the magnetic nozzle.

## Subkilowatt MPD Arc Thruster

In addition to performance measurements, the earliest work done on the subkilowatt thruster was to determine the dominant acceleration mechanism. Figure I-17 shows schematic views of the subkilowatt thruster and profiles of the plasma potential and electron pressure measured by Bowditch (ref. 11). The plasma potential profiles were obtained by emissive probes and the magnetic field lines by magnetic field probes. Generally the electric field is parallel to the magnetic field. This shows no serious currents can arise caused by $\vec{E} \times \vec{B}$ drifts. The potential profiles show that the accelerator voltage drops associated with ion acceleration occur out in the magnetic nozzle.

The electron pressure profiles were obtained by using a Langmuir probe to obtain the electron number density and electron temperature from which the electron pressure was calculated. The gradient of electron pressure divided by the electron density along the axis is found to be proportional to the electric field in that direction. This says that the acceleration occurs in a space-charge free region supported by the electron pressure gradient (refs. 11 and 12).

If the electron pressure is integrated over the area of the station shown at the edge of the nozzle, the resultant force approximates the measured thrust, thus further supporting this magnetic nozzle model. The ions get their energy at the expense of the random electron energy. The ions and electrons are tightly coupled by the requirement that no net currents leave the thruster. Since this was anticipated to be the dominant acceleration mechanism, earlier versions of low power MPD arc thrusters were termed magnetic-expansion thrusters (similar devices have also been

termed oscillating electron thrusters or nonequilibrium magnetically contained electrothermal thrusters).

Other diagnostic work done on this thruster has included determining (ref. 13) that most of the accelerator voltage drop occurs near the cathode. Hence, arc impedance can be controlled by varying the hollow cathode flow. This flow is a few percent of the total propellant flow.

## Magnetic Expansion Process

Walker and Seikel have examined analytically the type expansion process found in the low power MPD arc thruster. Specifically, the expansion of a fully ionized plasma containing hot electrons and cold ions is examined in the magnetic nozzle produced by a Helmholtz set of coils (fig. I-18). The analysis is restricted to near the axis of symmetry and the effects of thermal conduction are included since, as will be shown, these can be important.

The set of equations to be solved includes the electron and ion continuity and momentum equations, Maxwell's equations, and an electron energy equation. No asymptotic solutions to this nonlinear set of equations for large values of z were found using classical values of the conductivity for the plasma. As a result and due to the fact that in the experiments major fluctuations were present, an assumption was introduced that the electron collision time could be replaced by an effective time in the manner described in the earlier fluctuation discussion. In particular, the assumption was made that the effective Hall parameter be a constant throughout the flow. Such an assumption assumes a saturation of this parameter of the type previously described as being appropriate at least for MHD generators.

With this additional assumption, the solutions to the plasma expansion shown in figure I-19 were obtained. The ordinate is the ratio of the final ion energy to the initial electron energy - that is, the final ion energy at the end of the expansion divided by the random energy the electrons had back before the expansion started. This is plotted against the sonic point location. The sonic point location is relative to the downstream coil in the Helmholtz set: zero is at the plane of the coil, and the location is given in coil radii. The parameter in the analysis is a nondimensional parameter best though of as a nondimensional magnetic field.

These solutions illustrate a couple of points. First, the magnitude of the ratio of the final ion energy to the initial electron energy can be much larger than what you would get in an adiabatic expansion. The adiabatic expansion result is shown by the dotted line, and this illustrates how important the thermal conduction can be in such a process. The second point is that for sonic point locations near the plane of the

downstream coil the solutions are fairly insensitive to the sonic point location. However, if the sonic point moves a coil radii downstream of that plane, then the solutions become very sensitive to the sonic point location.

The results of this analysis can be used to make a power balance for the low power MPD arc thruster. The results of figure I-19 give the final energy of the ion in terms of the upstream temperature. As described earlier, in making a power balance for the ion sources, the anode losses for such a discharge are also a function of the upstream electron temperature as are the ionization losses. Thus, the results of figure I-19 can be combined with the minimum anode power and volume ionization power losses to make a power balance for the low power thruster. This results in predicting a limit to the efficiency as a function of specific impulse. The results of such a calculation are shown in the figure I-20. Calculations were done for xenon propellant, a discharge voltage of 100 volts, and an anode work function of 4.2 volts corresponding to molybdenum. To make these calculations the sonic point location was assumed to be at the plane of the downstream coil. Corresponding to every point along this theoretical limit curve of figure I-20 is an optimum discharge electron temperature and optimum nondimensional magnetic field.

Figure I-20 also shows the efficiency as a function of specific impulse of the present NASA-Lewis low power xenon MPD arc thrusters (ref. 8). The discrepancy between the experiments and the theoretical limit may indicate some substantial gains are possible in the experimental performance of such thrusters. Caution should be exercised though since to make these theoretical limit calculations required assuming the sonic point location. If the sonic point were actually much further downstream than the plane of the downstream coil, then the theoretical limit would be lower. This point brings up one of the big problems yet to be answered for such flows: Where does the sonic point occur and why?

This expansion process that has been described relative to the low power thruster is also present in the higher power devices. But for the high power devices a number of additional effects must be included; for example, it can be shown that the ion temperature must be included. The higher power devices are also only partially ionized. Some of the effects of swirl and pluming of current down into the nozzle may also have to be included. As a result, not much work has been done on the supersonic expansion for the high power thruster; there has, however, been some analytical work done upstream of the sonic point for these higher power devices.

## High Power MPD Subsonic Theory

Typical of the high power MPD arc thruster subsonic analyses is the work of

Workman (ref. 14). Basically, he considers the device to consist of two concentric electrodes with constant flow area upstream of the throat and a downstream diverging expansion region. He then considers the flow of a multicomponent chemically reacting fluid through a constant area duct with heat addition to drive the fluid sonic at the throat. As was pointed out in the preceding section and also by Seals and Hassan (ref. 15), one does not necessarily have to have the sonic point at the throat of the device since the Ohmic heating may extend downstream of the throat allowing the sonic point to occur in the downstream expansion region. The interesting point of Workman's analysis is the fact that the current tends to concentrate at the throat in a distance which is of the order of millimeters while typically the dimensions of these throats are of the order of centimeters. In other words, the current tends to concentrate in a sheet. This current sheet is also observed in the analysis of Rosciszewski (ref. 16).

There is at least some qualitative experimental justification for this result on the basis of the experiments of Shih (ref. 17) as shown in figure I-21. In these experiments Shih segments the anode in the gas flow direction to measure the anode current and heat flux distribution. The anode current distribution is shown by the solid curve. The electric current is very highly peaked in the throat of the device. Therefore, the current attaches over a short distance at the throat.

## High Power MHD Exhaust

Although the theory for the supersonic region of the high power MPD arc thruster is not well understood, some interesting diagnostic studies have been made of the plasma exhaust. One such study is to measure the axial velocity of each species in the plasma exhaust and to determine how they vary as the engine operating parameters are changed (refs. 18 and 19). The velocities were obtained by measuring the Doppler shifts of spectral lines emitted by the various plasma constituents.

Some typical results for the MPD arc operating on ammonia propellant are shown in figure I-22. Here the axial velocity of some plasma species is plotted as a function of axial distance from the anode exit plane. These data illustrate facts that were found to be true for all cases studied. The observed ion and neutral velocities always increased substantially in the magnetic nozzle region outside the thruster. The $N^{+}$ and $N^{++}$ ions always reached about the same peak velocity, and this velocity was always greater than that corresponding to the measured specific impulse. Fast neutrals were observed in every run and their velocities approached those corresponding to the measured specific impulse.

The variation of ion and neutral velocities was studied for a variety of operating

conditions. Consider the trends shown in figure I-23. The data show that increasing the arc power at constant mass flow rate results in higher specific impulse and thruster efficiency. In this case, the better performance is essentially due to an increase in the efficiency of converting the power that is put into the plasma into thrust. Both the ion and neutral velocities increase with increasing arc power. Other measurements also indicate that the degree of ionization and electron temperature increase with arc power in this case.

At constant specific impulse, figure I-23 shows that the efficiency increases with increasing mass flow rate. In this case the exhaust velocities do not change appreciably and it was found that the increased efficiency was due to a decrease in the anode heat loss.

## High Power MPD Losses

For the high power MPD arc thrusters the anode losses run from about 45 to 60 percent of the input power depending on mass flow rate, magnetic field, and arc current. The reason for the losses can be illustrated by returning to figure I-21. The dashed curve is the heat flux to the anode surface as a function of axial position along the anode. The solid curve is the current flux. Note that the two curves almost coincide.

This would seem to indicate that almost all of the anode power loss is carried by electrons in the arc current. Simple sheath considerations mentioned before require the anode heat loss per electron to be at least two times the electron temperature plus the anode surface work function. Upper limits on arc electron temperatures estimated using this rule vary from 10 to 15 electron volts. Such values are at least in qualitative agreement with the previously discussed one-dimensional subsonic high-power MPD theory.

The anode power loss also depends on arc voltage mode. At a given arc power, the current (and hence the anode power loss) is lower in the high voltage mode. Voltage mode behavior is closely related to the way current attaches to the cathode. In this connection, figure I-24 shows an interesting sequence of photographs obtained by McDonnell-Douglas. Each shot of figure I-24(b) shows the cathode tip of the radiation cooled thruster of figure I-24(a) viewed through the anode throat at about a $45^{\circ}$ angle. The time from the start of the sequence (in hours) and the arc voltage at the time of the photograph are shown alongside each picture. Note incidentally that the photographs were taken more than 500 hours into an endurance test of the radiation cooled thruster. The first case has the highest arc voltage and light emanating primarily from the tip of the cathode. In succeeding cases one sees a

progressive decrease in arc voltage and a progressive trend toward current attachment further back on the cathode. In the last case the voltage has dropped drastically and the current attachment has shifted to the extent that only the tip is dark.

Operating in the low voltage mode shown in this last picture is detrimental to thruster life. It does, however, produce somewhat higher arc efficiency in spite of the higher anode losses. Hence the power that is put into the gas is much more efficiently converted to thrust in the low voltage mode.

The present performance of the 30-kilowatt radiation cooled thruster (fig. I-24(a)) is shown in figure I-25. These data (ref. 20) show both that the efficiency increases with arc power and that at constant power the specific impulse can be varied over a wide range. This thruster was developed by McDonnell-Douglas under contract to NASA-Lewis (ref. 21). It represents the first truly radiation cooled high power MPD arc thruster. The thruster is designed with adequate insulation between the anode and the magnet so that a radiation cooled permanent magnet could be utilized.

We are presently looking into the processes which effect the way current attaches to the cathode. We hope that by learning to control this we can raise the arc voltage to lower anode losses while maintaining the advantage of the low voltage mode current distribution.

## Unsteady MPD Arc Phenomena

Thus far only the time average current distribution has been discussed. Its dynamic behavior is more complicated. MPD thrusters operate over a wide range of conditions with the current concentrated into a rotating spoke as depicted in figure I-26. The spoke rotates in the $\vec{j} \times \vec{B}$ direction along with the plasma flow. In the higher power thruster the frequency of rotation is usually from about 100 to 500 kilohertz (ref. 22). The frequency increases with increasing arc current or magnetic field strength and decreases with increasing mass flow rate or anode throat diameter.

In our typical data the current spoke is about one-third of a circle in width. It is very rich in harmonic content. Occasionally low order harmonics are larger than the fundamental. There is a complete absence of a phase difference between otherwise identical measurements made at different axial positions. This indicates that there is no component of propagation in the axial direction. For the low power MPD arc thruster, the same general picture holds but the spoke frequency is lower (10 to 60 kHz, ref. 23). Also present in this thruster is a total arc current ripple or pulsing fluctuation. In these experiments Burkhart also shows that the magnitude

of both the spoke and ripple current fluctuations could be affected by the ac impedance of arc circuit.

At present it is not clear whether the current spoke is detrimental to performance. It does, however, greatly complicate MPD arc theory and experiments to no clear advantage. One approach being considered, therefore, is to look for ways to get rid of it. Preliminary tests with the low-power thruster for example indicate that use of inductors in series with an azimuthally segmented anode will eliminate the current fluctuations on the segments.

## Rotating Spoke Theory

Smith (ref. 24) has theoretically studied the formation of MPD arc spokes as the result of instabilities generated by electron density and/or temperature fluctuations in the current sheet region of the device. The theory also predicts pulsations (as have been observed in the low power arcs) as well as rotational instabilities. However, only the purely rotational component has thus far been compared to experimental data. The data used are for the high power thruster experiments of Connolly et al. (ref. 22) and Malliaris (ref. 25). Typical results are shown in figures I-27 and I-28.

Frequency versus mass flow. - The order of magnitude agreement in figure I-27 is good; however, the theoretical curve tends to rise more abruptly than the data with increased current. This behavior may be associated with the breakdown of the fundamental spoke mode into a number of higher harmonics or may indeed result from the destabilization of new fundamental modes. Such nonlinear effects cannot be accounted for by the present linear theory but have (as was noted) been experimentally observed.

Frequency versus mass flow. - The interesting point in figure I-28 is the abrupt rise in frequency as one goes to low mass flows which are both experimentally observed and analytically predicted. This analysis has also found (consistent with experimental observations) that the spoke frequency increases with the magnetic field and decreases with increasing atomic mass of the working fluid.

Another theory based on the formation of spokes as a result of Simon-Hoh type instabilities in the gradient dominated region around the electrodes has been considered by Hassan (ref. 26). He has had some success in predicting the onset conditions measured at NASA-Langley (ref. 27).

## PULSED MPD ARCS

In contrast to the spoke characteristics of the steady-state low and high power MPD arc, if MPD arc devices are scaled to very high power levels (0.2 to 5 MW) and operate for less than milliseconds, no spokes are found to exist. These investigations of a pulsed megawatt arc plasma source at Lewis are the outgrowth of the coaxial plasma gun research summarized in reference 28.

Figures I-29 and I-30 show views of this pulsed megawatt MPD arc plasma source. Figure I-29 is a side view of the source, which is about a meter long. On the right is the dewar for the superconducting magnet. The magnet provides fields of from 0 to 2.5 tesla at its center where the arc chamber is.

The source operates for a fraction of a millisecond, sending plasma streaming to the right into an evacuated glassware test section. The arc is powered by a crowbarred capacitor bank and inductor and uses a puff source of gas. The electromagnetic hammer for the fast gas valve is shown on the left, and below it are the cables for the cathode heater.

A better view of the arc chamber is shown in figure I-30. This is an iron fillings map of the magnetic field in the arc chamber area. The anode is a simple copper ring and the cathode is a heated tungsten ribbon. Behind the cathode are the gas ports for the propellant.

The early work on this pulsed source determined that no spokes exist and investigated the voltage-current characteristics of the arc. Since this is a pulsed experiment and since voltage-current curves are sensitive to frequency, it would be well to review for a moment how arc characteristics can change with frequency. Figure I-31 shows the voltage-current curve for a resistor; this curve is linear, positive sloped, and does not change with frequency. Also shown in this figure is the static voltage-current characteristic for a simple, low-current arc. It is curvilinear, negative sloped, and the characteristic varies with frequency. With slow enough current variations the static curve is followed. As frequency increases, the dynamic curves gradually change form and slope until almost resistor-like characteristics occur at high frequency. This is the realm of the Lewis pulsed arc source being investigated.

Although argon and nitrogen have been examined in this source, this discussion is limited to nitrogen (ref. 29). Figure I-32 shows a series of four shots, each with a higher peak current. Each shot has the same mass flow and magnetic field. The last shot shows a peak current of 13 kiloamperes and a peak power of 2.5 megawatts. Each shot represents about 100 microseconds of data, with time progressing toward lesser current values. These are dynamic characteristics taken at various points along the static curve, which lies somewhere in the shaded area. We have arbitrarily

shown the approximate static curve going through the midpoints of the dynamic curves. If the mass flow is held constant but the magnetic field is increased, then the shaded area becomes less negatively sloped. Thus the family of shots provides dynamic as well as approximate static characteristics, which are both important characteristics for the control, powering, and classification of arcs.

Another experiment now in progress employs laser scattering diagnosis in the exhaust 0.50 meter downstream of the device. Preliminary results show the exhaust electron density to be about $10^{20}$ particles per cubic meter and an electron temperature of a few electron volts. Combining the density measurement with a Faraday cup measurement in that area shows the stream velocity to be $1\times10^{4}$ to $2\times10^{4}$ meters per second. In a future experiment we hope to measure transient pressures, both static and dynamic.

## THRUSTER TEST FACILITIES

NASA-Lewis has two large vacuum facilities (ref. 30) for testing electric and electromagnetic thrusters (fig. I-33) and a number of smaller facilities. In these facilities ion thrusters and MPD arc thrusters are tested at sufficiently low background pressures so that the problems of electrical breakdown and background mass entrainment are not present.

Without facilities capable of providing such low background pressures, erroneous performance measurements and beam diagnostics may be obtained. Thus, background pressure effects for MPD arcs were investigated at Lewis (ref. 31). Figure I-34 shows some illustrative results obtained for a MPD thruster running on hydrogen propellant with the background pressure increased by bleeding nitrogen into the vacuum tank. The upper portion of the figure shows how the measured thrust changed as a result of increasing the background pressure. The lower portion shows how the axial velocity of the hydrogen propellant and the product of the velocity and intensity of the background nitrogen ions change with increasing pressure. This latter quantity is used as an indicator of how the background gas entrainment effects change.

As one starts at the normal operating pressure and bleeds nitrogen into the tank, the propellant velocity is unchanged for a while and then begins to decrease. At essentially the same pressure the background nitrogen ion spectrum line intensity and Doppler shift become detectable. As the pressure is further increased the propellant velocity continues to decrease and the background entrainment increases rapidly. The former effect will reduce the measured thrust and the entrainment will increase it. Thus the observed thrust can either increase or decrease depending on

which effect is dominant. Mass entrainment can double the observed thrust at a pressure of around 0.2 torr.

Consequently, the efficiencies reported for thruster studies made in facilities that do not have the pumping speed necessary to supply the proper low pressure environment are somewhat questionable. Furthermore, beam diagnostic studies in these facilities could also be questioned since one could not separate the effects of the primary propellant and background gas.

## SUMMARY OF MPD EXPERIMENTS

In summarizing the MPD arc experiments, we might indicate that we have had fair success making measurements of plasma properties out in the beam. Probes can be used to measure electron temperature, number density, and beam power flux. Using spectroscopic Doppler shift techniques yields detailed information on the velocities of the particles in the beam. More complete diagnostic studies using these techniques coupled with extensions to the analysis of the plasma magnetic nozzle expansion discussed herein should lead to an understanding of the acceleration processes.

The interelectrode region, however, is another matter. The energy density is too high for conventional probes to last more than a few hundred milliseconds. The spatial resolution required is too fine for water-cooled probes. Both probe and spectroscopic measurements are greatly complicated by the rotating current spoke, and although some analysis is available, it is clear that much more work is required in this region to obtain a good understanding of device operation.

## SUMMARY

To summarize the plasma processes in the electron bombardment ion thruster and MPD arc thruster, we have shown that in both types of thruster the major inefficiencies are the result of the same plasma processes. In both cases these are (1) the fundamental power losses associated with carrying current to an anode, and (2) the loss of power associated with ionizing a plasma.

Fortunately, in the ion thruster the total power expended in the plasma discharge ion source can be kept small compared to the ion acceleration power and high efficiency can be obtained.

In MPD arc thrusters all the power is put into the plasma discharge, and thus the anode losses are a large fraction of the total power. Since the anode power loss

is directly proportional to current, the most obvious method of lowering this loss is to operate the arcs at a higher voltage. We are exploring this approach as well as examining the possibility of lowering the power required for ionization by using only partially ionized plasma propellants.

## REFERENCES


1. Jahn, Robert G.: Physics of Electric Propulsion. McGraw-Hill Book Co., Inc., 1968.
2. Mickelsen, William R.; and Kaufman, Harold R.: Status of Electrostatic Thrustors for Space Propulsion. NASA TN D-2172, 1964.
3. Domitz, Stanley; Kosmahl, H. G.; Ramins, Peter; and Stevens, N. John: Survey of Electromagnetic Accelerators for Space Propulsion. NASA TN D-3332, 1966.
4. Wallner, Lewis E.; and Czika, Joseph, Jr.: Arc-Jet Thrustor for Space Propulsion. NASA TN D-2868, 1965.
5. Kaufman, Harold R.: An Ion Rocket with an Electron Bombardment Ion Source. NASA TN D-585, 1961.
6. Sovie, Ronald J.; and Klein, Barry M.: Volume Ion Production in a Tenuous Helium Plasma. NASA TN D-2324, 1964.
7. Sovie, Ronald J.; and Dugan, John V., Jr.: Energy Required for Ion Production by Electron Bombardment in Helium, Argon, and Cesium. Presented at the 17th Annual American Physical Society Gaseous Electronics Conference, Atlantic City, N.J., Oct. 14-16, 1964.
8. Sovie, Ronald J.; and Dugan, John V., Jr.: Effects of Metastable Atoms on Volume Ion Production in a Tenuous Helium Plasma. NASA TN D-3121, 1965.
9. Dugan, John V., Jr.; and Sovie, Ronald J.: Volume Ion Production Costs in Tenuous Plasmas: A General Atom Theory and Detailed Results for Helium, Argon, and Cesium. NASA TN D-4150, 1967.
10. Sobles, Albert: Quasi-Linear Plane Wave Study of Electrothermal Instabilities. Electricity from MHD, Vol. 1. International Atomic Energy Agency, 1968, pp. 499-518.
11. Bowditch, David N.: Investigation of the Discharge and Exhaust Beam of a Small Arc Plasma Thrustor. Paper 66-195, AIAA, Mar. 1966.

12. Seikel, George R.; Bowditch, David N.; and Domitz, Stanley: Application of Magnetic-Expansion Plasma Thrustors to Satellite Station Keeping and Attitude Control Missions. Paper 64-677, AIAA, Aug. 1964.

13. Johansen, A. E.; Bowditch, D. N.; and Burkhart, J. A.: Experimental Performance of a Low-Power MPD Arc Thrustor. Paper 67-50, AIAA, Jan. 1967.

14. Workman, J. B.: Arc Structure in a Magnetic Annular Discharge. AIAA J., vol. 7, no. 3, Mar. 1969, pp. 512-519.

15. Seals, R. K., Jr.; and Hassen, H. A.: Analysis of MPD Arcs with Non-equilibrium Ionization. AIAA J., vol. 6, no. 12, Dec. 1968, pp. 2273-2278.

16. Rosciszewski, J.: Acceleration Process in a MPD Arc Jet. Proceedings of Tenth Symposium on Engineering Aspects of Magnetohydrodynamics, MIT, 1969, pp. 112-116.

17. Shih, K. T.: Anode Current and Heat Flux Distributions in an MPD Engine. Paper 69-244, AIAA, Mar. 1969.

18. Sovie, R. J.; and Connolly, D. J.: Doppler Measurements of the Exhaust Velocities in an MPD Thruster. Bull. Am. Phys. Soc., vol. 13, no. 11, Nov. 1968, p. 1513.

19. Sovie, R. J.; and Connolly, D. J.: A Study of the Axial Velcoties in an Ammonia MPD Thruster. AIAA J., vol. 7, no. 4, Apr. 1969, pp. 723-725.

20. Connolly, Denis J.; and Sovie, Ronald J.: Performance of Radiation Cooled Magnetoplasmadynamic Arc Thrusters. NASA TM X-1908, 1969.

21. Esker, D. W.; Kroutil, J. C.; and Checkley, R. J.: Radiation Cooled MPD Arc Thruster. NASA CR 72557, 1969.

22. Connolly, Denis J.; Sovie, Ronald J.; Michels, Charles J.; and Burkhart, James A.: Low Environmental Pressure MPD Arc Tests. AIAA J., vol. 6, no. 7, July 1968, pp. 1271-1276.

23. Burkhart, James A.: Segmented Anode, $CO_2$-$H_2$ Performance and Hollow Cathode Erosion Tests on a Low Power MPD Acr Thruster. Paper 69-242, AIAA, Mar. 1969.

24. Smith, J. Marlin: Electrothermal Instability - An Explanation of the MPD Arc Thruster Rotating Spoke Phenomenon. Paper 69-231, AIAA, Mar. 1969.

25. Malliaris, A. C.: Investigation of Acceleration Mechanisms in MPD Accelerators. Rep. AVSSD-0044-68-CR, Avco Corp. (ARL-68-0078, DDC No. AD-674615), Apr. 1968.

26. Hassan, H. A.; and Thompson, Charles C.: Onset of Instabilities in Coaxial Hall Current Accelerators. Paper 69-230, AIAA, Mar. 1969.

27. Allario, Frank; Jarrett, Olin, Jr.; and Hess, Robert V.: Onset of Rotating Disturbance in the Interelectrode Region and Exhaust Jet of an MPD Arc. Paper 69-232, AIAA, Mar. 1969.

28. Michels, Charles J.: A Resume of Research on Coaxial Plasma Guns Performed at Lewis Research Center. Presented at the Seminar on Coaxial Plasma Guns, Catholic Univ. of Amer. Washington, D.C., May 10, 1968.

29. Michels, Charles J.: Dynamic Current-Voltage Characteristics of a Nitrogen MPD-Arc Plasma Source. Presented at the 1969 Fall Meeting of the Ohio Section of the American Physical Society, Columbus, Ohio, Oct. 12-18, 1969.

30. Finke, Robert C.; Holmes, Arthur D.; and Keller, Thomas A.: Space Environment Facility for Electric Propulsion Systems Research. NASA TN D-2774, 1965.

31. Connolly, D. J.; and Sovie, R. J.: The Effect of Background Pressure and Magnetic Field Shape on MPD Thruster Performance. Paper 69-243, AIAA, Mar. 1969.

# BIBLIOGRAPHY

This bibliography comprises publications authored by the members of the NASA Lewis Research Center Staff.


Anon.: Proceedings of the NASA-University Conference on the Science and Technology of Space Exploration. Vols. 1 and 2. NASA SP-11, 1962.

Baldwin, L. V.; and Sandborn, V. A.: Theory and Application of Hot-Wire Calorimeter for Measurement of Ion Beam Power. Paper 1389-60, ARS, Nov. 1960.

Baldwin, Lionel V.; and Sandborn, Virgil A.: Hot-Wire Calorimetery: Theory and Application to Ion Rocket Research. NASA TR R-98, 1961.

Banks, Bruce: Composite Ion Accelerator Grids. Presented at the 3rd Electrochemical Society International Conference on Electron and Ion Beam Science and Technology, Boston, Mass., May 6-9, 1968.

Banks, Bruce A.: A Fabrication Process for Glass Coated Electron-Bombardment Ion Thruster Grid. NASA TN D-5320, 1969.

Banks, Bruce A.; and Richley, Edward A.: Radially Slotted Grids for a Kaufman Ion Thruster. J. Spacecraft Rockets, vol. 4, no. 11, Nov. 1967, pp. 1562-1563.

Bechtel, Robert T.: Discharge Chamber Optimization of the SERT II Thruster. J. Spacecraft Rockets, vol. 5, no. 7, July 1968, pp. 795-800.

Bechtel, Robert T.: Performance and Control of a 30-Centimeter Diameter, Low Impulse Kaufman Thruster. Paper 69-238, AIAA, Mar. 1969.

Bechtel, R. T.; Csiky, G. A.; and Byers, D. C.: Performance of a 15-Centimeter Diameter, Hollow-Cathode Kaufman Thrustor. Paper 68-88, AIAA, Jan. 1968.

Bogart, Carl D.; and Richley, Edward A.: Space-Charge-Flow Computer Program. NASA TN D-3394, 1966.

Bowditch, David N.: Investigation of the Discharge and Exhaust Beam of a Small Arc Plasma Thrustor. Paper 66-195, AIAA, Mar. 1966.

Bowditch, David N.: A Langmuir Calorimetric Probe to Determine Average Energy Per Ion in a Tenuous Plasma Beam. AIAA J., vol. 5, no. 2, Feb. 1967, pp. 362-363.

Brown, Dennis W.: Some Requirements of Electric and Chemical Thrust Systems for Space Station Drag Cancellation. NASA TN D-1835, 1964.

Brown, Dennis W.: Low-Thrust Orbit Raising in Continuous Sunlight. NASA TN D-2072, 1964.

Burkhart, James A.: Segmented Anode, $CO_2$-$H_2$ Performance and Hollow Cathode Erosion Tests on a Low Power MPD Arc Thruster. Paper 69-242, AIAA, Mar. 1969.

Byers, David C.: Performance of Various Oxide-Magazine Cathodes in Kaufman Thrusters. NASA TN D-5074, 1969.

Byers, David C.: Effect of Power Supply Impedance on the SERT II Neutralizer. NASA TM X-52543, 1969.

Byers, David C.: An Experimental Investigation of a High-Voltage Electron-Bombardment Ion Thruster. J. Electrochem. Soc., vol. 116, no. 1, Jan. 1969, pp. 9-17.

Byers, David C.; Kerslake, William R.; and Grobman, Jack: Experimental Investigation of Heavy-Molecule Propellants in an Electron-Bombardment Thrustor. NASA TN D-2401, 1964.

Byers, David C.; and Staggs, John F.: SERT II Flight-Type Thruster System Performance. Paper 69-235, AIAA, Mar. 1969.

Childs, J. H.: Design of Ion Rockets and Test Facilities. Paper 59-103, Inst. Aeron. Sci., June 1959.

Childs, J. Howard: Theoretical Performance of Reverse-Feed Cesium Ion Engines. NASA TN D-876, 1961.

Childs, J. Howard; and Cybulski, Ronald J.: SERT and Early Electric Propulsion Systems. Astron. Aerospace Eng., vol. 1, no. 4, May 1963, pp. 112-117.

Childs, J. Howard; and Mickelsen, William R.: Grid Electrode Ion Rockets for Low Specific Impulse Missions. Presented at Second AFOSR Symposium on Advanced Propulsion Concepts, Boston, Mass., Oct. 7-8, 1959.

Chubb, Donald L.: Ionizing Shock Structure in a Monatomic Gas. Rep. 34, Columbia Univ., Mar. 1967. (Available from DDC as AD-663211.)

Chubb, Donald L.; and Seikel, George R.: Basic Studies of a Low Density Hall Current Ion Accelerator. NASA TN D-3250, 1966. Also Paper 66-76, AIAA, Jan. 1966.

Cohen, Allan J.: A Numerical Analysis of Direct Nuclear Electrogenerator Cells that Use Cerium 144 Beta-Emitting Radioisotope Sources. NASA TN D-2070, 1963.

Cohen, Allan J.: Onset of Anomalous Diffusion in Electron-Bombardment Ion Thrustor. NASA TN D-3731, 1966.

Cohen, Allan J.: Anomalous Diffusion in a Plasma Formed from the Exhaust Beam of an Electron-Bombardment Ion Thruster. NASA TN D-4758, 1968.

Cohen, Allan J.: An Electron-Bombardment Thruster Operated with a Cusped Magnetic Field. NASA TN D-5448, 1969.

Cohen, Allan J.; and Koral, Kenneth F.: Backscattering and Secondary-Electron Emission from Metal Targets of Various Thicknesses. NASA TN D-2782, 1965.

Cohen, Allan J.; and Low, Charles A., Jr.: A Parametric Study of Direct Nuclear Electrogenerator Cells Using a Beta Emitting Source. Paper 63048-B, AIAA, Mar. 1963.

Cook, Harlan; and Richley, Edward A.: Measurements of Efflux Patterns and Flow Rates from Cylindrical Tubes in Free-Molecule and Slip Flows. NASA TN D-2480, 1964.

Cooper, Dale W.; and Kuhns, Perry W.: Measurement of Ion and Electron Densities of Electron-Bombardment Ion-Thrustor Beam. NASA TN D-3761, 1966.

Connolly, Denis J.: Radiation from Sources Immersed in a Partly Ionized Gas. Rep. A-41, Case Inst. Tech. (NASA CR-94598), 1968.

Connolly, D. J.; and Sovie, R. J.: The Effect of Background Pressure and Magnetic Field Shape on MPD Thruster Performance. Paper 69-243, AIAA, Mar. 1969.

Connolly, Denis J.; Sovie, Ronald J.; Michels, Charles J.; and Burkhart, James A.: Low Environmental Pressure MPD Arc Tests. AIAA J., vol. 6, no. 7, July 1968, pp. 1271-1276.

Connolly, Denis J.; and Tanenbaum, B. Samuel: Radiation from Current Sources in an Isotropic Plasma. J. Appl. Phys., vol. 38, no. 6, May 1967, pp. 2557-2562.

Csiky, George A.: Measurements of Some Properties of a Discharge from a Hollow Cathode. NASA TN D-4966, 1969.

Csiky, George A.: Investigation of a Hollow Cathode Discharge Plasma. Paper 69-258, AIAA, Mar. 1969.

Cybulski, R. J.; and Kotnik, J. T.: Evaluation of a Cesium-Ion Rocket Employing a Large Porous Tungsten Ionizer. AIAA J., vol. 1, no. 6, June 1963, pp. 1293-1297.

Cybulski, Ronald J.; Kotnik, Joseph T.; and Lockwood, David L.: Experimental Performance of an Ion Rocket Engine Using A Rectangular-Slab Porous-Tungsten Emitter. NASA TN D-1321, 1962.

Cybulski, Ronald J.; and Lockwood, David L.: An Experimental Evaluation of Two-Dimensional Ion Engine with Charge Neutralization. Paper 61-82-1776, Inst. Aeron. Sci., June 1961.

Cybulski, Ronald J.; Richley, Edward A.; and Keller, Thomas A.: Application of Liquid-Helium Cryopumping to Large Electric Rocket Vacuum Facilities. 1961 Vacuum Symposium Transactions. Vol. 2. Luther E. Preuss, ed., Macmillan Co., 1962, pp. 1279-1284.

Dangle, E. E.; and Lockwood, D. L.: NASA Experimental Research with Ion Rockets. Paper 1126-60, ARS, May 1960.

Domitz, Stanley: Experimental Evaluation of a Direct-Current Low-Pressure Plasma Source. NASA TN D-1659, 1963.

Domitz, Stanley; and Pawlik, Eugene V.: Beam Current Measuring Device for Ion Engine Research. AIAA J., vol. 1, no. 3, Mar. 1963, pp. 712-713.

Dugan, John V., Jr.; and Rice, James H.: A Computer Plotting Description of Ion-Molecule Collisions with Long-Lived Capture Complexes. NASA TN D-5407, 1969.

Dugan, John V., Jr.; and Sovie, Ronald J.: Volume Ion Production Costs in Tenuous Plasmas: A General Atom Theory and Detailed Results for Helium, Argon, and Cesium. NASA TN D-4150, 1967.

Evvard, J. C.: Electric Space Propulsion. Electrical Eng., vol. 79, no. 7, July 1960, pp. 555-563.

Evvard, John C.: A Viewpoint on Space Propulsion and Power-Generation Systems. Proceedings of Fourth International Symposium on Space Technology and Science. Tamiya Nomura, ed., Japan Publications Trading Co., 1963, pp. 417-426.

Evvard, John C.: How Much Future for Electric Propulsion? Astron. Aerospace Eng., vol. 1, no. 7, Aug. 1963, pp. 92-97.

Evvard, John C.: Perspective on Aerospace Propulsion Systems. Ann. N. Y. Acad. Sci., vol. 134, Nov. 22, 1965, pp. 342-354.

Evvard, John C.: Renewed Optimism in Electric Propulsion. Astron. Aeron., vol. 4, no. 2, Feb. 1966, pp. 77-78.

Finke, Robert C.: A Study of Parameters Affecting the Maximum Voltage Capabilities of Shielded Negative Dielectric Junction Vacuum Insulators. Presented at the Second International Symposium on Insulation of High Voltages in Vacuum, Cambridge, Mass., Sept. 7-9, 1966.

Finke, Robert C.; Holmes, Arthur D.; and Keller, Thomas A.: Space Environment Facility for Electric Propulsion Systems Research. NASA TN D-2774, 1965.

Friedlander, Alan L.: Analysis of Guidance Perturbations for a Low-Thrust Mars Orbiter Mission Using SNAP-8. NASA TN D-1433, 1962.

Gold, Harold: A Spacecraft for Ion Thrustor Flight Tests. Paper 865B, SAE, Apr. 1964.

Goldin, Daniel S.: A Thermodynamic Flow Analysis of Particle Formation Efficiency in a Mixed Flow Colloid Thrustor. Paper 67-85, AIAA, Jan. 1967.

Goldin, Daniel S.; and Kvitek, George L.: An Analysis of Particle Formation Efficiency in a Colloid Thrustor. Paper 66-253, AIAA, Mar. 1966.

Goldin, Daniel S.; and Norgren, Carl T.: Thrust Measurements of Colloidal Particles as an Indication of Particle Size and Thrustor Operation. Paper 63050, AIAA, Mar. 1963.

Hamza, Vladimir: Numerical Solution of Axially Symmetric Poisson Equation; Theory and Application to Ion-Thrustor Analysis. NASA TN D-1711, 1963.

Hamza, Vladimir; and Richley, Edward A.: Numerical Solution of Two-Dimensional Poisson Equation: Theory and Application to Electrostatic-Ion-Engine Analysis. NASA TN D-1323, 1962.

Hamza, Vladimir; and Richley, Edward A.: Numerical Evaluation of Ion-Thrustor Optics. NASA TN D-1665, 1963.

Headley, Larry C.: Status of Porous Ionizers for Contact Ionization of Cesium. NASA TN D-3997, 1967.

Hrach, Frank J.: Out-Of-The-Ecliptic-Plane Probe Mission Employing Electric Propulsion. NASA TN D-4455, 1968.

Johansen, A. E.; Bowditch, D. N.; and Burkhart, J. A.: Experimental Performance of a Low-Power MPD Arc Thrustor. Paper 67-50, AIAA, Jan. 1967.

Johansen, Albert E.; and Palmer, Raymond W.: Lightweight Magnets for MPD Arcs. Paper 67-686, AIAA, Sept. 1967.

Jones, Robert E.: Results of Large Vacuum Facility Tests of an MPD Arc Thruster. AIAA J., vol. 4, no. 8, Aug. 1966, pp. 1455-1456.

Jones, Robert E.; and Palmer, Raymond W.: Traveling Wave Plasma Engine Program at NASA Lewis Research Center. Proceedings of the 3rd Symposium on Engineering Aspects of Magnetohydrodynamics. Norman W. Mather and George W. Sutton, eds., Gordon and Breach Science Publ., 1964, pp. 383-399.

Jones, Robert E.; and Palmer, Raymond W.: Experimental Investigation of a Constant-Velocity Traveling Magnetic Wave Plasma Engine. NASA TN D-2676, 1965.

Kaufman, Harold R.: One-Dimensional Analysis of Ion Rockets. NASA TN D-261, 1960.

Kaufman, Harold R.: The Neutralization of Ion-Rocket Beams. NASA TN D-1055, 1961.

Kaufman, Harold R.: An Ion Rocket with an Electron-Bombardment Ion Source. NASA TN D-585, 1961.

Kaufman, Harold R.: Electron Diffusion in a Turbulent Plasma. NASA TN D-1324, 1962.

Kaufman, Harold R.: The Electron-Bombardment Ion Rocket. Advanced Propulsion Concepts. Vol. 1. Gordon and Breach Science Publ., 1963, pp. 3-17.

Kaufman, Harold R.: Performance Correlation for Electron-Bombardment Ion Sources. NASA TN D-3041, 1965.

Kaufman, Harold R.; and Reader, Paul D.: Experimental Performance of Ion Rockets Employing Electron-Bombardment Ion Sources. Paper 1374-60, ARS, Nov. 1960.

Keller, Thomas A.: NASA Electric Rocket Test Facilities. 1960 Vacuum Symposium Transactions. C. Robert Meissner, ed., Pergamon Press, 1961, pp. 161-167. Also presented at Symposium on Rocket Operations at Simulated High Altitudes and in Space, Tullahoma, Tenn., June 28-29, 1961.

Kemp, Robert F.; Sellen, J. M., Jr.; and Pawlik, Eugene V.: Beam Neutralization Tests of a Flight Model Electron Bombardment Engine. Paper 2663-62, ARS, Nov. 1962.

Kemp, Robert F.; Sellen, J. M., Jr.; and Pawlik, Eugene V.: Neutralizer Tests on a Flight-Model Electron-Bombardment Thrustor. NASA TN D-1733, 1963.

Kerrisk, D. J.; and Kaufman, H. R.: Electric Propulsion Systems for Primary Spacecraft Propulsion. Paper 67-424, AIAA, July 1967.

Kerslake, William R.: Accelerator Grid Tests on an Electron-Bombardment Ion Rocket. NASA TN D-1168, 1962.

Kerslake, William R.: Charge-Exchange Effects on the Accelerator Impingement of an Electron-Bombardment Ion Rocket. NASA TN D-1657, 1963.

Kerslake, William R.: Cathode Durability in the Mercury Electron-Bombardment Ion Thrustor. Paper 64-683, AIAA, Aug. 1964.

Kerslake, William R.: Preliminary Operation of Oxide-Coated Brush Cathodes in Electron-Bombardment Ion Thrustors. NASA TM X-1105, 1965.

Kerslake, William R.: Oxide-Cathode Durability in the Mercury Electron-Bombardment Ion Engine. NASA TN D-3818, 1967.

Kerslake, William R.; Byers, David C.; and Staggs, John F.: SERT II Experimental Thrustor System. Paper 67-700, AIAA, Sept. 1967.

Kerslake, William R.; Margosian, Paul M.; and Wasserbauer, Joseph F.: Experimental Mercury Bombardment Thruster at Sub-Millipound Test. AIAA J., vol. 5, no. 4, Apr. 1967, pp. 683-691.

Kerslake, William R.; and Pawlik, Eugene V.: Additional Studies of Screen and Accelerator Grids for Electron-Bombardment Ion Thrustors. NASA TN D-1411, 1963.

Koral, Kenneth F.: Prebreakdown Currents, High Voltage Conditioning and Ultimate Voltage for a Large-Gap Concentric Cylinder Configuration in Vacuum. Presented at the Second International Symposium on Insulation of High Voltages in Vacuum, Cambridge, Mass., Sept. 7-9, 1966.

Koral, Kenneth F.: High-Voltage Characteristics of a Large-Gap Coaxial-Cylinder Electrode. NASA TN D-3949, 1967.

Koral, Kenneth F.; and Cohen, Allan J.: Empirical Equations for Electron Back Scattering Coefficients. NASA TN D-2909, 1965.

Kotnik, J. Thomas: Evaluation of a Hollow, Cylindrical, Contact-Ion Source. NASA TN D-1187, 1962.

Kotnik, J. Thomas; and Sater, Bernard L.: Power-Conditioning Requirements for Ion Rockets. IEEE Trans. on Aerospace, vol. AS-2, Apr. 1964, pp. 496-504.

Lathem, Walter C.: Effects of Electrode Misalinements in Kaufman Thrusters. J. Spacecraft Rockets, vol. 5, no. 6, June 1968, pp. 735-737.

Lathem, Walter C.: A New Technique for Simulating Space-Charge Potential Distributions. J. Spacecraft Rockets, vol. 5, no. 6, June 1968, pp. 737-738.

Lathem, Walter C.: Ion Accelerator Designs for Kaufman Thrusters. Paper 69-261, AIAA, Mar. 1969.

Lathem, Walter C.; and Staggs, John F.: Divergent-Flow Contact-Ionization Electrostatic Thrustor for Satellite Attitude Control and Station Keeping. NASA TN D-4420, 1968.

Lockwood, David L.; and Cybulski, Ronald J.: Performance Evaluation of a Two-Dimensional Ion Rocket Using Through-Feed and Porous Tungsten Ionizers. NASA TN D-766, 1961.

Lockwood, David L.; and Hamza, Vladimir: Space-Charge-Flow Theory and Electrode Design for Electrostatic Rocket Engines. NASA TN D-1461, 1962.

Lockwood, David L.; Mickelsen, William R.; and Hamza, Vladimir: Analytic Space-Charge Flow and Theoretical Electrostatic Rocket Engine Performance. Paper 2400-62, ARS, Mar. 1962.

Low, Charles A., Jr.: Radioisotope Heating for Contact Ionization Thrustors. Paper 67-735, AIAA, Sept. 1967.

Low, Charles A., Jr.; and Mickelsen, William R.: A Radioisotope Electrostatic Propulsion System. Trans. Am. Nucl. Soc., vol. 5, no. 2, Nov. 1962, p. 429.

Low, Charles A., Jr.; and Mickelsen, William R.: An Electrostatic Propulsion System with a Direct Nuclear Electrogenerator. Aerospace Eng., vol. 21, no. 12, Dec. 1962, pp. 58-59, 72-87.

MacKay, John S.; and Rossa, Leonard G.: A Variational Method for the Optimization of Interplanetary Round-Trip Trajectories. NASA TN D-1660, 1963.

MacKay, John S.; Zola, Charles L.; Rossa, Leonard G.; Fishbach, Laurence H.; Strack, William C.; and Hrach, Frank J.: Manned Mars Landing Missions Using Electric Propulsion. NASA TN D-3194, 1966.

Margosian, Paul M.: Parametric Study of a Thermoelectrostatic Generator For Space Applications. NASA TN D-2763, 1965.

Margosian, Paul M.: Preliminary Tests of Insulated Accelerator Grid for Electron-Bombardment Thrustor. NASA TM X-1342, 1967.

Margosian, Paul M.; and Kerslake, William R.: Experimental Evaluation of a Two-Directional Electron-Bombardment Ion Thrustor. AIAA J., vol. 5, no. 5, May 1967, pp. 833-839.

Maslowski, Edward A.: Experimental Data on Pumping of Mercury Ion Beams by Liquid-Nitrogen-Cooled Condensers. NASA TN D-3231, 1966.

Michels, Charles J.: Study of Coaxial Plasma-Gun Exhaust. Bull. Am. Phys. Soc., vol. 8, no. 5, 1963, p. 441.

Michels, Charles J.; and Ramins, Peter: Performance of Coaxial Plasma Gun with Various Propellants. Phys. Fluids, vol. 7, no. 11, pt. 2, Nov. 1964, pp. S71-S74.

Michels, Charles J.: Some Transient Electrical Characteristics of the Exhaust of a Self-Crowbarred Coaxial Plasma Gun. NASA TN D-2571, 1965.

Michels, Charles J.: Coaxial Plasma Gun Research at Lewis Research Center. NASA TM X-1600, 1968.

Michels, Charles J.: A Resume of Research on Coaxial Plasma Guns Performed at Lewis Research Center. Presented at the Seminar on Coaxial Plasma Guns, Catholic Univ. of America, Washington, D. C., May 10, 1968.

Michels, Charles J.: Dynamic Current-Voltage Characteristics of a Nitrogen MPD-Arc Plasma Source. Presented at the Fall Meeting of the Ohio Section of the Am. Phys. Soc., Columbus, Ohio, Oct. 17-18, 1969.

Michels, C. J.; Heighway, J. E.; and Johansen, A. E.: Analytical and Experimental Performance of Capacitor Powered Coaxial Plasma Guns. AIAA J., vol. 4, no. 5, May 1966, pp. 823-830.

Michels, Charles J.; and Hettel, Henry J.: Transient Spectral Study of Discharges in Coaxial Plasma Guns. Proceedings of the American Physical Society Topical Conference on Pulsed-High-Density Plasmas. Rep. LA-3770, Los Alamos Scientific Lab., Sept. 29, 1967, pp. E6-1 to E6-5.

Michels, Charles J.; and Hettel, Henry J.: Correlation of Transient Spectra with Performance in Coaxial Plasma Guns. NASA TN D-4385, 1968.

Michels, Charles J.; and Johansen, Albert E.: Experimental and Theoretical Performance of Coaxial Plasma Guns. NASA TN D-3469, 1966.

Michels, Charles J.; and Terdan, Fred F.: Characteristics of a 5-Kilojoule, Ignitron-Switched, Fast-Capacitor Bank. NASA TN D-2808, 1965.

Mickelsen, William R.: Electric Propulsion for Space Flight. Aerospace Eng., vol. 19, no. 11, Nov. 1960, pp. 6-11, 36-52.

Mickelsen, William R.: Comparative Performance of Electrostatic Rocket Engines. Paper 62-74, Inst. Aerospace Sci., Jan. 1962.

Mickelsen, William R.: Theoretical Performance of Electrostatic Thrustors with Analytic Space-Charge Flows. NASA TR R-174, 1963.

Mickelsen, William R.: NASA Research on Heavy-Particle Electrostatic Thrustors. Paper 63-19, Inst. Aerospace Sci., Jan. 1963.

Mickelsen, William R.: Electric Propulsion. Space/Aeronautics 1964/65 R&D Handbook, vol. 42, no. 4, Sept. 1964, pp. 50-53.

Mickelsen, William R.: Performance Parameters for Electric-Propulsion Systems. J. Spacecraft Rockets, vol. 3, no. 2, Feb. 1966, pp. 213-218.

Mickelsen, William R.; and Childs, J. Howard: Theoretical Analysis of Ultra-high Vacuum Condensers. Ref. Sci. Instr., vol. 29, no. 10, Oct. 1958, pp. 871-873.

Mickelsen, William R.; and Kaufman, Harold R.: Status of Electrostatic Thrustors for Space Propulsion. NASA TN D-2172, 1964.

Mickelsen, William R.; and Kaufman, Harold R.: Electrostatic Thrustors for Space Propulsion, Present and Future. J. Brit. Interplanet. Soc., vol. 19, pt. 8, Apr. 1964, pp. 319-337.

Mickelson, William R.; and Low, Charles A., Jr.: Potentials of Radioisotope Electrostatic Propulsion. Astron. Aerospace Eng., vol. 1, no. 9, Oct. 1963, pp. 52-57.

Mickelson, William R.; and MacKay, John S.: Interplanetary Flight with Electric Propulsion. Astron. Aeron., vol. 3, no. 1, Jan. 1965, pp. 44-49.

Milder, Nelson L.: Fragmentation of Anthracene in an Electron-Bombardment Ion Source. NASA TN D-2592, 1965.

Milder, Nelson L.: A Survey and Evaluation of Research on the Discharge Chamber Plasma of a Kaufman Thruster. Paper 69-494, AIAA, June 1969.

Milder, Nelson L.; and Kaufman, Harold R.: Analysis of Electron Analog Simulation of Ion Containment in Magnetic Fields. NASA TN D-5217, 1969.

Milder, Nelson L.; and Kerslake, William R.: Evaluation of Filament Deterioration in Electron-Bombardment Ion Sources. NASA TN D-2173, 1964.

Mirels, Harold: Two-Dimensional Ion Beams with Small Lateral Spreading. NASA TN D-679, 1961.

Mirels, Harold; and Rosenbaum, Burt M.: Analysis of One-Dimensional Ion Rocket With Grid Neutralization. NASA TN D-266, 1960.

Moeckel, W. E.: Trajectories with Constant Tangential Thrust in Central Gravitational Fields. NASA TR R-53, 1959.

Moeckel, W. E.: Propulsion Methods in Astronautics. Advances in Aeronautical Sciences. Vol. 2. Pergamon Press, 1959, pp. 1078-1097.

Moeckel, W. E.: Fast Interplanetary Missions with Low-Thrust Propulsion Systems. NASA TR R-79, 1960.

Moeckel, Wolfgang E.; et al.: Satellite and Space Propulsion Systems. NASA TN D-285, 1960.

Moeckel, W. E.: Status of Electric Propulsion Systems for Space Missions. Advances in Cryogenic Engineering. Vol. 6. K. D. Timmerhaus, ed., Plenum Press, 1961, pp. 3-19.

Moeckel, W. E.: Electric Propulsion Systems for Mars Missions. Exploration of Mars. Vol. 15 of Advances in the Astronautical Sciences. George W. Morgenthaler, ed., Western Periodicals Co., 1963, pp. 79-103.

Moeckel, W. E.: Promises and Potentialities of Electric Propulsion-Status of Thrustor Performance. Paper 66-1024, AIAA, Nov. 1966.

Moeckel, W. E.: Electric Propulsion. Science, vol. 142, Oct. 11, 1963, pp. 172-178.

Nakanishi, Shigeo: Experimental Investigation of a High-Voltage Isolation Device for Ion-Thrustor Propellant Feed. NASA TN D-3535, 1966.

Nakanishi, Shigeo: Experimental Investigation of Mercury Propellant Feed Isolators for Kaufman Thrusters. NASA TM X-1579, 1968.

Nakanishi, S.; Banks, B. A.; and Richley, E. A.: High-Perveance Accelerator Grids for Low-Voltage Kaufman Thrusters. J. Spacecraft Rockets, vol. 5, no. 3, Mar. 1968, pp. 356-358.

Nakanishi, S.; and Pawlik, E. V.: Experimental Investigation of a 1.5-M-Diam Kaufman Thruster. J. Spacecraft Rockets, vol. 5, no. 7, July 1968, pp. 801-807.

Nakanishi, Shigeo; Pawlik, Eugene V.; and Baur, Charles W.: Experimental Evaluation of Steady-State Control Properties of an Electron-Bombardment Ion Thrustor. NASA TN D-2171, 1964.

Nichols, Lester D.: Comparison of Brayton and Rankine Cycle Magnetogas-dynamic Space-Power Generation Systems. NASA TN D-5085, 1969.

Nichols, Lester D.; and Mantenieks, Maris A.: Analytical and Experimental Studies of MHD Generator Cathodes Emitting in a "Spot" Mode. Presented at the ASME Winter Annual Meeting, Los Angeles, Calif., Nov. 16-21, 1969.

Nieberding, William C.; and Lovell, Robert R.: Thrust Measurement of Sert I Ion Thrustors. NASA TN D-3407, 1966.

Norgren, Carl T.: Onboard Colloidal Particle Generator for Electrostatic Engines. Electric Propulsion Development. Vol. 9 of Progress in Astronautics and Aeronautics. Ernst Stuhlinger, ed., Academic Press, 1963, pp. 407-434.

Norgren, Carl T.; and Goldin, Daniel S.: Experimental Analysis of the Exhaust Beam from a Colloid Thrustor. AIAA J., vol. 3, no. 10, Oct. 1965, pp. 1943-1945.

Norgren, Carl T.; Goldin, Daniel S.; and Connolly, Denis J.: Colloid Thrustor Beam Analysis: Design and Operation of a Suitable Quadrupole Mass Filter. NASA TN D-3036, 1965.

Palmer, Raymond W.; and Jones, Robert E.: Experimental Investigation of a Variable-Length Constant-Velocity Traveling Magnetic Wave Plasma Accelerator. NASA TN D-4205, 1967.

Palmer, Raymond W.; Jones, Robert E.; and Seikel, George, R.: Analytical Investigations of Coil-System Design Parameters for a Constant-Velocity Traveling Magnetic Wave Plasma Engine. NASA TN D-2278, 1964.

Pawlik, Eugene V.: An Experimental Evaluation of Array of Three Electron-Bombardment Ion Thrustors. NASA TN D-2597, 1965.

Pawlik, Eugene V.; Margosian, Paul M.; and Staggs, John F.: A Technique for Obtaining Plasma-Sheath Configurations and Ion Optics for an Electron-Bombardment Ion Thrustor. NASA TN D-2804, 1965.

Pawlik, Eugene V.; and Nakanishi, Shigeo: Experimental Evaluation of Size Effects on Steady-State Control Properties of Electron-Bombardment Ion Thrustor. NASA TN D-2470, 1964.

Pawlik, Eugene V.; Nakanishi, Shigeo; and Algeri, Harvey R.: Some Dynamic Characteristics of an Electron-Bombardment Ion Thrustor. NASA TN D-4204, 1967.

Pawlik, Eugene V.; and Reader, Paul D.: Accelerator Grid Durability Tests of Mercury Electron-Bombardment Ion Thrustors. NASA TN D-4054, 1967.

Pawlik, Eugene V.; and Wenger, Norman C.: Performance Evaluation of a Mercury-Propellant Feed System for a Flight-Model Ion Engine. NASA TN D-1213, 1962.

Ramler, James R.: Low-Thrust Orbit Raising in Continuous Sunlight While Thrusting in a Plane Perpendicular to the Earth-Sun Line. NASA TN D-4104, 1967.

Rawlin, Vincent K.; and Kerslake, William R.: Durability of the SERT II Hollow Cathode and Future Applications of Hollow Cathodes. Paper 69-304, AIAA, Mar. 1969.

Rawlin, V. K.; and Pawlik, E. V.: A Mercury Plasma-Bridge Neutralizer. J. Spacecraft Rockets, vol. 5, no. 7, July 1968, pp. 814-820.

Reader, Paul D.: Investigation of a 10-Centimeter-Diameter Electron-Bombardment Ion Rocket. NASA TN D-1163, 1962.

Reader, Paul D.: Scale Effects on Ion Rocket Performance. ARS. J., vol. 32, no. 5, May 1962, pp. 711-714.

Reader, Paul D.: Ion Rocket with a Permanent Magnet. Astron. Aerospace Eng., vol. 1, no. 9, Oct. 1963, p. 83.

Reader, Paul D.: The Operation of an Electron-Bombardment Ion Source with Various Gases. Presented at the International Conference on Electron and Ion Beam Science and Technology, Electrochem. Soc. and the Am. Inst. Mech. Eng., Toronto, Canada, May 5-7, 1964.

Reader, Paul D.: Experimental Performance of a 50 Centimeter Diameter Electron-Bombardment Ion Rocket. Paper 64-689, AIAA, Aug. 1964.

Reader, Paul D.: Experimental Effects of Propellant-Introduction Mode on Electron-Bombardment Ion Rocket Performance. NASA TN D-2587, 1965.

Reader, Paul D.: Durability Tests of Mercury Electron-Bombardment Ion Thrustors. Paper 66-231, AIAA, Mar. 1966.

Reader, Paul D.; and Finke, Robert C.: An Electron-Bombardment Ion Rocket Operated with Alternating-Current Supplies. NASA TN D-1457, 1962.

Reader, P. D.; and King, H. J.: Systems Characteristics of Liquid Mercury Cathode Thrusters. Paper 69-237, AIAA, Mar. 1969.

Reader, Paul D.; and Mickelsen, William R.: Ion Propulsion Systems for Spacecraft. J. Spacecraft Rockets, vol. 2, no. 4, July-Aug. 1965, pp. 577-583.

Reader, Paul D.; and Pawlik, Eugene V.: Cathode Durability Tests in Mercury Electron-Bombardment Ion Thrustors. NASA TN D-4055, 1967.

Reader, Paul D.; and Regetz, John D., Jr.: A Delta Boosted, Electrically Raised Direct Broadcast Synchronous Satellite. Paper 69-1104, AIAA, Oct. 1969.

Reshotko, Eli: Resonance in a Cold Multiconstituent Plasma at Arbitrary Orientation to the Magnetic Field. NASA TN D-1875, 1963.

Reynolds, Thaine W.: Estimation of Critical Temperature for Surface Ion Currents from Electron Emission Data. NASA TN D-1307, 1962.

Reynolds, Thaine W.; and Childs, J. Howard: A Graphical Method for Estimating Ion-Rocket Performance. NASA TN D-466, 1960.

Reynolds, Thaine W.; and Childs, J. Howard: A Comparison of Reverse-Feed and Porous-Tungsten Ion Engines. NASA TN D-1166, 1962.

Reynolds, Thaine W.; and Kreps, Lawrence W.: Gas Flow, Emittance, and Ion Current Capabilities of Porous Tungsten. NASA TN D-871, 1961.

Reynolds, Thaine W.; and Richley, Edward A.: Thermionic Emission from Cesium-Coated Electrostatic Ion-Thrustor Electrodes. NASA TN D-1879, 1963.

Reynolds, Thaine W.; and Richley, Edward A.: Flux Patterns Resulting From Free-Molecule Flow Through Converging and Diverging Slots. NASA TN D-1864, 1964.

Reynolds, Thaine W.; and Richley, Edward A.: Analysis of Free-Molecule Flow with Surface Diffusion Through Cylindrical Tubes. NASA TN D-3225, 1966.

Reynolds, Thaine W.; and Richley, Edward A.: Free-Molecule Flow and Surface Diffusion Through Slots and Tubes - A Summary. NASA TR R-255, 1967.

Reynolds, Thaine W.; and Richley, Edward A.: Propellant Condensation on Surfaces Near An Electric Rocket Exhaust. Paper 69-270, AIAA, Mar. 1969.

Richley, Edward A.: NASA Electrostatic-Thrustor Research and Instrumentation. Presented at Ohio State University Seminar on Experimental Techniques in High-Speed Aerodynamics and Gas Dynamics, Columbus, Ohio, July 8-24, 1963.

Richley, Edward A.; and Bogart, Carl D.: Numerical Solutions of Knudsen Flow Entering a Circular Tube through a Small Axial Orifice. NASA TN D-2115, 1964.

Richley, Edward A.; and Cybulski, Ronald J.: High-Vacuum Condenser Design: Experimental Effects from Cesium and Mercury Ion Beams. NASA TN D-1217, 1962.

Richley, Edward A.; Cybulski, Ronald J.; and Keller, Thomas A.: Experimental Evaluation of High-Vacuum Condensers in Large Vacuum Facilities. 1961 Vacuum Symposium Transactions. Vol. 2. Luther E. Preuss, ed., Macmillan Co., 1962, pp. 1285-1291.

Richley, Edward A.; and Kerslake, William R.: Bombardment Thruster Investigations at the Lewis Research Center. Paper 68-542, AIAA, June 1968.

Richley, Edward A.; and Mickelsen, William R.: Effects of Molecular Flow in Plasma Generation and Some Analyses of Space Charge Flow in Ion Acceleration. Paper 64-7, AIAA, Jan. 1964.

Richley, Edward A.; and Reynolds, Thaine W.: Numerical Solutions of Free-Molecule Flow in Converging and Diverging Tubes and Slots. NASA TN D-2330, 1964.

Richley, E. A.; Sandborn, V. A.; Baldwin, L. V.; and Dangle, E. E.: Comparative Measurements of Beam Power in Ion-Rocket Research. NASA TN D-845, 1961.

Rossa, Leonard G.: A Parametric Study of Constant Thrust, Electrically Propelled Mars and Venus Orbiting Probes. NASA TN D-2154, 1964.

Saunders, Neal T.: Experimental Method of Producing Porous Tungsten for Ion Rocket Engines. NASA TN D-864, 1961.

Schertler, Ronald J.: Outgassing Characteristics of an Epoxy-Impregnated Magnet Coil. NASA TM X-1813, 1969.

Schertler, Ronald J.; and Norgren, Carl T.: Experimental Investigation of Charging Submicron Carbon Powder for Colloidal Particle Thrustors. NASA TN D-3657, 1966.

Schwirian, Richard E.: A New Momentum Integral Method for Treating Magnetohydrodynamic and Simple Hydrodynamic Entrance Flows. NASA TN D-5215, 1969. Also Paper 69-724, AIAA, June 1969.

Seikel, George R.: Generation of Thrust-Electromagnetic Thrustors. Electric Propulsion for Spacecraft. NASA SP-22, 1962, pp. 19-24.

Seikel, George R.: Plasma. Space/Aeronautics, vol. 43, no. 4, Apr. 1965, pp. 40-45.

Seikel, George R.; Bowditch, David N.; and Domitz, Stanley: Application of Magnetic-Expansion Plasma Thrustors to Satellite Station Keeping and Attitude Control Missions. Paper 64-677, AIAA, Aug. 1964.

Seikel, George R.; and Chubb, Donald L.: Simulation of Solar-Wing Magnetosphere Interactions. Bull. Am. Phys. Soc., vol. 13, no. 7, July 1968, p. 959.

Seikel, G. R.; and Reshotko, E.: Hall Current Ion Accelerator. Bull. Am. Phys. Soc., vol. 7, no. 6, June 19, 1962, p. 414.

Shattuck, Russell D.; and Denington, Robert J.: Status and Future Engineering Problems of Electric Propulsion Systems. 2nd Manned Space Flight Meeting, AIAA, 1963, pp. 341-350.

Smith, J. Marlin: Electrothermal Instabilities in the Entrance Region of an MHD Generator. Bull. Am. Phys. Soc., vol. 13, no. 11, Nov. 1968, p. 1564.

Smith, J. Marlin: Electrothermal Instability - An Explanation of the MPD Arc Thruster Rotating Spoke Phenomenon. Paper 69-231, AIAA, Mar. 1969.

Smith, John R.: Self-Consistent Many-Electron Theory of Electron Work Functions and Surface Potential Characteristics for Selected Metals. Phys. Rev., vol. 181, no. 2, May 10, 1969, pp. 522-529.

Sovie, Ronald J.: Volume Ion-Production Efficiency and Spectroscopic Diagnostics in a Helium Plasma. Bull. Am. Phys. Soc., vol. 8, no. 5, 1963, p. 424.

Sovie, Ronald J.: Spectroscopic Determination of Electron Temperature and Percentage Ionization in a Helium Plasma. Phys. Fluids, vol. 7, no. 4, Apr. 1964, pp. 613-614.

Sovie, R. J.: The Effects of Cascading and Metastable Atoms on the Determination of Electron Temperature from Relative Line Intensities in a Tenuous Helium Plasma. J. Quant. Spectrosc. Radiat. Transfer, vol. 8, no. 2, Feb. 1968, pp. 833-838.

Sovie, R. J.: The Effect of Optical Thickness on Spectroscopic Diagnostics and Volume Ion Production in Tenuous Helium Plasmas. Bull. Am. Phys. Soc., vol. 14, no. 2, Feb. 1969, p. 257.

Sovie, R. J.; and Connolly, D. J.: Doppler Measurements of the Exhaust Velocities in an MPD Thruster. Bull. Am. Phys. Soc., vol. 13, no. 11, Nov. 1968, p. 1513.

Sovie, R. J.; and Connolly, D. J.: A Study of the Axial Velocities in an Ammonia MPD Thruster. AIAA J., vol. 7, no. 4, Apr. 1969, pp. 723-725.

Sovie, R. J.; and Dugan, J. V., Jr.: Energy Required for Ion Production by Electron Bombardment in Helium, Argon, and Cesium. Bull. Am. Phys. Soc., vol. 10, no. 2, 1965, p. 179.

Sovie, Ronald J.; and Dugan, John V., Jr.: Effects of Metastable Atoms on Volume Ion Production in a Tenuous Helium Plasma. NASA TN D-3121, 1965.

Sovie, R. J.; and Dugan, J. V., Jr.: Volume Ion Production Costs in Tenuous Plasmas. Bull. Am. Phys. Soc., vol. 12, no. 2, Feb. 1967, p. 239.

Sovie, Ronald J.; and Klein, Barry M.: Volume Ion Production in a Tenuous Helium Plasma. NASA TN D-2324, 1964.

Sovie, R. J.; and Seikel, G. R.: rf Induction Heating and Production of Plasmas. Bull. Am. Phys. Soc., vol. 8, no. 2, 1963, p. 153.

Sovie, Ronald J.; and Seikel, George R.: Radio-Frequency Induction Heating of Low-Pressure Plasma. NASA TN D-4206, 1967. See also Bull. Am. Phys. Soc., vol. 12, no. 5, 1967, p. 813; and Paper 67-732, AIAA, Sept. 1967.

Staggs, John F.: An Electrolytic Tank Analog for Two-Dimensional Analysis of Electrostatic-Thrustor Optics. NASA TN D-2803, 1965.

Staggs, John F.; Gula, William P.; and Kerslake, William R.: Distribution of Neutral Atoms and Charge-Exchange Ions Downstream of an Ion Thruster. J. Spacecraft Rockets, vol. 5, no. 2, Feb. 1968, pp. 159-164.

Staggs, John F.; and Lathem, Walter C.: Experimental Performance of a Low-Thrust, Divergent-Flow, Contact-Ionization Electrostatic Thruster. J. Spacecraft Rockets, vol. 4, no. 5, May 1967, pp. 610-615.

Staggs, John F.: Richley, Edward A.; and Gula, William P.: Ion Extractor System Design. AIAA J., vol. 5, no. 2, Feb. 1967, pp. 359-360.

Stankiewicz, N.: Feasibility of Applying Field-Ion Emission to Electrostatic Rocket Engines. NASA TN D-1563, 1963.

Stankiewicz, N.: Field Emission Charging of Metallic Colloids. NASA TN D-2078, 1963.

Stankiewicz, Norbert: Limits of Validity of Radiationless Decay of High-Density Plasmas. NASA TN D-3372, 1966.

Stankiewicz, Norbert: Thermodynamic Study of Plasmas Using the Principle of Maximum Entropy. NASA TN D-4621, 1968.

Stankiewicz, N.: The Ellipsoidal Velocity Distribution Function. NASA TN D-5026, 1969.

Stevens, N. J.; and Briehl, D. C.: Thermal Investigation of an Ion Engine Microthrustor. NASA TM X-1473, 1967.

Stover, John B.: Electric Breakdown and Arcing in Experimental Ion Thrustor Systems. Paper 63-057, AIAA, Mar. 1963.

Stover, John B.: Effect of Thrustor Arcing on Ion Rocket System Design. Paper 64-682, AIAA, Aug. 1964.

Strack, William C.: Combined High-Low Thrust Propulsion for the Close Solar Probe Mission. NASA TN D-3145, 1965.

Strack, William C.; and Huff, Vearl N.: The N-Body Code - A General FORTRAN Code for the Numerical Solution of Space Mechanics Problems of an IBM 7090 Computer. NASA TN D-1730, 1963.

Strack, William C.; and Zola, C. L.: Solar-Electric Propulsion Probes for Exploring the Solar System. NASA TM X-52318, 1967.

Walker, E. L.; and Tanenbaum, B. Samuel: Investigation of Kinetic Models for Gas Mixtures. Phys. Fluids, vol. 11, no. 9, Sept. 1968, pp. 1951-1954.

Walker, E. L.; and Tanenbaum, B. Samuel: Transport Equations for a Weakly Ionized Electron Gas. Phys. Fluids, vol. 11, no. 9, Sept. 1968, pp. 1955-1958.

Wasserbauer, Joseph F.: Experimental Performance of a High-Current-Density Cylindrical Concave Porous Tungsten Emitter for Ion Thrustors. Paper 63-029, AIAA, Mar. 1963.

Wasserbauer, Joseph F.: Field-Enhanced Thermionic Emission From Electrodes of Cesium Ion Thrustor. NASA TN D-2635, 1965.

Wasserbauer, Joseph F.: A 5-Centimeter-Diameter Electron-Bombardment Thrustor with Permanent Magnets. NASA TN D-3628, 1966.

Zimmerman, Arthur V.; MacKay, John S.; and Rossa, Leonard G.: Optimum Low-Acceleration Trajectories for Interplanetary Transfers. NASA TN D-1456, 1963.

Zola, Charles L.: Trajectory Methods in Mission Analysis for Low-Thrust Vehicles. Paper 64-51, AIAA, Jan. 1964.

Zola, Charles L.: Jovian Planet Missions for Solar Cell Powered Electric Propulsion Spacecraft. Paper 68-118, AIAA, Jan. 1968.

TABLE I-1. - SUMMARY OF 30-CENTIMETER-DIAMETER THRUSTER PERFORMANCE

| | | |
|---|---|---|
| Beam power | 600 V × 1.5 A | 900 W |
| Discharge power | 35 V × 7.5 A<br>(175 eV × 1.5 A) | 262 W |
| Power losses: | | 165 W |
| Accelerator | 1200 V × 0.07 A | 84 W |
| Vaporizer/feed[a] | | 13 W |
| Cathode tip/keeper[a] | | 13 W |
| Neutralizer[a] | | 55 W |

[a]Estimate based on current SERT II data.

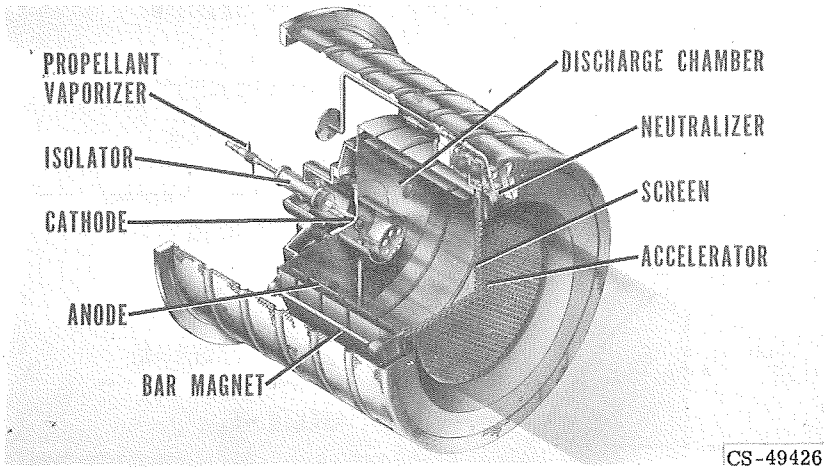


Figure I-1. - Electron-bombardment ion thruster.

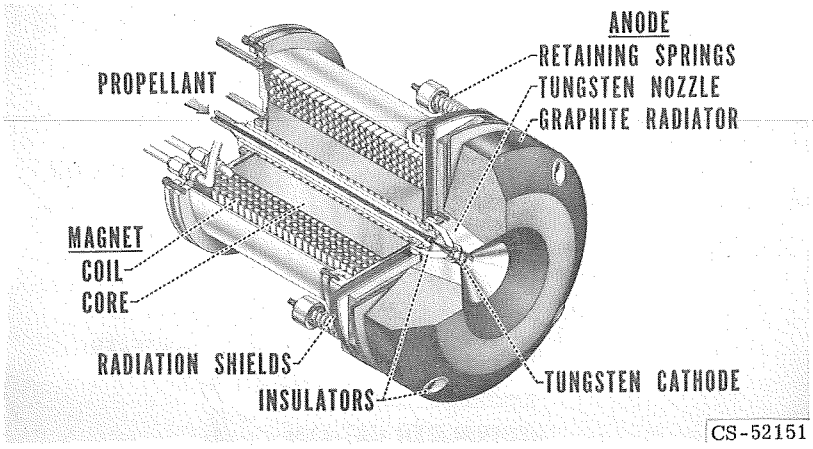


Figure I-2. - 30-Kilowatt MPD arc thruster.

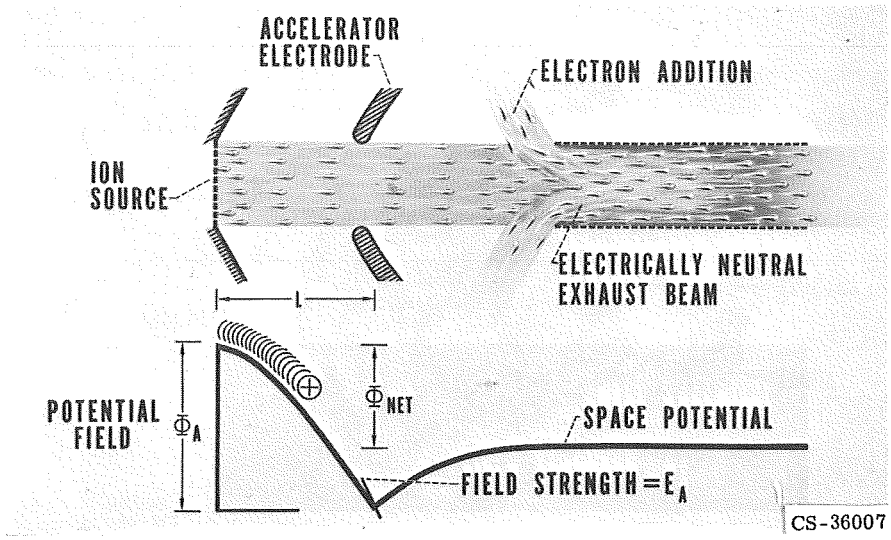


Figure I-3. - Electrostatic acceleration.

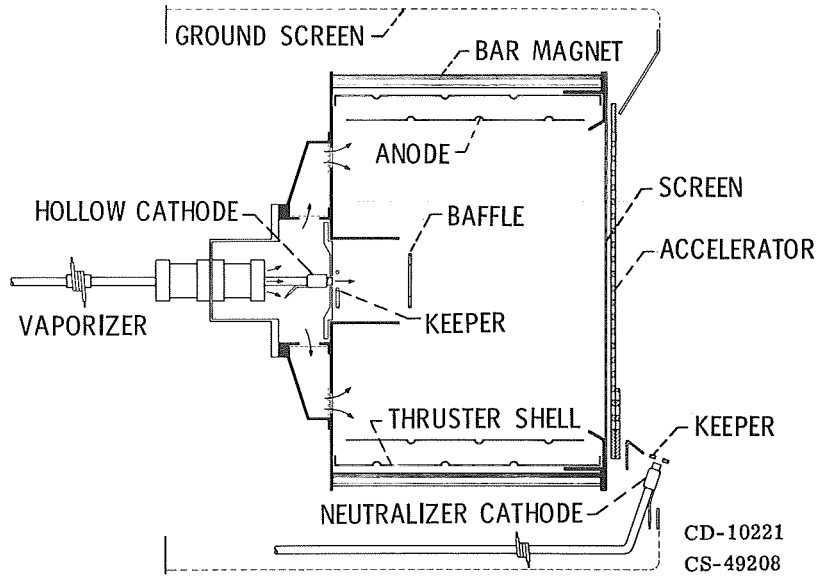


Figure I-4. - 15-Centimeter-diameter experimental SERT II thruster.

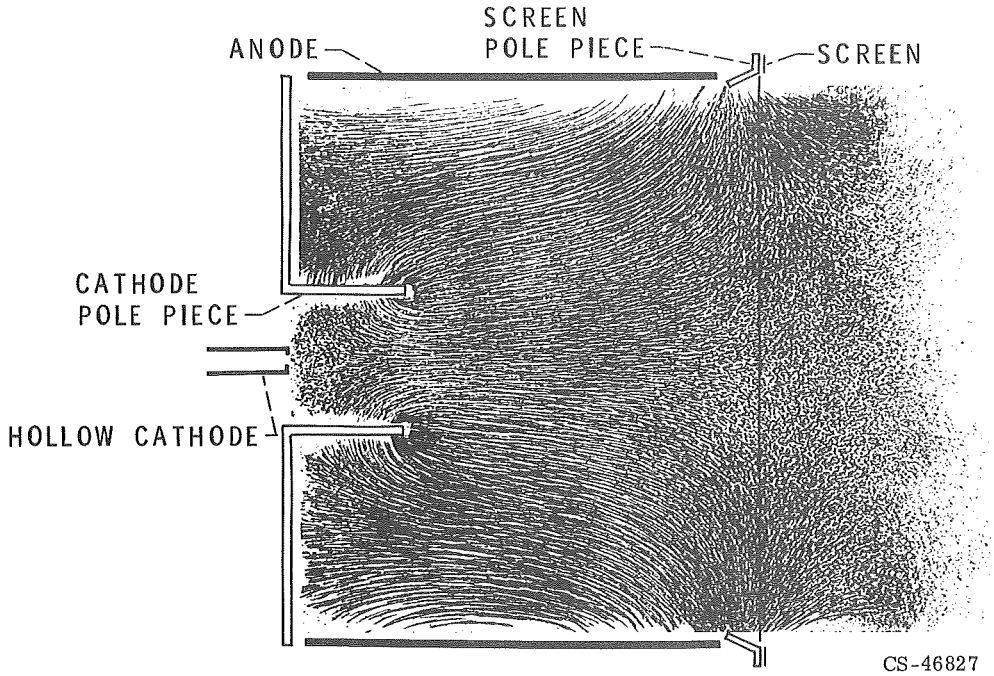


Figure I-5. - SERT II thruster magnetic field map.

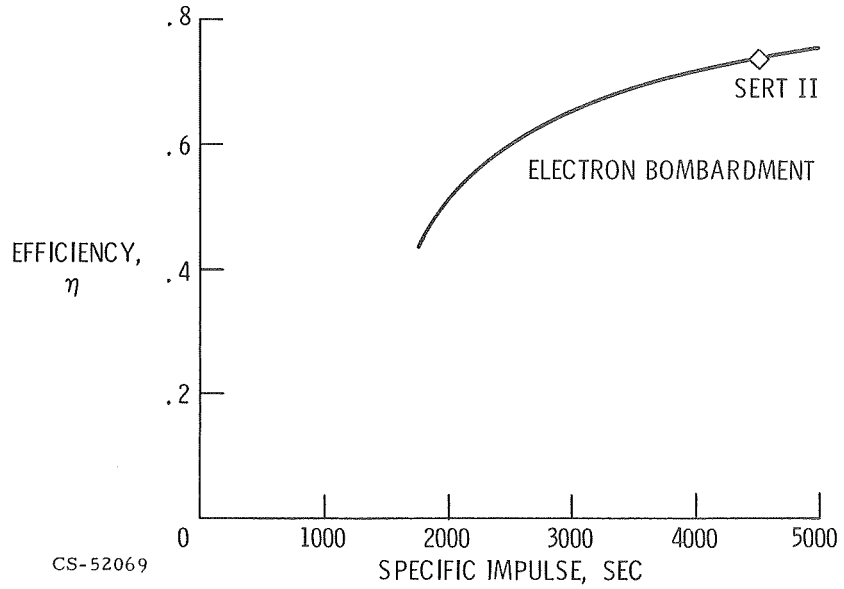


Figure I-6. - Thruster performance.

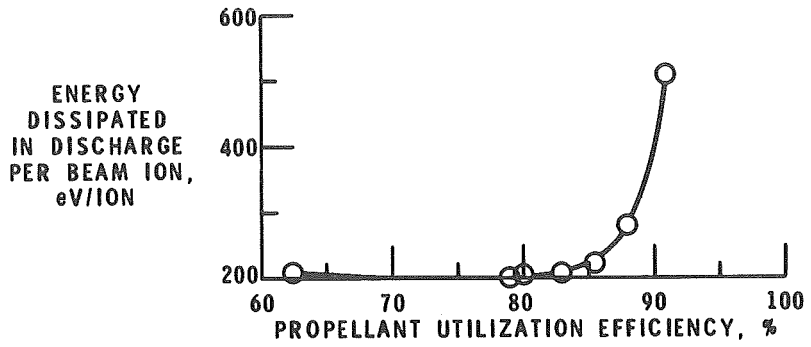


CS-43923

Figure I-7. - Variation of energy dissipated in discharge per beam ion with propellant utilization efficiency.

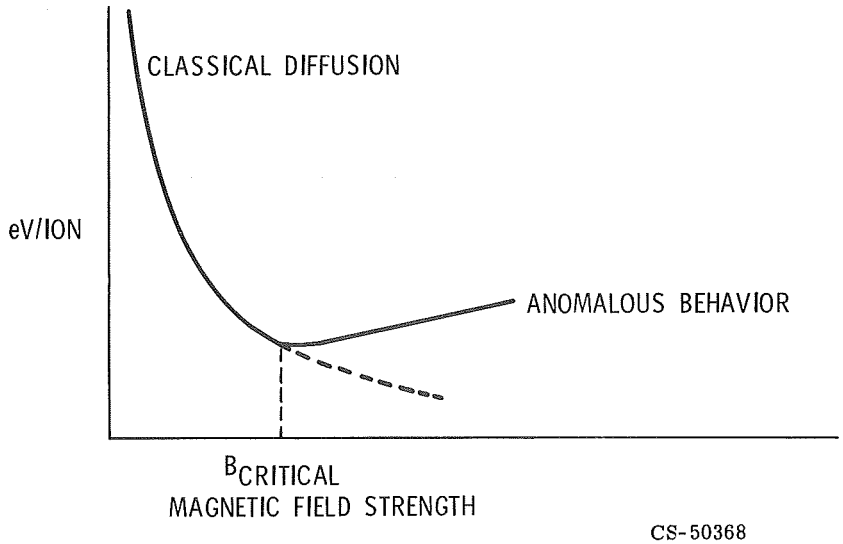


CS-50368

Figure I-8. - Discharge energy loss against magnetic field strength.

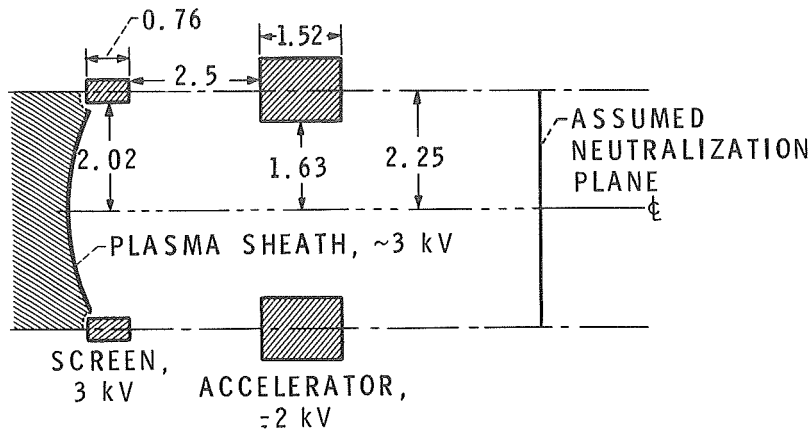


Figure I-9. - Single hole of SERT II grid system. Dimensions are in millimeters.

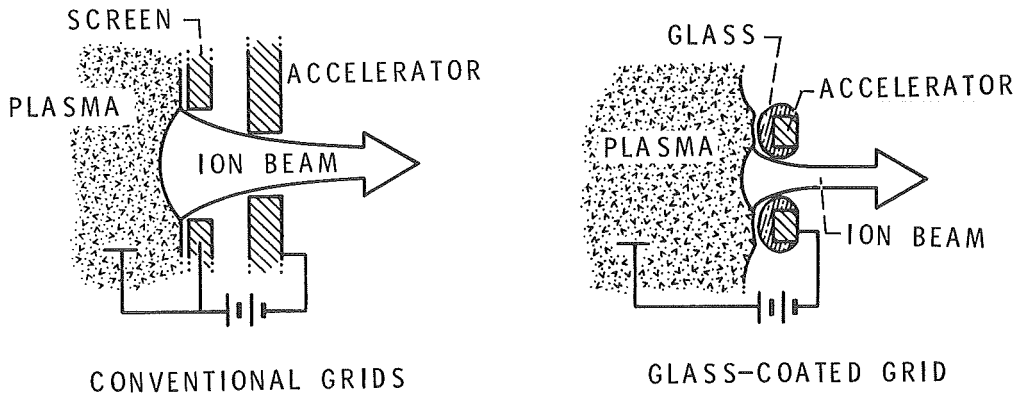


Figure I-10. - Comparison of accelerator grid concepts.

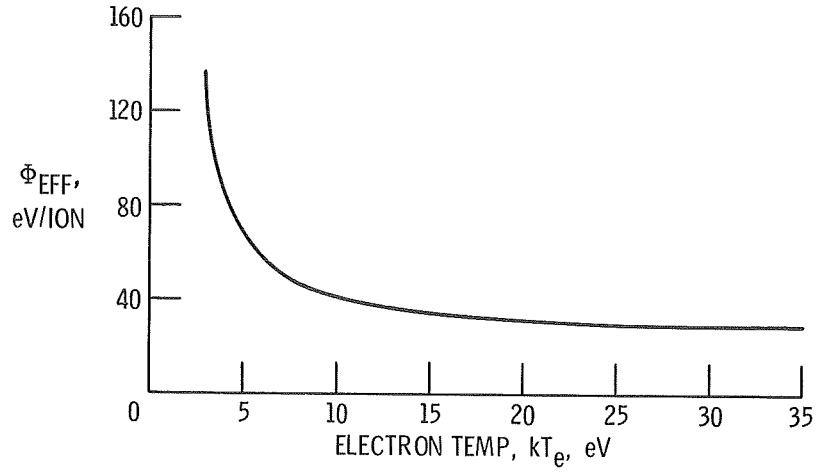


Figure I-11. - Volume ion production cost for mercury.

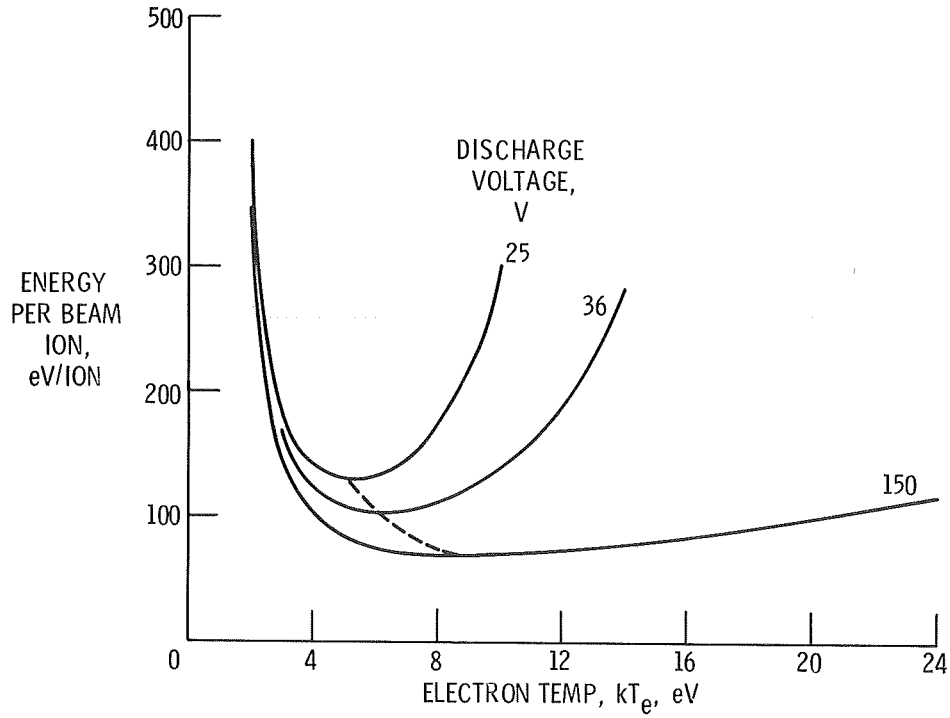


Figure I-12. - Direct current mercury source performance limit. Anode work function, $\Phi_A$ = 4.5 volts.

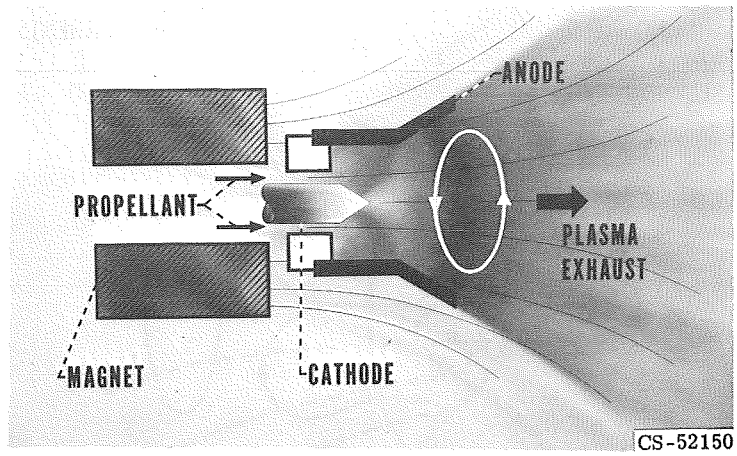


Figure I-13. - MPD arc thruster.

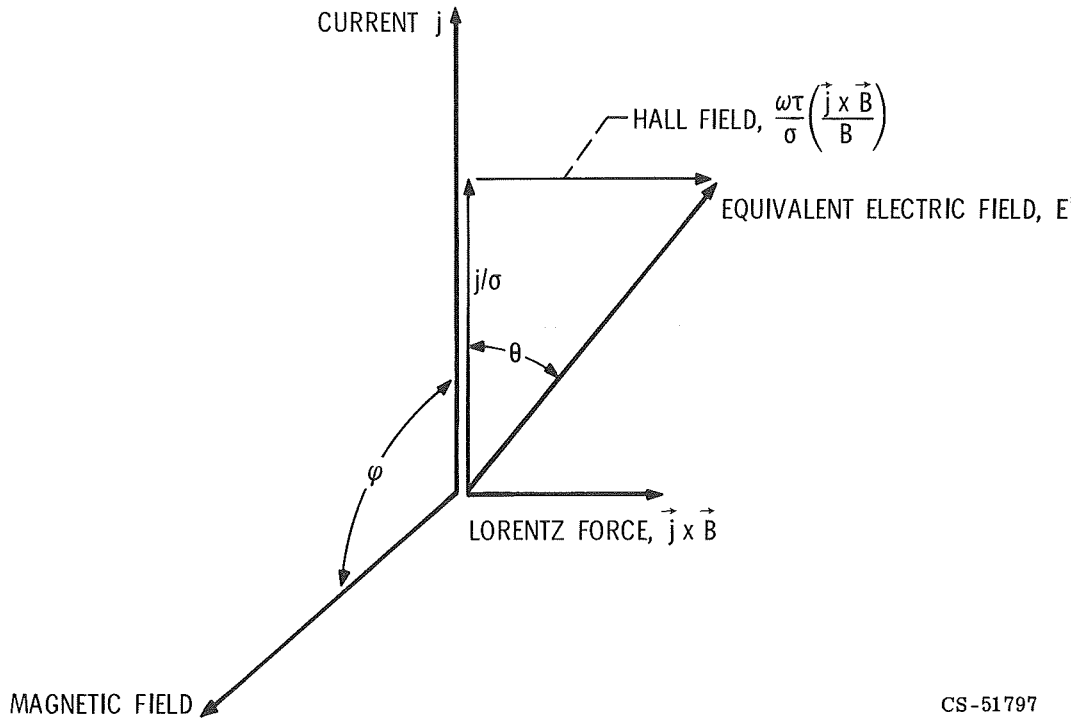


Figure I-14. - Vector diagram of plasma current, magnetic field, and electric field.

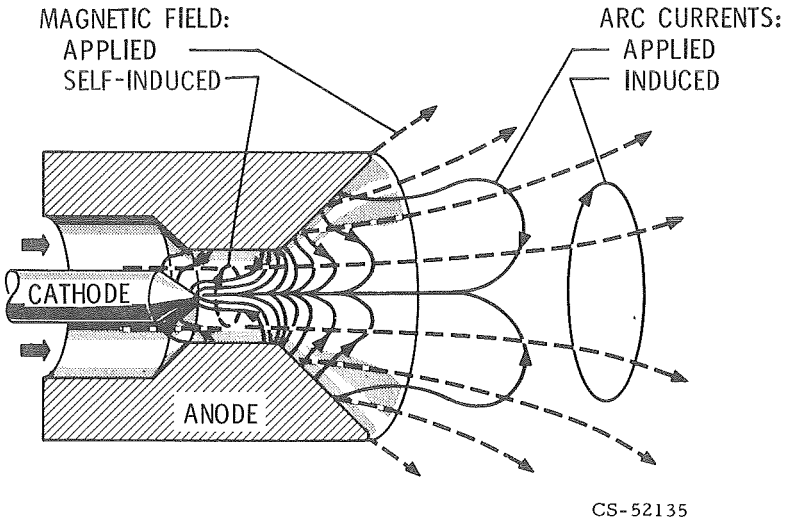


Figure I-15. - MPD arc thruster currents and magnetic fields.

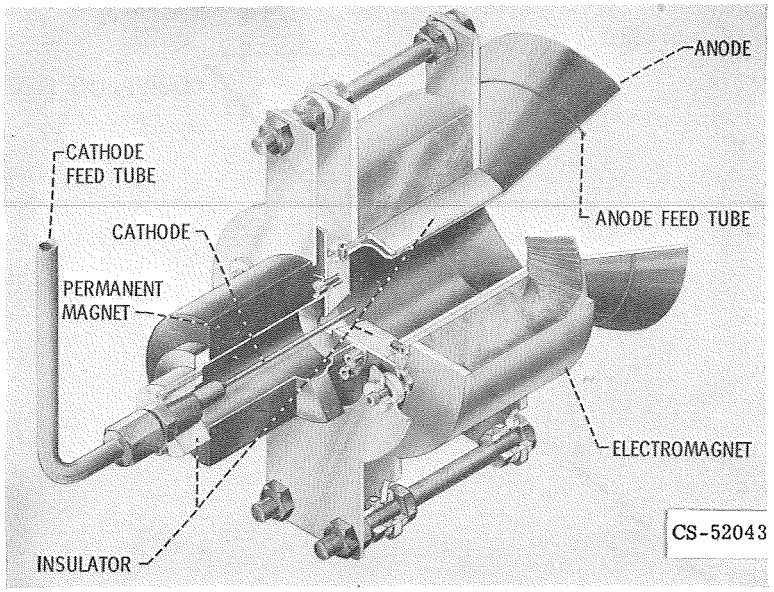


Figure I-16. - 1/2-Kilowatt MPD arc thruster.

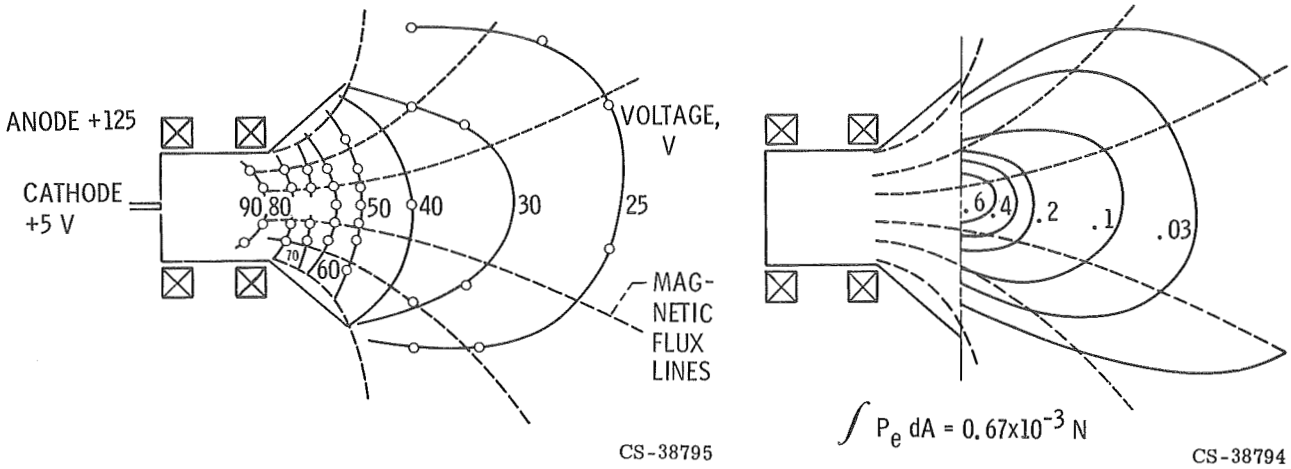


(a) Plasma potential profiles.

(b) Electron gas pressure profiles.

Figure I-17. - Subkilowatt MPD arc thruster.

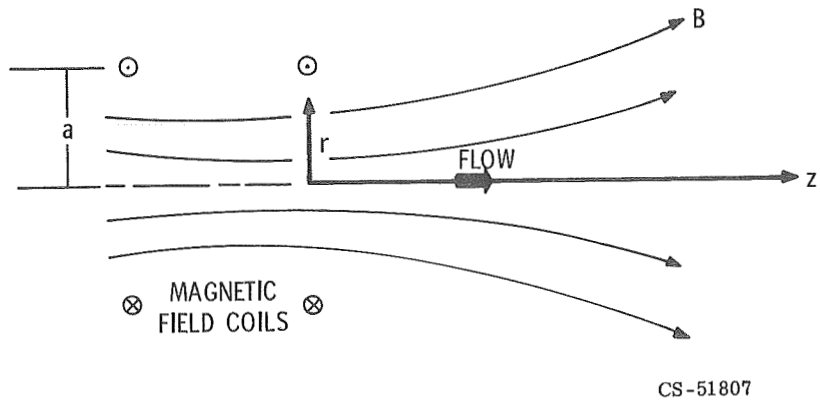


Figure I-18. - Plasma expansion in a magnetic nozzle.

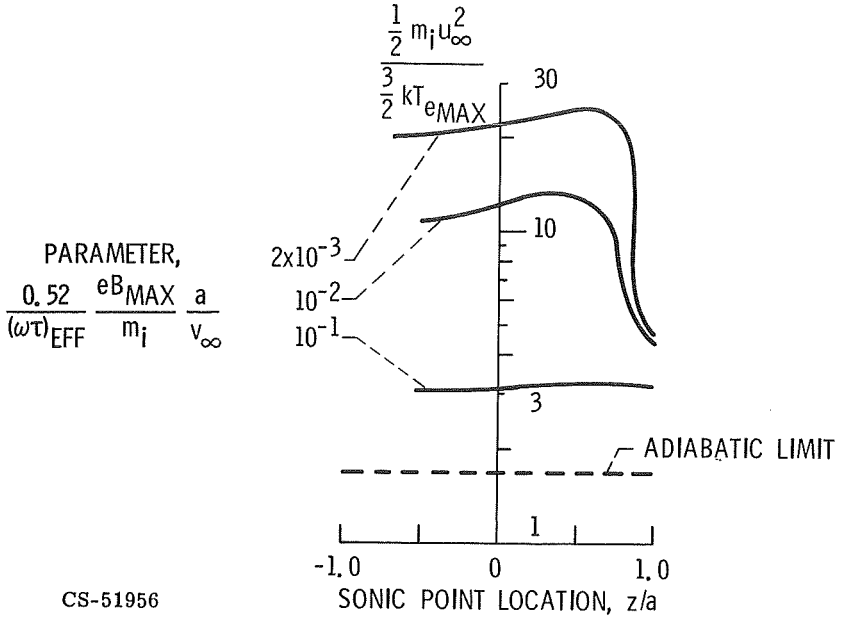


Figure I-19. - Ratio of final ion to initial electron energy as function of sonic point location.

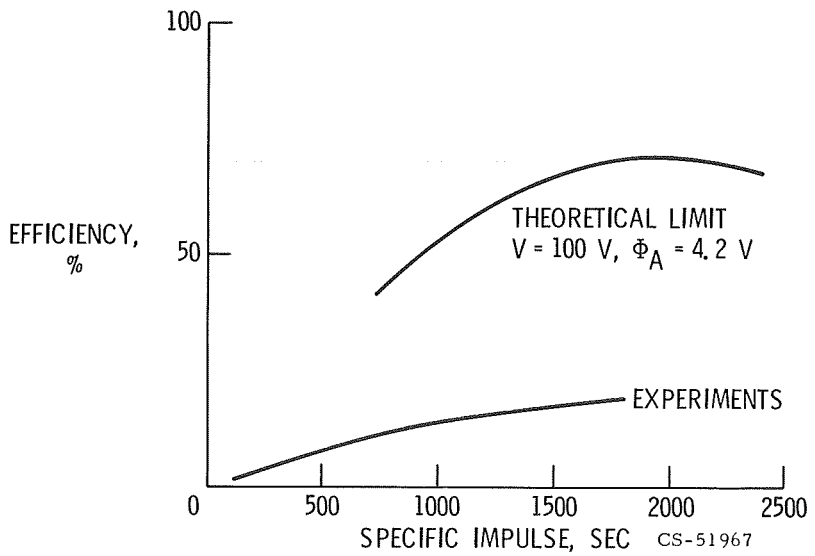


Figure I-20. - Low power xenon MPD arc thruster.

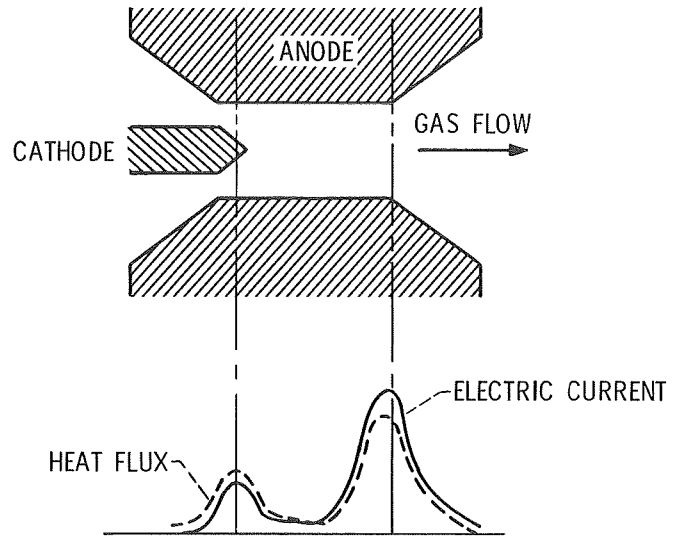


CS-52070

Figure I-21. - Anode current and heat flux distribution.

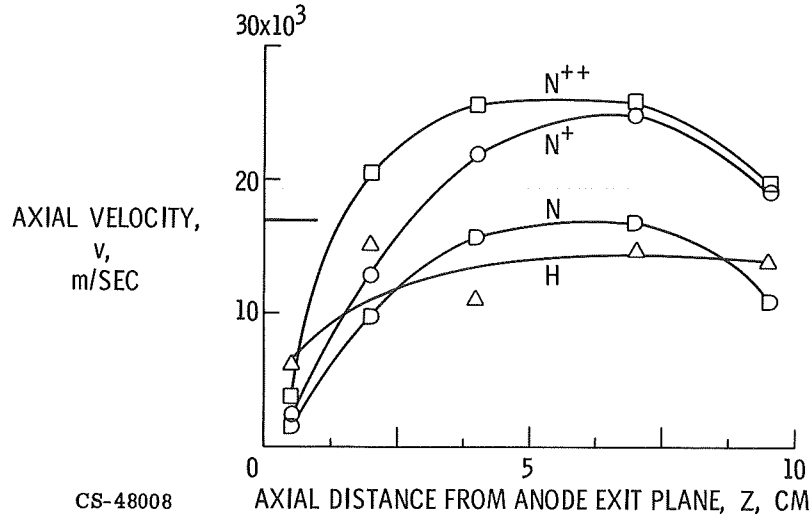


CS-48008

Figure I-22. - Axial velocity as function of axial distance. Specific impulse, 1765 seconds.

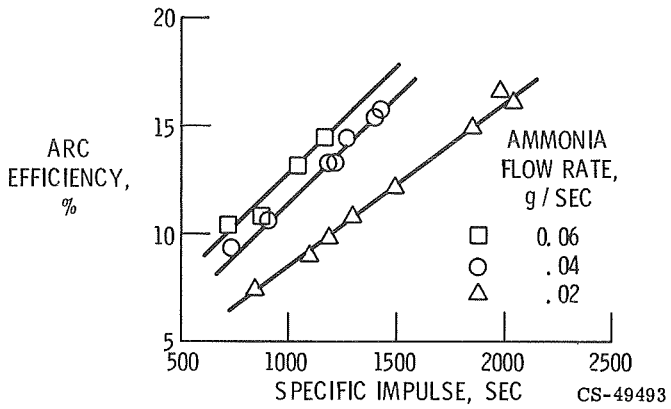


Figure I-23. - Arc efficiency as function of specific impulse.

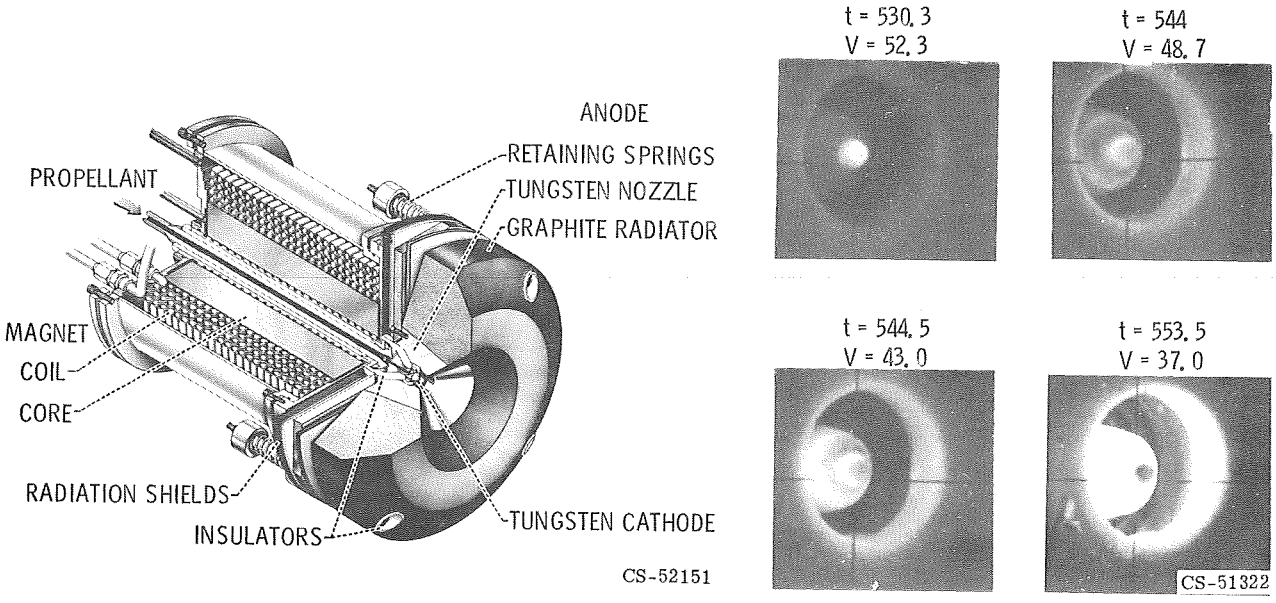


(a) 30-Kilowatt MPD arc thruster.

(b) Progressive change in cathode attachment.

Figure I-24. - Relation between arc voltage and cathode current attachment.

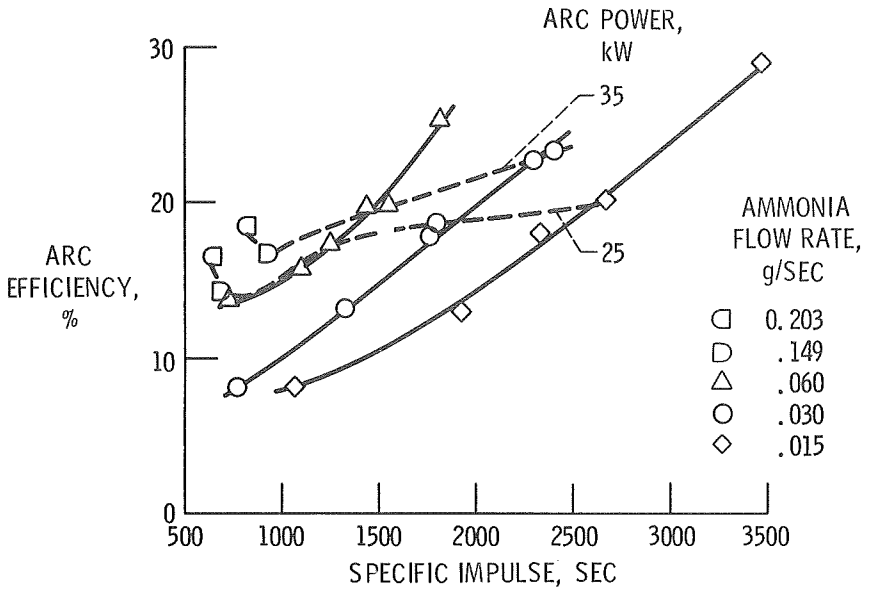


Figure I-25. - 30-Kilowatt thruster efficiency as function of specific impulse.

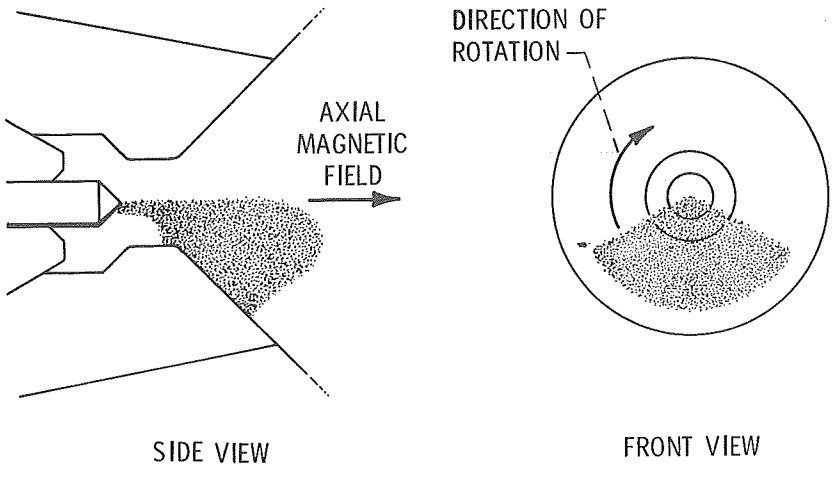


Figure I-26. - Rotating current spoke.

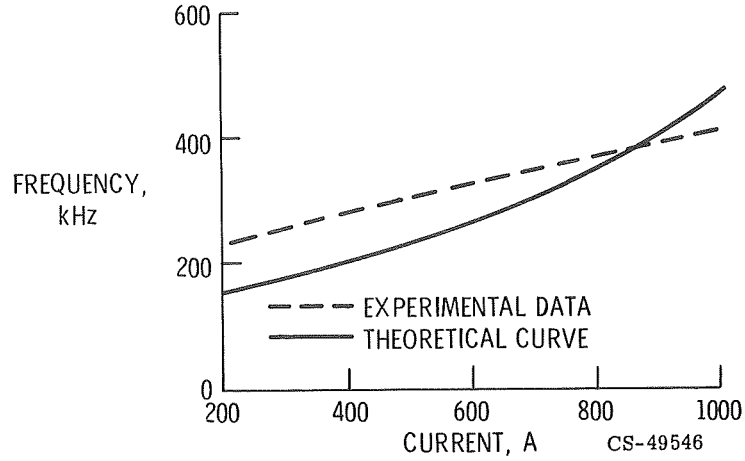


Figure I-27. - Frequency as function of current in ammonia. Mass flow, 0.03 gram per second; magnetic field, 0.100 tesla.

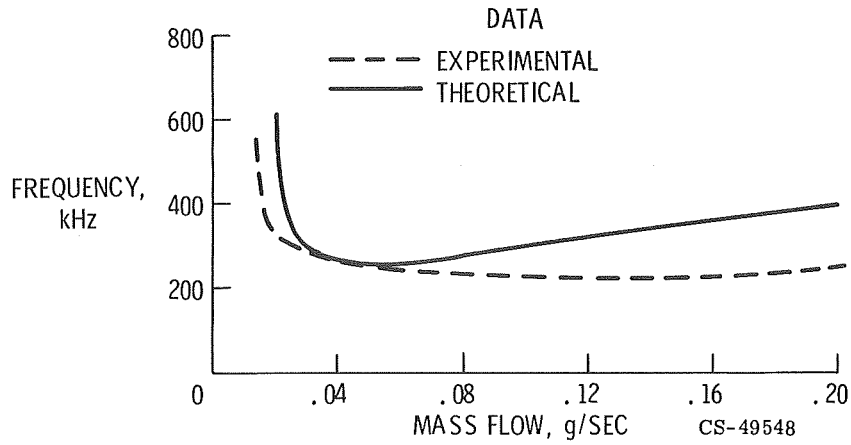


Figure I-28. - Frequency as function of mass flow in ammonia. Current, 600 amperes; magnetic field, 0.125 tesla.

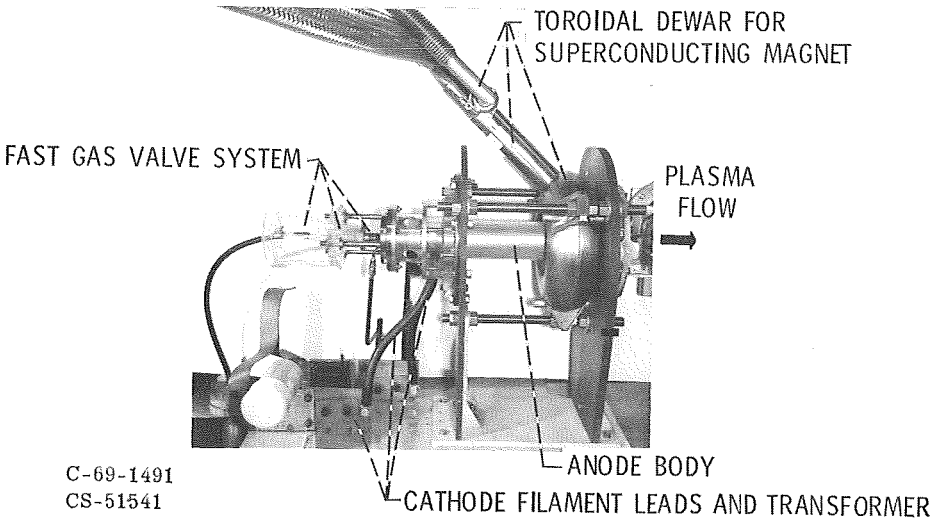


Figure I-29. - Megawatt MPD-arc plasma source.

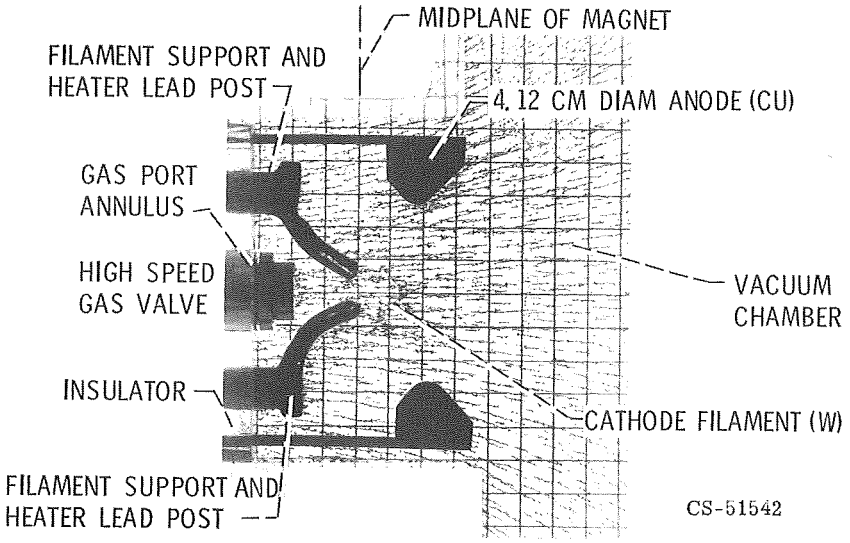


Figure I-30. - Arc chamber.

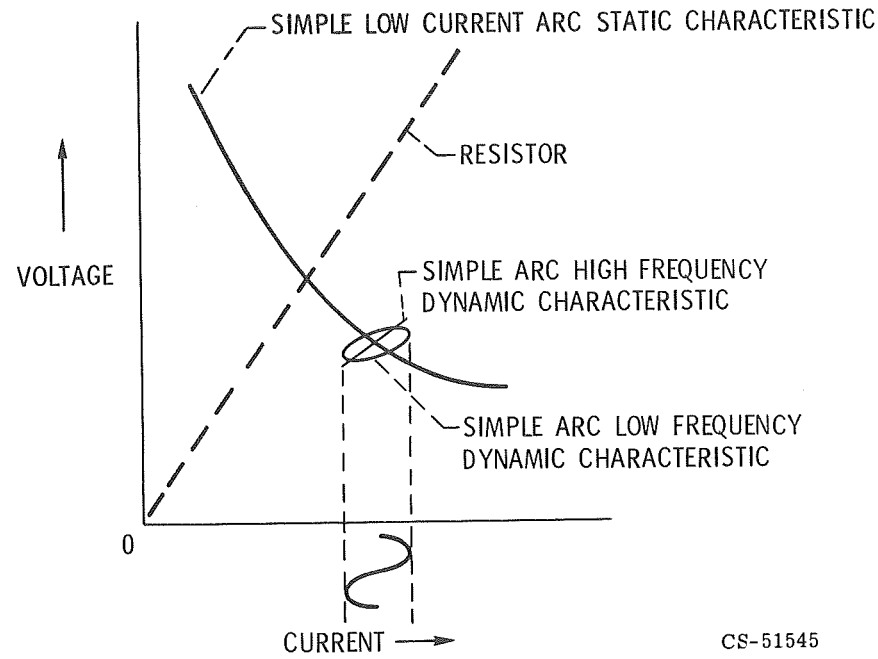


Figure I-31. - General voltage-current characteristic.

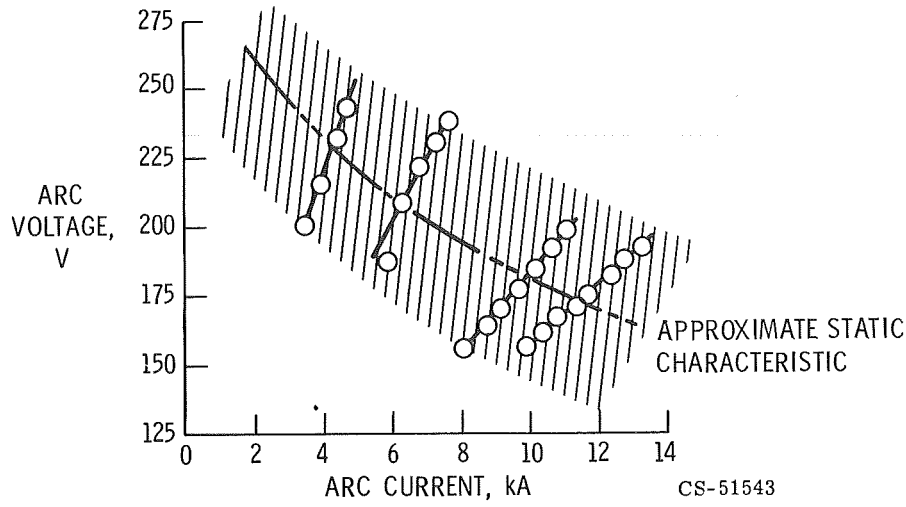


Figure I-32. - Dynamic characteristics of megawatt MPD-arc source. Magnetic field, 0.75 tesla.

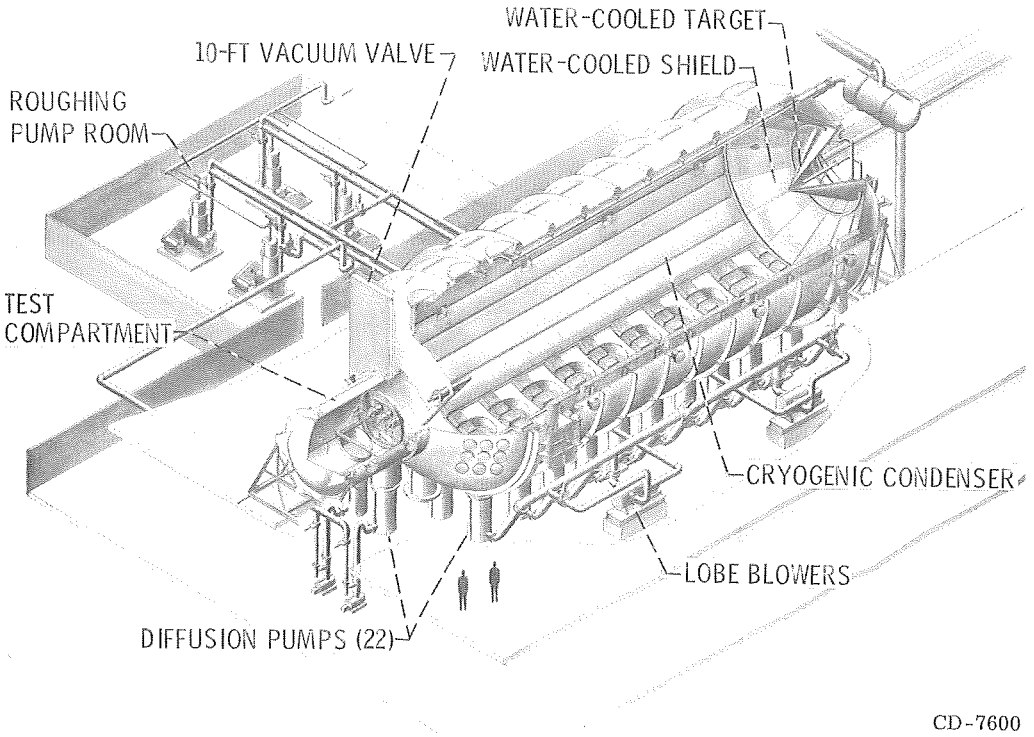


(a) Cutaway view of 25-foot-diameter tank.

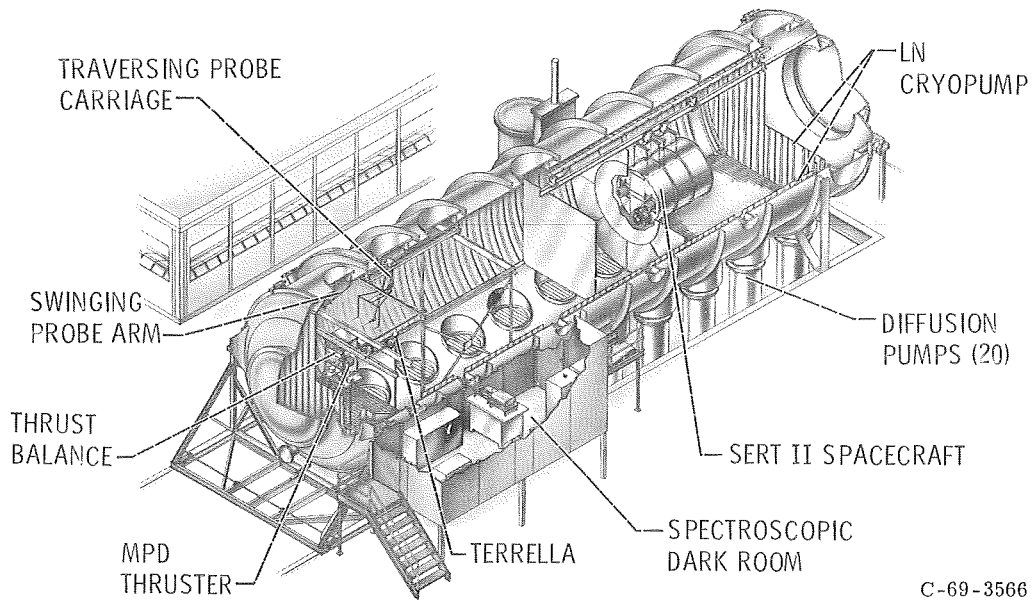


(b) Cutaway view of 15-foot-diameter tank.

**Figure I-33. - Electropropulsion test facility.**

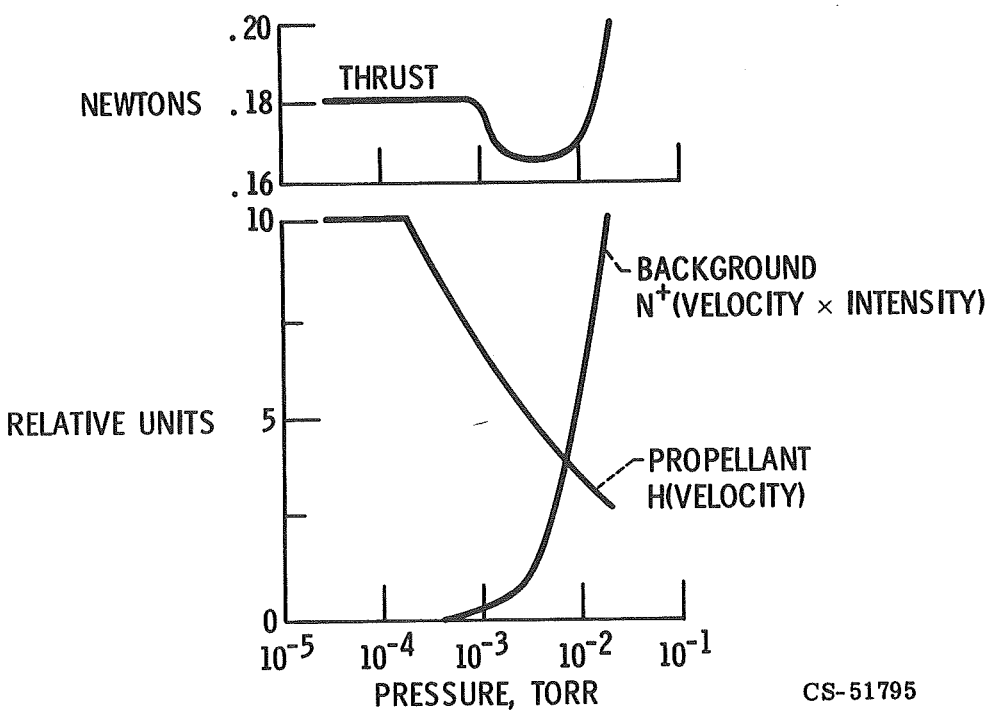


Figure I-34. - Relation between measured thrust and spectroscopic measurements in exhaust.

# II. CLOSED-CYCLE MAGNETOGASDYNAMIC POWER GENERATION

Lester D. Nichols

One application of the research at Lewis Research Center in plasma physics is in the field of direct energy conversion, specifically in the field of magnetohydrodynamic power generation. The principles of operation of these generators are reviewed first. Figure II-1 shows a magnetic field in the vertical direction, a conductor in the horizontal direction, and electrodes attached to the sides of the conductor. When the conductor moves perpendicular to the magnetic field, a voltage is induced whose direction is perpendicular to both the direction of the magnetic field and the direction of velocity of the conductor. If an electrical circuit with a load is completed between the electrodes, then electrical power is generated. This principle does not change if the conductor is a solid, a liquid, or a gas. When a liquid or a gas is used, then the generator is usually called a magnetohydrodynamic (MHD) generator, although "magnetogasdynamic" is preferable for generators that use gaseous conductors.

MHD power generation offers several advantages. In thermodynamic cycle turboalternator systems, thermal energy is transferred to a gas or vapor at a high pressure. This fluid is then expanded to a low pressure in a turbine. If one could utilize the expanding fluid itself as a conductor, then the need for rotating machinery could be eliminated. The stresses in static equipment are less than in rotating machinery. Since material strength decreases with temperature, the lower stress requirements make it possible to use fluids at much higher temperatures. This aspect makes an MHD generator a candidate for space application as well as for high efficiency ground-based systems. Also, MHD offers the possibility of very large generator power levels because the principle of induced voltage involves body (or volume) forces rather than surface forces such as turbines. MHD systems may be simpler than turboalternator systems because of the lack of seals, bearings, and other auxiliary equipment associated with rotating machinery. For an MHD system it is necessary to have only a moving conductor in a magnetic field.

## TYPES OF GENERATORS

Figure II-2 shows the schematic of a closed thermodynamic cycle MHD generator system. The magnetic field is applied in the generator volume. The velocity is obtained by heating a gas to a high temperature at a high pressure and then expanding the gas to a low pressure and high velocity. The kinetic energy is then taken from the fluid by the generator, and the fluid is cooled, compressed, and heated for a return through the generator. In an open cycle system, the fluid does not return to the compressor but is exhausted to the environment. However, the fluids that can be easily accelerated - namely, the gases and the vapors - do not have high conductivity at temperatures below 2500 K and pressures above 1 atmosphere. Two approaches have been suggested to get around this problem. One approach, suggested by Dave Elliott of JPL, is to transfer the kinetic energy of the expanded gas with low conductivity to a liquid metal with a high conductivity. This technique has problems that are mainly ones of fluid mechanical interraction and induction generator design. Although this approach may be promising in space, it is not discussed in the paper since there is no element of plasma physics involved. The other approach to solving the low conductivity problem is to raise the conductivity of the gas. This can be achieved by heating the electrons to 2500 K. Here again the attempts are divided into two groups as shown in table II-1. One group raises the temperature of the gas to heat the electrons and obtain high equilibrium conductivity, and the other group tries to raise the temperature of the electrons only and obtain a high nonequilibrium conductivity. These two groups can be characterized by the difference in the method of providing the high temperature fluid.

### Open Thermodynamic Cycle

If the energy is provided as a result of a chemical or nuclear reaction in the gas itself, then temperatures above the melting point of solids can be used if adequate cooling is provided for any solids exposed to these hot gases. Presently the high temperature is provided by the combustion of liquid fuels in either oxygen or preheated air. The systems are open cycle, and the combustion products are released into the atmosphere. The temperatures attainable this way are sufficient to provide adequate conductivity if potassium, or some other easily ionizable seed, is added. Figure II-3 shows one such unit. This generator, built by the Avco-Everett Research Laboratory in Boston, Massachusetts, has delivered 31.3 megawatts for a period of about 1 minute. The burner is to the left and the magnetic field on the right. The fuel is alcohol burning in oxygen. Other generating units

are constructed in Japan and the Soviet Union. The applications for these generators include a topping cycle for a central station power plant, an emergency or peaking generator to be used on an intermittent basis, or any application involving a large amount of power for a short time.

These open cycle units have operated for periods up to 50 hours using liquid fuel. The present development in this field is directed toward coal combustion. Programs to develop long life electrodes and insulators as well as seed material recovery systems are under way. There is also some evidence that operation at high power densities may involve a fluid mechanical problem called generator "stall" where boundary layer separation occurs. The limits on this phenomenon must be studied. Because of the ground-based application of these generators, research and development has been sponsored by private industry and to some extent by the Department of Defense. Many problems associated with these equilibrium generators are quite different from the nonequilibrium generators.

### Closed Thermodynamic Cycle

Consider an alternate method of providing the high temperature gas. If the energy is to be transferred to the gas from hot solid surfaces, such as a solid core reactor, the gas temperature is limited to temperatures below 2500 K where the equilibrium conductivity (at pressures necessary for efficient energy conversion) is too low. This problem may not exist in case of liquid or gas core reactors, and it may be possible to utilize equilibrium conductivities in a closed cycle with these reactors. However, to use gas MHD generators with solid core reactors some form of nonequilibrium conductivity (e.g., using electric fields) must be found. The effort at Lewis is directed toward studying the feasibility of nonequilibrium conductivity generators for use in space in conjunction with a solid core nuclear reactor. (Fig. II-4 is an isometric drawing of the Lewis MHD generator.) Research groups in Russia, Germany, and Italy, as well as the United States, are also concerned with this problem. In the United States, the other groups are located at MIT, G.E., and AVCO.

## GENERATOR CURRENT-VOLTAGE CHARACTERISTICS

Figure II-5 gives a schematic fiew of an MHD generator. The working fluid enters the generator from the left, and the magnetic field direction is into the plane of the figure. As the fluid passes through the generator the ions move toward the top

and the electrons toward the bottom. This charge separation creates an electric field $E_F$ in the positive direction, for the coordinate system chosen. At the same time there is a tendency for the electrons to be slowed down by the magnetic field. This tendency is larger for greater values of the Hall parameter. The ions, on the other hand, are coupled more strongly to the neutrals and are less affected by the magnetic field. This phenomenon also gives rise to a charge separation, with the ions tending to migrate to the downstream end of the generator. This charge separation also creates an electric field $E_H$, called the Hall field, in a direction opposite to the velocity. If electrical circuits are provided for currents in the induced field or Faraday direction $j_F$ and in the Hall direction $j_H$ (which have resistances denoted by $R_F$ and $R_H$, respectively), then the currents and fields in the generator can be controlled because of their dependence on the circuit resistances. This dependence can be calculated by using Ohm's law for the external circuitry and the variation of Ohm's law, which is appropriate for the gas resistance inside the generator. The vector representation of this Ohm's law, along with the vector diagram representing solutions to this equation, is shown in figure II-6. This Ohm's law was discussed in the paper by Seikel et al. The vectors $\sigma\vec{u} \times \vec{B}$, $\sigma\vec{E}_F$, and $\sigma\vec{E}_H$ are shown in figure II-5. The result of these vectors is the vector $\sigma(\vec{E} + \vec{u} \times \vec{B})$, and from the form of the Ohm's law, the two terms that add up to this vector must be at right angles to each other. Therefore, the locus of points of the current vector must lie on a semicircle as shown in the figure. It is evident how the direction of the current and electric fields can change depending on the Hall parameter and the induced voltage. It is possible to use Ohm's law for the generator and the external circuitry to solve for the currents and voltages inside the generator as a function of the induced voltage, the Hall parameter, and the magnitudes of the external resistances.

## ELECTRON HEATING

As a result of the current flowing inside the generator, energy is added to the electrons proportional to the scalar product of the current and the effective electric field. This energy is called joule heating. In order for the electrons to maintain a steady-state energy level, they must, in turn, get rid of this energy; this is done by collisions with the neutrals and ions. The amount of energy delivered to the heavy particles is porportional to the difference between the electron temperature and the heavy particle temperature. The proportionality constant depends on the particular heavy particle involved in the collision. If internal energy levels can be excited, then larger amounts of energy can be transferred in the collision. This is the situation, for example, when diatomic and polyatomic molecules are present.

For this reason, the largest temperature difference is obtained when atoms are used. The important parameters governing the behavior of the joule heating are the Hall parameter, the type of atoms, and the ratios of the external circuit resistance to the internal generator resistance. These ratios are denoted by $\rho_x$ and $\rho_y$ for the Hall and Faraday directions, respectively.

Figure II-7 shows the amount of electron temperature elevation over the gas atom and ion temperature as a function of the Hall parameter. The Faraday resistance ratio is taken as one which would represent maximum power generation for a generator with constant internal impedance. There are several curves that correspond to different values of the resistance in the Hall direction $\rho_x$, which goes from 0 to $\infty$. At values of 0 and $\infty$ the names Faraday Continuous and Faraday Segmented have been applied, respectively. It is noted, first of all, that as the Hall parameter increases, the electron temperature increases. Second, for a given Hall parameter, the electron temperature increases with increasing Hall resistance ratio. This is the concept being studied to provide a nonequilibrium conductivity in the generator. As the electron temperature increases, the number of electrons increases and, hence, the conductivity is elevated.

The elevation in electron temperature is greatest at open circuit in the Hall direction, because this corresponds to the largest Hall electric field. There is a twofold advantage here: First, an $\vec{E}\times\vec{B}$ drift velocity is added to the $\vec{u}\times\vec{B}$ drift velocity, thereby enhancing the current; and second, as a result of the increased current, there is increased electron heating and a consequent electron temperature rise. The temperature elevation depends quite critically on the ability to prevent the Hall currents from flowing.

This nonequilibrium process is, of course, not new. It is the situation in any discharge tube. The only difference is the use of the induced voltage resulting from the motion of the conductor through the magnetic field as the driving voltage. Experimental verification of this result has been obtained with a magnetic field for both a stationary gas with an applied voltage and a flowing gas with an induced voltage. The largest effect in the latter case has been obtained by using MHD generators operating in shock tubes.

## EFFECT OF FLUCTUATIONS

As mentioned previously, any Hall current decreases the amount of electron heating, primarily because of the reduction in the Hall electric field. John Smith in the previous paper discussed the effects of fluctuating components of the Hall current and the fact that they also can reduce the Hall voltage. In that sense, then,

fluctuations and Hall leakage have the same effect. A comparison between these two effects is shown in figure II-8. The effective Hall parameter, which is defined as the ratio of the Hall field to the difference between the induced and Faraday field, is plotted as a function of the Hall parameter. As before, the Faraday resistance ratio is 1.0. The ideal curves represent the effect of leakage resistance. With infinite resistance, the effective Hall parameter equals the Hall parameter. As the leakage resistance decreases, so does the effective Hall parameter. At a resistance ratio of 10 the effective Hall parameter is below 2.0. Also shown in this figure is the curve considering instabilities with no Hall leakage for the case of cesium-seeded argon at 2000 K and a Mach number of 0.5. Notice that for this situation the effective Hall parameter is also below 2.0. These calculations are based on an instability model developed by Dr. Albert Solbes of MIT. He shows that this model agrees well with some observed experimental evidence. This curve indicates that resistance ratios must be around 100 or greater in order to be limited only by the instabilities.

As mentioned previously, there is quite a difference between the amount of nonequilibrium conductivity obtained in the shock tube and that obtained in steady-flow generators. This difference may be related to our experience with the MPD thrusters. At high power levels and short times, as discussed by Charles Michels, two differences are observed: the discharge becomes more "resistor-like" and less "arc-like", and there is no rotating spoke. It is possible that both differences can be explained by the short time period which may be too short for instabilities to develop into a full fledged fluctuation, or turbulence. This short time period may also prevent the development of current shorting paths that are found in the longer time generators.

## Effect of Impurities

Now a generator is considered with a large resistance ratio, and the effect of carbon monoxide impurities is examined. These impurities lower the electron temperature and ultimately the power output. Figure II-9 shows the effect of both fluctuations and the impurities on the power density of an MHD generator with no Hall leakage. Conditions in this figure are the same as in the previous one, except that the magnetic field strength is fixed at 1.0 tesla and the load parameter varied from open circuit to short circuit. Curve e is considered first. This curve shows the equilibrium conductivity, which is the conductivity given by the gas conditions and not a function of the joule heating or of the load parameter. This equilibrium conductivity provides a power density of about 0.3 megawatt per cubic meter at a

load parameter corresponding to a Faraday resistance ratio of 1. For the ideal curve (no impurities and no instabilities), two things may be observed. The power density is increased by about a factor of 20, and the peak shifts to regions of lower load parameter. Curve b illustrates the effect of instabilities above load parameters of about 0.2. The power density drops off rather rapidly. Curve c, which considers the effect of impurities only, shows the power density with the addition of 1000 ppm of carbon monoxide. The effects of other diatomic impurities are roughly the same as for carbon monoxide. The maximum power density is reduced to about 15 times the equilibrium value, and its value is below that of the ideal case and that of the instability case (for load parameters below 0.38). Curve d shows the effect of both impurities and instabilities. The peak is shifted even further toward short circuit, and the maximum is only about a factor of 3 greater than equilibrium. Also, for load parameters above 0.5, the curve lies below the equilibrium curve. As a result of this calculation it seems that the impurity level must be kept well below the value of 1000 ppm. It should be mentioned that the effect of both instabilities and impurities can be lessened by using a supersonic Mach number.

As a result of these studies performed at Lewis, it seems reasonable to require resistance ratios in the Hall direction to be in the hundreds and impurities to be below 1000 ppm (and perhaps as low as 100 ppm). Fluctuation are probably going to exist, so they must be included in any performance analysis.

## SPACE POWER SYSTEM STUDY

In order to determine the operating parameters to be used in the experimental program, a system study of a possible MHD system for use in space is considered. In this study it is important to include the efficiency of such generators. Figure II-10 shows the isentropic efficiency of an ideal MHD generator designed for minimum volume and operating with an outlet to inlet pressure ratio of 0.5 as a function of load parameter. Note that the efficiency is higher at larger values of the load parameter. This is in conflict with the power density requirement which indicates higher power density at low values of the load parameter. In space, the dictates of generator efficiency must be respected since the reactor and shielding weight will probably be the dominant weight of any space power system. Notice also that, for a given generator efficiency, as the Mach number increases so must the load parameter, which, in turn, tends to lower the power output. This is an effect that tends to offset many of the advantages of supersonic Mach number as far as nonequilibrium effects are concerned.

The results of the system study are now examined. The generator for the

system is assumed to be operating as part of a Brayton cycle. The working fluid is neon, the cesium seed fraction is 0.003, the Mach number is 2.0, the generator pressure ratio is 0.5, and the length is 0.5 meter. These specifications correspond to approximately a 1-megawatt generator at 10 atmospheres. The efficiency and radiator area are chosen such that these values equaled corresponding values for a potassium turbine with an inlet temperature of 2000° F (1365 K). The instability analysis of Solbes is used to account for fluctuations. Figure II-11 shows the results of this study where the magnetic field strength is plotted on the ordinate as a function of the maximum cycle temperature with pressure as a parameter. The temperature range spans the regions from 1500 K, which is approximately the limit for turbines, to 2500 K, which is approximately the value for which equilibrium conductivity is sufficient for MHD systems. Consider the point at 2000 K and 10 tesla. The required pressure is then seen to be 10 atmospheres. This point represents a possible system operating point. The pressure is sufficiently high to provide adequate reactor heat transfer. The magnetic field strength is within the present day state of the art. The temperature of the working fluid is approximately the same as that achieved for the nuclear rocket program. However, the temperature is probably the most difficult value to achieve for long time periods. Notice the effects if operation is attempted at a lower temperature. If the magnetic field strength is kept constant, then the pressure decreases and reactor heat transfer will suffer. On the other hand, if the pressure is kept constant, then the magnetic field requirements increase and may be larger than available superconducting materials can provide. It seems reasonable, therefore, to try to develop an MHD generator to operate at 2000 K, which is therefore the temperature chosen for our experiment. The Hall parameter for this condition is about 12 and the effective Hall parameter is about 0.36. For the experiment both the magnetic field strength and the system pressure have been lowered by a factor of 5, while still maintaining the Hall parameter value of 12. Of course, the power density is decreased, but the feasibility of the technique of nonequilibrium ionization can still be studied. The facility uses argon, has a graphite resistance heater, and is capable of operating to at least a 2100 K maximum temperature.

## LEWIS EXPERIMENTAL RESULTS

The first item to consider is the amount of impurities in the facility. Because of the graphite resistance heater, hydrogen and carbon monoxide impurities are released. It has been possible to maintain the level of these impurities down to about 500 ppm with a purge flow which removes the impurities at their generation rate.

We have taken precautions to provide as high a value as possible of the wall resistance in the Hall and Faraday directions. Figure II-12 shows the present test section. The gas flow is into the figure. The outer stainless steel supporting structure and the insulating bricks can be seen. Ceramic keys are used to hold the bricks in place, and the electrodes are not touching the surfaces, so that any cesium on the surface will not provide a shorting path. All insulating surfaces exposed to the cesium are coated with a higher purity aluminum oxide in an attempt to reduce any chemical reaction with cesium. The cesium injection tube is at the entrance. It is now possible to maintain resistance to ground at around 2 kilohms, even after cesium has been injected. However, the possibility that during the time of injection the cesium does lower this resistance cannot be eliminated.

We feel that this resistance is about as high as it can be for the wall temperatures being used. Therefore, a further increase in the resistance ratio must be made by reducing the internal generator resistance (especially if the value of leakage resistance decreases with the injection of cesium). It is possible to cool the walls, but this procedure does not seem compatible with an efficient generator, unless, of course, it is a very large generator. Also, at a lower temperature, the effect of cesium deposit on the walls may even be enhanced.

There is another reason for trying to reduce the generator resistance. The joule heating of the electrons can occur only when the current flows, and since generators are inherently voltage generators, the current can flow only when the internal impedance is low. Therefore, some means must be used to create ions to provide the conductivity to get the procedure started. This is called preionization because it occurs before the gas enters the generator. Therefore, the solution to the preionization problem may also hold the solution to the excessive leakage problem.

In some of our recent tests, the possibility has been investigated of applying a voltage to successive electrode pairs of the generator as a method of preionization. If the effective discharge resistance decreases for successive electrode pairs, then the preionization is successful. In figure II-13(a) the effective discharge resistance is plotted as a function of seed fraction for three successive electrode pairs. The magnetic field strength is about 1.0 tesla. The effective discharge resistance, or the generator resistance, decreases when going from electrode pair 3 to 4 to 5. The resistance increases, if anything, with seed fractions above 0.1 percent. At a seed fraction of 0, the effective discharge resistance becomes very large.

Figure II-13(b) shows the effect of the magnetic field strength on the generator resistance. Again the effective resistance is plotted for three successive electrode pairs. The resistances are plotted as a function of the magnetic field strength for a

seed fraction of about 0.05 percent. Successive discharges do apparently reduce the discharge resistance. Also, the resistance increases with increasing magnetic field strength for all electrode pairs. At the highest magnetic field strength the discharge became unstable and the current, rather than going directly across the channel, shorted along the channel and passed through one of the load circuits downstream.

The encouraging feature of the data shown by these two slides is that after sufficient preionizing the discharge resistance is reduced below 20 ohms. If the leakage resistance can be held above 2000 ohms, then a resistance ratio of above 100 can be maintained. This condition is necessary for the attainment of non-equilibrium ionization. Hopefully, further reduction in the discharge region is possible with more preionization.

In our future research, we plan to concentrate on the preionization of the plasma. It is this area which holds the most promise for developing elevated electron temperatures. We would like to study the means of controlling the cathode sheath drop and the mode of electrode emission. We will also try to reduce those factors which tend to hinder the achievement of electron heating. One possibility is to operate with a supersonic generator. This seems to provide a larger region of load parameter where detrimental effects of impurities and instabilities can be reduced. There is also the possibility of operating with a different geometry. There are, for example, generators made with diagonal conducting walls along the equipotential surfaces of the generator. There is some evidence that the performance is better for this geometry. A very attractive feature of these generators is that the number of load circuits can be reduced to one, rather than equal to the number of electrode pairs as in the Faraday generator. Finally, it may be of interest to raise the magnetic field strength and the pressure to generate larger amounts of power. This will require the use of superconducting magnets. Another advantage of these magnets is the possibility of increased access to the test section for diagnostic equipment and instrumentation.

The goal of our research is to determine the lowest maximum cycle temperature for which one can still achieve reasonably good performance with an MHD generator.

# BIBLIOGRAPHY

This bibliography comprises publications authored by the members of the NASA Lewis Research Center Staff.


Bishop, Allan R.; and Nichols, Lester D.: Effect of Electrothermal Instabilities on Brayton- and Rankine-Cycle Magnetohydrodynamic Space Power Generation Systems. NASA TN D-5461, 1969.

Dugan, J. V., Jr.; Lyman, F. A.; and Albers, L. U.: Solution of the Boltzmann and Rate Equations for the Electron Distribution Function and State Populations in Nonequilibrium MHD Plasmas. Electricity from MHD. Vol. 2. International Atomic Energy Agency, 1966, pp. 85-100.

Lamberti, Joseph M.; and Saunders, Neal T.: Compatibility of Cesium Vapor with Selected Materials at Temperatures to 1200° F. NASA TN D-1739, 1963.

Lyman, F. A.; and Dugan, J. V., Jr.: Electron Distribution Function and Number Density in a Nonequilibrium Seeded Gas. Seventh Symposium on Engineering Aspects of Magnetohydrodynamics. ASME, 1966, pp. 94-95.

Heighway, John E.; and Nichols, Lester D.: Brayton Cycle Magnetohydrodynamic Power Generation with Nonequilibrium Conductivity. NASA TN D-2651, 1965.

Mantenieks, M. A.; and Nichols, L. D.: Current-Voltage Measurements in a Supersonic MHD Generator with an Arc Heated Argon Plasma. Engineering Developments in Energy Conversion. ASME, 1965, pp. 33-48.

Nichols, Lester D.: Analysis of a Radial-Flow Hall Current Magnetohydrodynamic Generator. NASA TN D-2973, 1965.

Nichols, L. D.: Criteria for Use of Rankine-MHD Systems in Space. Electricity from MHD. Vol. 2. International Atomic Energy Agency, 1966, pp. 765-778, 1109.

Nichols, Lester D.: Non Equilibrium Ionization in MHD Generators for Use as Part of a Rankine Cycle in Space. Seventh Symposium on Engineering Aspects of Magnetohydrodynamics. ASME, 1966, pp. 87-88.

Nichols, Lester D.: Comparison of Brayton and Rankine Cycle Magnetogasdynamic Space-Power Generation Systems. NASA TN D-5085, 1969.

Nichols, Lester D.; and Mantenieks, Maris A.: Analytical and Experimental Studies of MHD Generator Cathodes Emitting in a "Spot" Mode. NASA TN D-5414, 1969. Also presented at the ASME Winter Annual Meeting, Nov. 16-21, 1969.

Nichols, Lester D.; Morgan, James L.; Nagy, Lawrence A.; Lamberti, Joseph M.; and Ellson, Robert A.: Design and Preliminary Operation of the Lewis Magnetohydrodynamic Generator Facility. NASA TN D-4867, 1968.

Schwirian, Richard E.: Effects of Magnetic Reynolds Number in MHD Induction Machine. MS Thesis, Case Inst. Tech., 1964.

Schwirian, Richard E.: Electrical Conduction from a Cold Electrode to a Supersonic Plasma. Ph. D. Thesis, Case Western Reserve Univ., 1968.

Schwirian, Richard E.: A New Momentum Integral Method for Treating Magnetohydrodynamic and Simple Hydrodynamic Entrance Flows. NASA TN D-5215, 1969. Also Paper 69-724, AIAA, June 1969.

TABLE II-1. - HIGH GAS CONDUCTIVITY

| Method of heating gas | Gas temperature, K | Method of heating electrons | Thermodynamic cycle |
|---|---|---|---|
| Heat exchanger | <2500 | Electric fields | Closed |
| Chemical or nuclear reaction | >2500 | Collisions | Open |

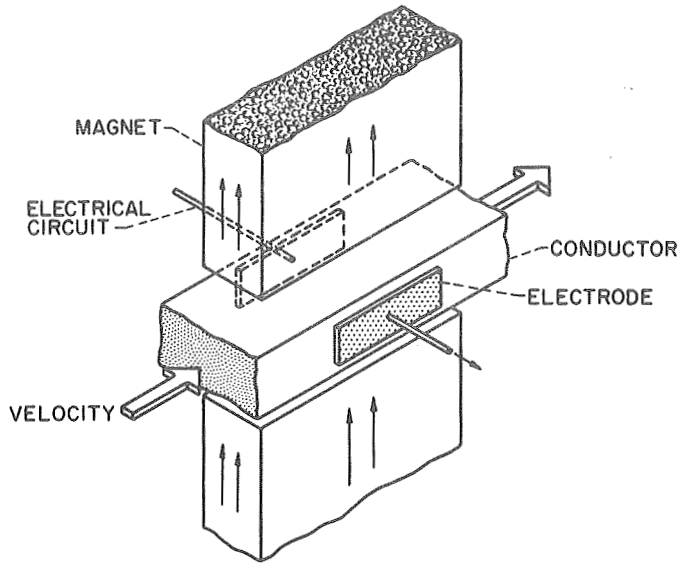


CS-26152

Figure II-1. - Conductor moving in magnetic field.

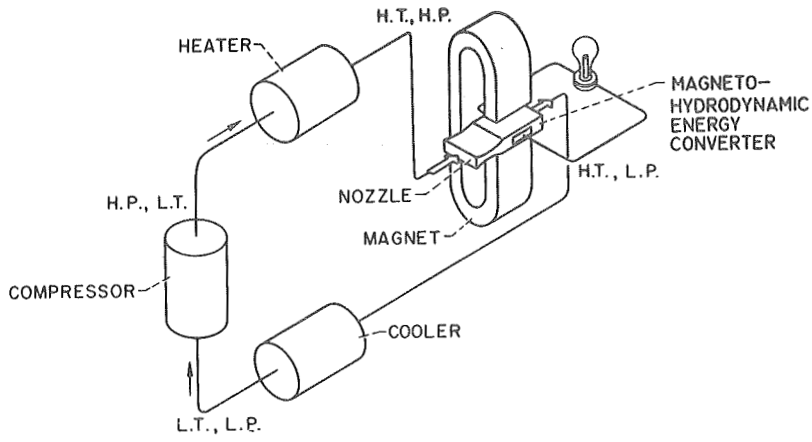


CS-26151

Figure II-2. - Power generator cycle with MHD energy converter.

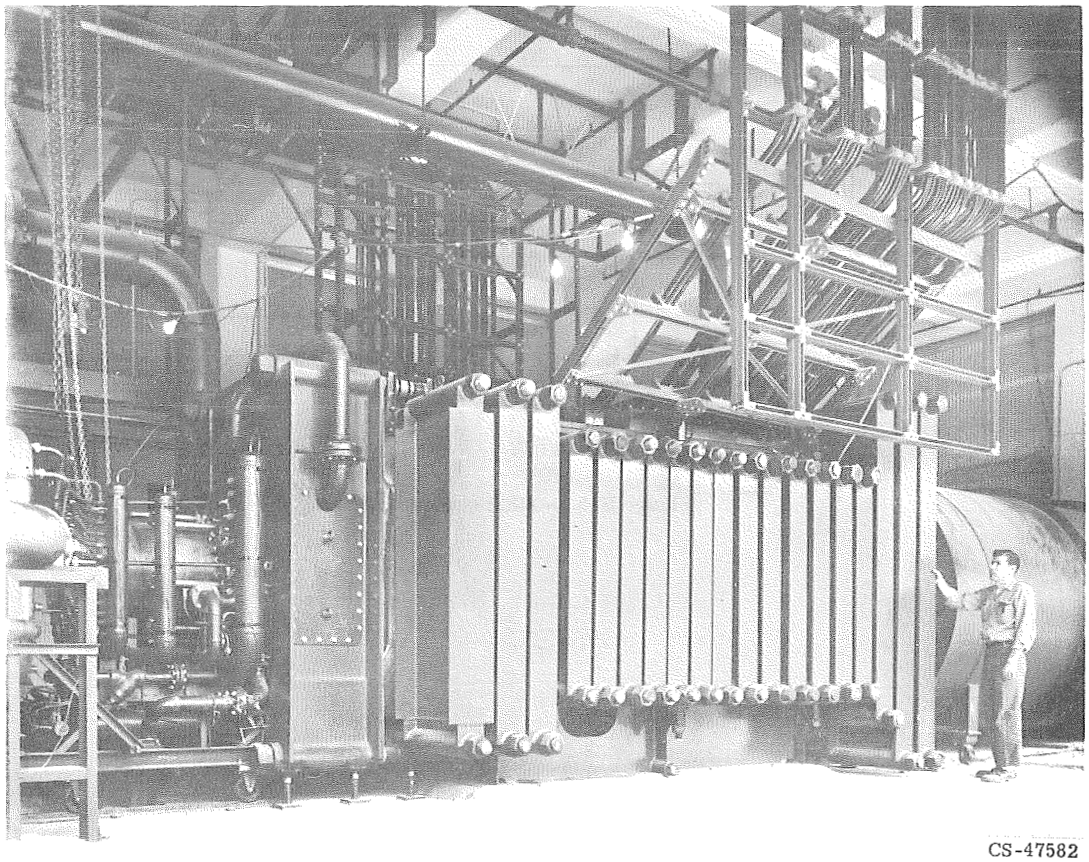

CS-47582

Figure II-3. - 31.3 Megawatts electric combustion-fired MHD generator.

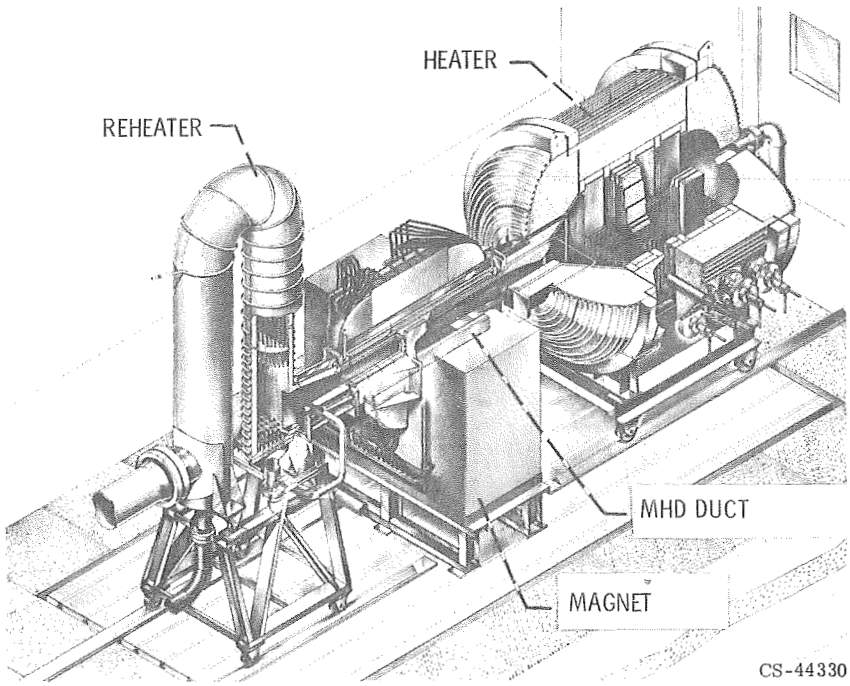


CS-44330

Figure II-4. - MHD generator experiment.

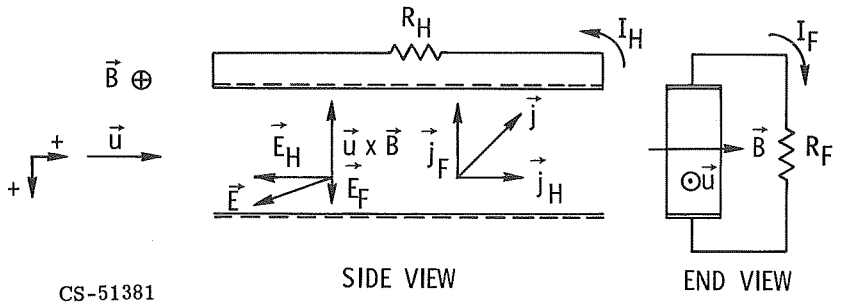


CS-51381

Figure II-5. - MHD generator.

CS-51381

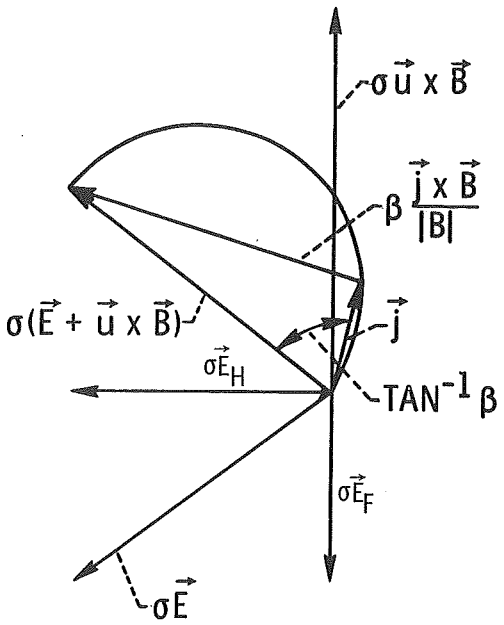


OHM'S LAW

$$\vec{j}+\beta\frac{\vec{j}\times\vec{B}}{|B|}=\sigma(\vec{E}+\vec{u}\times\vec{B})$$

CS-51382

Figure II-6. - Electric field vector diagram ($|\vec{u}\times\vec{B}|>\vec{E}_F$).

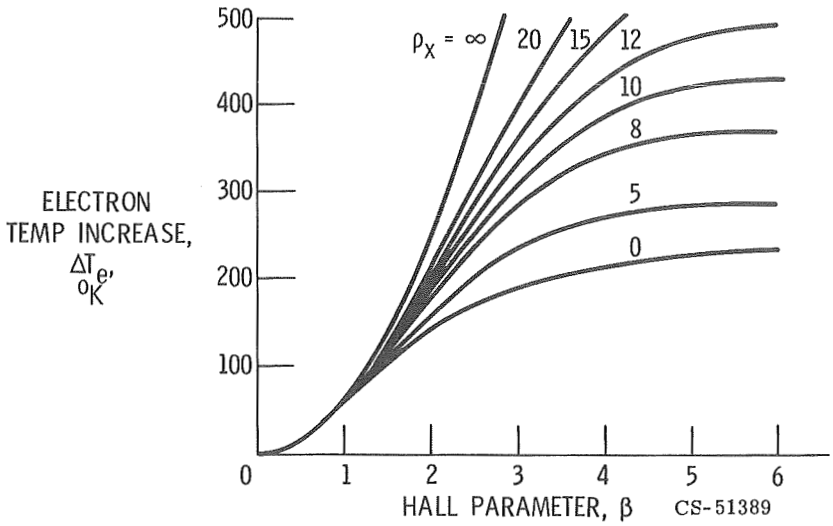


Figure II-7. - Electron temperature increase in Faraday segmented generator. $p_y = 1$; $(\gamma M^2 T/3\delta) = 257.5$ K.

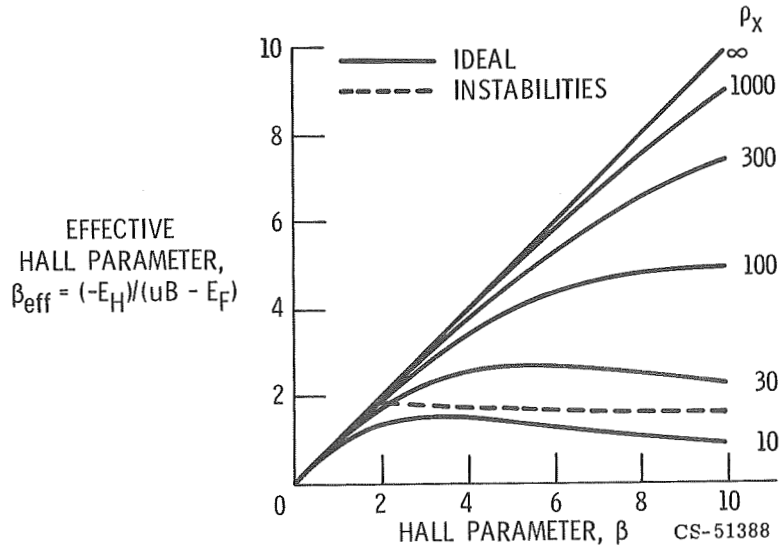


Figure II-8. - Effect of Hall current and instabilities on effective Hall parameter.

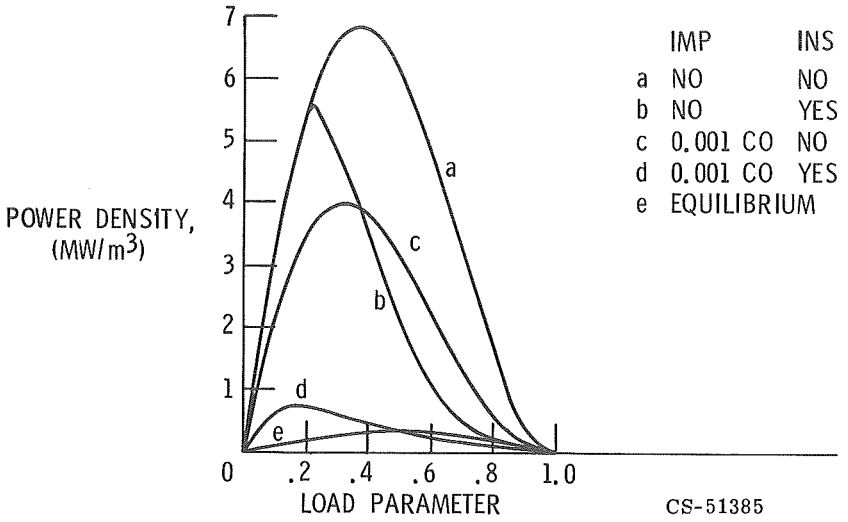


Figure II-9. - MHD generator power density. Mach number, 0.5; T = 2000 K; P = $2 \times 10^5$ newtons per square meter.

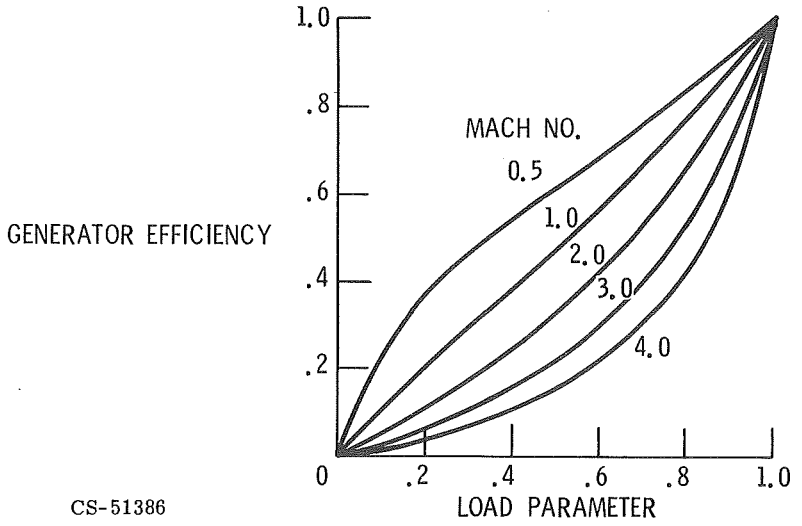


Figure II-10. - MHD generator efficiency. Pressure ratio, 0.5.

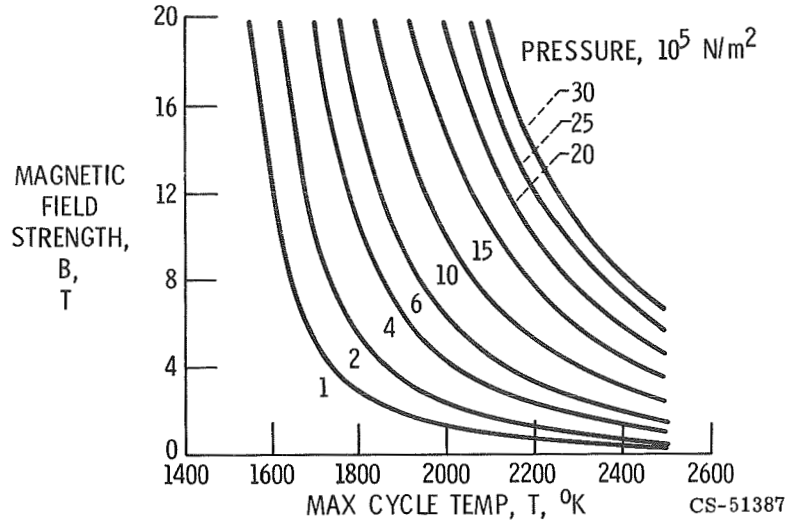


Figure II-11. - Required magnetic field strength for Brayton cycle MHD. Mach number, 2.0; Ne - 0.003 Cs; generator length, 0.5 meter.

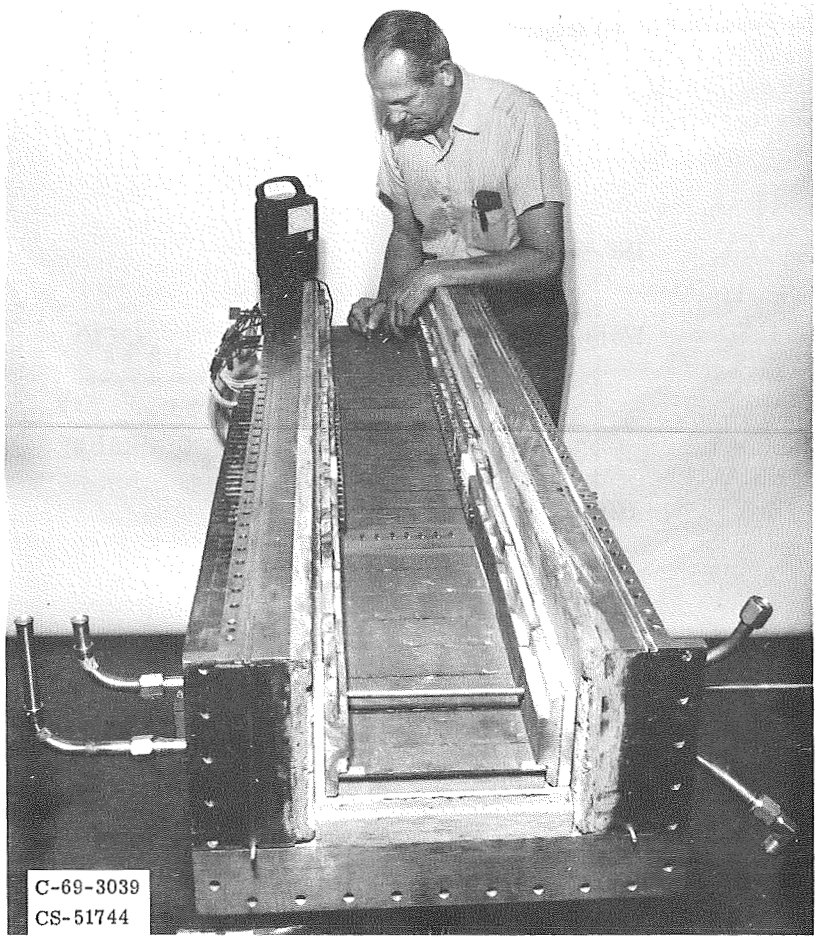


Figure II-12. - MHD generator.

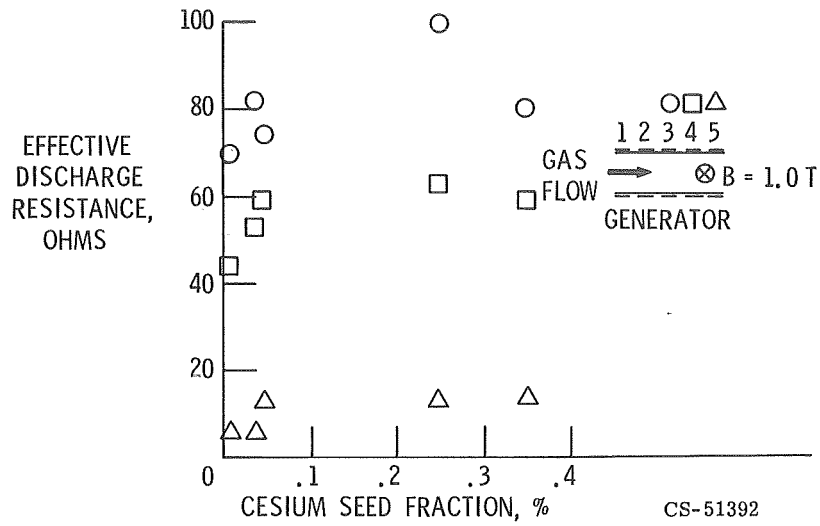


(a) Magnetic field strength, B = 1.0 tesla.

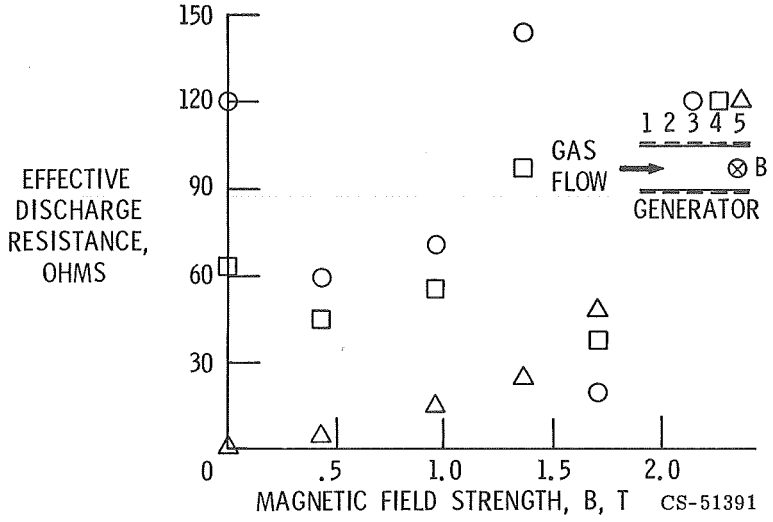


(b) Seed fraction, S = 0.05 percent.

Figure II-13. - Effective discharge resistance for argon seeded with cesium.

# III. PLASMA HEATING AND CONTAINMENT

Warren D. Rayle, John J. Reinmann, J. Reece Roth,
and Donald R. Sigman

One of the most important goals of our work on plasma heating and confinement is the possibility of controlled thermonuclear fusion for space power and propulsion. As pointed out in the INTRODUCTION, the thermonuclear rocket is potentially the best propulsion system yet envisioned for missions with large payloads. Although this discussion will be oriented toward fusion, we also have a broader objective which is to acquiare knowledge and to obtain a better understanding of plasma processes. Such knowledge and understanding are useful for other potential applications of plasma technology.

Controlled fusion research has been conducted by many talented scientists for nearly two decades. No one can predict just when fusion will become a reality. In the meantime, we need to keep abreast of new results and knowledge in this important sector of plasma physics. Active work in the plasma heating and confinement fields not only serves this purpose but also permits us to make significant contributions which aid both the study of fusion and other aspects of plasma technology in which NASA has a vital interest.

After presenting a brief review of some of the basic factors of interest to controlled fusion, a sample of the NASA Lewis work in the plasma heating and confinement areas will be presented. Two plasma heating studies will be covered in some detail. Work related to the understanding of plasma losses from confinement will be briefly touched upon.

## FUSION CONSIDERATIONS

A good estimate of the required operating parameters of a fusion reactor may be obtained by performing energy-balance calculations on the overall power plant. The light elements of interest for fusion reactors are deuterium, tritium, and helium-3. The deuterium-tritium fuel mixture, which releases most of its energy in the form of high-energy neutrons, is considered for ground power applications. The deuterium - helium-3 mixture releases most of its energy to charged particles,

and it will be used for space propulsion or for direct conversion of charged-particle energy into electrical power.

Some of the required parameters for deuterium - tritium or deuterium - helium-3 reactors are shown in the following table:

| | |
|---|---|
| Temperature, K | $10^8$ to $10^9$ |
| Confinement time, sec | 0.1 to 1.0 |
| Density, particle/$m^3$ | $10^{20}$ to $10^{22}$ |
| Magnetic field, T | 5 to 10 |

If positively charged ions are to undergo a fusion collision, then as they approach each other, their kinetic energies must be high enough to overcome the electrostatic repulsion. This requires plasmas with extremely high ion temperatures on the order of $10^8$ to $10^9$ degrees.

The probability that a particle will undergo a fusion event is proportional to the amount of time the particle remains in the reactor (confinement time). Feasibility studies indicate that confinement times on the order of 0.1 to 1 second are required.

The fusion power density is porportional to the square of the plasma number density. For the power levels of interest, number densities on the order of $10^{20}$ to $10^{22}$ particles per cubic meter are required.

In all proposed fusion reactor schemes, plasmas are confined with the aid of magnetic fields. The field strengths required are on the order of 5 to 10 teslas. To efficiently produce these high fields over the large reactor volumes, we would use superconducting coils.

The major obstacle in fusion research is inadequate confinement time. The longest confinement time in a thermalized, hot-ion plasma experiment is about 0.02 second, and most experiments give times on the order of a millisecond or less. Because of these rapid loss rates, it is difficult to produce a high-density, high-temperature plasma. Therefore, the major fusion research problems at present are (1) plasma confinement and (2) plasma production and heating.

Confinement studies are conducted in several different magnetic-field configurations. These magnetic geometries include both open-ended, and closed systems. Examples of these two systems are shown in figures III-1 and III-2. Figure III-1 is an example of an open-ended magnetic-mirror machine. Radial diffusion to the walls is reduced by the axial magnetic fields, while plasma end losses are reduced by increasing the field intensity at the ends. Some of the plasma approaching the ends gets reflected back towards the center of the machine. The higher field regions are therefore called magnetic mirrors.

A toroidal magnetic geometry (shown in fig. III-2) was devised to eliminate end losses of mirror systems. Plasma circulates around the major axis of the

torus and diffuses along the minor radius to the walls.

Until recently, the experimental loss rates in both of these geometries exceeded the classical, or collisional loss rates. These anomalously high losses are generally attributed to plasma instabilities. A plasma can become unstable in many ways, including both macroscopic and microscopic instabilities. In a macroscopic instability there is gross motion of the plasma to the wall. Gross motions can be controlled by magnetic wells and by magnetic shear configurations, to be discussed later. The microscopic instabilities are more akin to fluid dynamic turbulence. The result of these instabilities is increased diffusion to the wall. They may be caused by density and temperature gradients in the plasma or by non-Maxwellian velocity distributions of the ions or electrons.

All these instabilities derive from the fact that the plasma is not in a true state of thermodynamic equilibrium, If the plasma relaxes to the equibrium state, it can release free energy that can drive the instabilities. To avoid this, we must either eliminate the nonequilibrium condition or prevent the plasma from relaxing to the equilibrium state.

The magnetic-well concept is a means of preventing the plasma from relaxing to the equilibrium state. This concept is illustrated in figure III-3. The circles represent surfaces of constant magnetic-field intensity. The center of the circles is the minimum magnetic-field intensity point. The intensity increases away from the center. The plasma is placed in the center of the magnetic well. Since the plasma is dimagnetic, if it tries to move outward into the higher field intensity region, it will be pushed back toward the center. These surfaces of constant magnetic-field intensity should not be confused with the magnetic-field lines. The field lines actually intersect these surfaces.

An example of an open-ended magnetic-well configuration is shown in figure III-4. To produce the magnetic well, so-called quadrupole fields are superposed on the simple magnetic mirror. The quadrupole field consists of four linear conductors alined parallel to the axis of the mirror field. The current in adjacent bars runs in opposite directions and produces the magnetic-field pattern shown in the upper right-hand corner of the figure. The result of superposing the two fields is shown at the bottom. The magnetic well is located in the central region. Magnetic wells have proved completely effective in eliminating macroscopic instabilities in open-ended systems.

Although it is not obvious from figure III-4, the magnetic-field lines must bulge toward the center of the plasma in a magnetic well. When field lines close on themselves, as in a torus, it is not possible to have the field lines bulge toward the plasma everywhere. Therefore, a true magnetic well is not possible in the toroidal geometry. However, theory shows that the macroscopic instabilities may be stabi-

lized in toroids by using average magnetic wells. An example of a toroidal average magnetic well is shown in figure III-5. Four current-carrying conductors are immersed in the plasma. The current flows in the same direction in all four bars. The magnetic-field pattern is shown in the inset. In the central region, the field lines bulge toward the plasma, but in the region outside the bars, the field lines bulge away from the plasma. These so-called toroidal multipoles are valuable for testing theory, and for gaining insight into the mechanisms of diffusion. But since the conductors are immersed in the plasma, they could not be used in a fusion reactor. The conductors would be burned up by the hot plasma.

The other way to control macroscopic instabilities in a torus is by application of magnetic shear. A toroidal machine with magnetic shear would have field lines as shown in figure III-6. The field lines spiral around the minor axis, and the amount of twist of the spiral varies along the minor radius.

Toroidal shear fields are produced by the usual toroidal windings plus another set of current-carrying conductors. These additional conductors can either be placed external to the plasma or be immersed in the plasma. Since a fusion plasma has very high electrical conductivity, the plasma can act as a current-carrying conductor. By transformer action a current can be induced to flow in the plasma along the minor axis to provide the shear field. The experiment that has produced the best combination of confinement time, ion temperature, and density was conducted in the Tokamak T-3, a toroidal machine with magnetic shear. This Russian machine has received a great deal of publicity lately. In this experiment the magnetic shear is produced by inducing a current to flow in the plasma along the minor axis of the torus.

Let us now consider methods to control microscopic instabilities. Because of the relatively simple geometry of the open-ended systems, the theoretical understanding of microscopic instabilities in such systems is fairly complete. The theory also suggests ways of eliminating most of the instabilities. This usually requires a more randomized ion velocity distribution than can be produced experimentally at this time. Unfortunately, even if the instabilities are controlled, and the losses are caused only by classical diffusion, the energy balance is marginal. Some way is needed to further reduce the end losses below the classical values to make a feasible reactor. There are several methods under study to reduce mirror end losses. The feasibility of open-ended machines will probably rest on the success of these schemes.

In toroidal systems, there are some indications that both macroscopic and microscopic instabilities occur. Unfortunately, the toroidal geometry is so complicated that the theory of microscopic instabilities is far from complete, and there are fewer theoretical guidelines for their control. Until about 1965, experimental confinement

times in toroidal machines were in approximate agreement with the so-called Bohm diffusion equation. The confinement time for Bohm diffusion is directly proportional to the magnetic field and inversely proportional to the electron temperature:

$$\tau_{\text{Bohm}} \propto \frac{B}{T_e}$$

This is an empirical relation that Bohm found to hold in experiments conducted on ion sources in magnetic fields. Bohm offered no theoretical derivation of the relation, but the same functional form of the variables can be derived by the use of a dimensional argument.

In contrast, the confinement time for classical or collisional diffusion is proportional to the square of the magnetic field and to the square root of the electron temperature:

$$\tau_{\text{classical}} \propto \frac{B^2 T_e^{1/2}}{n}$$

For typical reactor design conditions the classical confinement time is several orders of magnitude larger than the Bohm confinement time.

Fortunately, in a toroidal machine classical confinement times are not required. The actual confinement time must be about 100 to 1000 times that of Bohm. This is one clear advantage that the toroidal machine has over the open-ended system. As previously noted, in a feasible open-ended system, the end losses will probably have to be less than the classical losses.

After 1965, experimental confinement times in toroidal systems continued to increase up to about 100 Bohm times. Very recently, it was announced that 300 Bohm times were achieved in a toroidal multipole experiment. Thus, prospects for toroidal machines look good.

It is worth pointing out that relatively long confinement times are not the only encouraging feature of the recent toroidal experiments. In his recent talk at the Bucharest meeting, Galeev reported that radial diffusion in the Tokomak could be explained entirely by binary collisions, without having to invoke collective effects or some instability related diffusion process. The loss rate is higher than classical diffusion because the average random-walk step size in the Tokomak is the average separation between drift surfaces before and after a binary collision. These drift surfaces are separated by a distance greater than the gyroradius, which is the step size for classical diffusion.

It would certainly simplify matters considerably if classical scattering ideas could explain the losses in the toroidal machines.

The present status of one aspect of fusion research can be summarized with the aid of the so-called Lawson diagram (see fig. III-7). This is a plot of ion temperature against the product of density and confinement time. In energy balance calculations, n and $\tau$ always appear as the product. A reactor will operate in the upper right-hand corner. The darker the shading, the better the chance for a workable reactor.

The 2X and Scylla machines are open-ended machines in the United States. The C-stellarator is a toroidal machine at the Princeton Plasma Physics Laboratory, and Tokamak is a Russian toroidal machine. The arrows lead to open circles which are the predicted operating points for new machines that are being built and that will be operational in a few years. If the scaling laws are correct for these machines, this would indeed be significant progress toward controlled fusion. Incidentally, the C-stellarator is now being converted into a Tokamak machine.

## ION-CYCLOTRON RESONANCE HEATING

### Theoretical Considerations

The problems of confinement and stability have received a great deal of attention, and progress is evident. Here at Lewis Research Center, we have devoted a greater fraction of our experimental effort to problems of plasma heating, particularly in the steady state. One such study involves the use of ion-cyclotron resonance heating. This is a process whereby energy is transferred to a plasma in the form of electromagnetic waves. Then, once in the plasma, the wave energy is converted to ion energy.

A plasma column such as shown in figure III-8 will support the propagation of electromagnetic waves. If a current carrying coil is wrapped around the plasma column and excited by a generator of frequency $\omega$, energy can be transferred to a set of waves called natural modes that satisfy the boundary conditions of the plasma and can thus propagate along the column. The wavelengths of these modes are functions of the plasma parameters and the boundary conditions. For waves with a frequency approximately equal to the ion-cyclotron frequency, the wavelengths are strongly dependent on the magnetic field confining the plasma.

The concept of cyclotron heating requires that energy from a specially constructed radiofrequency coil be coupled into these waves in the plasma at frequencies slightly below the ion-cyclotron frequency. Because the current directions in adja-

cent coil sections are opposite, this specially designed coil (called a Stix coil after its inventor) produces fields which vary sinusoidally in the axial direction. The coil can thus be said to have a wavelength $\lambda_0$ associated with it which equals the distance between corresponding points on the first and third sections. With a coil like this, it is then possible to couple significant amounts of energy to a natural mode of the plasma when the wavelength of the coil is the same as that of the natural mode. Thus, in a wavelength sense, there exists a resonance coupling. The wavelength of a natural mode is usually made to match that of the coil by varying the magnetic field.

Recently, many calculations of the power that could be transferred to these plasma waves by a Stix coil have been made. A parametric study has included the effects of magnetic field, density, density gradients, temperature, and collisions as well as geometric effects such as plasma column radius and radiofrequency coil dimensions. The results of some of our calculations are shown in figure III-9 as curves of power transferred to the plasma against magnetic field with ion temperature as a parameter. For fields such that the wave frequency equals the ion-cyclotron frequency, the efficiency of coupling is low. But, as the magnetic field is increased, the wavelengths of the most fundamental natural modes become closer to that of the Stix coil. Finally the wavelength resonance is achieved, and there is a maximum in the coupling. Under proper conditions the efficiency of coupling can be 80 percent.

One of the more interesting parameters studied with regard to power transfer is that of ion temperature. We found that, as the ion temperature increases, the maximum power transfer to the plasma decreases. This is also shown in figure III-9. In this figure the Stix coil wavelength was 41 centimeters and the electron density $2\times10^{18}$ particles per cubic meter. The reduction in coupling with increased temperature is more severe for shorter Stix coil wavelength and/or lower electron density. Efficient coupling of energy to waves must be done in a part of the plasma where the ion temperature is not too high.

Once energy is coupled to the waves, they propagate along the plasma column out each end of the Stix coil. At this point the wave characteristics are studied to make sure the Stix coil has generated the wave with the characteristics desired for the next phase of the heating scheme, that of damping of the wave and conversion of the wave energy into ion energy. The waves will be damped by a process called ion-cyclotron damping if the wave propagates (as shown in fig. III-10) into a region where the confining field as a function of axial position has been lowered to the point where the ion-cyclotron frequency equals the wave frequency. In the region where the field has started to decrease, the wavelength will start to shorten, and the wave amplitude will increase in a manner similar to that of a water wave approaching a

beach. This region is therefore referred to as a "magnetic beach."

When the ion-cyclotron frequency becomes sufficiently close to the wave frequency, there will be many particles that feel the fields of the wave at exactly the cyclotron frequency and are thus heated. What is accomplished here is a heating of ions by a radiofrequency field whose effective (or Doppler shifted) frequency is the ion-cyclotron frequency.

This may appear to many as a rather cumbersome way to heat a plasma. First a plasma wave is generated; then the wave is used to heat ions. One would naturally prefer a more direct approach. Why not just wrap a simple solenoid around a plasma column and heat ions inside the coil by driving it at the ion gyrofrequency? This approach has been tried, but it was discovered that a space charge builds up in the plasma producing electric fields in opposition to those applied (i.e., there was a shielding of the plasma from the applied external field). Energy is transferred much more efficiently to the plasma in the wave generating scheme.

## Experimental Work

Figure III-11 is a schematic of the steady-state ion-cyclotron resonance apparatus now being used at Lewis. There is a plasma column immersed in a magnetic field (maximum value, 1 tesla). The Stix coil (wavelength, 41 cm) is located in the center, and is supplied by a radiofrequency generator of 6.5 megahertz. The magnetic beach where the waves are damped is placed just inside the mirror. The region between the coil and the beach is where various probes are placed to measure the properties of the wave being propagated.

Figure III-12 shows a plot of measured power transfer to the plasma from the Stix coil against the applied direct-current magnetic field. There is a maximum in the coupling at a point very close to that predicted by the theory. Although it is difficult to know precisely all the plasma parameter values necessary to calculate the magnitude of the coupling, a "best guess" set of values may be used to predict the magnitude to within 20 percent.

We now look at some data taken in the region of propagation immediately outside the Stix coil. The ion-cyclotron wave has a time varying component of magnetic field in the axial direction, and the amplitude and phase of this field can be measured by a probe. The output of this probe is viewed as a sinusoidal signal on an oscilloscope where the amplitude is proportional to the strength of the wave and the phase is determined relative to the radiofrequency voltage on the Stix coil. Figure III-13 is a plot of the measured phase of the wave against the axial position of the probe for two different values of magnetic field. The distance over which a

phase change of $2\pi$ occurs equals the wavelength of the wave. Theory tells us that the closer the wave frequency is to the ion-cyclotron frequency, the shorter the wavelength (i.e., the steeper the slope of the curve). This is exactly what you see presented here with the wave frequency being closer to the cyclotron frequency for the curve on the left.

Now, let us move on to look at some data taken in the vicinity of the magnetic beach. Theoretically the amplitude of the axial magnetic field of the wave should increase as the magnetic field decreases, thus making the ion-cyclotron frequency approach the wave frequency. However, when the cyclotron frequency gets sufficiently close to the wave frequency, ion-cyclotron damping becomes strong, the wave amplitude decreases rapidly, and ions are heated. Figure III-14 shows measured wave amplitude plotted as a function of axial position. The wave is propagating to the right, and the magnetic field is decreasing to the right. The point labeled magnetic beach region is where the wave and cyclotron frequencies are equal. The amplitude initially increases and subsequently damps. The actual rate of damping and the point at which damping begins depends on the axial temperature of the plasma.

The ion motion perpendicular to the magnetic field produces a reduction in the direct-current magnetic field (i.e., a diamagnetism). By measuring this reduction in direct-current field, it is then possible to determine the temperature to show that we are truly heating the plasma with the ion-cyclotron wave. To measure the change, a diamagnetic loop is used. The change in magnetic flux is measured through this loop as the plasma is extinguished. Figure III-15 gives temperature (derived from diamagnetic loop measurements) as a function of axial position, and it clearly shows that in the vicinity of the magnetic beach the temperature is much higher than elsewhere, reaching a value greater than 500 electron volts at the center of the beach. The electron density of the plasma was about $2\times10^{18}$ particles per cubic meter. In pulsed experiments at the Princeton Plasma Physics Laboratory ion-cyclotron heating has been used to heat plasmas in magnetic beaches to several kilovolts.

To summarize, it appears that ion-cyclotron damping is an efficient and effective way to heat plasma ions in plasmas contained in the simple magnetic configurations discussed. The question does remain, however, as to whether cyclotron heating will be effective in more complex confining fields devised for the purpose of making the plasma more stable. And whether this process proves usable on the ultimate fusion machines, either alone or in conjunction with other heating methods, it has already proven its value in producing hot, dense plasmas for fusion research. In our future plans, a major objective is to apply ion-cyclotron res-

onance heating (ICRH) to open-ended magnetic wells. The purpose of these tests is to experimentally study the generation, propagation, and damping of waves in the more complex magnetic fields of these wells.

Initial work on the well will be conducted on the present apparatus as shown on figure III-16. This experiment involves the conversion of one of our beaches into a shallow magnetic well by wrapping quadrupole windings around the test section. A later experimental study is planned for a superconducting magnetic mirror apparatus now under construction which will have the capability of producing magnetic fields up to 8 teslas.

One possible scheme for applying IRCH to an open-ended magnetic well is shown on figure III-17. Ion-cyclotron waves would be generated at the two ends of the system (in the mirrors) and propagate towards the center where they give up their energy to ions in the magnetic wells. This may have the added benefit of testing a scheme to reduce end losses in open-ended systems. Experiments at Princeton Plasma Physics Laboratory indicate that ions are accelerated away from the Stix coil. It may be possible to use this acceleration effect to keep particles from escaping out the ends of the magnetic well. As mentioned earlier, some method to reduce end losses is crucial to the feasibility of open-ended reactors.

## MODIFIED PENNING DISCHARGE

A second type of plasma heating process being studied here involves the use of high-voltage direct-current power in what is called a "modified Penning discharge." These two heating studies represent an interesting contrast in approaches. In the ion-cyclotron heating work, you may recall, we started with a theoretical concept and attempted to verify it experimentally and to refine and improve it. In the high-voltage direct-current heating study, we started with an experimentally observed phenomenon and attempted to construct a theoretical model and to improve the process experimentally.

### Initial Observations of Ion Heating

A magnetic mirror machine is created by two superconducting coils located in a 1-meter-diameter vacuum tank. (Figs. III-18 and III-19 are schematics of the experiment configuration.) It is possible to produce a maximum magnetic field up to 2.0 teslas at the coils. The anode ring has a high positive dc potential of up to several tens of kilovolts. Neutral molecules within the containment volume are ionized by trapped electrons. The ions produced are heated by fluctuating electric fields

and are eventually lost out of the mirrors. A photograph of the plasma is shown in figure III-20. The shape of the plasma conforms to that of the magnetic field. The vertical element in the middle is the anode ring, which is maintained at a high positive potential.

The energy of the ions escaping through one of the magnetic mirrors was measured with a retarding potential-energy analyzer. The curve of figure III-21 represents the flux of ions whose axial energy exceeds the value shown on the abscissa. Also shown is the best-fitting integrated Maxwellian distribution curve. This curve has several interesting features not anticipated at the outset of the experiment. The first is that the velocity distribution is Maxwellian along a radius in velocity space, even in the high-energy tail. It was surprising to find that the particles were thermalized in the relatively short time (typically 25 $\mu$sec) and that they were confined between the mirrors. The second interesting feature was the very high ion kinetic temperatures observed (710 eV, in the case shown). These high ion temperatures were accompanied by low electron temperatures (no more than about 200 eV). These features are very desirable in fusion applications, since one normally prefers to dump the power supply energy into the ions rather than the electrons. The Maxwellianization of the ion velocity distribution is desirable, since the plasma will contain one less reservoir of free energy to drive macroscopic and microscopic instabilities.

These high ion temperatures were investigated further, with the results shown in figure III-22. The ion kinetic temperature is shown plotted as a function of direct-current anode voltage for four background pressures of deuterium gas. The kinetic temperature is approximately linearly proportional to the anode voltage up to the limit of the power supply used. This suggests that ions of any desired energy can be produced by going to a sufficiently high anode voltage. The only other steady-state heating system to produce such high ion temperatures is the Burnout-V device at Oak Ridge National Laboratory. There the ions are accompanied by very hot electrons, up to several hundred keV in energy, so a different heating process is probably operating in that case.

## Continuity-Equation Oscillation

The interesting results from this modified Penning discharge demanded an understanding of the physical phenomena responsible for them. A floating Langmuir probe was inserted into the plasma to study the spectrum of the electrostatic potential fluctuations. The output of this probe was connected to a spectrum analyzer, with the results shown in figure III-23. The peak at zero frequency is an internally generated marker. This spectrum reveals a fundamental at about 6800 hertz, sev-

eral harmonics, and a continuous spectrum that can be followed out to 2 megahertz.

It is tempting to make the analogy with conventional hydrodynamics and explain the high ion kinetic temperatures as a consequence of energy being dumped from the power supply into the plasma at the fundamental frequency, followed by a cascading up in frequency and down in scale size until it is dissipated in thermal energy of the ions.

The characteristics of this turbulence spectrum were studied to see whether this might explain the high ion energies. The identification of the fundamental frequency immediately presented a problem. Its low frequency (6800 Hz in the example shown) in a mirror field whose maximum value was typically 1 tesla was much too low to be associated with the plasma frequency or the ion or electron gyrofrequencies. It was also too low by orders of magnitude to be plausibly connected with $E \times B$ or grad-B drifts. Parametric variation of the plasma properties showed that the frequency of this oscillation depended on both the electron and neutral number densities, but not on the magnetic field.

The retarding potential energy analyzer was used to measure the efflux of ions as a function of time. Results are shown in figure III-24. The zero level is the baseline between pulses. The charged-particle efflux displays pulsar-like sharp, narrow peaks between broad, flat minima. For different plasma conditions, these pulses display fine structure, periodic interpulses and other interesting detailed features. The particle efflux, the light output, and the electrostatic fluctuations were in phase at the same frequency. The light output was monitored at two axial and azimuthal stations with a pair of photomultipliers, and showed that the plasma was oscillating in unison with a single phase and frequency.

These characteristics suggested that the oscillation in question is a new phenomenon, and this subsequently proved to be the case. This oscillation was labeled the continuity-equation oscillation, because it arises as a consequence of periodic solutions to the coupled pair of continuity equations for neutrals and charged particles in a slightly ionized gas. The frequency is porportional to the square root of the product of electron and neutral number densities, and is independent of magnetic field. An exact solution to this pair of equations is shown in figure III-25. The ordinate is relative electron number density; the abscissa is time. There are four values of the relative peak-to-peak amplitude $\eta$. At high peak-to-peak amplitudes, the solutions have the characteristic waveform we saw in the particle efflux - sharp, narrow peaks between broad, flat minima.

The oscillation frequency was systematically studied as a function of the electron and neutral number densities. Figure III-26 shows the results. The observed frequency is plotted as a function of the product of relative electron and neutral

number density. The square root dependence predicted theoretically holds over a range of 5 orders of magnitude in the density product.

The oscillation arises from an effect usually ignored in elementary kinetic theory arguments: The transit time delays that result when particles move along their mean free path to the point of interest. The effect is most apparent in apparatus like this one, in which the mean free paths are relatively long. These time delays introduce a lag between the particle production and loss processes in the plasma, and this, in turn, causes a relaxation oscillation in the neutral and charged-particle number densities.

That's the interpretation of the physical phenomena as they occur in this experiment. It seems possible, though, to describe the class of oscillations in more general terms. Whenever the production rate of each species depends on factors including the instantaneous populations of both species, one may look for oscillatory solutions. These oscillations can occur in other contexts. Similar pairs of equations have been used to describe ecological systems in which there occur periodically fluctuating populations of predator and prey. They have also been used to describe certain oscillatory chemical reactions.

In this modified Penning discharge, the characteristics of the oscillation depend solely on the parameters appearing in the two continuity equations. The equations representing conservation of momentum and energy must be satisfied, of course, but they play no role in the oscillation beyond determining the coefficients of the terms in the continuity equations.

## Observations of Quasi-Linear Mode Coupling

With an explanation of the fundamental oscillation frequency, attention was then turned to understanding other aspects of the ion heating process. The ion heating process was studied with the apparatus shown in figure III-27. A powerful alternating-current amplifier was connected to the anode ring in parallel with the high-voltage, direct-current supply normally used. The effect of a sinusoidal excitation imposed on the anode ring on the spectrum of electrostatic potential fluctuations was measured with the capacitive probe shown. The resulting spectra for two background pressures are shown in figures III-28 and III-29. The frequency range is from zero to 100 kilohertz. The externally excited frequency is on the left, followed by several of its harmonics. At higher frequencies, one can see the continuity-equation frequency, its harmonics, and sideband modulations at the imposed frequency. It seems a clear illustration of quasi-linear mode coupling in the plasma, and is particularly interesting in view of the very low frequencies involved

and the presence in the background of a continuous, fully developed, nonlinear turbulent spectrum.

The following table summarizes the best temperatures, densities, and confinement times simultaneously observed in this experiment thus far:

| | |
|---|---|
| Ion kinetic temperature, $T_i$, keV | 5 |
| Electron kinetic temperature, $T_e$, eV | 200 |
| Plasma number density, $n_e$, particle/$m^3$ | $2\times10^{16}$ |
| Ion confinement time, $\mu$sec | 27 |

The ion temperatures listed are gratifying, but the densities and confinement times are quite low. These are now limited by the rapid loss of ions out the mirrors. Confinement time and density can be improved with a closed configuration such as shown in figure III-30 - a bumpy torus. This consists of 12 magnetic mirrors end-to-end in a toroidal array. Such a superconducting magnet facility is presently under consideration for future use in this experiment. The modified Penning discharge scheme will be applied to this configuration. It is one of the few steady-state plasma injection and heating schemes capable of being applied to a toroidal geometry. A reasonable goal for the bumpy torus would be an increase of a factor of 10 in confinement time and number density.

## STUDIES RELATED TO CONFINEMENT

### Random-Walk Approximation

Two studies related to confinement are underway at Lewis. One of these, an analytical approach, uses a computer to simulate the plasma behavior. Gerald Englert has been developing a technique which may permit the approximate solution of plasma problems over a wide range of conditions. He calls this technique "random-walk approximation." To date he has applied it to the problem of particle diffusion in velocity space in a magnetic-mirror configuration. The basic idea is this: Let the particle's velocity be represented by a magnitude $V$ and an angle to the magnetic field $\theta$. The changes in velocity resulting from collisions with other particles can be represented as probabilities. There is a certain probability that the velocity will change by an increment in $V$ and in $\theta$.

Given expressions for these probabilities, the computer can "walk" the particles over a two-dimensional grid in velocity space. By using iterations, and reasonably large steps, an equilibrium distribution of particles can be found without undue computer time. The probabilities that bias the random walk are obtained by

comparing the random-walk with the Fokker-Planck equation, and assuming the coefficients of like terms to be the same. The procedure is not the same as the Monte Carlo method. Monte Carlo would select a step of variable length and direction, based on the physics of binary encounters. The random-walk method takes large steps, in effect averaging over a large number of binary encounters, thereby reducing computer time.

Figure III-31 shows the equilibrium solution for one test case. The distribution in velocity magnitude is plotted; that is, the relative number of particles possessing any particular value of V. The case chosen was one for which an analytical approximation was available (shown by the curve). Note that the random-walk values exhibit approximately the same shape as the analytical result, and that the two values of mirror ratio show little effect.

Another question of great interest is the rate at which particles escape from the system. (They migrate into the loss cone.) Figure III-32 shows the random-walk loss rate plotted against the reciprocal of the logarithm of the mirror ratio. A good, linear fit is evident. This agrees with the functional relation predicted by some of the analytical approximations for this case.

In principle, the random-walk method could be used for more complex cases. Englert has started looking at cases involving physical space gradients. The big question to be answered is where do we get the values of the random-walk biases for more complex cases? Possibly, experiment might provide them.

## Plasma Turbulence

The phenomenon of anomalous diffusion has often been associated with fluctuations in the plasma, although the nature of the connection in many real plasmas has yet to be rigorously established. As yet, the nature of the fluctuations to be expected in any given plasma cannot be predicted. First, we need a better understanding of the fluctuations as they actually occur. What is the spectrum? What is the source of energy? How are the various frequencies related? Is the fluctuation a purely random process or does it possess a coherence in space or time? For that matter, which plasma parameters are doing the fluctuating: density, temperature, or potential?

John Serafini, studying this problem has given us some answers. In figure III-33 his experimental device is shown. This is a crossed field device: the electric field is axial, the magnetic field radial. Into the annular plasma volume probes of various sorts may be inserted to detect the locally fluctuating quantities.

Using Langmuir probes, he obtains turbulence spectra such as are shown in figure III-34. Notice that for the three operating conditions, generally similar spectra occur. A peak appears at a relatively low frequency followed by a rather smooth decline at higher frequencies. For these measurements, the fluctuating quantity is the plasma density - a conclusion based on the behavior of the probe as the bias was varied. A detailed study of the spatial correlation of the various parts of the spectrum shows that the peak represents a coherent plasma oscillation - a helical mode. The higher frequencies are noncoherent, with no measurable propagation lag. There is, then, the superposition of two basically different kinds of fluctuations. The relation of these two types of fluctuations may be seen from figure III-34. Notice that the ordinate is a logarithmic scale, so that the actual amplitude varies quite substantially along the three curves. The increasing strength of the coherent oscillation - the peak of the curve - is accomplished by a rising level of signal strength even at the very high frequencies. Such a concurrent variation suggests that the energy in the high-frequency part of the spectrum derives from the coherent oscillation. Many means may be proposed to account for the coupling or energy transfer within the spectrum. The important implication is that the existance of a single mode of plasma oscillation may induce quasi-random or turbulent fluctuations over a wide frequency range. The data do not provide conclusive proof of this relation. However, the concept of energy being supplied via a coherent plasma oscillation, and thence to the turbulent spectrum at higher frequencies is intuitively appealing and consistent with the available data.

It is particularly important to determine experimentally the connection between turbulence or fluctuations of various kinds and the actual diffusion of the plasma particles across the magnetic field. A new device with parallel magnetic and electric fields is being constructed to permit such measurements.

In summary, we have discussed some of the basics of the fusion research field and dwelt on the two steady-state heating processes being studied here at Lewis. In addition, we have touched briefly on work related to plasma confinement and losses from confinement. The purpose of this discussion has not been to present a comprehensive or even a well-balanced picture of our work in these fields. Rather we have tried to convey our viewpoints and objectives, and a summary of the results we have obtained in our studies.

# BIBLIOGRAPHY

This bibliography comprises publications authored by the members of the NASA Lewis Research Center Staff.


Englert, Gerald W.: Towards Thermonuclear Rocket Propulsion. New Scientist, vol. 16, Oct. 4, 1962, pp. 16-18.

Englert, Gerald W.: Study of Thermonuclear Propulsion Using Superconducting Magnets. Third Symposium on Engineering Aspects of Magnetohydrodynamics. Norman W. Mather and George W. Sutton, eds., Gordon and Breach Science Publ., 1964, pp. 645-671.

Englert, Gerald W.: High-Energy Ion Beams Used to Accelerate Hydrogen Propellant Along Magnetic Tube of Flux. NASA TN D-3656, 1966.

Flax, Lawrence: Theoretical Investigation of Ultrasonic Attenuation for Free Electrons in the Presence of a Magnetic Field. NASA TN D-3723, 1966.

Flax, Lawrence; and Simmons, Joseph H.: Magnetic Field Outside Perfect Rectangular Conductors. NASA TN D-3572, 1966.

Flax, L.; and Trivisonno, J.: Oscillatory Magnetoacoustic Attenuation. Phys. Letters, vol. 22, no. 5, Sept. 15, 1966, pp. 569-570.

Hettel, Henry J.; Krawec, Roman; Prok, George M.; and Swett, Clyde C.: Enhancement of Ion Cyclotron Waves in Hydrogen Helium Mixtures. NASA TN D-4271, 1968.

Howes, Walton L.: Effect of Initial Velocity on One-Dimensional, Ambipolar, Space-Charge Currents. NASA TN D-2425, 1964.

Krawec, Roman: An Instrument for Electronic Differentiation of Current-Voltage Characteristics. NASA TN D-2161, 1964.

Krawec, Roman: Steady-State Composition of a Low-Density Nonequilibrium Hydrogen Plasma. NASA TN D-3457, 1966.

Krawec, Roman: Radial Density and Temperature Profiles at the Ion Cyclotron Wave Resonance Point. AIAA J., vol. 4, no. 12, Dec. 1966, pp. 2166-2170.

Krawec, Roman: Electronic Analog for Performing Abel Inversion. Rev. Sci. Instr., vol. 39, no. 3, Mar. 1968, pp. 402-404.

Krawec, Roman: General Operating Characteristics of a Backstreaming Direct-Current Plasma Generator. NASA TN D-4604, 1968.

Krawec, Roman; Prok, George M.; and Swett, Clyde C.: Evaluation of Two Direct-Current Methods of Plasma Production for Use in Magnetic Mirror Experiments. NASA TN D-2862, 1965.

Maslen, S. H.: Fusion for Space Propulsion. IRE Trans. on Mil. Elect., vol. MIL-3, no. 2, Apr. 1959, pp. 52-57.

Monnin, Carl F.; and Prok, George M.: Comparison of Gryzinski's and Born's Approximations for Inelastic Scattering in Atomic Hydrogen. NASA TN D-2903, 1965.

Monnin, Carl F.; and Prok, George M.: Energy Transfer and Ion Cost in a Hydrogen Plasma. NASA TN D-5319, 1969.

Monnin, Carl F.; and Reinmann, John J.: Stability of Two-Fluid Wheel Flows with an Imposed Uniform Axial Magnetic Field. NASA TN D-5372, 1969.

Prok, George M.: Two-Step Process to Increase Atomic Hydrogen Ion Production in Low-Pressure Radiofrequency Discharge. NASA TN D-2912, 1965.

Prok, George M.; and McLean, Clifford A.: Intensity and Intensitv Ratio of Principal Singlet and Triplet Lines of Molecular Hydrogen. NASA TN D-2522, 1964.

Prok, George M.; and Monnin, Carl F.: Energy Required for Proton Production by Electron Impact in Mixtures of Atomic and Molecular Hydrogen. Bull. Am. Phys. Soc., vol. 13, no. 2, Feb. 1968, p. 299.

Prok, George M.; Monnin, Carl F.; and Hettel, Henry J.: Estimation of Electron Impact Excitation Cross Sections of Molecular Hydrogen. NASA TN D-4004, 1967.

Prok, G. M.; Monnin, C. F.; and Hettel, H. J.: Molecular Hydrogen Inelastic Electron Impact Cross sections - A Semiclassical Method. J. Quant. Spectrosc. Radiat. Transfer, vol. 9, no. 3, Mar. 1969, pp. 361-369.

Reynolds, Thaine W.; and Richley, Edward A.: Propellant Condensation on Surfaces near an Electric Rocket Exhaust. Presented at Seventh Electric Propulsion Conference, Williamsburg, Va., March 3-5, 1969.

Roth, J. Reece: Nonadiabatic Particle Losses in Axisymmetric and Multipolar Magnetic Fields. NASA TN D-3164, 1965.

Roth, J. Reece: Modification of Penning Discharge Useful in Plasma Physics Experiments. Rev. Sci. Instr., vol. 37, no. 8, Aug. 1966, pp. 1100-1101.

Roth, J. Reece: Optimization of Adiabatic Magnetic Mirror Fields for Controlled Fusion Research. NASA TM X-1251, 1966.

Roth, J. Reece: New Mechanism for Low-Frequency Oscillations in Partially Ionized Gases. Phys. Fluids, vol. 10, no. 12, Dec. 1967, pp. 2712-2714.

Roth, J. Reece: Plasma Stability and the Bohr - van Leeuwen Theorem. NASA TN D-3880, 1967.

Roth, J. Reece: Possible Applications of the Continuity-Equation Plasma Oscillation to Pulsars and Other Periodic Astrophysical Phenomena. NASA TN D-5078, 1969.

Roth, J. Reece: Periodic Small-Amplitude Solutions to Volterra's Problem of Two Conflicting Populations and Their Application to the Plasma Continuity Equations. J. Math. Phys., vol. 10, no. 8, Aug. 1969, pp. 1412-1414.

Roth, J. Reece: A Theory of Moving Striations Based on the Continuity-Equation Plasma Oscillation. Presented at the 9th International Conference on Phenomena in Ionized Gases, Bucharest, Romania, Sept. 1-6, 1969.

Roth, J. Reece; Freeman, Donald C., Jr.; and Haid, David A.: Superconducting Magnet Facility for Plasma Physics Research. Rev. Sci. Instr., vol. 36, no. 10, Oct. 1965, pp. 1481-1485.

Serafini, John S.: Correlation Measurements of Plasma Fluctuations in a Hall-Current Accelerator. Bull. Am. Phys. Soc., vol. 13, no. 2, Feb. 1968, p. 278.

Serafini, John S.: Utility of Conventional Turbulence Experimental Methods in the Study of Plasma Fluctuations. Bull. Am. Phys. Soc., vol. 13, no. 5, May 1968, p. 824.

Sigman, Donald R.: Radiofrequency Power Transfer to Ion-Cyclotron Waves in a Collision-Free Magnetoplasma. NASA TN D-3361, 1966.

Sigman, Donald R.; Krawec, Roman; Hettel, Henry J.; and Swett, Clyde C.: Further Experiments on Ion-Cyclotron-Wave Generation in the RF Self-Sustained Mode. Bull. Am. Phys. Soc., vol. 13, no. 11, Nov. 1968, p. 1509.

Sigman, Donald R.; and Reinmann, John J.: Ion Cyclotron Wave Generation in Uniform and Nonuniform Plasma Including Electron Inertia Effects. NASA TN D-4058, 1967.

Sigman, Donald R.; and Reinmann, John J.: Power Transfer to Ion Cyclotron Waves in a Two Ion Species Plasma. NASA TM X-1481, 1967.

Sigman, Donald R.; and Reinmann, John J.: Power Coupling and Wave Fields of Ion-Cyclotron Waves in a Finite Length System. Presented at the 10th Annual Meeting of the American Physical Society, Miami Beach, Fla., Nov. 13-16, 1968.

Swett, Clyde C.: Experiments on Inductive and Capacitive Radio-Frequency Heating of a Hydrogen Plasma in a Magnetic Field. NASA TN D-2717, 1965.

Swett, Clyde C.: Effect of Magnetic Beach on RF Power Absorption in Ion Cyclotron Resonance. Bull. Am. Phys. Soc., vol. 11, no. 4, June 1966, p. 450.

Swett, Clyde C.; and Krawec, Roman: Preliminary Observations of RF Power Transfer to a Hydrogen Plasma at Frequencies Near the Ion Cyclotron Frequency. Third Symposium on Engineering Aspects of Magnetohydrodynamics. Norman W. Mather and George W. Sutton, eds., Gordon and Breach Science Publ., 1964, pp. 599-614.

Swett, Clyde C.; and Krawec, Roman: Experiments on Ion-Cyclotron Wave Generation, Using an Electrostatically Shielded RF Coil. Bull. Am. Phys. Soc., vol. 10, no. 4, 1965, p. 509.

Swett, Clyde C.; and Krawec, Roman: Operation of an Ion-Cyclotron-Wave-Generation Apparatus in a RF Self-Sustained Mode. Bull. Am. Phys. Soc., vol. 13, no. 2, Feb. 1968, p. 278.

Woollett, Richard R.: Electromagnetic Wave Propagation in a Cold, Collisionless Atomic Hydrogen Plasma. NASA TN D-2071, 1964.

Woollett, Richard R.: Frequency Ranges for Existence of Waves in a Cold, Collisionless Hydrogen Plasma. NASA TN D-2273, 1964.

Woollett, Richard R.: Energy Addition to an Atomic Hydrogen Plasma at Off-Resonant Conditions. NASA TN D-2982, 1965.

Woollett, Richard R.: Error in Induced Electric Field Modes Under Stix Coil Resulting from Assumption of Orthogonality of Natural Plasma Modes. NASA TN D-3255, 1966.

Woollett, Richard R.: Magnitude of Nonlinearities in Collisionless Magnetoplasma Waves. NASA TN D-3778, 1967.

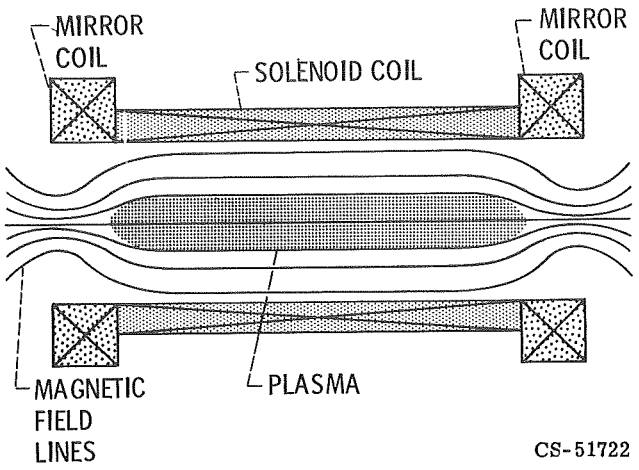


Figure III-1. - Plasma confined in magnetic mirror system.

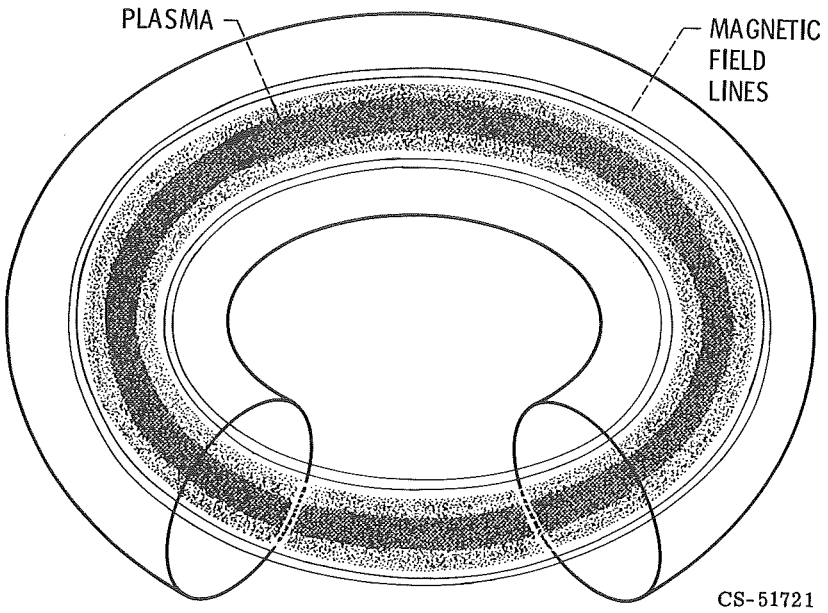


Figure III-2. - Plasma confined in torus.

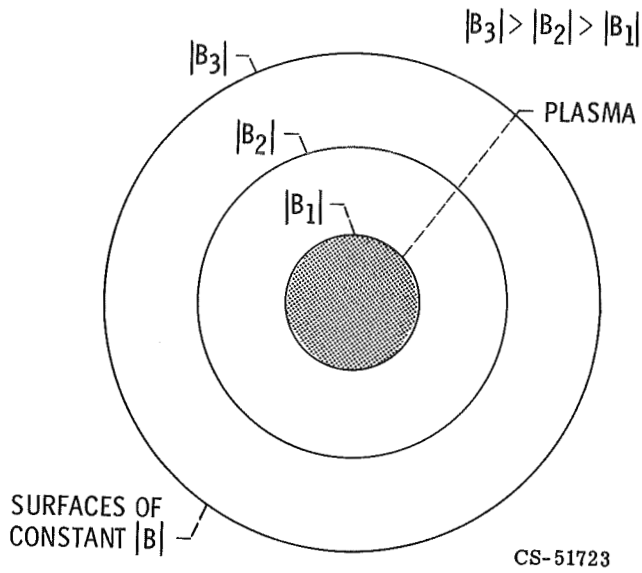


Figure III-3. - Magnetic well.

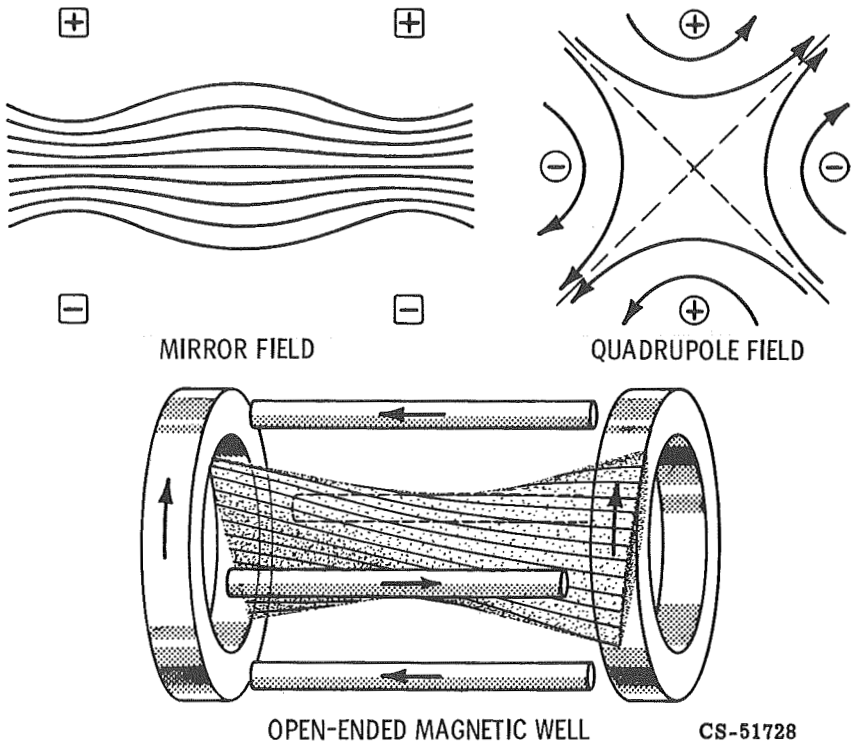


Figure III-4. - Plasma confined in open-ended magnetic well.

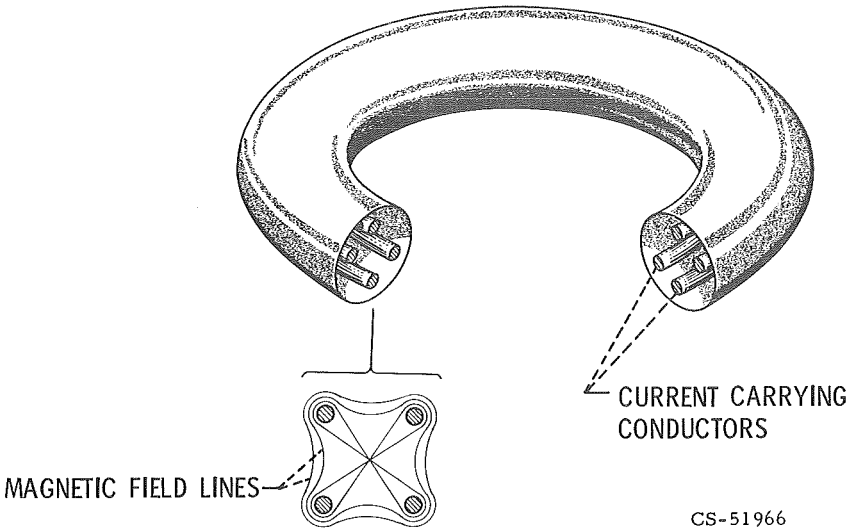


Figure III-5. - Toroidal magnetic-well geometry.

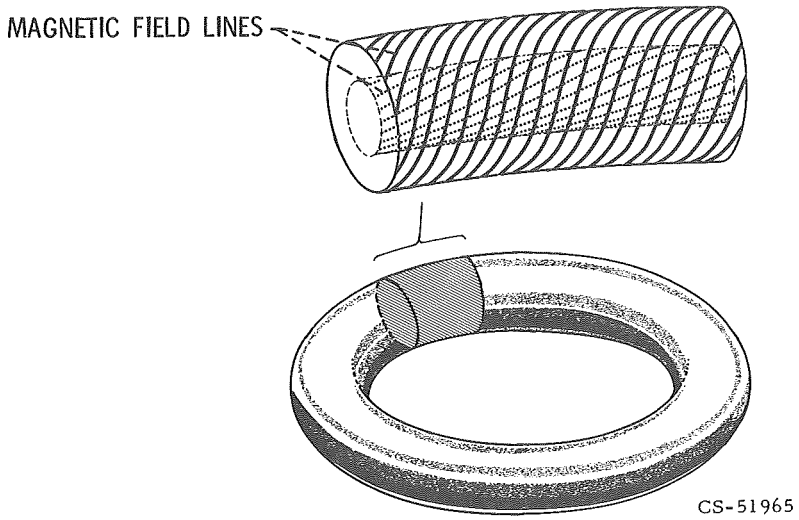


Figure III-6. - Toroidal magnetic field with shear.

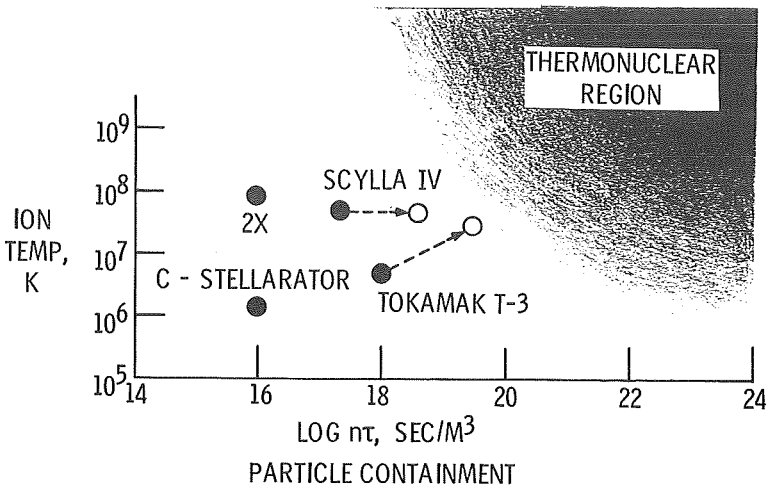


Figure III-7. - Lawson diagram.

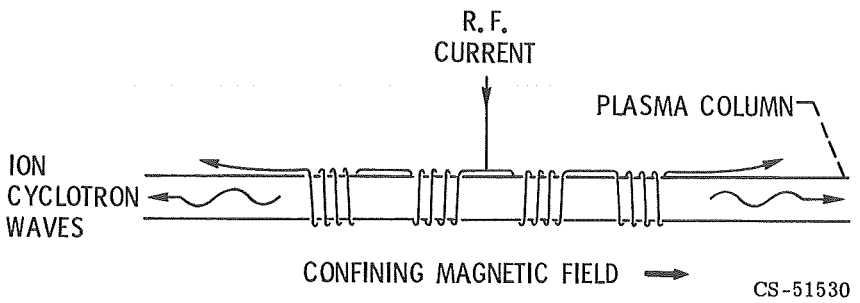


Figure III-8. - Four-section Stix coil for generating ion-cyclotron waves.

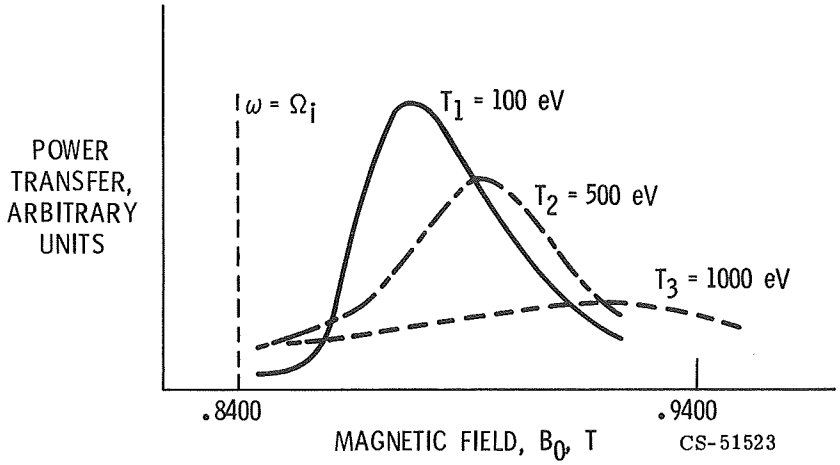


Figure III-9. - Theoretical power transfer as function of magnetic field with ion temperature as parameter.

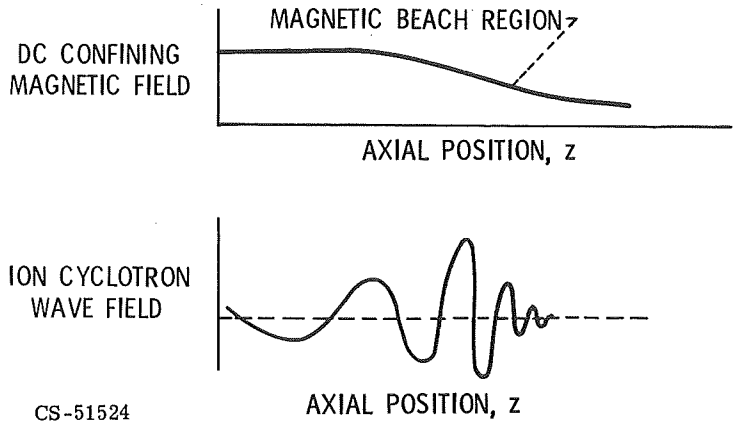


Figure III-10. - Wave damping in magnetic beach.

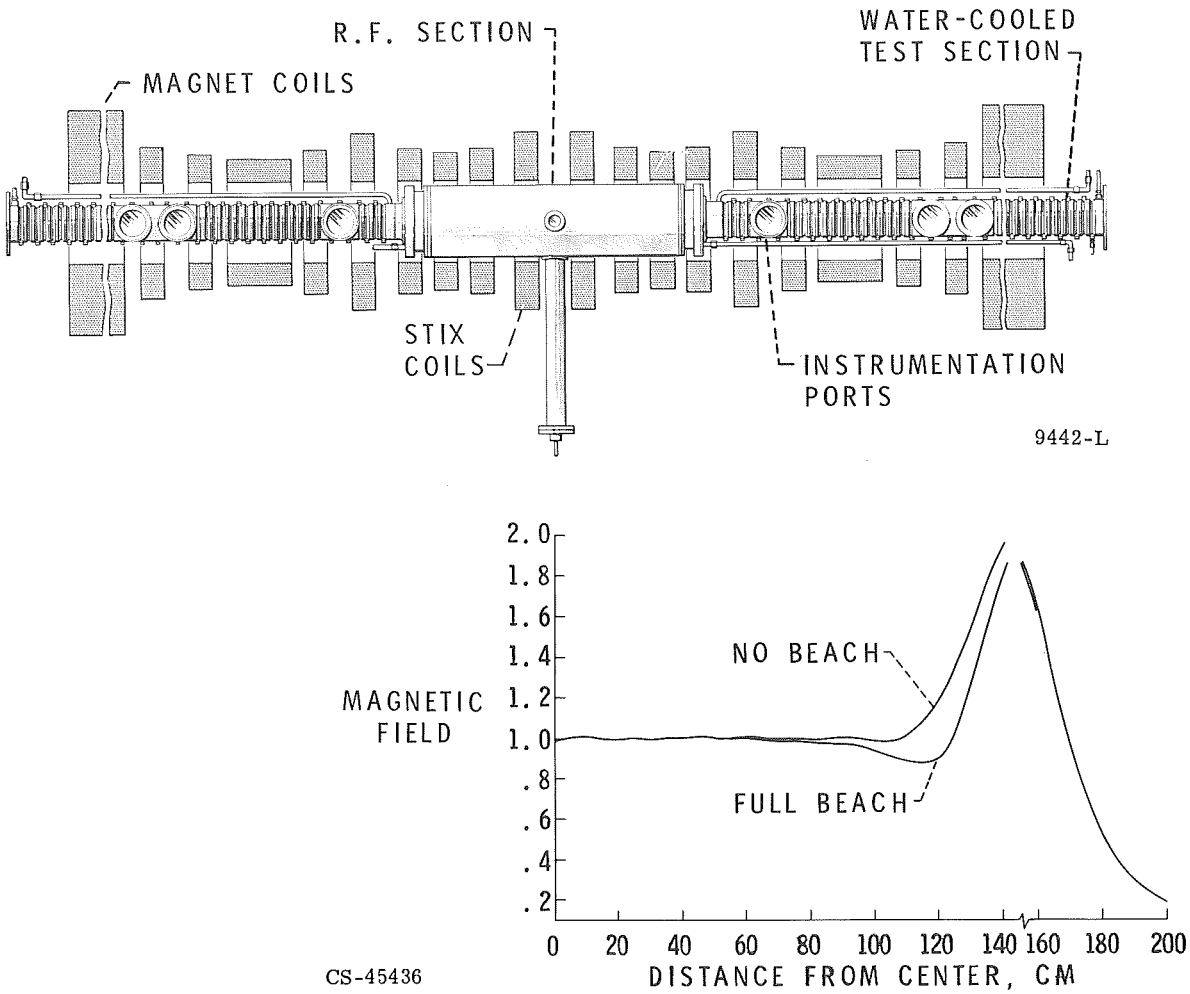


Figure III-11. - Ion cyclotron resonance apparatus.

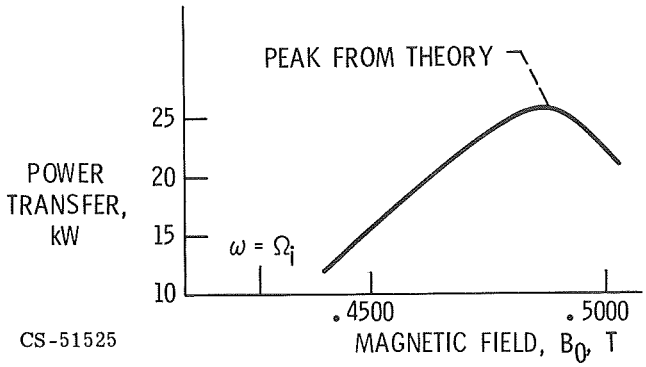


Figure III-12. - Experimental power transfer as function of magnetic field.

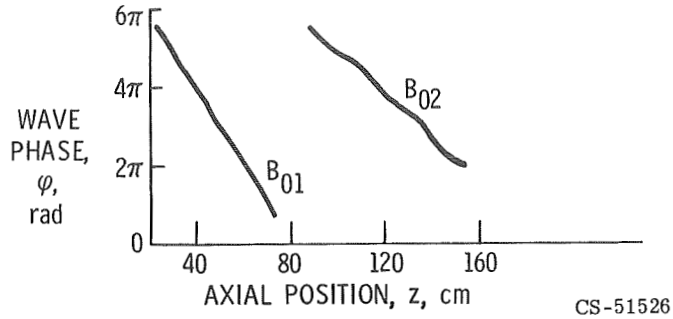


Figure III-13. - Ion-cyclotron wave phase for $B_z$ as function of axial position for two values of magnetic field ($B_{01} < B_{02}$).

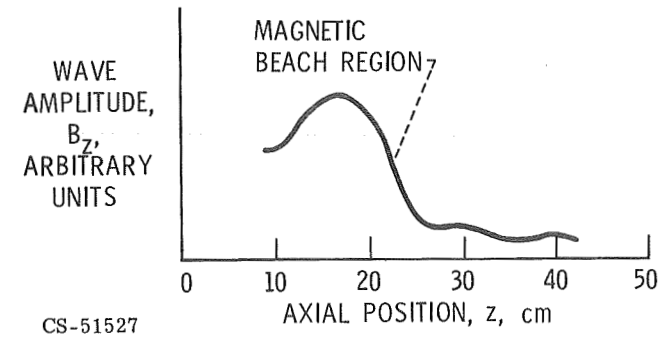


Figure III-14. - Ion-cyclotron wave amplitude $B_z$ as function of axial position.

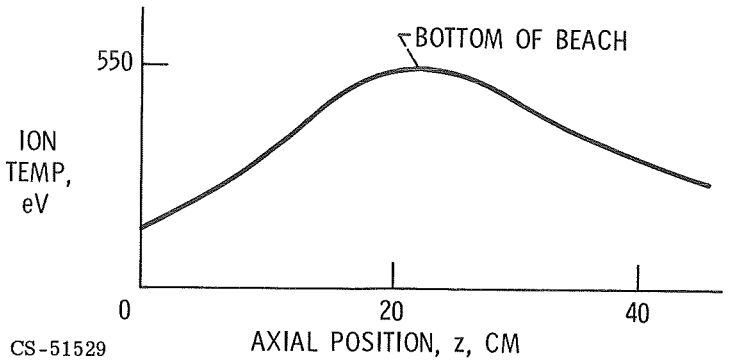


Figure III-15. - Ion temperature from diamagnetic loop in beach region.

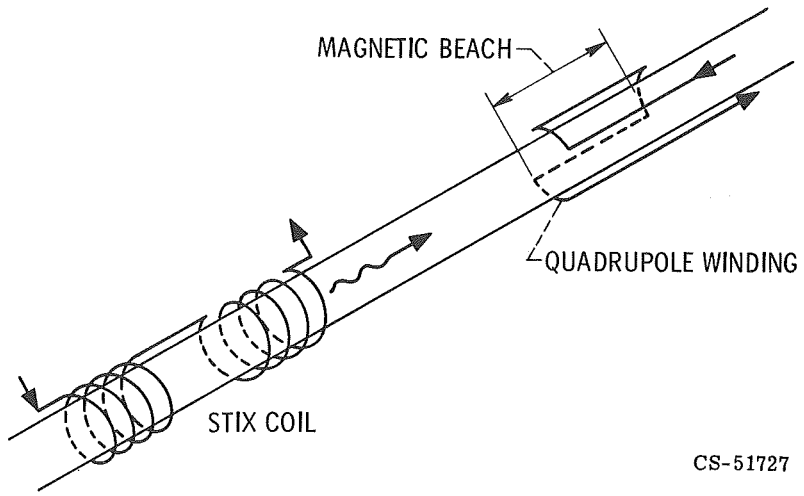


Figure III-16. - Experimental arrangement to study ion-cyclotron wave propagation in magnetic well.

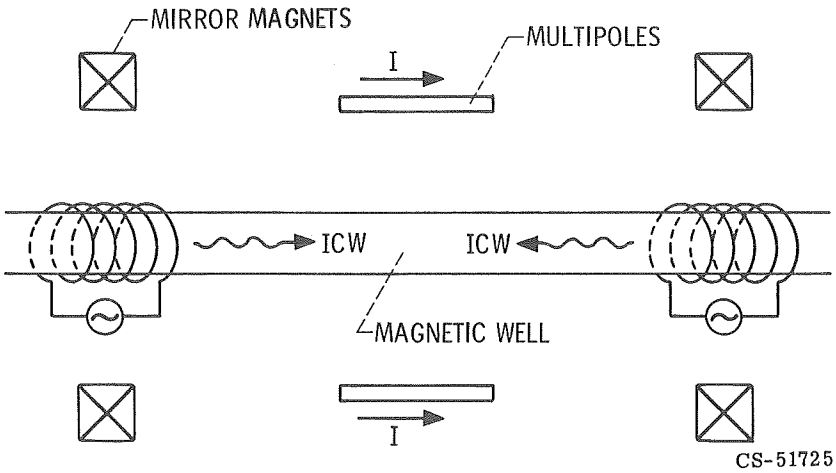


Figure III-17. - Ion cyclotron resonance heating applied to open magnetic wells.

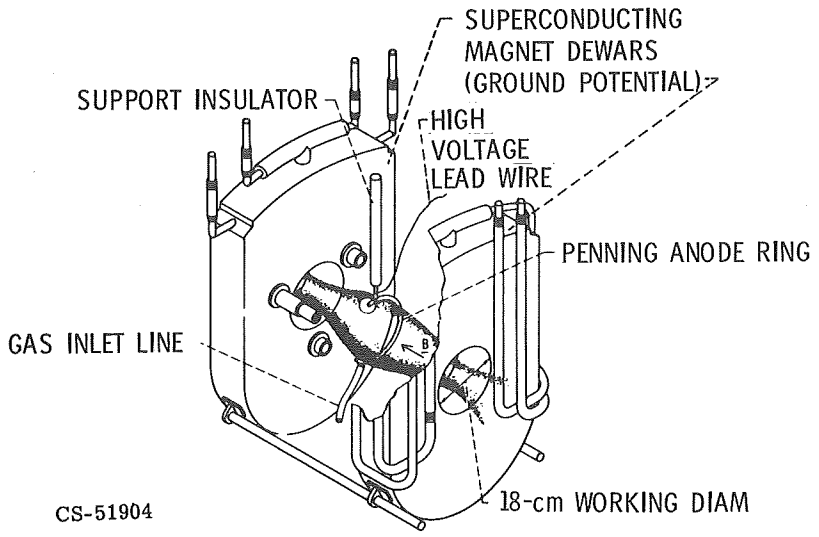


Figure III-18. - Discharge operating configuration and detail of anode ring.

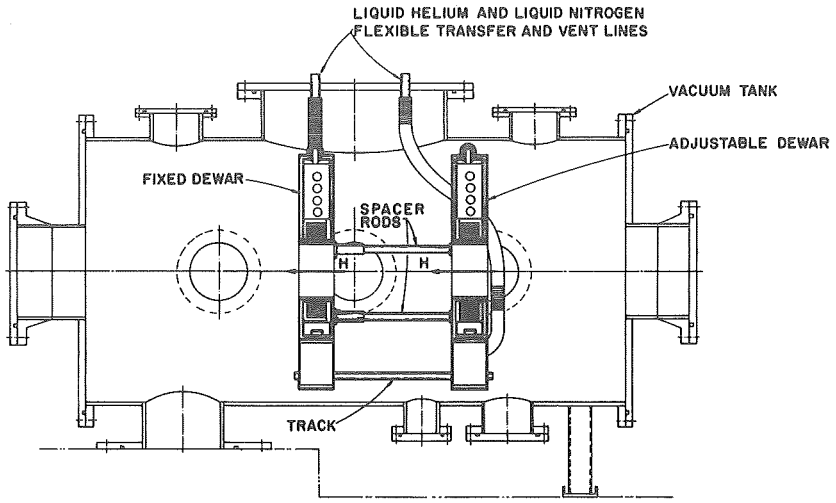


CS-35346

Figure III-19. - Isometric cutaway drawing of vacuum tank.

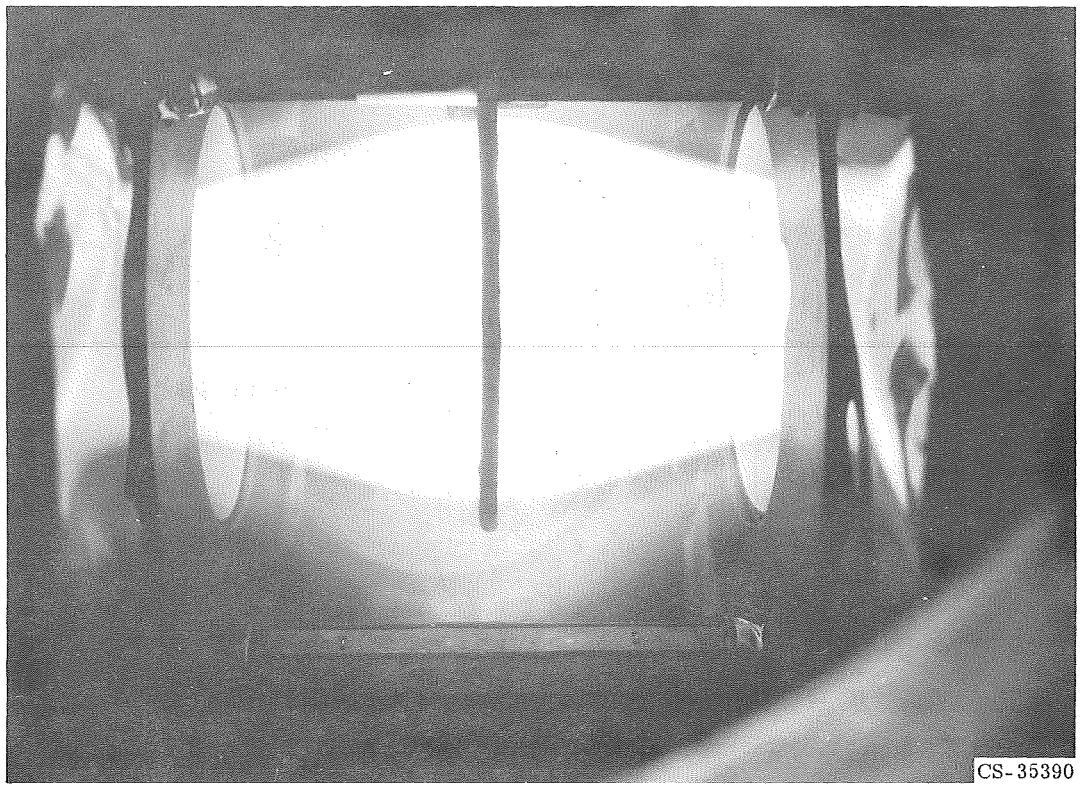

CS-35390

Figure III-20. - Photograph of plasma.

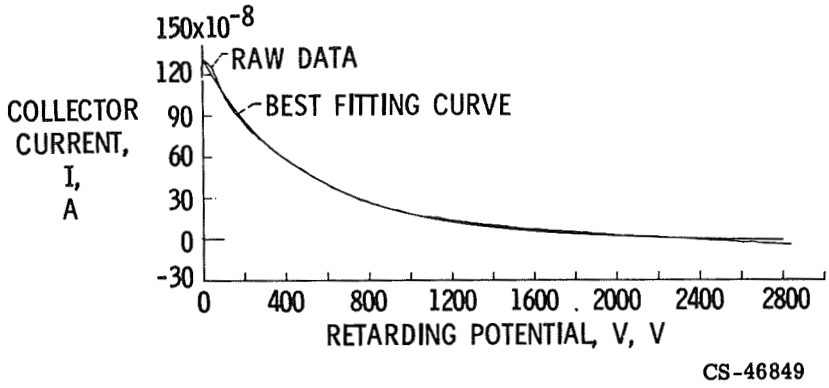


Figure III-21. - Measurement of retarding potential-energy analyzer. Kinetic temperature, 710 electron volts.

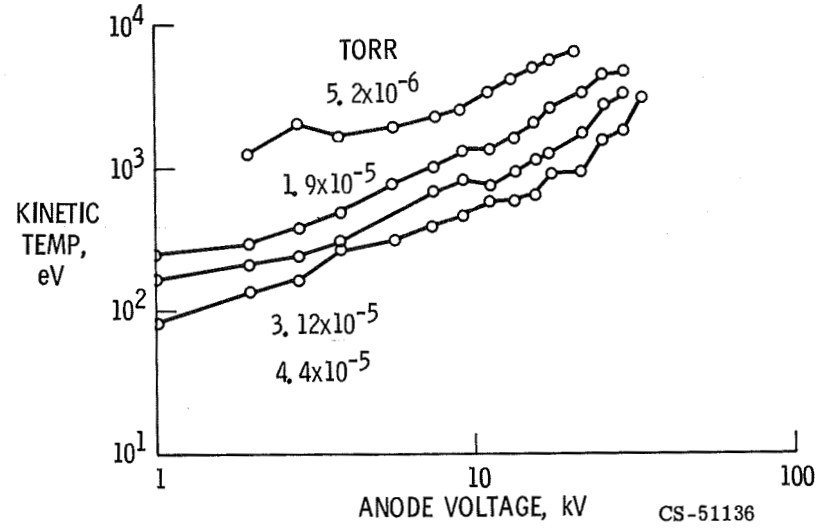


Figure III-22. - Relation of anode voltage to deuterium kinetic temperature for various background gas pressure. $B_{max}$ = 2.0 T.

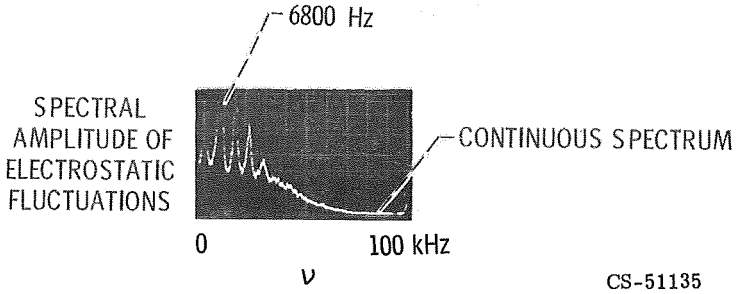


Figure III-23. - Electrostatic potential fluctuations.

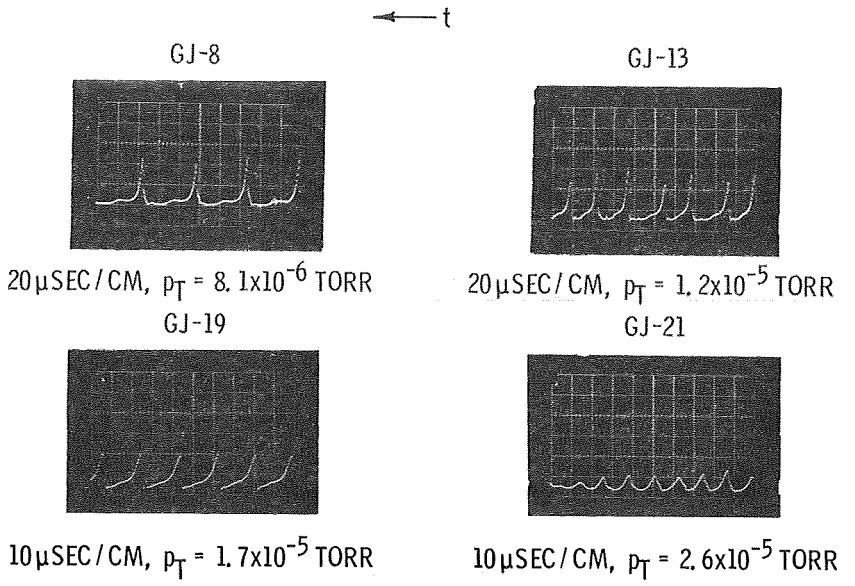


Figure III-24. - Charged particle efflux as function of time.

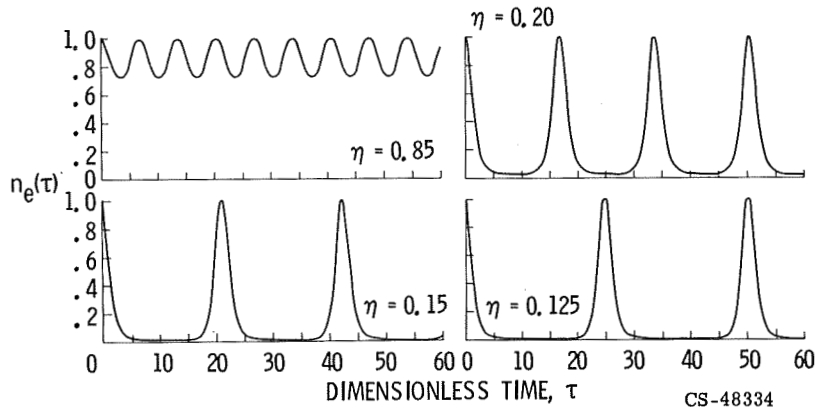


Figure III-25. - Relative number density as function of time.

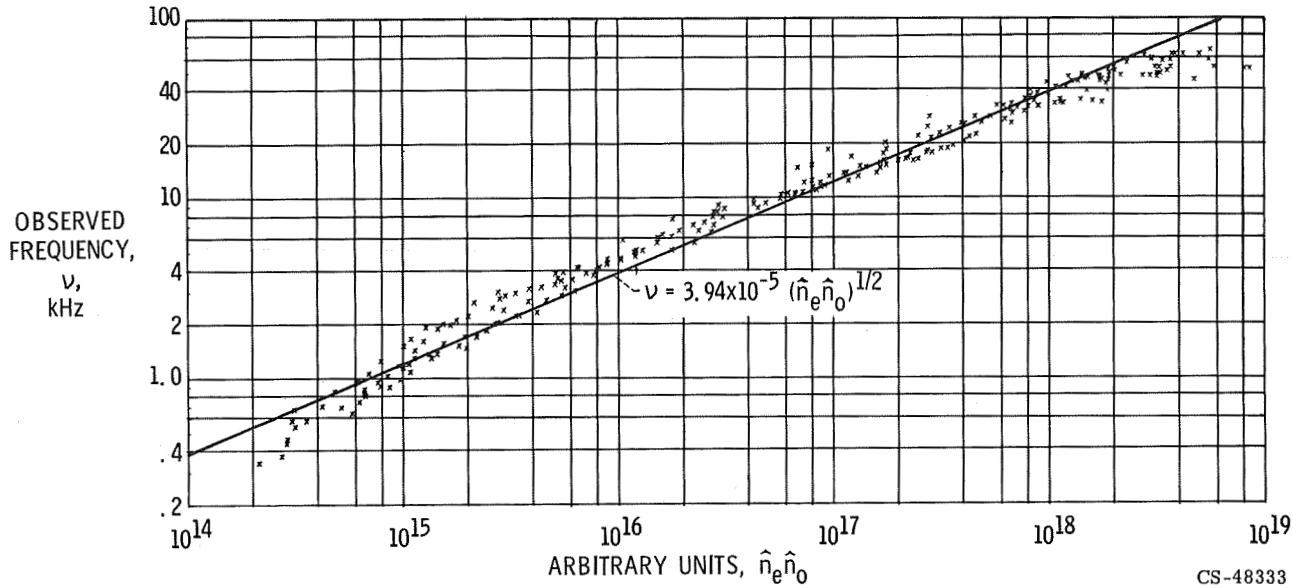


Figure III-26. - Observed frequency as function of product of average electron and neutral number densities.

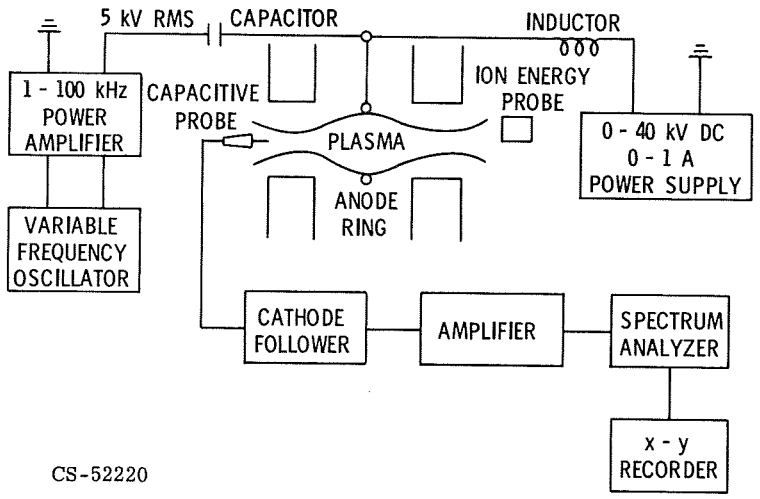


Figure III-27. - Apparatus for investigation of external modulation of anode voltage.

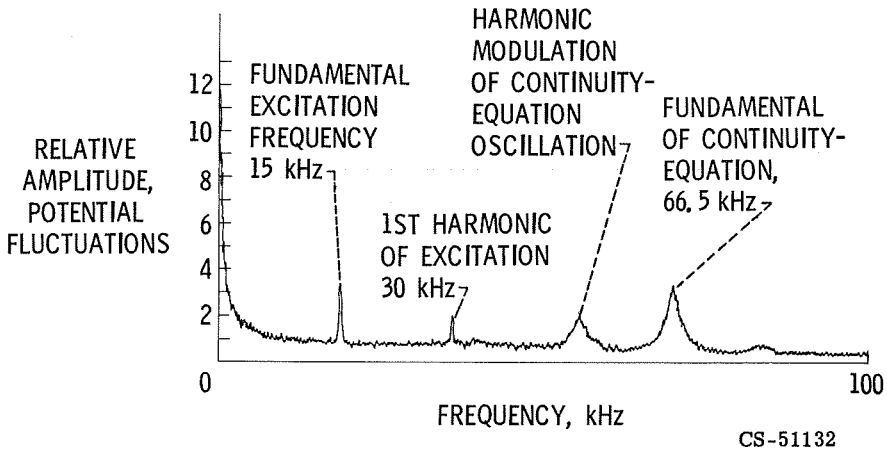


Figure III-28. - Spectrum of potential fluctuations; medium background pressure, $7 \times 10^{-5}$ torr.

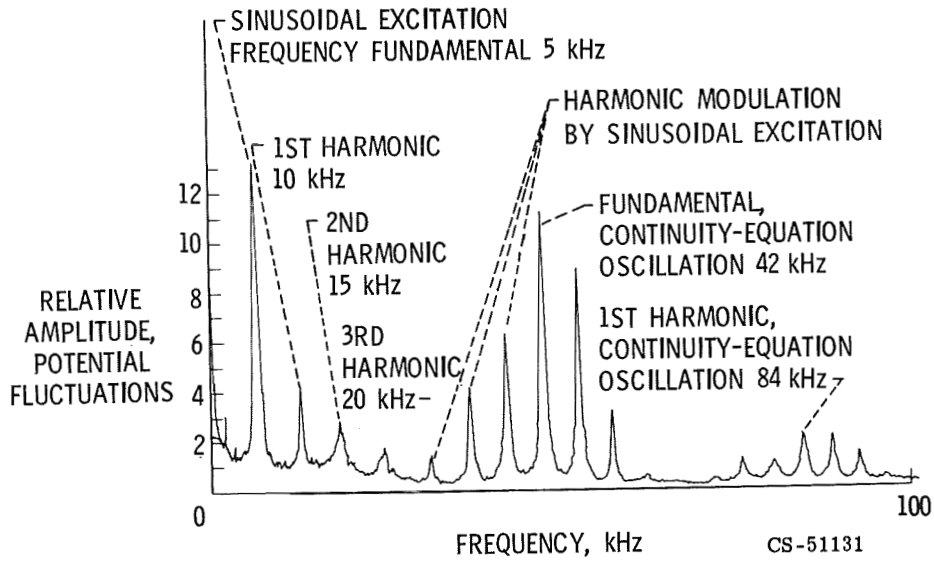


Figure III-29. - Spectrum of potential fluctuations; low background pressure, $\sim 4.5 \times 10^{-5}$ torr.

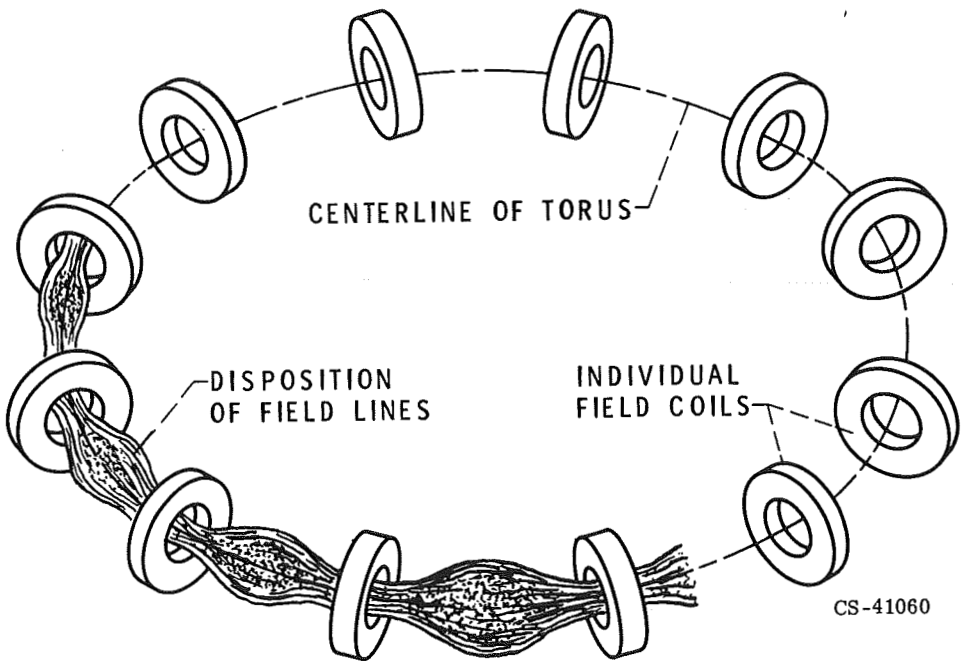


Figure III-30. - Bumpy torus concept.

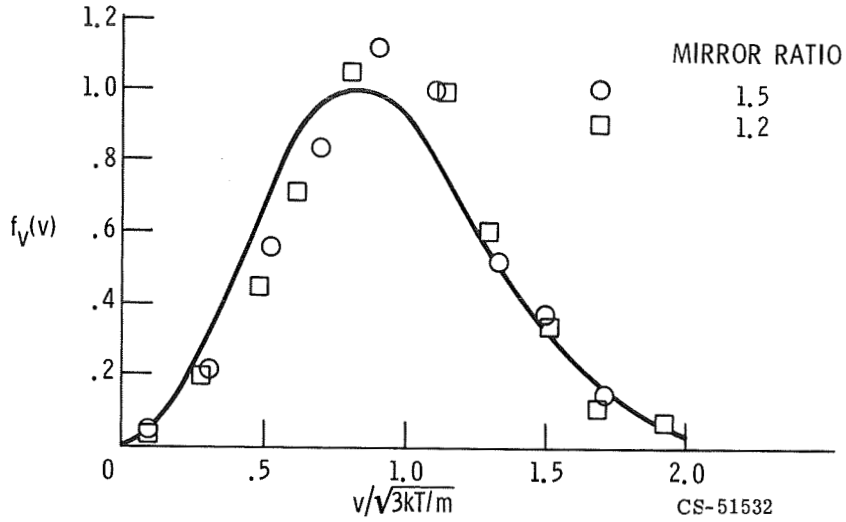


Figure III-31. - Marginal distribution in velocity magnitude.

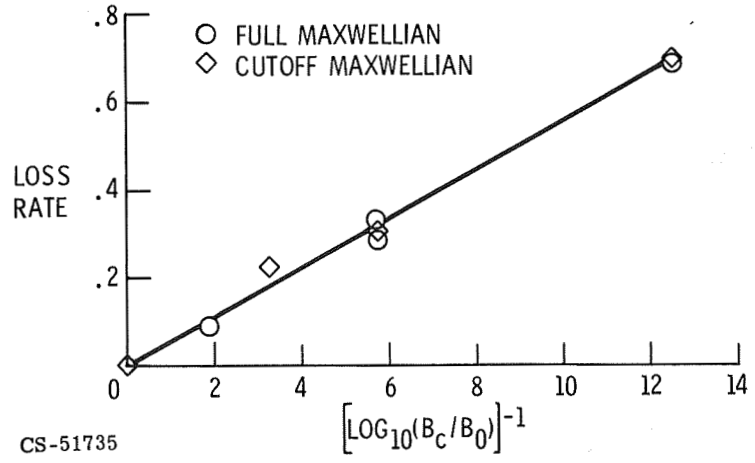


Figure III-32. - Random-walk loss rates.

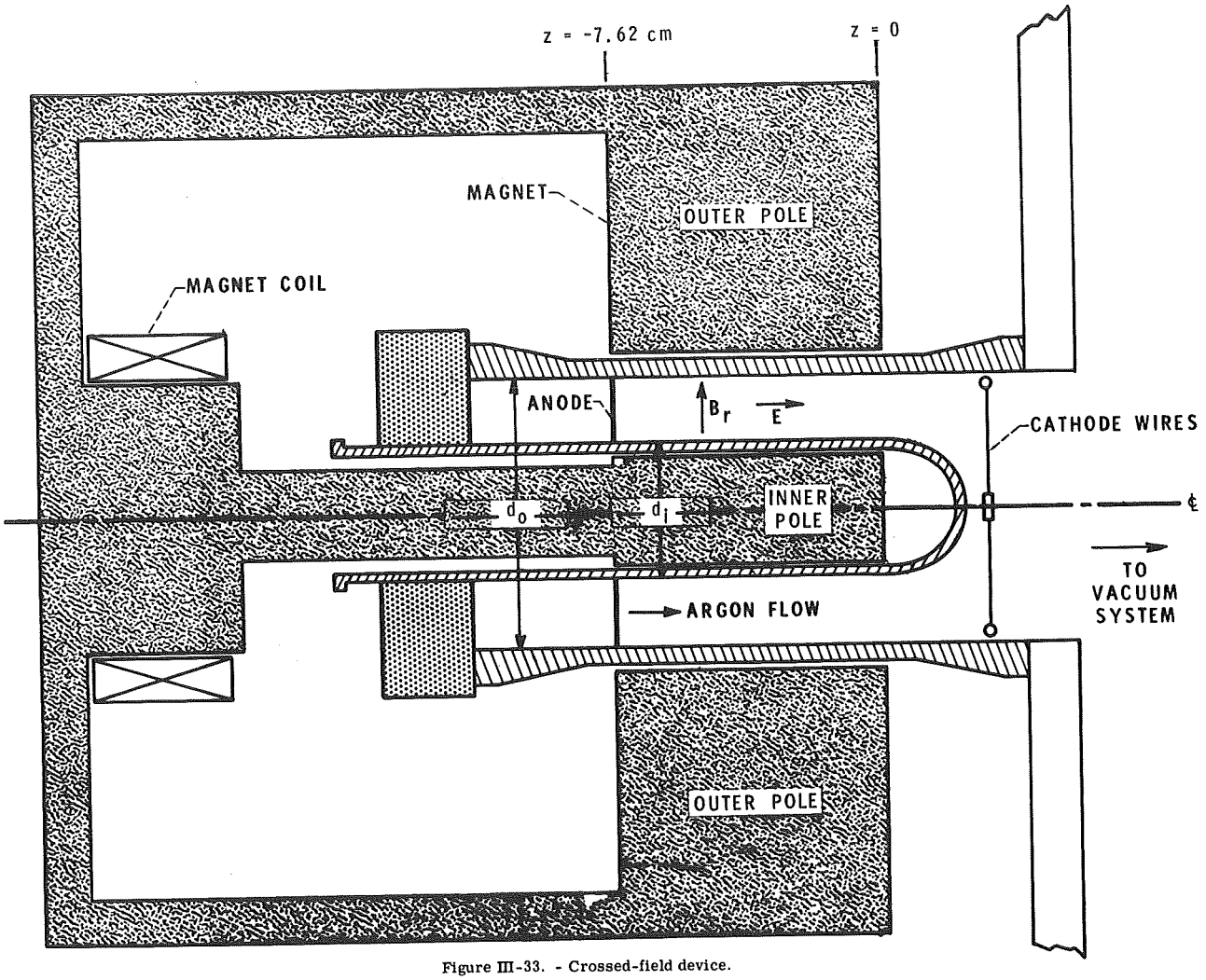


Figure III-33. - Crossed-field device.

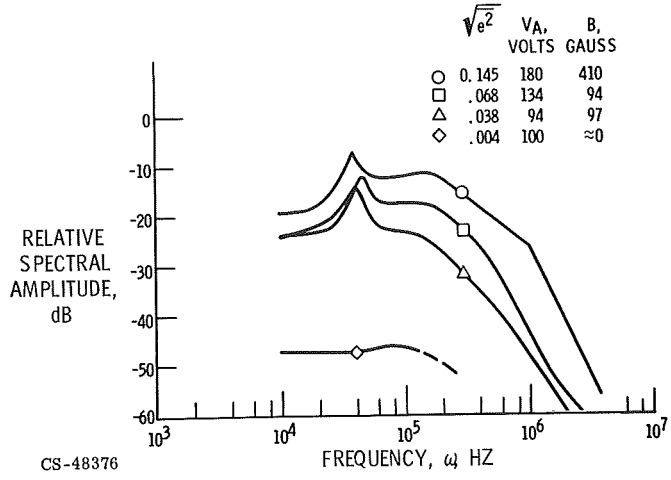


Figure III-34. - Amplitude spectra of plasma fluctuations.

# IV. THERMIONIC PLASMAS

Harold E. Neustadter

All thermionic energy converters[1] depend on the fact that when a metal is heated it emits electrons, a phenomenon in many ways analogous to the liberation of steam particles when water is heated. This basic property of materials was first noted by Thomas Edison in 1883. The proposal to harness this property to achieve direct energy conversion is credited to Schlichter in 1915. Work on actual devices is considerably more recent, being first reported by Hatsopolous in 1956 and Wilson in 1957, although a thorough examination of the thermionic emission of electrons from the combination of materials most often used today, namely, cesium coated tungsten, was conducted by Langmuir in the 1920's.

The current interest in thermionic research is heavily influenced by a desire to take full advantage of the high temperatures available from nuclear reactors, particularly in the space environment. Since thermionic converters might well operate with a heat rejection of approximately $10^3$ K, and since heat rejection itself varies as $T^4$, thermionic systems should allow for a major reduction in radiator size and hence in specific weight when compared to other lower temperature systems. In common with other direct conversion devices, the thermionic converter has no moving parts. However, it is very distinct from other systems in that it has a high power density, with values of the order of 10 watts per square centimeter currently attainable. The most probable space applications of thermionic conversion systems include power generation for long trips and/or large payloads.

The simplest version of the thermionic converter, namely, the vacuum diode, is shown in figure IV-1(a). The vacuum diode consists of two electrodes, an emitter and a collector, encased in a container which maintains the vacuum and a source of heat to drive the electrons.

Insight into the principles of operation of the vacuum converter can be obtained by looking at figure IV-1(b), which shows a typical interelectrode potential profile for the vacuum converter. On the left is the emitter, with the zero of energy chosen at its Fermi level. The collector with its Fermi level is on the right. Phi is used to indicate the work function. Lower case $\varphi$ is the vacuum work function, that is,

---

[1]The introductory portion of this report follows to a considerable extent the approaches used in refs. 1 and 2.

the amount of energy measured from the Fermi level that an electron needs to escape to vacuum from the interior of a solid. The subscripts e and c stand for emitter and collector, respectively. To trace the path of an electron through one energy conversion cycle, start with an electron that is initially near the emitter Fermi level. If it receives an energy greater than $\varphi_e$, it can leave the emitter, where it immediately encounters another barrier, $\Delta\varphi_e$, the space charge barrier resulting from the electrons which preceded it. If the electron initially received an energy greater than $\Phi_e = \varphi_e + \Delta\varphi_e$, it will climb the barrier and move across the interelectrode space to reach the collector. Here it gives up $\varphi_c$ as heat in moving down to the collector Fermi level. However, a net potential difference v remains between the Fermi levels of the two electrodes, so that, if the emitter and the collector are connected, the electron continues on through the external load performing work on its way.

The following table illustrates some of the physical constraints (ref. 1). For heat-resistant transition metals $\varphi$ is typically 4 to 5 volts. With a judicious

| Metal | Work function |
|---|---|
| Molybdenum | 4.20 |
| Nickel | 4.61 |
| Platinum | 5.32 |
| Tantalum | 4.19 |
| Tungsten | 4.52 |
| Cesium | 1.89 |
| Tungsten-cesium | 1.5 |
| Tungsten-barium | 1.6 |
| Tungsten-thorium | 2.7 |

choice of materials, such as an emitter with $\varphi \sim 5.3$ volts and a collector with $\varphi \sim 4.2$ volts, and optimizing the external load losses, one might be able to get an output voltage v of the order of 1 volt. Thus, in order to obtain power output, which is the product of the current I and the output voltage v, of 10 watts per square centimeter, we need current of approximately 10 amperes per square centimeter. However, as indicated in equation (1), the emission current I depends strongly on $\Phi_e$:

$$I = AT_e^2 e^{-\left(e\Phi_e/kT_e\right)} \tag{1}$$

The crucial feature here is that I decreases exponentially as $\Phi_e$ increases. In practice, adequate current densities are unattainable in vacuum diodes because the space charge $\Delta\varphi_e$ and hence $\Phi_e$ are too large. One might hope to minimize the damaging effects of space charge buildup by going to lower temperatures, using lower work function materials and/or reducing the interelectrode spacing. However, even these approaches require uniform interelectrode spacing of a fraction of a mil to be maintained over a very large temperature range and have so far presented difficult design and stability problems, although new approaches in this direction are currently contemplated.

The most direct, and for some time now the most promising, approach has been the introduction of a sufficiently dense gas of positive ions to neutralize the electrostatic field of the electrons. Primary attention has focused, therefore, on the plasma converter. Cesium is the most commonly used gas because of its low ionization potential. As shown in figure IV-2(a), the cesium converter is a modified vacuum converter which allows for the addition of cesium vapor to the interelectrode region. The density of the vapor is determined by the temperature of the cesium reservoir. The cesium enters the interelectrode region as a gas of neutral atoms and is subsequently ionized by either surface ionization at the hot emitter (unignited mode) or volume ionization in the interelectrode region (ignited mode).

The consequences of introducing cesium can be seen in figure IV-2(b). The primary benefit derived from a cesium plasma is the neutralization of the space charge, that is, reduction of $\Delta\varphi_e$. Another nontrivial benefit, however, is that some of the cesium atoms absorb on the collector, which is relatively cool, while those that come in contact with the emitter, which is hot, will boil off. As shown in the table of work functions, this will lower the collector work function close to that of cesium with the beneficial consequence of increased output voltage.

For a number of reasons including reliability, ease of acquisition, and direct usefulness to development engineers, the principal analytic tool for thermionic converters is the plot of current against voltage, or I-v curve. Figure IV-3 shows one such plot; actually it is a composite of various I-v curves presented slightly out of proportion in order to indicate all the features of interest more clearly.

The major feature is the existence of two modes of operation. These correspond to the two ionizing processes mentioned earlier. The lower portion shows the unignited mode, in which the cesium ions are produced by surface contact ionization. The upper curve shows the ignited mode, in which the ionization takes place in the interelectrode region as a result of electron-atom collisions. Within

these two modes, the major I-v characteristics are further classified by

(1) The deep retarding region which results from the application of a reverse bias voltage to the diode

(2) The apparent saturation region which is a result of either space charge limitation when the electron space charge is incompletely neutralized or the collection of all electrons when there is an adequate (excess) supply of ions

(3) The region of preignition and negative resistance in which a violet-pink glow discharge forms at one point in front of the emitter and eventually covers the entire emitter

(4) That part of the ignited mode, sometimes referred to as the obstructed region, in which there is dark space directly in front of the emitter and an orange flow in the interelectrode region

The second mode appears most promising for power production since the product of I and v is greatest. It has been possible to produce in typical experimental devices current densities of 50 amperes per square centimeter near 0.5 volt for power densities greater than 20 watts per square centimeter.

The paper thus far has dealt with the thermionic conversion process. Now consider the role played by the plasma itself. For perfect neutralization, it is necessary that

$$n_+ = n_- \tag{2}$$

where n is the number density, (+) refers to ions, and (-) refers to electrons. Note that this in no way implies that the current densities are equal. Quite the contrary; the current is given by

$$I_\pm = n_\pm e u_\pm \tag{3}$$

where u is the mean velocity. In thermal equilibrium the kinetic energies are equal:

$$\frac{1}{2} m_+ u_+^2 = \frac{1}{2} m_- u_-^2 \tag{4}$$

so that, for cesium,

$$\frac{I_-}{I_+} = \frac{m_+}{m_-} = 492$$

This leads to the definition of the ion richness parameter $\beta$ as

$$\beta = 492 \frac{I_+}{I} \tag{5}$$

The converter is electron rich when $\beta \ll 1$, ion rich when $\beta \gg 1$, and approximately neutralized when $\beta \sim 1$.

The second parameter is pd, the product of the pressure and the interelectrode spacing. It is approximately proportional to the number of electron mean free paths in the converter. The effects of $\beta$ and pd as parameters (ref. 2) are shown in figure IV-4. The major axes define a space in $\beta$ and pd. Superposed on this is a set of four different I-v curves. Each I-v curve presents the results of operation of the same plane parallel cesium vapor thermionic converter. The striking differences between the four curves arise from the different combinations of $\beta$ and pd at which each is operated. Curve B is typical of a converter operating at $\beta < 1$ and pd $< 10$. The curve shows the full range of operation shown in figure IV-3 with the exception that the small current region is considerably contracted. If $\beta$ is kept the same, but pd (the number of mean free paths) increases, the transition and negative resistance regions disappear and the converter operation goes smoothly from ignited to unignited modes, as shown by curve A. As both $\beta$ and pd are increased, we would find that the apparent saturation region is completely absent as in curve C.

Figure IV-5 shows a typical set of interelectrode potential diagrams for the ignited mode as measured by Baksht and coworkers and reported in the Journal of Soviet Physics (ref. 3). The emitter is on the left, and the different curves are for the various spacings indicated. The difference between the potential heights at the emitter and collector is the internal plasma loss of the order of 1 volt. Most of this loss represents energy required to maintain the plasma while a lesser source of loss to be considered is back heating of the emitter by the plasma. Considerable effort has been directed toward obtaining a better understanding of these loss processes. At this point we should note that, in addition to the usual difficulties of analysis present in all plasmas, there are further complications unique to thermionic plasmas. These include the active nature of the container walls. That is, the walls emit and collect electrons and ions as an essential part of the device operation. Also, the plasma dimensions are very small, that is,

the space between emitter and collector is usually of the order of 5 to 10 mils.

The Lewis Research Center has carried on a program of theoretical and experimental work designed to enhance our knowledge of thermionic plasma processes and thus ultimately to improve the converter performance. Two theoretical studies of the plasma have been undertaken with emphasis given to the role played by the sheaths or boundary layer between the electrodes and the bulk plasma. In a work by James F. Morris the sheath parameters were coupled to electrodes as well as the plasma in a formulation which allowed for feedback between the components, as opposed to the more primitive theories which replaced the sheaths by passive boundary conditions. In addition to giving new insights into plasma processes under unignited isothermal conditions, it eliminated such inconsistencies of the earlier theories as the existence of a net current at equilibrium (ref. 4). Another theoretical study undertaken by Peter Sockol applied transport theory to the sheath itself in the unignited mode (ref. 5). This study is currently being extended to the ignited mode with emphasis on understanding the mechanism of nonthermal ionization in the immediate vicinity of the emitter. The matter of heat loss to the emitter from the plasma has been analyzed by Roland Breitwieser, who developed a technique based on application of quite general thermodynamic constraints to the analysis of I-v curves (ref. 6).

An experimental program to evaluate a possible new technique for reducing the losses incurred in maintaining the plasma was initiated a few years ago by Ralph Forman. His work involved the investigation of the enhanced electrical properties of a converter when placed in the radiation field of a nuclear reactor (ref. 7). Figure IV-6 depicts the envisioned process. It was anticipated that the $\gamma$-rays present in a reactor would as a result of interaction with the converter electrodes cause the generation of large numbers of relatively low energy electrons. These secondary electrons would, upon collision with the gas atoms present in the interelectrode space, excite (and possibly ionize some) neutral atoms. These atoms being in excited states rather than in the ground state would be more easily ionized to produce ignition. Preliminary in-pile investigations have exhibited some of the anticipated features, as shown in figure IV-6. These data are for a cylindrical thoriated tungsten emitter operating in a xenon environment. In the absence of $\gamma$ radiation the current is negligible at low voltages, and ignition occurs near 8 volts, which is approximately the energy of the first excited state for xenon. When the same convertor is operated in a reactor, two changes occur. First, there is an enhancement of the low voltage output believed to result from the ionization by secondary electrons, and second, there is a drop in the voltage necessary to cause ignition believed to result from the higher density of excited states. These changes become

more pronounced as the $\gamma$ radiation flux increases. It is anticipated by analogy with the $\beta$-pd plots of figure IV-4 that, with a judicious choice of operating conditions (e.g., the gas and its pressure, electrode materials, interelectrode spacing), it should be possible to cause further enhancement and obtain ignition at much lower voltage. If this hoped for behavior should materialize, there are two possible applications. One, there is the possibility of sufficient enhancement to generate useful power in the unignited mode. Two, there is the possibility that in the ignited mode cesium could be replaced by an inert gas. Cesium initially found favor because of its low ionization potential, but the $\gamma$-rays would in effect give inert gases effective ionization potentials that are nearly that of cesium. This substitution of inert gas for cesium would eliminate many of the materials compatibility difficulties arising from the highly corrosive nature of cesium. In spite of the favorable preliminary results obtained thus far, this program, by virtue of being an in-reactor study, is very difficult to perform and expensive to maintain. However, since the reactor generated $\gamma$-rays do not interact directly with the neutral gas atoms but rather serve only to generate secondary electrons, it was suggested that for test purposes it might be possible to generate secondary electrons from a source other than a reactor. This was investigated theoretically and indeed found to be feasible. Figure IV-7 shows a schematic drawing of the experimental reactor simulation setup that is being operated by Robert Bacigalupi using the Lewis Research Center Dynamitron (ref. 8). The electron beam incident from the left is generated in the Dynamitron, passes through the thin collector, and strikes the emitter causing both electrodes to emit secondary electrons. It has proved possible using the Dynamitron and a converter similar to the one used by Forman to generate secondary electron fluxes similar to those present in the reactor environment, and thus to reproduce out of core the I-v curves previously obtained in the reactor. Work is presently under way to extend the operating range of this setup. As a further check on the accuracy of this analysis, namely, that the enhanced operation does come from the interaction of secondary electrons with the plasma, and also as a more versatile technique for determining the effects of using different gases and electrodes, a separate microwave diagnostic experiment is currently being initiated by James Dayton. In this, the arrangement is similar to the converter experiment in the Dynamitron except that the diode is replaced by a simple container of gas. The plasma is irradiated by a microwave signal of variable frequency, and the reflected signal is compared with the incident signal. The type of information generated this way is shown in figure IV-8. When the beam of the Dynamitron is off, the reflected signal is as shown by curve A, there being a sharp resonant absorption by the plasma at a characteristic frequency. When the beam is turned on, the microwave signal is reflected as in curve B. The frequency shift can

be related to the charge density while the resonance broadening is related to collision frequency $\nu$, as shown in the following equations:

$$\frac{\Delta f}{f_0} \cong \frac{1}{2}\frac{n}{n_c} \tag{6}$$

$$\frac{\delta f_1}{f_1} - \frac{\delta f_0}{f_0} \cong \frac{\Delta f_0 \nu}{\pi f_0^2} \tag{7}$$

It is anticipated that this dual program will permit rather rapid investigation of a large number of electrode materials and plasma combinations. Of particular interest are the effect that the introduction of a Penning mixture[2] might have on plasma densities and the effect that the secondary electrons might have on recombination rates. While this latter research activity is still in its early phase, it already promises to yield much information of value to an overall understanding of plasma phenomena in the thermionic energy conversion process.

## REFERENCES


1. Walsh, Edward M.: Energy Conversion: Electrochemical, Direct, Nuclear. Ronald Press Co., 1967, ch. 7.
2. Bullis, Robert H.; et al.: The Plasma Physics of Thermionic Converters. J. Appl. Phys., vol. 38, no. 9, Aug. 1967, pp. 3425-3438.
3. Baksht, F. G.; et al.: Low-Voltage Arc in Thermionic Converters - Comparison Between Theory and Experiment. Soviet Phys. - Tech. Phys., vol. 13, no. 7, Jan. 1969, pp. 893-907.
4. Morris, James F.: Isothermal Diode '68. Seventh Annual Thermionic Conversion Specialist Conference. IEEE, 1968, pp. 202-208.
5. Sockol, Peter M.: Sheath Structure in the Unignited Mode. Seventh Annual Thermionic Conversion Specialist Conference. IEEE, 1968, pp. 209-215.


---

[2] A Penning mixture is a combination of two gases such that one species has a metastable state (e.g., neon at 16.6 V) slightly above the ionization potential of the other species (e.g., argon at 15.7 V). In such instances the ionization process can be quite efficient.

6. Breitwieser, Roland: Electron Cooling and Plasma Heating of Thermionic Converters. Seventh Annual Thermionic Conversion Specialist Conference. IEEE, 1968, pp. 235-241.

7. Forman, Ralph: Electrical Properties of Xenon-Filled Thermionic Diodes. NASA TN D-4368, 1968. (See also J. Appl. Phys., vol. 39, no. 9, Aug. 1968, pp. 4351-4355.)

8. Bacigalupi, R. J.: Simulation of In-Pile Effects on Thermionic Diodes. Paper presented at Thermionics Specialist Conf., Carmel Calif., Oct. 21-23, 1969.

# BIBLIOGRAPHY

This bibliography comprises publications authored by the members of the NASA Lewis Research Center Staff.


Bacigalupi, Robert J.: Surface Topography of Single Crystals of Face-Centered-Cubic, Body-Centered-Cubic, Sodium Chloride, Diamond, and Zinc-Blende Structures. NASA TN D-2275, 1964.

Bacigalupi, Robert J.; and Neustadter, Harold E.: Dependence of Adsorption Properties on Surface Structure for Body-Centered-Cubic Substrates. NASA TN D-3141, 1965.

Bacigalupi, Robert J.; and Thinger, Byron E.: Gamma Flux and Heat Deposition in Plum Brook Reactor - Comparison of Calculation and Experiment. NASA TM X-1539, 1968.

Barton, Gilbert C.; and Ferrante, John: Faceting from CO Adsorption on Mo(111). J. Chem. Phys., vol. 48, no. 10, May 15, 1968, pp. 4791-4793.

Branstetter, J. Robert: Some Practical Aspects of Surface Temperature Measurement by Optical and Ratio Pyrometers. NASA TN D-3604, 1966.

Branstetter, J. Robert; and Schaal, Robert D.: Thermal Emittance Behavior of Small Cavities Located on Refractory Metal Surfaces. Presented at the IEEE Thermionic Conversion Specialist Conference, San Diego, Calif., Oct. 25-27, 1965.

Breitwieser, Roland: Some Considerations of an A. C. Thermionic Converter. Proceedings of the 3rd Government-Industry Roundtable Discussions. Vol. II - Applied Research on Thermionic Converters and System Concepts. Rep. PIC-ELE-TI-209/1.1, vol. 2, Pennsylvania Univ., Jan 30, 1962, pp. 4-1 to 4-5.

Breitwieser, Roland: Cesium Diode Operation in Three Modes. Proceedings of the 23rd Annual Physical Electronics Conference, MIT, 1963, pp. 267-280.

Breitwieser, Roland: On the Relation of Ion and Electron Emission to Diode Diagnostics. IEEE Thermionic Conversion Specialist Conference, 1963, pp. 17-26.

Breitwieser, Roland; and Rush, Wayne: Saha-Langmuir Surface Ionization Relation. Presented at the IEEE Thermionic Conversion Specialist Conference, San Diego, Calif., Oct. 25-27, 1965.

Breitwieser, Roland; and Schwartz, Herman: Thermionics. Space Power Systems Advanced Technology Conference. NASA SP-131, 1966, pp. 239-268.

Brooks, Sidney: A Geometrical Representation for the High Frequency Dielectric Tensor of a Temperate Plasma. NASA TM X-1054, 1965.

Button, Susan L.; and Morris, James F.: Computer Programs for Plane Collisionless Sheaths Between Field-Modified Emitter and Thermally Ionized Plasma Exemplified by Cesium. NASA TM X-1562, 1968.

Button, Susan L.; and Morris, James F.: A Computer Program for Interactions of Polycrystalline-Tungsten Electrodes with Cesium Plasmas. NASA TM X-1637, 1968.

Butze, Helmut F.; and Smith, Arthur L.: Experimental Investigation of Chemical Regeneration of Surfaces in Simulated Thermionic Diodes. NASA TN D-1877, 1963.

Carr, Kenneth: Tables of Thermionic Properties of the Elements and Compounds. NASA TM X-52263, 1967.

Coopersmith, Michael H.; and Neustadter, Harold E.: Relaxation-Time Approximation for the Mobility of Electrons in Helium. Phys. Rev., vol. 161, no. 1, Sept. 5, 1967, pp. 168-172.

Ferrante, John; and Barton, Gilbert C.: Low-Energy Electron Diffraction Study of Oxygen Adsorption on Molybdenum (111) Surface. NASA TN D-4735, 1968.

Forman, R.: Electrical Properties of Inert Gas Plasmas Generated in Thermionic Cold-Cathode Diodes by Radiation in a Nuclear Reactor. J. Appl. Phys., vol. 36, no. 4, Apr. 1965, pp. 1344-1350.

Forman, Ralph: Measurements on Xenon Filled Nuclear Irradiated Thermionic Diodes. Thermionic Conversion Specialist Conference, IEEE, 1967, pp. 56-61.

Goldstein, Arthur W.; Braun, Willis H.; and Rose, James R.: Generation of Alternating Current by a Power Diode. NASA TM X-1099, 1965.

Goldstein, Arthur W.; Braun, Willis H.; and Rose, James R.: Alternating-Current Thermionic Power Diode with Magnetic Regeneration. J. Spacecraft Rockets, vol. 3, no. 6, June 1966, pp. 927-928.

Goldstein, C. M.: Theoretical Current-Voltage Curve in Low-Pressure Cesium Diode for Electron-Rich Emission. J. Appl. Phys., vol. 35, no. 3, pt. 1, Mar. 1964, pp. 728-729.

Goldstein, Charles M.: Monte Carlo Method for the Calculation of Transport Properties in a Low-Density Ionized Gas. NASA TN D-2959, 1965.

Goldstein, Charles M.: Numerical Integration by Gaussian Quadrature. Presented at the 24th Semiannual SHARE Meeting, Los Angeles, Calif., Mar. 1, 1965.

Goldstein, Charles M.: Computation of Electron Diode Characteristics by Monte Carlo Method Including Effect of Collisions. Presented at the ENEA-IEE International Conference on Thermionic Electrical Power Generation, London, Sept. 20-25, 1965.

Goldstein, Charles M.: Possible Sources of Instability in the Collisionless Thermionic Diode. NASA TM X-1245, 1966.

Goldstein, Charles M.: Electron Flow in Low-Density Argon Gas Including Space-Charge and Elastic Collisions. NASA TN D-4087, 1967.

Goldstein, Charles M.: Electron Flow in Low-Density Argon Gas Including Space-Charge and Elastic Collisions. J. Appl. Phys., vol. 38, no. 7, June 1967, pp. 2977-2984.

Goldstein, Charles M.: Collisionless Cylindrical Diode. NASA TN D-4516, 1968.

Goldstein, Charles M.; and Goldstein, Arthur W.: A Single-Collision Model for Electron-Beam Currents Between Plane Electrodes. NASA TN D-3058, 1965.

Kampos, Samuel: Effective Radius of a Cesium Atom in Ground State and First Excited State. NASA TM X-52057, 1964.

Kaufman, Warner B.; Tischler, Richard F.; and Breitwieser, Roland: A High-Temperature, Electrically Insulating Cermet Seal Having High Strength and Thermal Conductance. Thermionic Conversion Specialist Conference, IEEE, 1967, pp. 260-270.

Lancashire, Richard B.: Study of Plasma Diagnostics Using Laser Interferometry with Emphasis on its Application to Cesium Plasmas. NASA TM X-1652, 1968.

Lancashire, Richard B.: Refractive Index: Particle Density Correlation for Nonequilibrium Cesium Plasmas Probed by a Multifrequency Helium-Neon Laser. NASA TN D-5328, 1969.

Luke, Keung P.: Analytical Study of the Work Function Characteristics of a Metal Immersed in Cesium Vapor-Surface Contribution. Presented at the 24th Annual Conference on Physical Electronics, MIT, Mar. 25-27, 1964.

Luke, Keung P.; and Smith, John R.: Theoretical Study of Zero-Field Electron Work Function of Metal Immersed in Gas - Direct Application to Cesium Thermionic Diode. NASA TN D-2357, 1964.

Manista, Eugene J.; and Sheldon, John W.: Preliminary Experiments with a Velocity-Selected Atomic-Beam Apparatus. NASA TN D-2557, 1964.

Manista, Eugene J.: Distortion of Atomic-Beam Velocity Distributions Due to Classical Hard-Sphere Gas Scattering. NASA TN D-2617, 1965.

Manista, Eugene J.; and Sheldon, John W.: Influence of Opposing Slits on Molecular Flow from an Isothermal Enclosure at Low Densities. NASA TN D-2986, 1965.

Morris, James F.: Damping of Quantized Longitudinal Electron Oscillations in a Nondegenerate Plasma. Phys. Fluids, vol. 5, no. 11, Nov. 1962, pp. 1480-1481.

Morris, James F.: Dispersion and Damping of Longitudinal Electron Oscillations in Thermal Plasmas. NASA TN D-1734, 1963.

Morris, James F.: Reply to Comments by Burt, Klevans, and Wu. Phys. Fluids, vol. 6, no. 9, Sept. 1963, pp. 1365-1366.

Morris, James F.: Thermal Field Emission with a Terminated Image Potential. NASA TN D-2784, 1965.

Morris, James F.: Calculations of Thermal, Field Emission for a Terminated Image Potential. NASA SP-3023, 1966.

Morris, James F.: Energy Transport by Thermal Field Emission. NASA TN D-3448, 1966.

Morris, James F.: Small Plasma Probes with Guard Rings and Thermocouples. NASA TM X-1294, 1966.

Morris, James F.: Emitter and Collector Sheaths for Cesium Thermionic Diodes with Polycrystalline Tungsten Electrodes. NASA TN D-4744, 1968.

Morris, James F.: Some Interactions of Polycrystalline Tungsten Electrodes with Cesium Plasmas. NASA TN D-4745, 1968.

Morris, James F.: Effects of Arrival Rates of Absorbate Ions and Atoms on Surface Coverage, Hence Work Functions, of Emitting Electrodes. NASA TN D-4369, 1968.

Morris, James F.: Collisionless Sheaths Between Field-Modified Emitters and Thermally Ionized Plasmas Exemplified by Cesium. NASA TN D-4376, 1968.

Morris, James F.: Pairs of Emitter and Collector Sheaths for Cesium Thermionic Diodes. NASA TN D-4419, 1968.

Morris, James F.: Plane Collisionless Sheaths Between Field-Modified Emitting Electrodes and Thermally Ionized Plasmas Exemplified by Cesium. J. Appl. Phys., vol. 39, no. 3, Feb. 15, 1968, pp. 1705-1717.

Morris, James F.: Reflections of Electron Beams in Thermionic Diodes. J. Appl. Phys., vol. 39, no. 13, Dec. 1968, pp. 6099-6100.

Neustadter, H. E.; and Bacigalupi, R. J.: Dependence of Adsorption Properties on Surface Structure for Body-Centered-Cubic Substrates. Surface Sci., vol. 6, no. 2, Feb. 1967, pp. 246-260.

Neustadter, Harold E.: Electron Mobility in Randomly Located Hard-Core Scatterers. Ph.D. Thesis, Case Western Reserve Univ., 1969.

Neustadter, Harold E.; and Coopersmith, Michael H.: Electron Mobility Transition in a Random System of Hard-Core Scatterers. Phys. Rev. Letters, vol. 23, no. 11, Sept. 15, 1969, pp. 585-589.

Neustadter, Harold E.; and Luke, Keung P.: Low-Coverage Heat of Adsorption. I - Alkali Metal Atoms on Tungsten; Atom-Metal Interaction Theories. NASA TN D-2430, 1964.

Neustadter, Harold E.; and Luke, Keung P.: Low-Coverage Heats of Adsorption. III - Alkali Metal Ions on Tungsten; Atom-Metal Interaction Theory. NASA TN D-2460, 1964.

Neustadter, Harold E.; Luke, Keung P.; and Sheahan, Thomas: Low-Coverage Heat of Adsorption. II - Alkali Metal Atoms on Tungsten; Lennard-Jones Atom-Atom Interaction Theory. NASA TN D-2431, 1964.

Nottingham, Wayne B.; and Breitwieser, Roland: Theoretical Background for Thermionic Conversion Including Space-Charge Theory, Schottky Theory, and the Isothermal Diode Sheath Theory. NASA TN D-3324, 1966.

Sanders, Newell D.; et al.: Electric Power Generation. Conference on New Technology. NASA SP-5015, 1964, pp. 65-89.

Schaefer, John W.; and Ferrante, John: Analytical Evaluation of Possible Non-cryogenic Propellants for Electrothermal Thrustors. NASA TN D-2253, 1964.

Sheldon, John W.: Correlation of Resonance Charge Exchange Cross-Section Data in the Low-Energy Range. Phys. Rev. Letters, vol. 8, no. 2, Jan. 15, 1962, pp. 64-65.

Sheldon, John W.: Mobilities of the Alkali Metal Ions in Their Own Vapor. J. Appl. Phys., vol. 34, no. 2, Feb. 1963, p. 444.

Sheldon, John W.: Mobility of Positive Ions in Their Own Gas: Determination of Average Momentum-Transfer Cross Section. NASA TN D-2408, 1964.

Sheldon, John W.: Semiclassical Calculation of the Differential Scattering Cross Section with Charge Exchange: Cesium Ions in Cesium Vapor. NASA TN D-2484, 1964.

Sheldon, John W.: A Comment On a New Method for Finding the Phase Shifts for the Schrödinger Equation. Acta Phys. Acad. Sci. Hung., vol. 17, 1964, pp. 399-400.

Sheldon, John W.: Cesium Ion-Neutral Scattering and Ion Mobility in the Low Field Limit. Presented at the IEEE Thermionic Conversion Specialist Conference, Cleveland, Ohio, Oct. 26-28, 1964.

Sheldon, John W.: Cesium-Cesium Cross Section and the Lennard-Jones Parameters. Presented at the IEEE Thermionic Conversion Specialist Conference, Cleveland, Ohio, Oct. 26-28, 1964.

Sheldon, John W.: Cross Section for Impact Ionization of H(1s) Atoms by H(1s) Atoms Near Threshold. NASA TN D-3134, 1965.

Sheldon, John W.: Cross Section for Ionization of Alkali Atoms by Collision with Excited Noble Gas Atoms. J. Appl. Phys., vol. 37, no. 7, June 1966, pp. 2928-2929.

Sheldon, J. W.; and Dugan, John V., Jr.: Semiclassical Calculation of Inelastic Cross Sections for Electron-Cesium Atomic Collision. J. Appl. Phys., vol. 36, no. 2, Feb. 1965, pp. 650-651.

Sheldon, John W.; and Manista, Eugene J.: Atomic Beam Determination of the Cesium-Cesium Total Scattering Cross Section. NASA TN D-3160, 1965.

Sockol, Peter M.: Nonequilibrium Expansion of a Plasma from a Thermionic Source. NASA TN D-2086, 1963.

Sockol, Peter M.: Transport Equations for a Partially Ionized Gas in an Electric Field. NASA TN D-2279, 1964.

Sockol, Peter M : Flow of Electrons Through a Neutral Scattering Gas in a Thermionic Diode. Presented at the IEEE Thermionic Conversion Specialist Conference, Cleveland, Ohio, Oct. 26-28, 1964.

Sockol, Peter M.: Flow of Electrons Through a Rarefied Gas Between Plane Parallel Electrodes. NASA TN D-3510, 1966.

Swigert, Paul; and Goldstein, Charles M.: Monte Carlo Code for Solution of Planar Electron-Diode Problems Including Electron-Neutral Elastic Collisions. NASA TN D-4043, 1967.

Tower, Leonard K.: An Analytical Study of the Continuous Chemical Regeneration of Surfaces. NASA TN D-1194, 1962.

Tower, L. K.: Analyses of the Chemical Regeneration of Sublimating Thermionic Components. Adv. Energy Conversion, vol. 3, no. 1, Jan.-Mar. 1963, pp. 185-198.

Tower, Leonard K.: A Preliminary Analysis of the Process of Desorption of Multiple Additives from Metals. Presented at the IEEE Thermionic Conversion Specialist Conference, San Diego, Calif., Oct. 25-27, 1965.

Tower, Leonard K.: Desorption Kinetics of Multiple Adsorbates - Cesium with Fluorine on Molybdenum and Tungsten. NASA TN D-3596, 1966.

Tower, Leonard K.: The Erected Dipole Model in the Adsorption of Cesium on Fluorinated Molybdenum. NASA TN D-3223, 1966.

Tower, Leonard K.: Baker's Computation of the Configurational Entropy of Large Atoms. J. Chem. Phys., vol. 47, no. 11, Dec. 1, 1967, pp. 4871-4872.

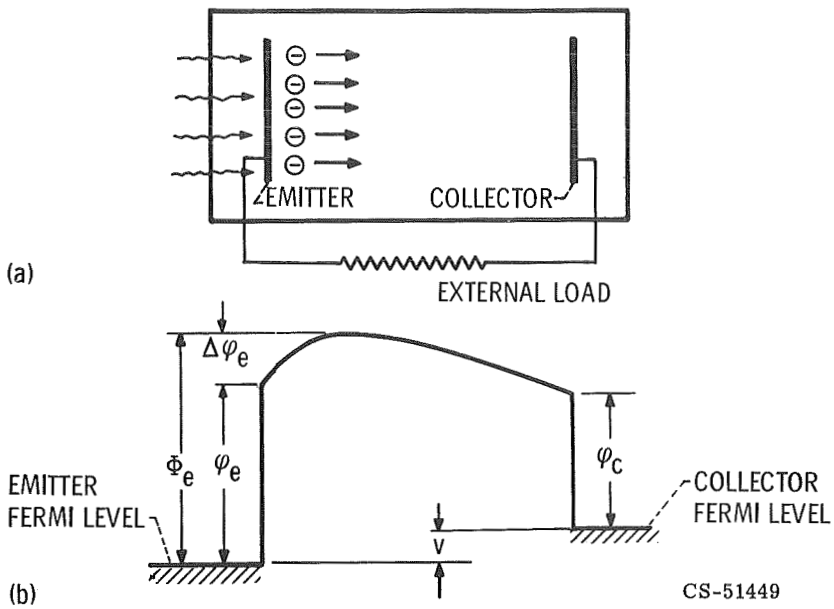


(a) Schematic diagram of thermionic converter.
(b) Interelectrode potential diagram.

Figure IV-1. - Vacuum thermionic energy converter.

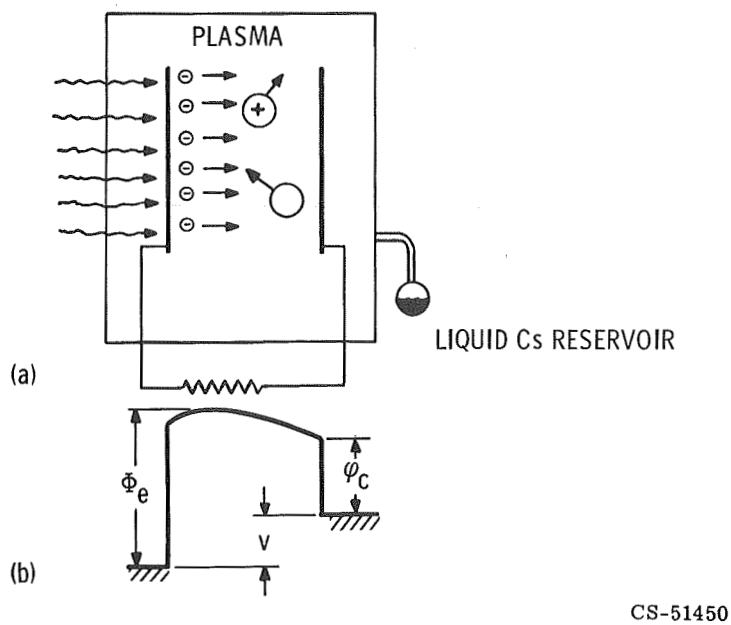


(a) Schematic diagram of thermionic converter.
(b) Interelectrode potential diagram.

Figure IV-2. - Plasma (cesium) thermionic energy converter.

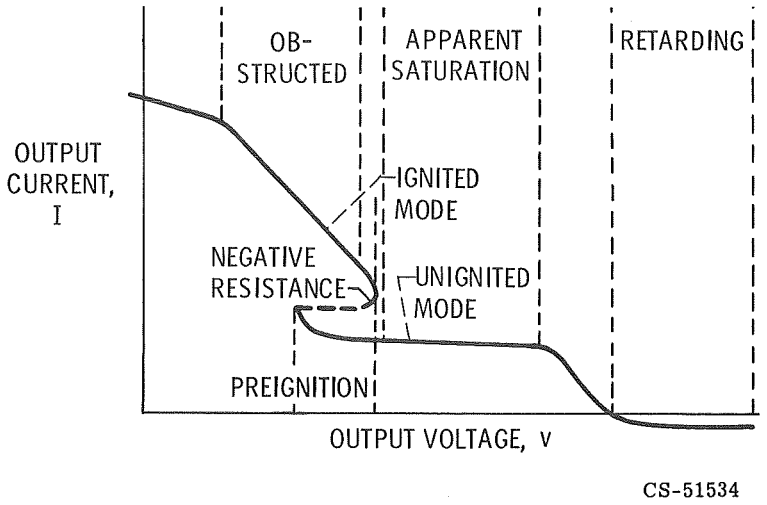


Figure IV-3. - Typical current-voltage characteristic for plasma thermionic energy converter (ref. 1).

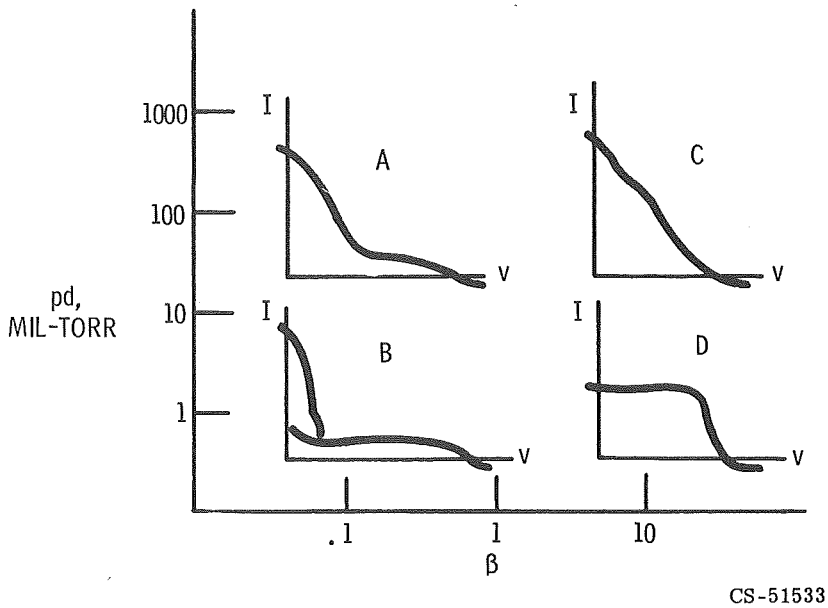


Figure IV-4. - Set of four current-voltage characteristics reflecting dependence of converter performance on ion richness parameter $\beta$ and pressure-spacing parameter pd (ref. 2).

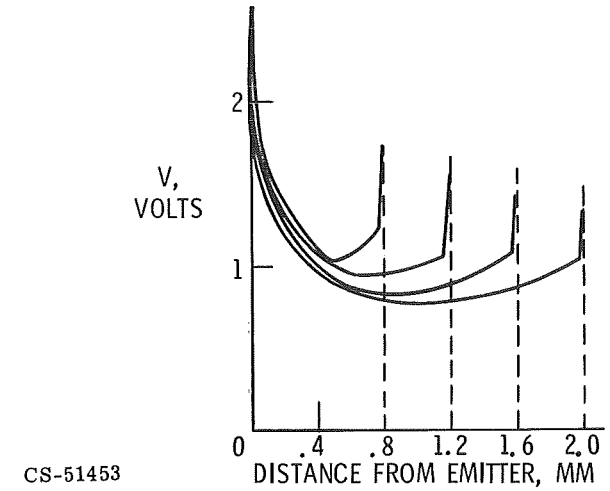


Figure IV-5. - Effect of electrode spacing on interelectrode potential. Cesium pressure, 1.0 millimeter of mercury; emitter temperature, 1680 K; current density, 1.7 amperes per square centimeter (ref. 3).

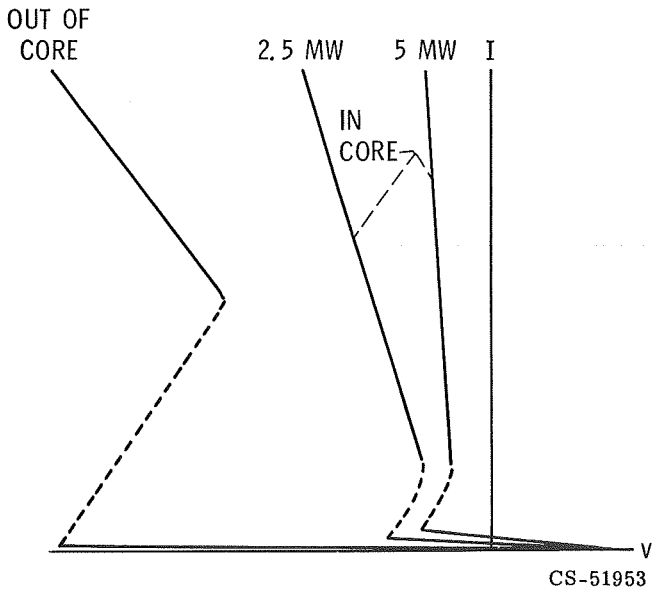


Figure IV-6. - Typical results for cylindrical converter operated in xenon environment. Power units (MW) correspond to power level of reactor employed (Sterling Forest) with 2.5 megawatts approximately equivalent to 0.75 watt per gram.

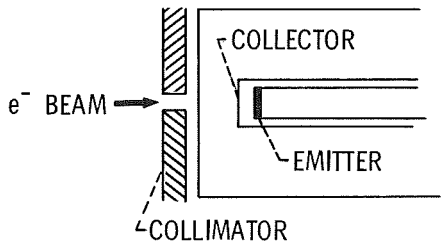


Figure IV-7. - Dynamitron simulation. Emitter, 2 percent thorium-tungsten; gas, xenon at 55 torr; spacing, 1 millimeter.

CS-51447

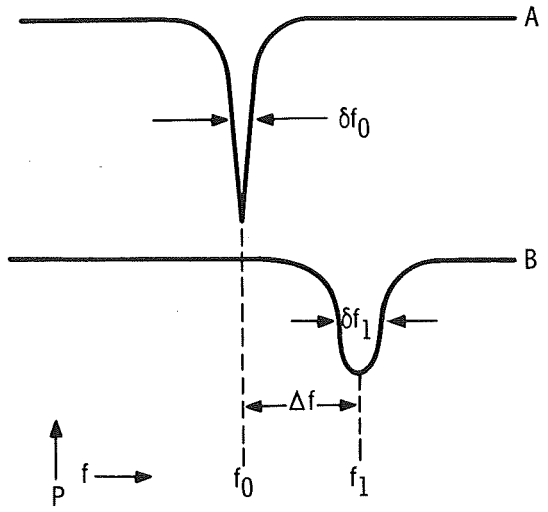


CS-51448

Figure IV-8. - Reflected signal obtained from microwave plasma analysis with electron beam off (curve A) and with electron beam on (curve B).

# V. CRYOGENIC AND SUPERCONDUCTING MAGNETS

James C. Laurence, Gerald V. Brown, Willard D. Coles, and Gale Fair

The Lewis Research Center has primary NASA responsibility for research on advanced concepts of power generation and propulsion. Some of these concepts require intense, large-volume, magnetic fields to be generated by lightweight equipment with low power consumption. Electric propulsion, magnetohydrodynamic power generation, thermonuclear power and propulsion, and space radiation shielding are some concepts for which such magnetic fields may be required.

The development of intense magnetic fields is also of importance for studies in a variety of disciplines, such as elementary particle physics (e.g., accelerators and bubble chambers), solid-state physics, and plasma physics. The range of size and field which are available in existing electromagnets is illustrated in figure V-1. The largest volume magnets are the bubble chamber magnets of Argonne National Laboratory, Brookhaven National Laboratory, and the French national laboratory at Saclay, which range in size to about 6 meters at 2 to 3 teslas. To put the measurement of magnetic flux density in perspective, the Earth's magnetic field is approximately $10^{-4}$ tesla (or 1 G) and a strong permanent magnet may range up to 1 tesla. The magnets described herein vary from 1 to a planned 30 teslas.

The work of Bitter and others at the Massachusetts Institute of Technology (MIT) resulted in a funding by the U.S. Air Force of a national magnet laboratory which is now known as the Francis Bitter National Magnet Laboratory. It has the largest concentration of high-field magnets in the world and is the center for research in intense fields. Their water-cooled copper solenoids reach flux densities of 22.5 teslas in a 3- to 4-centimeter bore, and 26.5 teslas in a very small volume with iron pole pieces.

The Lewis neon-cooled aluminum electromagnets have produced 20 teslas in a 11.5-centimeter-diameter volume and 14 teslas in a 30-centimeter-diameter volume. Lewis also has a 15-tesla superconducting magnet with a 16-centimeter-diameter bore (the largest and strongest superconducting magnet yet produced). Both MIT and McGill University are working on hybrid magnets - MIT on a superconducting magnet with a water-cooled insert, and McGill on a superconducting magnet with a cryocooled aluminum insert.

When the program to provide large-volume, intense magnetic fields was initia-

ted at Lewis, several different means of producing these fields were investigated. To reduce structural problems and simplify magnet construction and operation, it was decided to use low-impedance, high-current design. This design criterion was applied first to copper water-cooled coils, and later to aluminum cryogenically cooled coils.

A large homopolar generator (fig. V-2) and a transformer-rectifier power supply (fig. V-3) were selected as the power sources for the low-impedance electromagnets. The homopolar machine, a direct-current generator, supplies 3 megawatts power and a maximum of 200 000 amperes. The rectified alternating-current supply furnishes 1 megawatt with a maximum of 28 000 amperes.

The low-impedance concept has the following advantages:

(1) The magnet windings can be made in large cross sections to take advantage of the very heavy currents that can be drawn from the machine. These conductors are inherently stronger because of their size and may be nearly self-supporting in the fields produced.

(2) Since the potential difference between turns of a magnet designed according to this concept is small (of the order of a few volts), no special high-voltage insulation or water treatment is necessary. The cooling water can be drawn from the mains and disposed of in the sewer. In addition, there are no hazards because of high voltage.

(3) Cryogenic cooling of the conductors, which reduces their resistance by a factor of 1000 or more, can be used in the design of the magnets.

Two water-cooled magnets (one of which is shown in figs. V-4 and V-5, have been designed and built to operate from the homopolar generator. The magnet shown has a 10-centimeter bore and can reach 8.8 teslas.

It is hard to get high-current density, structural strength, and low-power consumption simultaneously in magnet windings. It is still harder to use the conductor material itself as the structure. The massive turns of the water-cooled magnets are self-supporting; but, at much higher current densities, pure copper is not strong enough to support itself. Some copper alloys (e.g., BeCu and ZrCu) have much higher strength with only moderately increased resistivity. However, still greater gains in strength and much lower resistivity are possible with specialization. Many steels have better elastic properties than the copper alloys and are better for structural support. On the other hand, some high-purity metals cooled to cryogenic temperatures have resistivities of only one-hundredth to one-thousandth that of copper at room temperature. Thus it is desirable to separate the functions of conduction and stress support. Greater strength and lower power consumption result. These are the principal advantages of cryogenically cooled (nonsuperconductive) electromagnets.

# CRYOGENIC MAGNETS

## Conductors and Coolants

The advantage of the cryogenically cooled but nonsuperconducting magnet systems comes from the low resistance of the conductor. Commercial copper, for example, has a resistance at the boiling point of helium that is one-hundredth its resistance at room temperature. The resistance ratio of a material, the ratio of the room-temperature resistance to the resistance at 4.2 K, is the working measure of the purity of the material. The temperature dependence of the resistivity for some pure metals with resistance ratios of about 1000 is shown in figure V-6. From this figure, it can be seen that the temperature range of importance is below 20 to 30 K. Commercial aluminum can be produced with a resistance ratio of 2000, and the temperature dependence of its resistivity is similar to that of copper shown in figure V-6.

Another significant factor in cryogenic magnet design is the magnetoresistance of the conductor, At these low temperatures, the resistance of a pure metal depends on the magnetic field. For example, in figure V-7, the data for the resistivity of copper to 11.5 teslas show a linear dependence on magnetic field strength. Figure V-8 shows data for aluminum taken at two temperatures. The aluminum magnetoresistance saturates at a low field, making this aluminum a strong candidate for high-field, cryogenically cooled electromagnets.

Below 30 K, the only coolant fluids are neon, hydrogen, and helium. Liquid helium, at 4.2 K, is not a good coolant for pool-boiling heat transfer because the latent heat of vaporization is so small. The hazards of liquid hydrogen preclude its use in a populated area such as the Lewis Research Center. The choice then was to use liquid neon at 27 K.

The only known source of the inert gas neon is the Earth's atmosphere, where it occurs at a concentration of about 18 ppm. Since neon is inert, there are no safety problems except those inherent with any cryogenic liquid. Large-scale production of oxygen for the steel industry during the last decade has made neon available in large supply at a considerable reduction in cost. Even so, the cost of operating with liquid neon is about $40 per liter, which is prohibitive unless the gas is recovered and reliquefied for reuse. The capital investment for the Lewis neon liquefier was one-third that of a cold-helium gas system large enough to cool the magnets. In addition, liquid neon is a desirable cryogen for a boiling-heat-transfer application because of its large latent heat per unit volume. Hence, liquid neon was chosen as the coolant for the Lewis cryogenic electromagnets.

The commercial high-purity aluminum, with about 17 ppm impurities and a re-

sistance ratio of 2000, was chosen as the conductor material for two magnets with inner diameters of 11.5 and 30 centimeters. Figure V-9 is a cutaway drawing of the completed 30-centimeter aluminum cryomagnet and its containment vessel. The construction of the cryostat is illustrated, including the vacuum jacket, the liquid-nitrogen jacket, and the trace lines for precooling of the magnet vessel and coils.

## Aluminum Magnet Construction

The construction of the aluminum coils is shown in figure V-10. Each turn of the magnet is a composite structure providing the current path, structural strength, coolant passages, and insulation. The high-purity aluminum conductor is 5 centimeters wide by 0.2 centimeter thick. It was anodized to produce a uniform coating of aluminum oxide on the surface. This coating serves to insulate the aluminum from the stainless-steel channel and to improve the boiling heat transfer by providing additional sites for incipient boiling. The stainless-steel channel supports the very soft, annealed aluminum on three sides and also provides the hoop strength and much of the turn-to-turn and coil-to-coil bearing surface. Flow channels for the liquid-neon coolant are provided by stainless-steel spacer bars held in place by a thin corrugated carrier ribbon of stainless steel. A glass and epoxy resin cloth provides insulation between turns.

Two bore sizes of this magnet have been built and have been in service for about 5 years. The magnet coils are electrically connected in a series-parallel arrangement to work within the voltage and current ranges of the homopolar generator.

A completed stack of these coils ready to be inserted in the cryostat is shown in figure V-11. Clearly shown in this figure are the bus bars and the intercoil connections. These must not only carry the current, but must resist the forces developed by the interaction of the current and the field.

The real usefulness of these magnets is determined by their operating characteristics. Some of the operating characteristics of the 20-tesla magnet are presented in figure V-12, which shows the change in resistance of the coils over the operating range. The change in resistance as the magnet is energized is caused by the change in magnetoresistance of the aluminum conductor as the field increases and by the heating of the conductor as the current increases. Because the liquid neon is boiling under saturated conditions into a fixed-volume vapor recovery tank, the temperature of the liquid rises some $3^{\circ}$ as the pressure in the system increases. This results in higher resistance values as the current is returned toward zero.

The operation of the liquid-neon-cooled magnets is limited by the capacity of the

refrigeration system, which is approximately 80 liters of liquid neon per hour. This limitation can be better expressed as one period of operation per day. The duration of a period of operation depends on the field strength desired. At maximum field (i.e., maximum power consumption), the time of operation is about 1 minute, including time to run up to field, time of operation at desired field strength, and time to shut down. The time is much longer, of course, for lower field ranges (about 4 min at 10 T). During a typical day's operation, one field sweep to 18 teslas and one to 16 teslas have been achieved. The power required for the maximum field (20 T) is 1 megawatt at 33 volts and 15 000 amperes in each of two parallel sets of coils (30 000 A total). The stored energy is approximately 10 megajoules. The total power consumed by the aluminum magnet is one-twentieth of the power required for water-cooled magnets of the same field strength and volume of field.

Some other advantages of the cryogenically cooled magnets are

(1) The fields can be swept quite rapidly, and for many experiments this is ideal.

(2) Ripple and noise fields are very small ($\approx 10^{-3}$ T).

(3) The general design is appropriate for solenoids of still higher field strength, higher than those possible with superconducting magnets made with presently known superconducting materials.

The major disadvantages of cryogenically cooled magnets are the short operating time at maximum field, the large capital investment for the refrigeration plant, and the large magnet coils and cryostats. Despite these disadvantages, the magnets are reliable and produce high-intensity fields for research in basic physics and in engineering applications.

What place do cryogenic magnets have in the future now that superconducting magnets, which require no power, are a reality? Recent work concerns methods of extending the field range of these magnets.

## Future Potential

Clearly, the future of cryogenic magnets will be in areas where superconducting magnets cannot function or are uneconomical. The most obvious regime where cryomagnets will be important is in fields too strong for superconductors. Above 15 teslas at present and above perhaps 20 teslas in the foreseeable future, superconductors cannot carry useful amounts of current. Thus it may always remain true that cryogenic magnets will be used to reach fields higher than those possible with the best superconductors. A planned improvement in the aluminum cryomagnet at Lewis should allow fields between 25 and 30 teslas to be reached for laboratory

research in solid-state physics and for engineering studies on materials to be used in high fields. Another area of some current interest is alternating-current or pulsed applications where the superconductors do exhibit resistance. Here the power expended in a high-purity cryogenic coil may be lower than in a superconducting coil. Furthermore, in other conditions where energy is dissipated in the magnet windings, such as by electromagnetic radiation and neutrons from a thermonuclear reaction, it may be necessary to operate the coil hotter than attainable critical temperatures of superconductors to reduce refrigeration power.

## Current Study Areas

At Lewis, engineering analysis is being directed at the very-high-field cryomagnet, with 30 teslas as the nominal design goal. This is twice the highest field so far attained with superconductors, and 7.5 teslas higher than the strongest steady field yet attained.

The crux of the engineering problem at this field level is the competition for space in the magnet windings between the three principal factors - current density, strength, and cooling. A fourth factor, insulation, is essential but usually not a problem. A 30-tesla solenoid must have a current density of the order of 5 to 10 kiloamperes per square centimeter to have reasonably compact windings. At these current densities, the force on a 1-foot length of 1-inch-square conductor in a 30-tesla field is between 40 and 80 tons. The $I^2R$ power dissipated in this volume is likely to exceed 100 watts for the purest available aluminum at helium temperature and 5 to 10 times as much for operation in hydrogen or neon. These power densities are very low compared to typical values in water-cooled magnets, but nevertheless pose moderate to severe problems for cryogenic coolants, which have relatively smaller heat capacities and latent heats. Finally, the extreme softness and low yield strength make plastic flow of very pure aluminum a definite problem because of the extremely large forces. These three problems - magnet mechanical strength, adequate cooling, and conductor softness - are paramount in the cryogenic magnet engineering problem.

The 30-tesla coil under design and study here at Lewis poses a very severe cooling problem. Figure V-13 contrasts the conductors of the existing cryomagnet and of the proposed 30-tesla insert coil. The cooling in the existing coil depends on natural convection of the liquid neon in the rather large cooling channels. In the new design (called "second generation"), the coolant is pumped through smaller channels to achieve much higher heat fluxes and thus to allow higher current densities. Less space is wasted in the new design because the material between cooling chan-

nels is aluminum, which can carry current, rather than steel filler or spacer bars. The purity of the aluminum to be used is not so high that its softness will cause any great problem. At the temperature of liquid neon, an increase in the purity of the aluminum does not offer much resistivity advantage over moderate purity.

Ultra-high-purity aluminum has recently been made commercially feasible for a magnet construction material. The advantage of this material is the lower residual resistance, but to take full advantage of the low resistance of this ultra-high-purity aluminum, the operating temperature must be dropped to 10 K or below. Thus, the only possible coolant is helium, either as a liquid or as a supercritical fluid. The solutions of the strength, cooling, and plastic-flow problems for this situation are different enough to merit the classification of such high-purity coils as "third-generation" cryogenic magnets. As yet no such third-generation coil is under detailed mechanical design. But, a preliminary look has been taken at the main features that such a coil might have.

First the conductor should be a thin, wide ribbon, backed up by a ribbon of steel or other strong material, as shown in figure V-14. The forces on the thin-ribbon conductor can thus be passed to the structure through a large bearing area, and large strains and plastic flow are thereby avoided. The grooved conductor design of the second-generation coils would be carried over. These interleaved ribbons of conductor and steel (and a suitable thin film of insulation) would be wound into the common "pancake" or "tape-wound" coil. The figure shows several thin ribbons of steel. Several thin ribbons are preferred to a single thick one so that the number of ribbons can vary from the inside of the coil to the outside. Variations in strength requirements from inside to outside make this desirable. In fact, analysis shows that if the total thickness of the bundle of steel ribbons varies in the appropriate way, the turn-to-turn forces that would pass through the soft aluminum can be reduced almost to zero. At the same time, a troublesome problem inherent in tape-wound coils, the tendency of the coils to loosen and unwind when energized, can be avoided. This unwinding is due to the outer turns of the coil stretching more than the inner ones. A numerical solution of an integral equation is required to find the proper variation of steel thickness. Figure V-15 shows one such result for a 30-tesla coil. The solid curve shows the desired variation in steel thickness as a function of radius. The dashed lines show how this calculated variation could be approximated by adding more thin steel ribbons as the coil is wound to give the greater rigidity needed in the outer turns.

Figure V-16 shows how a 20-tesla coil wound with these techniques would compare in winding size and in power requirement with the existing first-generation 20-tesla coil for the same inner diameter and length. Winding volume is only one-sixteenth as much and the required power only one twenty-fifth as much. The

superiority of the third-generation design is even more pronounced at still higher fields.

This is the direction of the present work at Lewis on cryogenic magnets. However, it is anticipated that most space applications will use superconducting magnets.

## SUPERCONDUCTING MAGNETS

The phenomenon of superconductivity in metals was first observed in the early 1900's. It is characterized by a total loss of resistance to electrical current in a step transition as temperature is reduced to near absolute zero. Since the first studies of the phenomenon, nearly all metals have been categorized as either superconducting or ferromagnetic at very low temperatures. Most of the metals revert to their normal resistance characteristics in relatively low magnetic field environments that are externally applied or self-generated by a current flow in the metal, or when their temperature exceeds a characteristic low critical temperature. These critical values are not mutually independent but are rather the extreme values of a bounding surface between the superconducting and normal states, as indicated in figure V-17. For values of current, magnetic field strength, and temperature less than critical, the material is superconducting. For values greater than these critical values (i.e., for points outside the critical surface), the materials are normal (resistive) conductors. A characteristic of these materials is the Meissner effect illustrated in figures V-18 and V-19. Figure V-18 shows a normal conductor, such as copper, where the flux lines completely penetrate the sample. Also shown is a superconductor which excludes the flux completely (e.g., tin). This phenomenon is characteristic of superconductors classified as type I. The type II superconductors are illustrated in figure V-19. The behavior is similar to that of type I superconductors in low fields, but at high fields the flux penetrates partially into the conductor and produces normal and superconducting regions.

Type I superconductors are further characterized by low values of critical temperature, while the type II materials have the highest known critical temperatures. In the type I materials, the flux enters the conductor at the critical field or critical temperature, and the conductor reverts to the resistive state. In type II materials, however, the flux enters in discrete packets with a gradual change to the normal state. It was not until 1961, with the discovery of materials capable of retaining their superconducting characteristics at high field strengths (over 20 T) and relatively high temperatures (to 20 K) and while carrying high current densi-

ties (over $10^6$ A/cm$^2$), that significant commercial use of superconductors could be made.

Current-against-field curves are indicative of the maximum current that a short sample of a type II superconductor can carry as a function of the applied magnetic field. These curves for three of the most commonly used superconducting materials are shown in figure V-20. The niobium-tin compound $Nb_3Sn$ is an intermetallic compound with the highest critical temperature $T_c$ and critical magnetic field strengh $H_c$ of the practical materials (18.5 K and 22 T). Niobium titanium (Nb-Ti) is an alloy with an $H_c$ somewhat greater than 11 T. This alloy has displaced Nb-Zr, an earlier development, in practical applications.

Figure V-21 shows the current density that can be carried by $Nb_3Sn$ produced by three different methods. Large variations like these are possible because current-carrying ability is determined by the number and nature of imperfections in the material. Magnetic flux penetrates high-field superconductors in individual tubes enclosed in a vortex of current, as shown in figure V-22. These so-called "flux lines" or vortices generate heat if they move through the superconductor, and may, in fact, drive the superconductor back into its normal state. It is thus necessary for the flux lines to be immobilized by blocking them with imperfections in the superconductor. These imperfections are called pinning sites. Dislocations, voids, and precipitates are among those imperfections known to be effective pinning sites. The more numerous and effective the pinning sites are, the more current the superconductor can carry. Unfortunately, during the charging period of a coil, the flux must move to some degree, and the resulting heating can decrease the effectiveness of the pinning sites, allowing more motion and more heating at an increasing rate. This magnetic and thermal runaway, called a flux jump, can drive a small part of the superconductor back into the normal state. This normal region may expand and cause the quench of the entire coil. A reliable method of preventing the spread of a normal region is to provide sufficient copper in parallel with the superconductor. The effect of the copper is to shunt the current around the normal region temporarily to allow the normal region to cool and become superconducting again. This composite conductor is known as a "stabilized conductor" and was first demonstrated by Kantrowitz and Stekly in 1965. The added copper gives stability at the considerable expense of a reduction in current density. Efforts to obtain stabilization with higher current density are discussed later in the section Stabilized Superconductors.

The Lewis Research Center has acquired a number of superconducting magnets with a large range of size and field strength, as shown in figure V-23. The solid circles represent Lewis superconducting magnets, and the solid squares the Lewis cryocooled magnets. The superconducting magnets with the largest bore diameters

are those built for a plasma physics facility, the Superconducting Magnetic Mirror Apparatus (SUMMA). The coils are 51 centimeters in inside diameter and have 4.5-tesla fields. Dr. Roth's plasma physics apparatus, the first built with superconducting magnets is also represented in figure V-23. It has an inside diameter of 18 centimeters and a 2.5-tesla field. Also shown are magnets used in solid-state physics research, as well as the 16-centimeter, 15-tesla magnet. The open circles denote the Argonne National Laboratory (ANL) and Brookhaven National Laboratory (BNL) bubble chamber magnets, while the diamonds denote the Bitter National Magnet Laboratory (NML) water-cooled magnets.

The cryostats for the Lewis magnets vary in size from a few liters to over 1400 liters liquid-helium capacity. Boiloff gas from the larger facilities is collected, and reliquefied in a system (fig. V-24) consisting of two hemispherical balloons 27.5 meters in diameter, a purification system, and two 100-liter-per-hour liquefiers. This liquid-helium system was originally acquired for, and is mostly used by, a space environment simulation facility.

The upper section of the largest magnet cryostat is shown in figure V-25. It has an inside diameter of almost 1 meter and is 4.2 meters in height, most of which is below floor level.

Some of the smaller magnets compared in figure V-23 are similar to those used at other laboratories, so the remaining discussion is concerned with those that are unique to Lewis.

The highest field attained anywhere thus far with superconducting magnets is about 15 teslas, which was attained with the 15-centimeter-bore magnet at Lewis. This magnet has a test volume approximately nine times that of the other highest-field superconducting magnets.

## Lewis 15-Centimeter-Bore, 15-Tesla Magnet

Design and construction of the 15-tesla magnet presented some problems which, though not unique, were intensified by the size and field strength requirements. The magnet and Dewar lid assembly is shown in figure V-26. The magnet is a solenoid with approximate dimensions of 15 centimeters in inside diameter, 50 centimeters in outside diameter, and 35 centimeters in length. Weight of the magnet is nearly 1000 pounds, and the stored energy when powered to maximum field strength approaches 2 megajoules.

At present, $Nb_3Sn$ is the only commercially available superconducting material which is suitable for use in a magnetic environment greater than about 10 teslas. The 90 000 meters of 1/4-centimeter-wide superconductive ribbon used in the mag-

net is a composite of $Nb_3Sn$, stainless steel, and silver. Stainless steel serves as a base for the vapor-deposited $Nb_3Sn$ and provides the high strength required. Silver plating is added to improve the stability of the superconductor. The thickness of each material is varied as a function of the characteristics required. Excess thickness of any of the materials is costly in terms of current density, and as a result is costly in magnet volume, materials, and performance.

Matching of the conductor to the field, strength, and stability requirements in different sections of the magnet led immediately to a modular design concept. Hoop stress on the conductor and compressive loading of the magnet windings and internal structure are necessarily high because of the high current densities required. Axial compressive loading of the windings builds up throughout the magnet as a result of the attractive force between conductors. To prevent compressive stress from exceeding the strength limits of the materials, load-bearing radial and axial members were required. The module walls serve this purpose, accepting and transmitting forces at various points in the magnet. A computer program was used to optimize the design, both as to strength and conductor characteristics. Figure V-27 shows various parts of the magnet. Twenty-two coil forms were used to wind the 30 electrically distinct modules.

Because of the large mass of the magnet, cooling of the internal parts was essential. Grooves and holes in the support structure provide passages for the inflow of liquid helium and for the escape of helium gas. No provision is made for helium passages within the windings. Heat is generated by localized "flux jump" penetrations or general transitions from superconductive to resistive modes. These transitions result in the collapse of the field and the release of all of the stored energy in a very short time period. When this occurs, the magnet is heated, and the helium is vaporized.

## Superconducting Magnetic Mirror Magnets

A set of 51-centimeter-bore magnets in an axial array is to be used in a superconducting magnetic mirror apparatus. Four of the six 51-centimeter magnets are quite similar in construction and materials to the 15-centimeter magnet. These magnets, shown in figure V-28, are not made from stabilized material, although one does use a copper-clad conductor. As a result, all these magnets are readily triggered into the superconducting-to-normal transition, or quench, and none achieved design current or field strength goals in their initial tests. However, by operating the magnets in superfluid helium, design values were, for the most part, obtained. Magnet performance was improved by factors of from 1.3 to 1.6 over

the performance obtained when 4.2 K helium was used.

Superfluid helium occurs as an increasing fraction of liquid helium as the temperature is reduced below 2.17 K. The characteristics of the superfluid are no less amazing than those of a superconductor, and indeed there are theoretical analogies between the two. The two characteristics of the superfluid which make it unique as a coolant are its extremely high thermal conductivity and extremely low viscosity. Within certain limits of heat flux, all the heat generated anywhere in the liquid is conducted essentially instantaneously to the surface of the liquid. When this behavior is combined with what is, for all practical purposes, zero viscosity, there results a coolant that literally searches for heat, penetrating even the smallest opening. This results in improved superconductor stability and allows the attainment of higher current values.

The remaining two 51-centimeter-bore magnets, not previously discussed, are shown in figure V-29 shortly after removal from the Dewar following a test. They are each 80 centimeters in outside diameter and 30 centimeters long. Weight of the magnet pair is over 2 tons. The magnets are made in three concentric modules, and are wound of stabilized NbTi and $Nb_3Sn$.

The two types of conductor used are illustrated in figure V-30. The innermost module, shown during assembly (fig. V-31), consists of 20 submodules of 1.25-centimeter-wide $Nb_3Sn$ ribbon stabilized with copper and strengthened with stainless steel. An intermittent insulation of mylar is used. This conductor is wound in pancake form. Outer modules (fig. V-32) are spool-wound using a 0.218-centimeter-square composite of copper and NbTi. Since this set of magnets is wound of stabilized materials, little additional performance benefit can be realized by operation of these magnets in superfluid helium.

## Stabilized Superconductors

The superconducting coils of today represent great advances over their normal predecessors. But they are not yet satisfactory for space applications. Whereas reliable, compact coils to reach high fields are needed, at present a choice must be made between compactness and reliability. The quest for compactness is really a quest for higher current density.

At present, the standard method of preventing thermal runaway is to place copper in parallel with the superconductor, as previously mentioned. But the amount of copper needed is several times the amount of superconductor, which makes the winding several times as large and massive. This is undesirable for aerospace magnets. The most obvious improvement is to use pure aluminum, which has much

higher electrical conductivity under magnet conditions than copper. The resulting composite conductor may look something like that shown in cross section in figure V-33(a). A substrate of steel for strength is first coated with superconductor on both sides and then clad with aluminum. The amount of aluminum needed could be very small, as pictured. The size of the same type of composite using copper is shown for comparison in figure V-33(b).

Bonding aluminum to other metals is difficult, but fortunately, a bond may not be necessary. If the aluminum is close enough to the superconductor for good magnetic coupling, induced eddy currents can prevent flux from moving too fast. The rate of heat generation is thus brought under control, and stability is achieved. At present, this appears to be the most promising and efficient stabilization method suitable for use with $Nb_3Sn$. Both experimental and analytical work is in progress here at Lewis and elsewhere on this use of aluminum.

The amount of aluminum needed and, hence, the attainable composite current density are rather difficult to calculate accurately, but the basic thinking goes like this. The flux must be restricted to move slowly enough that the heat generated in the superconductor can be conducted away without too much rise in temperature. Superconductors are such poor heat conductors that only very thin layers or very small diameter wires can be considered. Otherwise, the internal regions of the superconductor cannot be held below the critical temperature. For the layered geometry pictured in figure V-33, the required thickness of normal material varies as the cube of the superconductor thickness. This favors a thin superconductor. On the other hand, for a fixed thickness of substrate, the overall current density drops if the superconductor becomes very thin. Thus, for each substrate thickness, the right choice of superconductor and aluminum thicknesses gives the best current density. Figure V-34 shows the way in which the realizable overall current density depends on the basic substrate thickness. The upper envelope curve is obtained if forces can be neglected. The other curves are for various force-limited conditions where extra steel is needed for strength. If practical considerations allow thin substrates, superconductor layers, and aluminum layers, very good current densities can be achieved because the required amount of aluminum can be very small.

## Advanced Superconductivity Concepts

In this section, some of the research areas in superconductivity that promise to have the greatest effect on magnet and propulsion technology are discussed briefly. Currently, the most extensive and fruitful research area is the development of new alloys and intermetallic compounds that have higher critical fields or

critical temperatures, or both. The materials mentioned herein, such as $Nb_3Sn$ and NbTi, represent valuable products of this research. Because so little is known about the electronic properties of the many, many possible alloys and compounds, it is necessary to try different combinations by guesswork and intuition.

As an example of the effort involved in this area, consider the compound $Nb_3Sn$, which plays an important role in magnet technology. This is a compound of the transition metal niobium with the simple metal tin. The transition temperature for this compound is 18.5 K, still below the boiling point of hydrogen, and the critical field is about 22 teslas. For several years, this was the highest transition temperature known. Research into compounds of niobium with other simple metals has resulted in the recent discovery of the material $Nb_3 (Al_{1-X} Ge_X)$ with a transition temperature of about 20.7 K, a significant increase.

This research effort constitutes an attempt to understand the mechanism of superconductivity in metals and alloys of metals, within the framework of present knowledge about electronic properties of simple metals. The work discussed in the following paragraphs represents a search for a new mechanism for superconductivity, outside the realm of metals.

As a preface to this discussion of new mechanisms in superconductors, let us briefly review the mechanism of superconductivity in metals, at least as it is currently understood. Superconductivity arises from an attractive interaction between conduction electrons in a metal. Figure V-35 shows schematically how this interaction arises. An electron, with a negative charge, moves through the lattice of ion cores, displacing the ion cores from their normal positions. The result is a net positive charge in the region behind the passing electron. Another electron, following in the path of the first, feels a force due to this charge. The energy of this interaction between the electrons, and ultimately, the critical temperature of the superconductor, is determined by the speed with which the lattice can respond to these disturbances. This model for superconductivity is usually referred to as "the electron-phonon interaction."

The exciting new developments in superconductivity stem from attempts to find other mechanisms for an electron-electron interaction. The most interesting and controversial model has been proposed by Little, in the form of an organic superconductor. Figure V-36 shows, with artistic license, a model of a polymer chain with periodic side branches. Little's model for the interaction consists of an electron moving along the "spine" and causing a polarization of the charge in the side branches. In the same manner as in the electron-phonon interaction, this polarization causes a force on another electron moving along the spine. Little estimates that transition temperatures of the order of $10^3$ K might be feasible for a suitable polymer. Thus far, no experimental evidence for an organic superconductor has

been found, although several investigations are in progress.

The final, and most promising, model is the so-called "excitonic superconductor." Figure V-37 shows a portion of the boundary between a metal and a dielectric. An electron initially in the dielectric may be excited and hence move into the metal, leaving a hole behind. This hole acts essentially as a positive charge, attracting an electron in a surface state within the metal and thus creating the same type of attractive interaction as occurred in the other models. The critical temperature for this system is determined by the energy necessary to excite the initial electron, and could correspond to hundreds of degrees. A practical manifestation of this model seems to be a layered structure, composed of alternating sheets of metal and insulator, possibly in the form of a ribbon. Such an excitonic superconductor, having a high transition temperature, would certainly cause a breakthrough in magnet design and other engineering applications.

One word of caution should be noted, however. Very little is known about the properties of electrons in these materials. For example, even if an excitonic superconductor should be discovered, the critical field and critical current characteristics of the material determine its application to technology. So little is known about the superconducting state in these materials that nothing may be said about these critical parameters. In spite of these uncertainties, there are hopes that one or another of these concepts may lead to a revolutionary development in magnet technology.

In summary, the goal of a lightweight, stable, high-field, large-volume electromagnet has not yet been reached. Indeed, the common practice has been to increase the weight and decrease the current density of the superconducting magnet by including a large amount of copper (or other nonsuperconductor) as a stabilizer in parallel with the superconductor. In some respects, this means that the magnet is essentially a cryogenically cooled nonsuperconducting magnet, at least during some phases of its operation.

But there are some promising developments which may reverse this trend. Composites of normal metals and very many fine filaments of the superconductor, twisted and superimposed, are becoming available. Dynamic stabilization with high-purity aluminum will be realized. The future holds (1) a continuing search for high-field, high-current, and high-critical-temperature alloys and compounds; (2) attempts to develop high-critical-temperature organic materials; and (3) attempts to enhance superconducting properties by thin-film, sandwiched conductors.

The most exciting possibilities for new applications of the results of the magnet research and development of the last 10 years are high-field magnets for direct conversion of energy by MHD and thermonuclear power generation; power transmission in underground superconducting or cryogenically cooled lines; and rotating machinery with field coils and/or armatures with superconducting windings.

# BIBLIOGRAPHY

This bibliography comprises publications authored by the members of the NASA Lewis Research Center Staff.


Aron, P. R.; and Ahlgren, G. W.: Critical Surfaces for Commercial $Nb_3Sn$ Ribbon and Nb-25% Zr Wire. Advances in Cryogenic Engineering. Vol. 13. K. D. Timmerhaus, ed., Plenum Press, 1968, pp. 21-29.

Aron, Paul R.; and Chandrasekhar, B. S.: Magnetostriction in Single-Crystal Bismuth. Bull. Am. Phys. Soc., vol. 10, no. 9, Nov. 1965, p. 1201.

Aron, Paul R.; and Chandrasekhar, B. S.: Oscillatory Magnetostriction and Deformation Potentials in Bismuth. Bull. Am. Phys. Soc. vol. 14, no. 3, Mar. 1969, p. 306.

Boom, R. W.; and Laurence, J. C.: Force-Reduced Superconducting Toroidal Magnet Coils. Presented at the NAS-NRC Cryogenic Engineering Conference, Los Angeles, Calif., June 16-18, 1969.

Brown, Gerald V.: The Excitation Spectrum for a Bose Gas with Repulsive and Attractive Interactions. NASA TN D-4838, 1968.

Brown, Gerald V.: High-Field Cryogenic Magnets with Pure Aluminum Conductor. Presented at the Symposium on Engineering Problems of Fusion Research, Los Alamos, N. Mex., Apr. 8-11, 1969.

Brown, G. V.; and Coles, W. D.: High-Field Liquid-Neon-Cooled Electromagnets. Advances in Cryogenic Engineering. Vol. 11. K. D. Timmerhaus, ed., Plenum Press, 1966, pp. 638-642.

Brown, Gerald V.; and Coopersmith, Michael H.: Excitation Spectrum for a Bose Gas with Repulsive Core and Attractive Well. Phys. Rev., vol. 178, no. 1, Feb. 5, 1969, pp. 327-344.

Brown, Gerald V.; and Flax, Lawrence: Superposition Calculation of Thick Solenoid Fields from Semi-Infinite Solenoid Tables. NASA TN D-2494, 1964.

Brown, Gerald V.; and Flax, Lawrence: Superposition of Semi-Infinite Solenoids for Calculating Magnetic Fields of Thick Solenoids. J. Appl. Phys., vol. 35, no. 6, June 1964, pp. 1764-1767.

Brown, Gerald V.; Flax, Lawrence; Itean, Eugene C.; and Laurence, James C.: Axial and Radial Magnetic Fields of Thick, Finite-Length Solenoids. NASA TR-170, 1963.

Callaghan, Edmund E.; and Maslen, Stephen H.: The Magnetic Field of a Finite Solenoid. NASA TN D-465, 1960.

Callaghan, Edmund E.; and Flax, Lawrence: Radial Flux or Field of an Isotropic, Cylindrical Source of Finite Extent. NASA TN D-873, 1961.

Callaghan, Edmund E.: Anisotropic Effects in Helically Wound Superconducting Solenoids. NASA TN D-2083, 1963.

Callaghan, Edmund E.: Potential Advantages of Anisotropic Superconductors in "Force-Free" Solenoids. NASA TN D-2156, 1964.

Callaghan, Edmund E.; and Stoll, James C.: Azimuthal Magnetic Field of a Thick, Finite-Length, Helical Solenoid. NASA TN D-2372, 1964.

Coles, Willard D.; Brown, Gerald V.; Meyn, Erwin H.; and Schrader, E. R.: Pumped Helium Tests of a 51-Centimeter Bore Niobium-Tin Magnet. NASA TN D-5158, 1969.

Coles, W. D.; Laurence, J. C.; and Brown, G. V.: Cryogenic and Superconducting Magnet Research at the NASA Lewis Research Center. Presented at AIChE Sixty-Second Annual Meeting, Washington, D.C., Nov. 16-20, 1969.

Coles, W. D.; Schrader, E. R.; and Thompson, P. A.: A 14-Tesla 15-Centimeter-Bore Superconductive Magnet. Advances in Cryogenic Engineering. Vol. 13. K. D. Timmerhaus, ed., Plenum Press, 1968, pp. 142-149.

Fair, Gale: Theory of Galvanomagnetic Effects in Metals. Ph.D. Thesis, Case Western Reserve Univ., 1969.

Fair, Gale; and Taylor, P. L.: Exact Semiclassical Theory for Galvanomagnetic Effects in Metals. NASA TN D-4166, 1966.

Fakan, John C.; and Schrader, Edward R.: Experimental Evidence of Degradation Effects in Short Samples of Hard Superconductors. NASA TN D-2345, 1964.

Flax, L.: Monotonic Magnetostriction for Diamagnetic Materials. Phys. Letters, vol. 19, no. 6, Dec. 1, 1965, pp. 469-471.

Flax, Lawrence: The Theory of the Anisotropic Heisenberg Ferromagnet. Ph.D. Thesis, Colorado State Univ., 1969.

Flax, Lawrence; and Callaghan, Edmund E.: Magnetic Field from a Finite Thin Cone by Use of Legendre Polynomials. NASA TN D-2400, 1964.

Flax, Lawrence; and Raich, John C.: Spin-Wave Approximation for an Anisotropic Heisenberg Model. Bull. Am. Phys. Soc., vol. 13, no. 6, June 1968, p. 903.

Flax, Lawrence; and Raich, John C.: Random Phase Approximation for the Anisotropic Heisenberg Ferromagnet. NASA TN D-5286, 1969.

Flood, Dennis J.: Magnetothermal Oscillations in Pressure-Annealed, Pyrolytic Graphite. NASA TN D-5488, 1969.

Flood, D. J.: Molecular Vibration Spectra from Field Emission Energy Distribution. Phys. Letters, vol. 29A, no. 2, Apr. 7, 1969, pp. 100-101.

Flood, D. J.: Magnetothermal Oscillations in Pressure-Annealed Pyrolytic Graphite. Phys. Letters, vol. 30A, no. 3, Oct. 6, 1969, pp. 178-179.

Hudson, Wayne R.: Effect of Tensile Stress on Current-Carrying Capacity of Commercial Superconductors. NASA TN D-3745, 1966.

Hudson, Wayne R.; Copper Magnetoresistance Devices as Magnetometers. NASA TN D-3536, 1966.

Hudson, W. R.: Negative Magnetoresistance in Carbon Resistance Thermometers. Rev. Sci. Instr., vol. 39, no. 2, Feb. 1968, pp. 253-254.

Hudson, Wayne R.; and Jirberg, Russell J.: Nonlinear Flux Flow in Single Crystal Niobium. NASA TN D-5198, 1969.

Hudson, W. R.; Jirberg, R. J.; and Simmons, J. H.: Flux Pinning in Superconducting Niobium Thin Films. Phys. Letters, vol. 21, no. 5, June 15, 1966, pp. 493-494.

Jirberg, Russell J.: Superconductive Dust Cores for Inductive Elements. NASA TN D-5137, 1969.

Laurence, J. C.: High-Field Magnets and Magnetic Research at NASA Lewis Research Center. Presented at the Inst. Phys. and the Phys. Soc., Oxford Univ., London, England, 1963.

Laurence, J. C.: Superconductive Magnets at Lewis Research Centre of NASA. Cryogenic Engineering: Present Status and Future Development. Heywood-Temple Ind. Publ., Ltd., 1968, pp. 94-98.

Laurence, James C.; and Coles, Willard D.: Design, Construction, and Peformance of Cryogenically Cooled and Superconducting Electromagnets. Presented at the International Symposium on Magnet Technology, Stanford, Calif., Sept. 8-10, 1965.

Laurence, J. C.; and Coles, W. D.: A Superconducting Magnetic Bottle. Advances in Cryogenic Engineering. Vol. 11. K. D. Timmerhaus, ed., Plenum Press, 1966, pp. 643-651.

Laurence, J. C.; Coles, W. D.; Brown, G. V.; and Meyn, E. H.: Performance Tests of 51-cm Bore Superconductive Magnets for a Magnetic Mirror Apparatus. Presented at Cryogenic Engineering Conference, Los Angeles, Calif., June 16-18, 1969.

Laurence, J. C.; Meyn, E. H.; and Jirberg, R. J.: Variable-Voltage, Direct-Current Power Supplies for Energizing Cryogenically Cooled and Superconductive Electromagnets. Presented at the Symposium on Engineering Problems of Fusion Research, Los Alamos, N. Mex., Apr. 8-11, 1969.

Loomis, John S.; and Hudson, Wayne R.: Low-Temperature Resistance in Minimum and Magnetoresistance for Dilute Alloys of Iron in Copper. NASA TN D-4626, 1968.

Lucas, E. J.; de Winter, T.; Laurence, J.; and Coles, W.: The Design of an 88-kG, 20-in.-Bore Superconducting Magnet System. J. Appl. Phys., vol. 39, no. 6, May 1968, p. 2641.

Papell, S. Stephen; and Faber, Otto C., Jr.: On the Influence of Nonuniform Magnetic Fields on Ferromagnetic Colloidal Sols. NASA TN D-4676, 1968.

Sass, Andrew R.: Analysis of a Distributed Superconductive Energy Converter. IEEE Trans. on Aerospace, vol. AS-2, Apr. 1964, pp. 822-825.

Sass, A. R.: Image Properties of a Superconducting Ground Plane. J. Appl. Phys., vol. 35, no. 3, pt. 1, Mar. 1964, pp. 516-521.

Sass, A. R.; and Stoll, James C.: Magnetic Field of a Finite Helical Solenoid. NASA TN D-1993, 1963.

Sarafi, Zoltan W.: Ultrasonic Attenuation in Superconducting Tantalum. NASA TN D-4806, 1968.

Sarafi, Zoltan W.; and Meyn, Erwin H.: Effect of Mechanical Vibrations on the Performance of Superconducting Magnets. NASA TN D-3954, 1967.

Schroeder, P. A.; Wolf, R.; and Woollam, J. A.: Thermopowers and Resistivities of Silver-Palladium and Copper-Nickel Alloys. Phys. Rev., vol. 138, no. 1A, Apr. 5, 1965, pp. 105-111.

Stekly, Z. J. J.; Lucas, E. J.; de Winter, T.; Strauss, B.; DiSalvo, F.; Laurence, J. C.; and Coles, W. D.: Results of Tests on Models for an 88-kG, 51-cm-Bore-Diameter Solenoid. J. Appl. Phys., vol. 39, no. 6, May 1968, pp. 2641-2646.

Woollam, J. A.: A Simple A.C. Technique for Galvanomagnetic and Shubnikov-de Haas Measurements. Cryogenics, vol. 8, Oct. 1968, pp. 312-313.

Woollam, John A.: The Nernst-Ettingshausen Effect: Predictions and Experimental Results for Metallic Tin at Low Temperatures. Bull. Am. Phys. Soc., vol. 13, no. 12, Dec. 1968, p. 1645.

Woollam, John A.: Galvanomagnetic and Thermomagnetic Effects in White Tin in Fields to 3.3 Tesla and at Temperatures between $1.2^{o}$ and $4.2^{o}$ K. NASA TN D-5227, 1969.

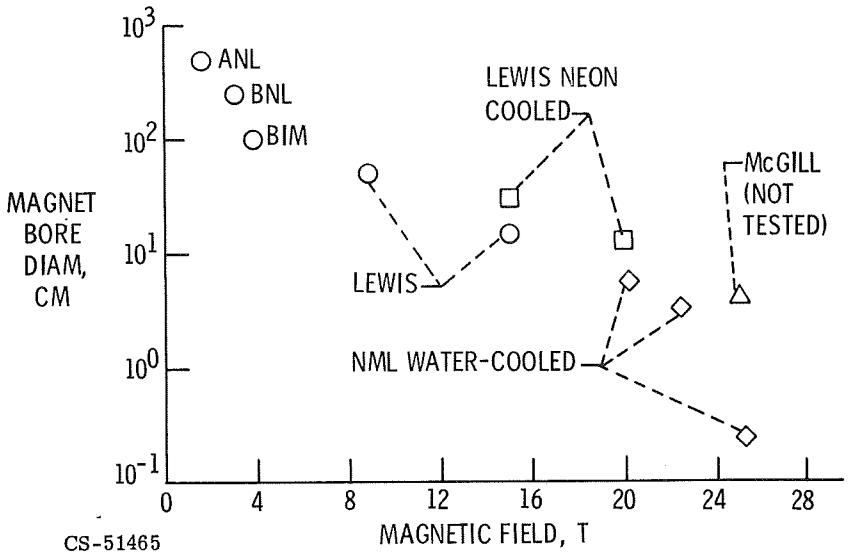


Figure V-1. - Magnet comparison.

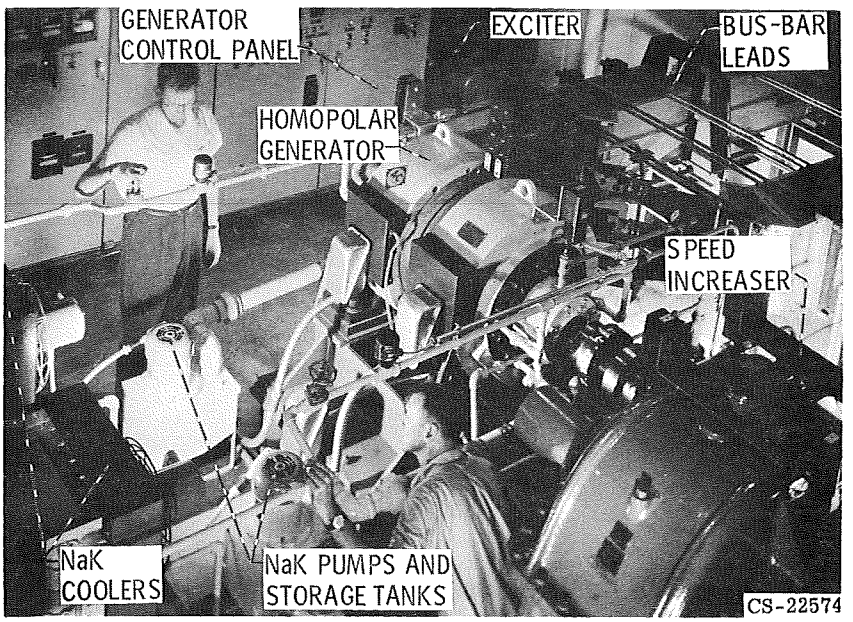


Figure V-2. - Homopolar generator installation. Drive motor off picture to right.

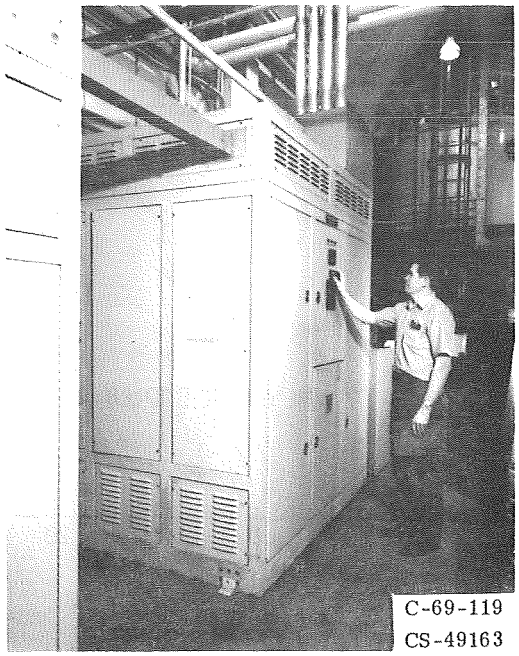

C-69-119
CS-49163

Figure V-3. - Transformer-rectifier power supply.

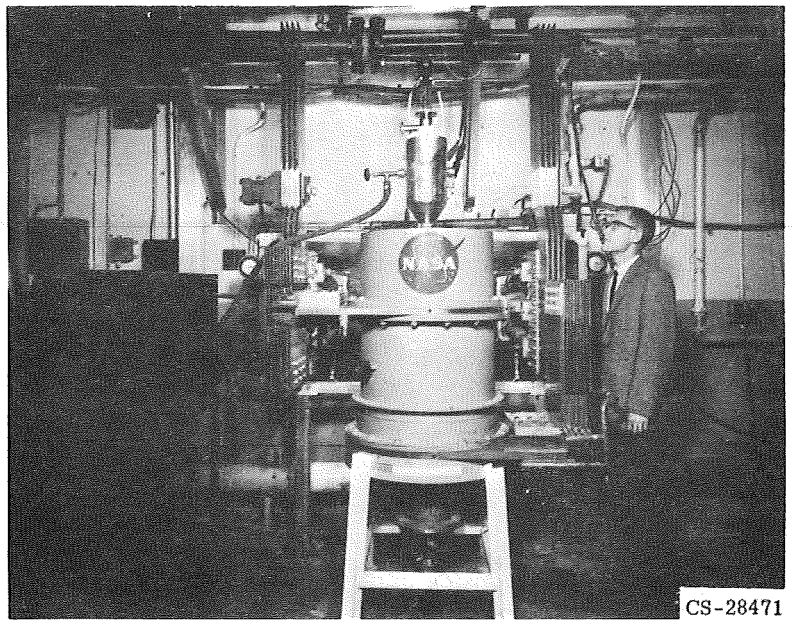

CS-28471

Figure V-4. - Water-cooled 8.8-tesla magnet.

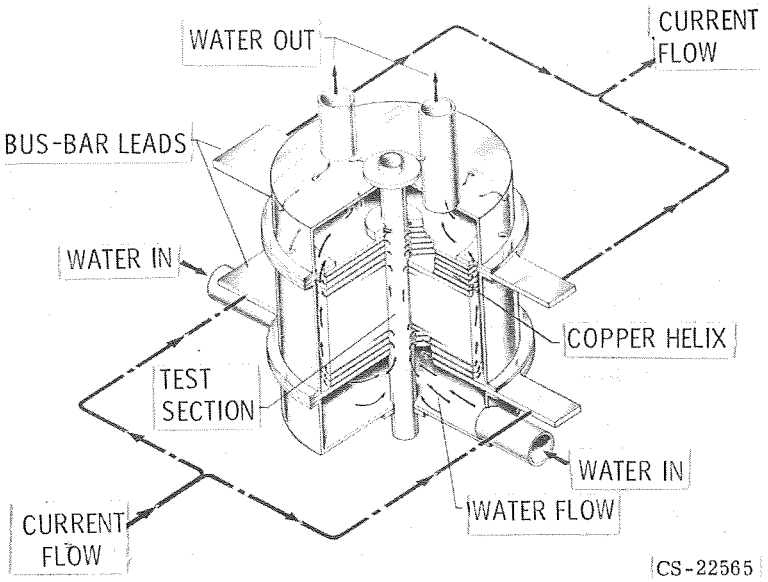


Figure V-5. - Cutaway view of water-cooled magnet.

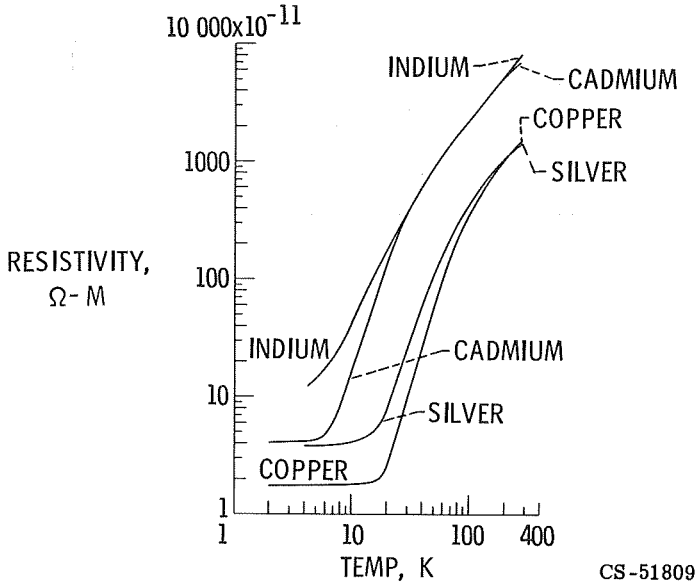


Figure V-6. - Resistivity-temperature relation for some pure metals.

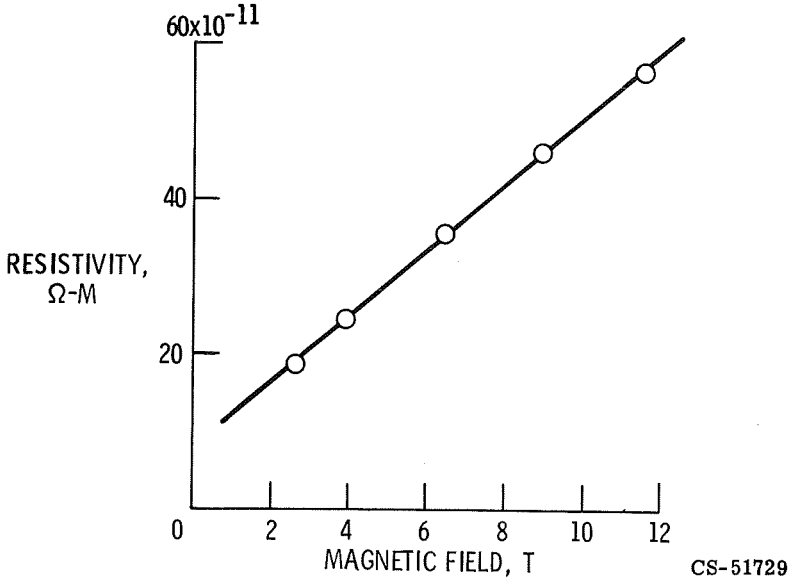


Figure V-7. - High-field magnetoresistivity of copper at 4.2 K.

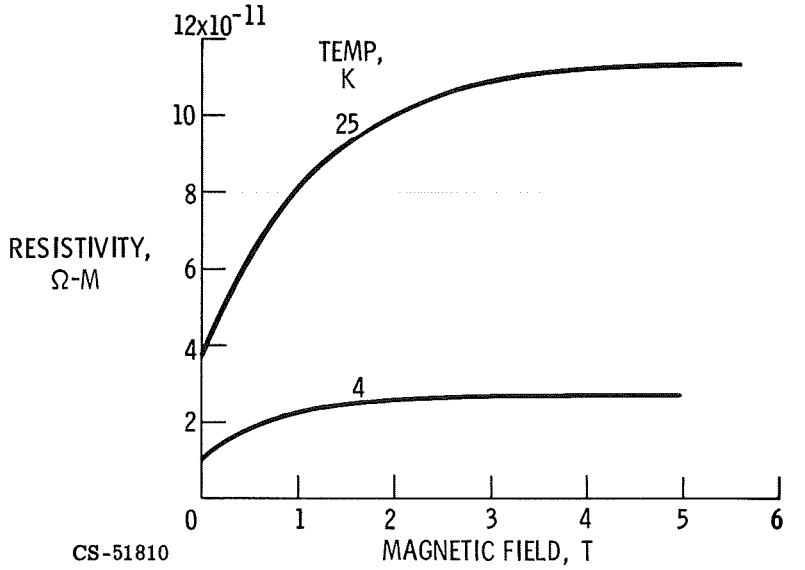


Figure V-8. - Magnetoresistivity of aluminum at two temperatures.

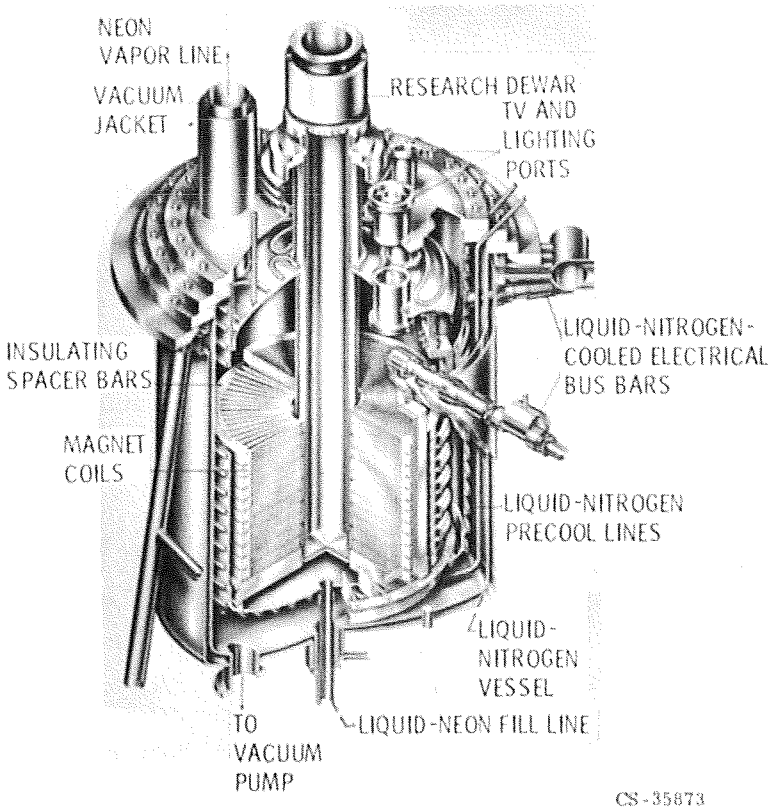


Figure V-9. - Thirty-centimeter coils in magnet vessel.

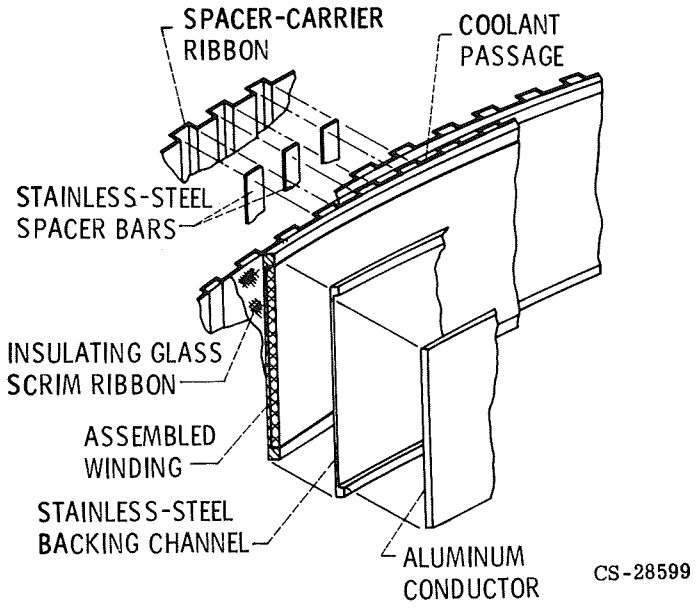


Figure V-10. - Details of coil construction.

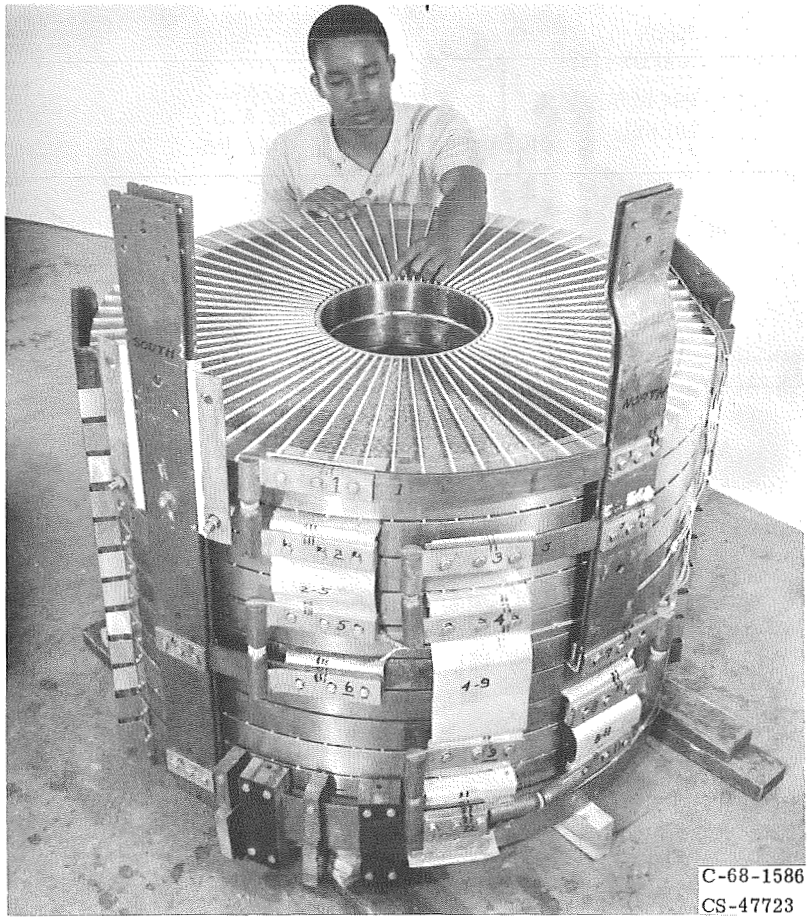


Figure V-11. - Twelve 30-centimeter-bore, liquid-neon-cooled aluminum magnet coils.

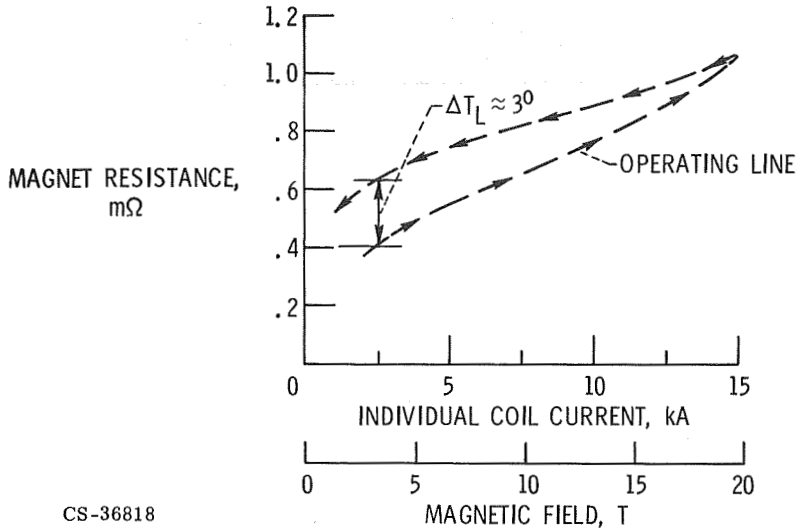


Figure V-12. - Resistance of eight coils in series-parallel for 11-centimeter-bore, 20-tesla magnet.

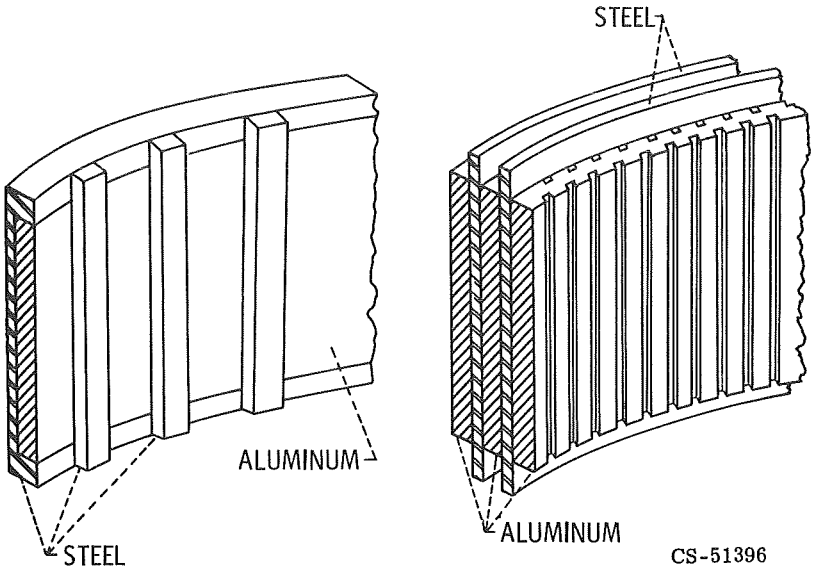


(a) Existing coil, nucleate boiling design.

(b) Proposed, nonboiling forced-convection design.

Figure V-13. - Comparison of conductors for existing cryomagnet and proposed 30-tesla design.

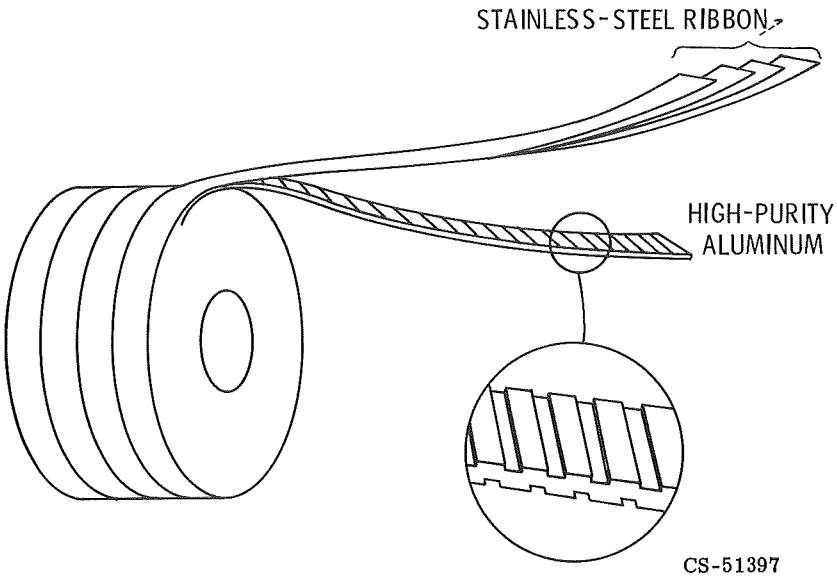


Figure V-14. - Third-generation-cryomagnet concept.

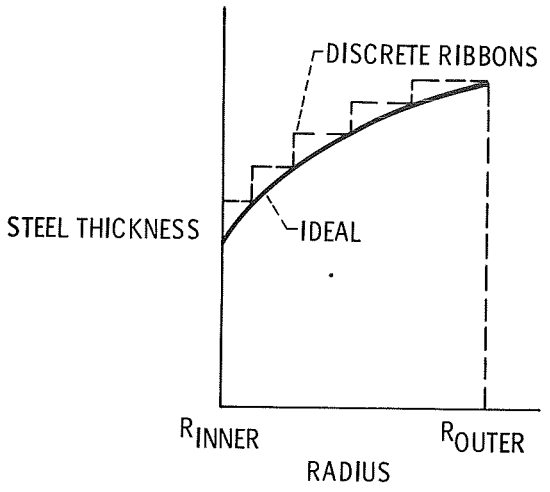


Figure V-15. - Variable structure thickness of 30-tesla coil.

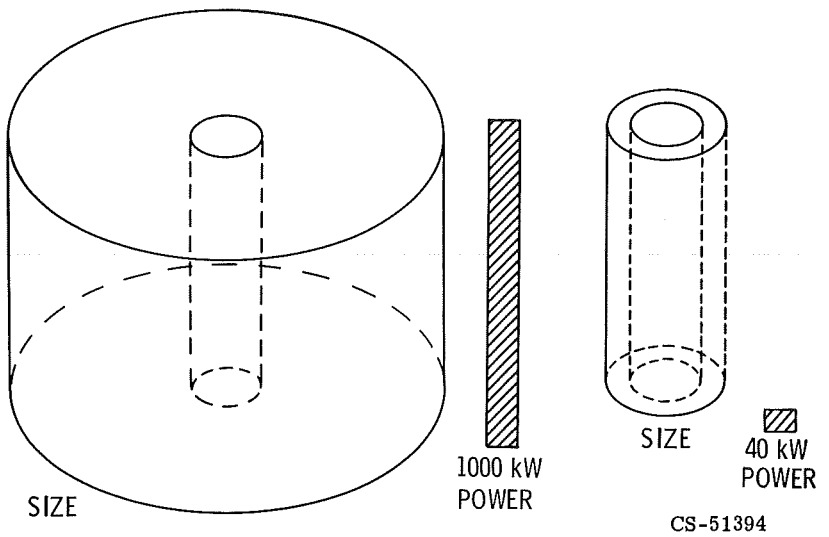


(a) Existing first-generation magnet.

(b) Third-generation concept.

Figure V-16. - Comparison of winding size and power requirement of existing 20-tesla magnet and third-generation concept.

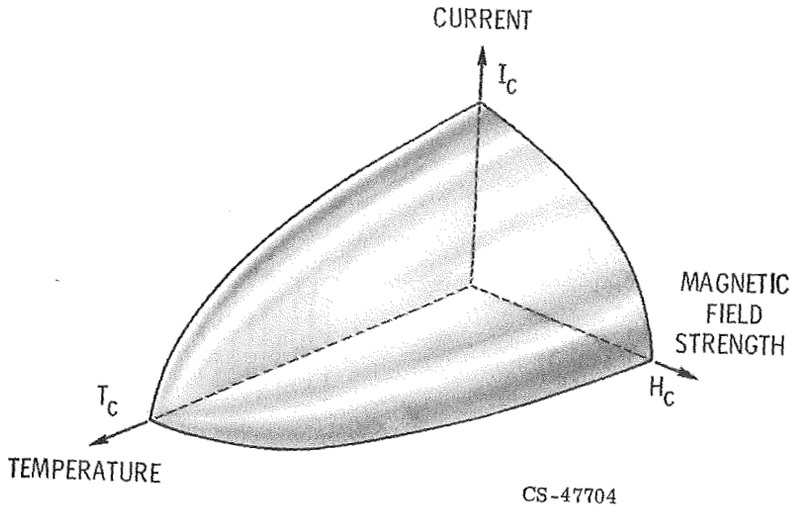


Figure V-17. - Critical surface of superconductor.

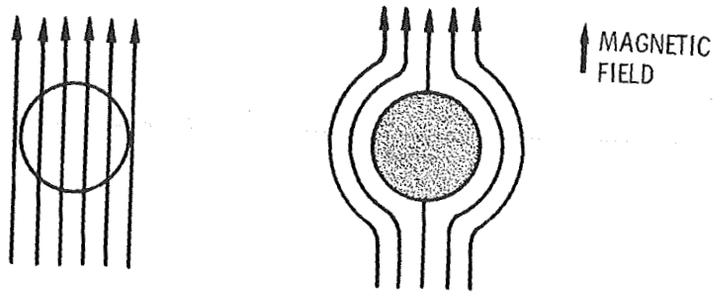


Figure V-18. - Meissner effect (magnetic field exclusion) in type I superconductor, compared with magnetic field in normal conductor.

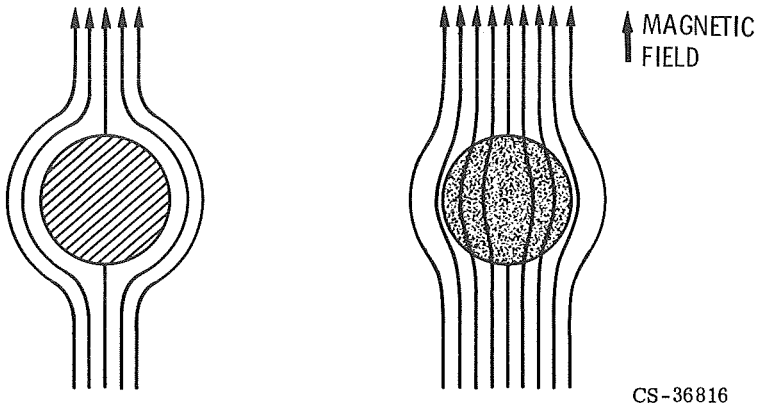


(a) At low fields (Meissner effect).

(b) At high fields.

Figure V-19. - Magnetic field behavior of high-current, high-field superconductors (type II).

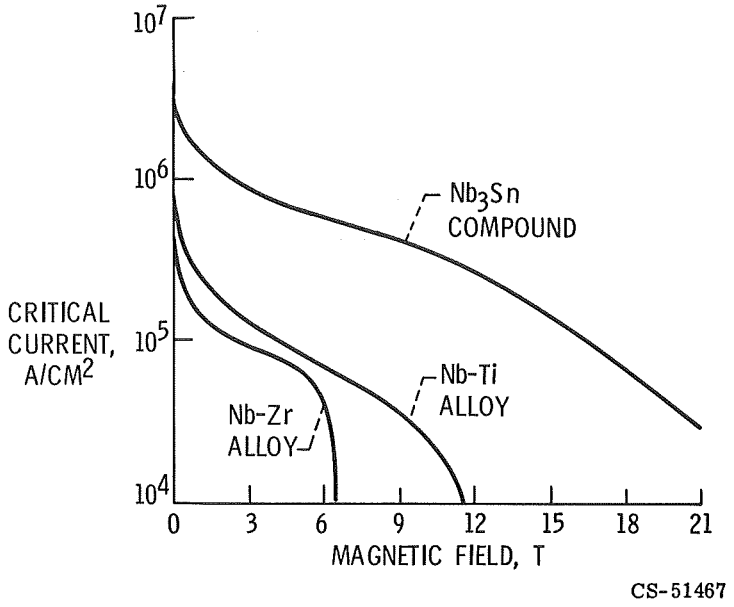


Figure V-20. - Critical current of three type II superconductors as function of magnetic field.

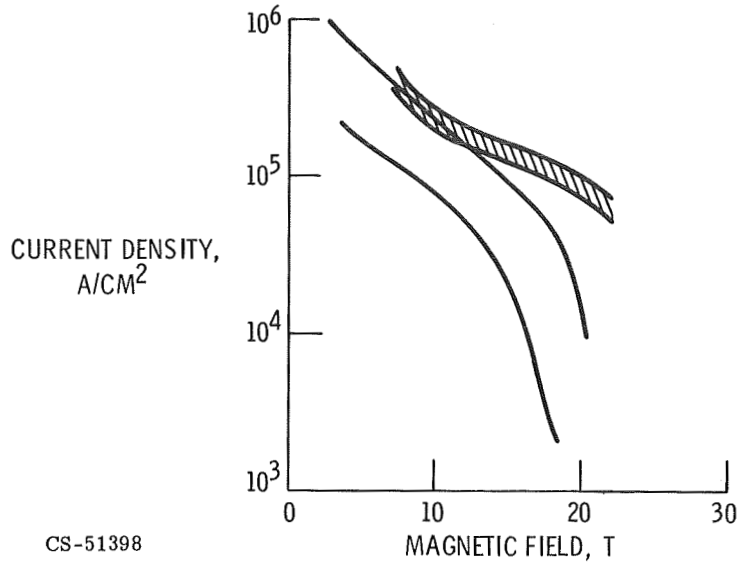


Figure V-21. - Critical current densities for $Nb_3Sn$ produced by three different methods.

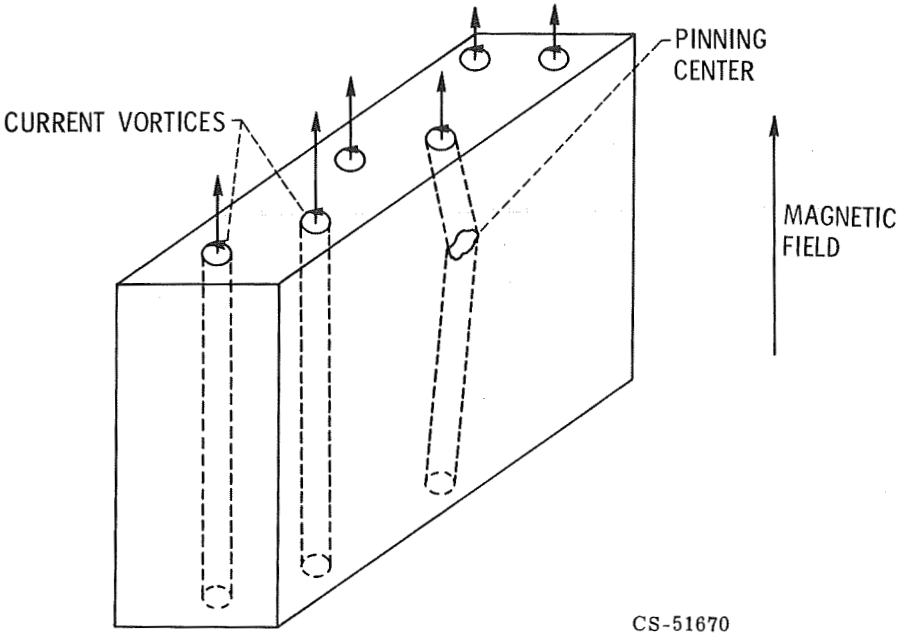


Figure V-22. - Flux lines in type II superconductors.

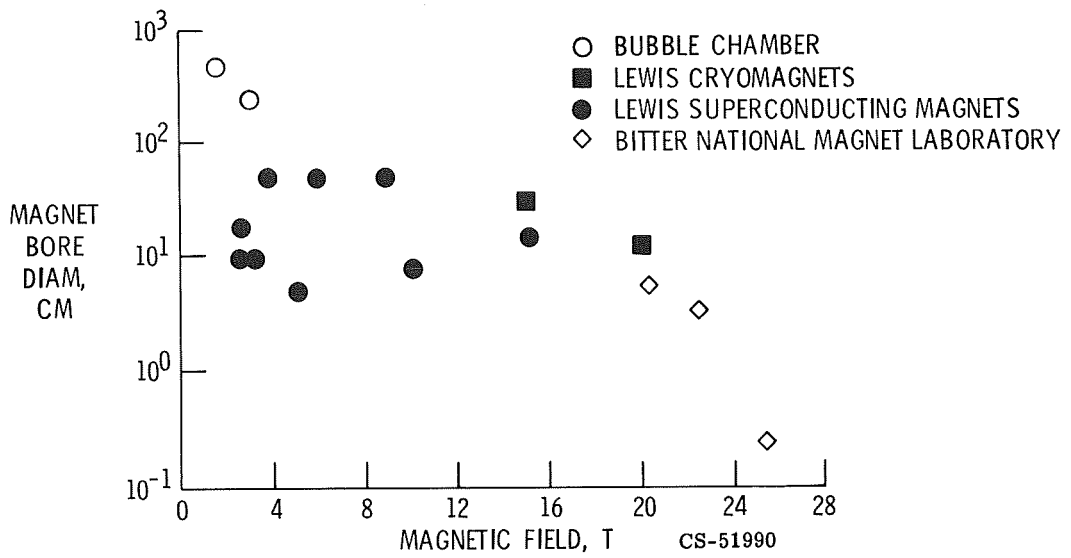


Figure V-23. - Magnet comparison.

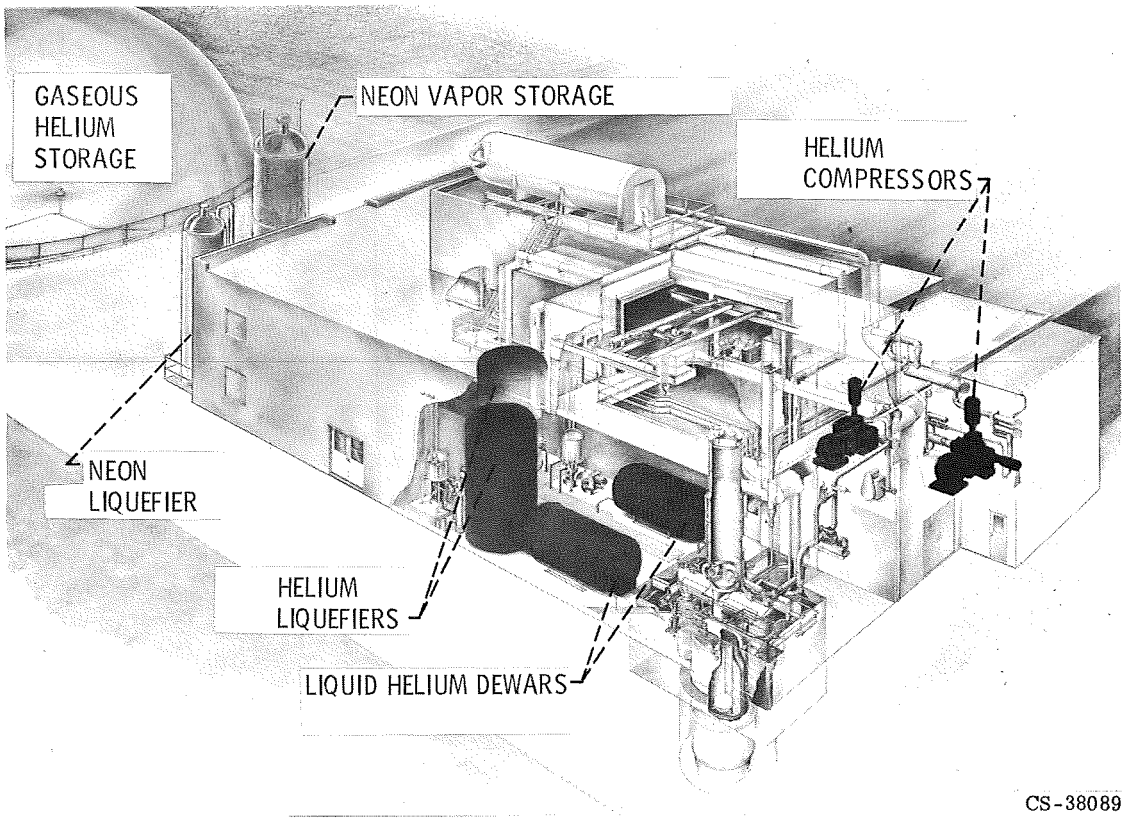


Figure V-24. - Helium reliquefaction system.

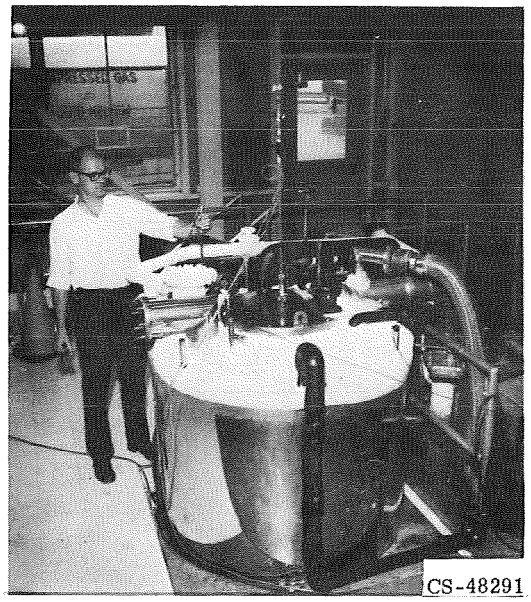


**Figure V-25. - Upper section of largest magnet cryostat; inside diameter, 96.5 centimeters; height, 4.2 meters.**

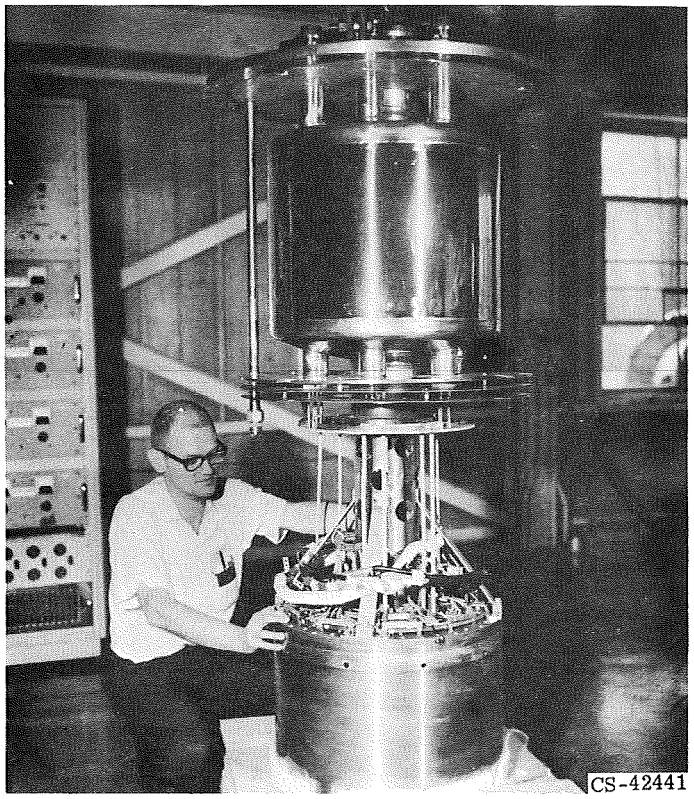


Figure V-26. - Fifteen-centimeter-bore, 15-tesla magnet and Dewar lid.


Figure V-27. - Components of magnet.

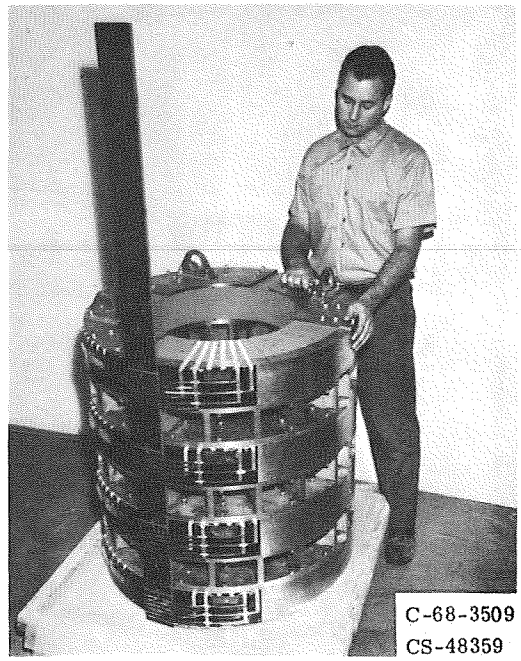


Figure V-28. - Four 51-centimeter-bore superconducting magnets.

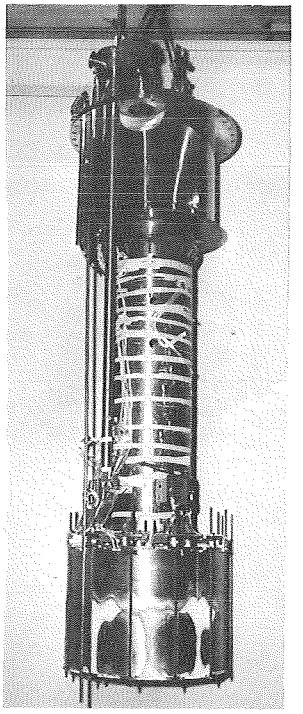


C-69-315
CS-50312

Figure V-29. - Stabilized, 51-centimeter-bore superconducting magnets mounted for testing.

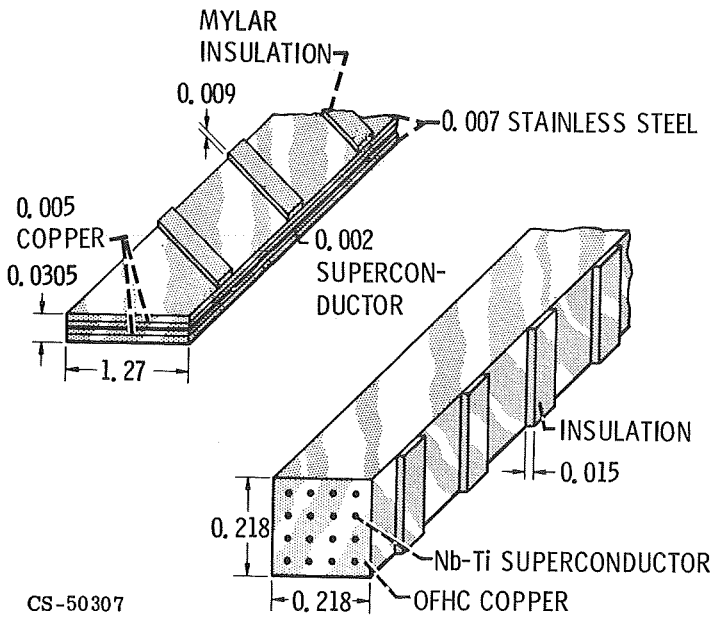


(a) $Nb_3Sn$ conductor (stabilized).

(b) Nb-Ti conductor (stabilized).

Figure V-30. - Superconductors and insulation. (Dimensions are in cm.)

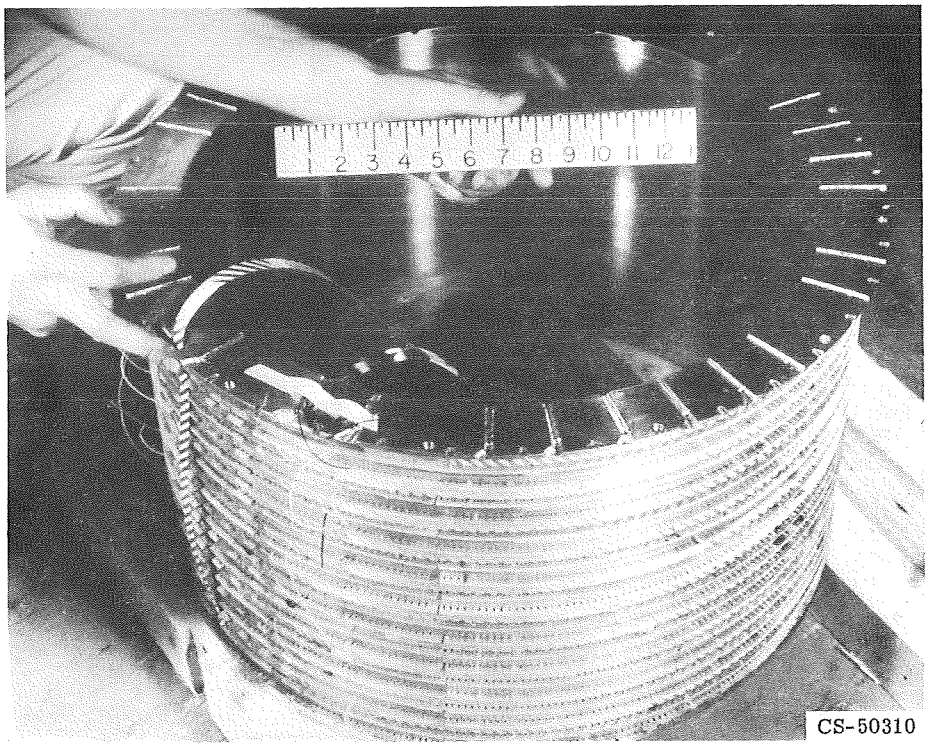


Figure V-31. - Inner module wound with $Nb_3Sn$ tape.

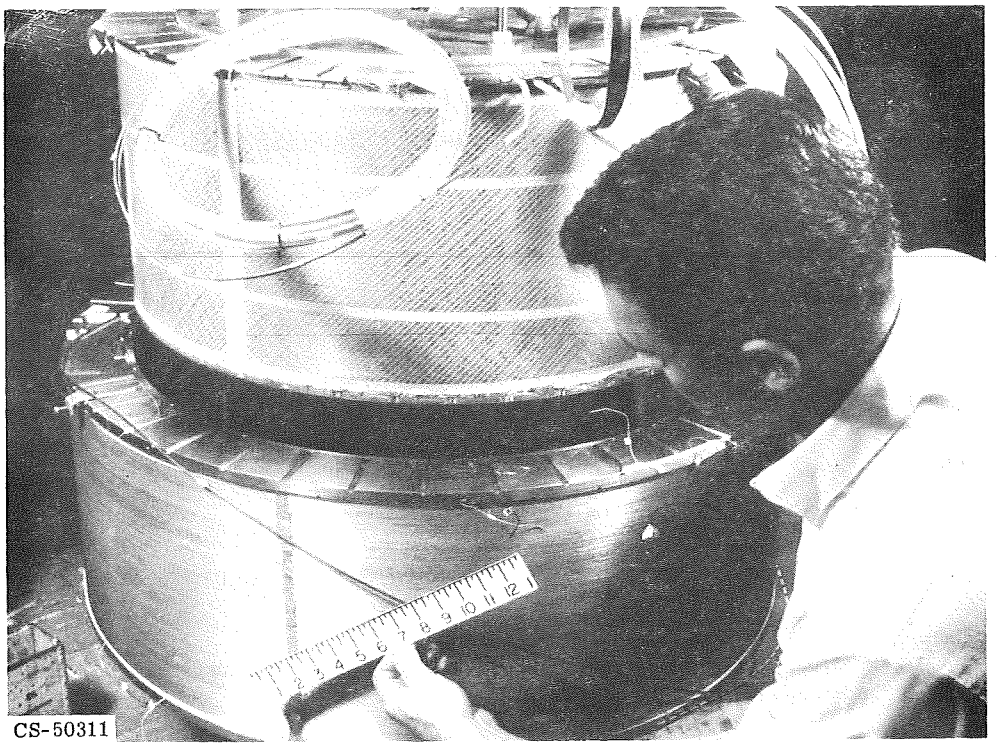


Figure V-32. - Outer and middle modules.

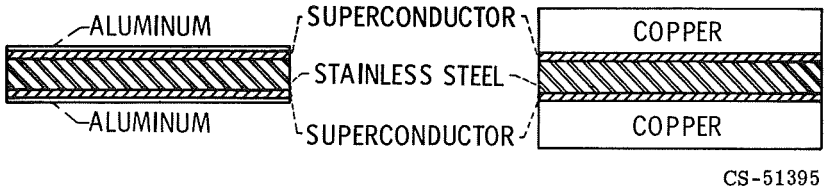


(a) Aluminum-clad conductor. (b) Copper-clad conductor.

Figure V-33. - Comparison of stabilized composites.

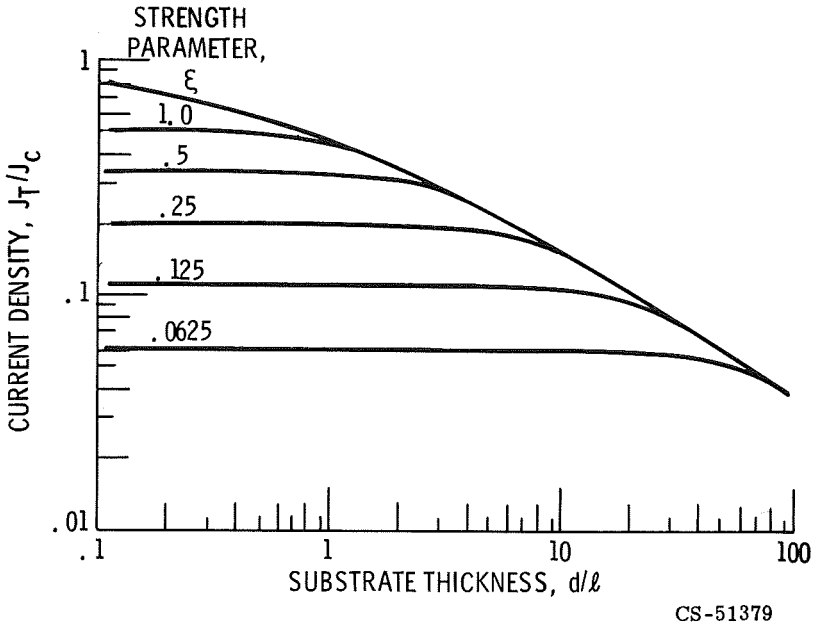


Figure V-34. - Current density as function of substrate thickness.

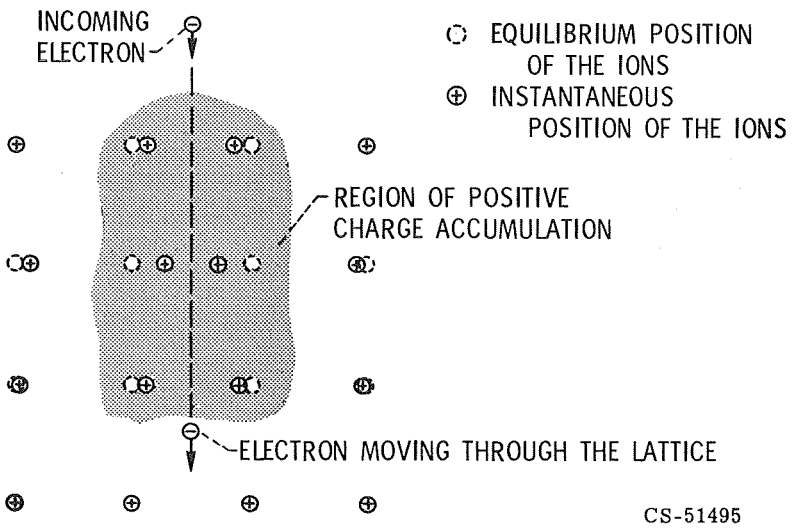


Figure V-35. - Electron-phonon interaction.

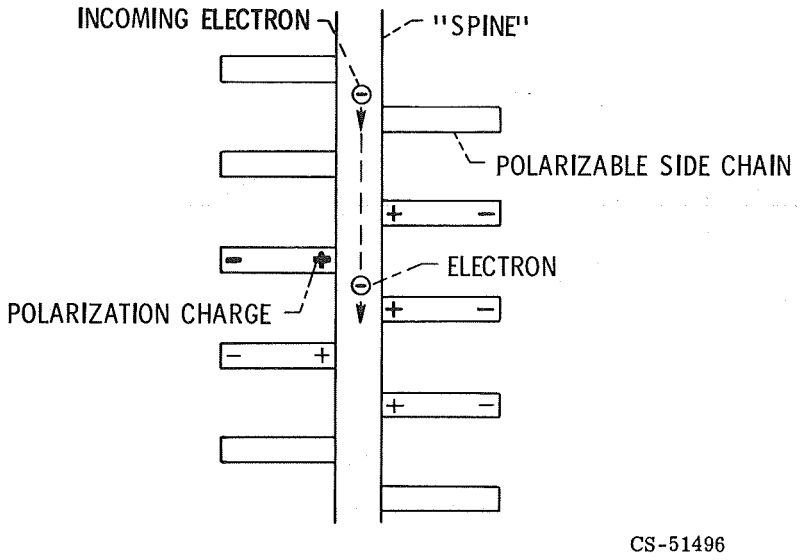


Figure V-36. - Superconductive organic molecule.

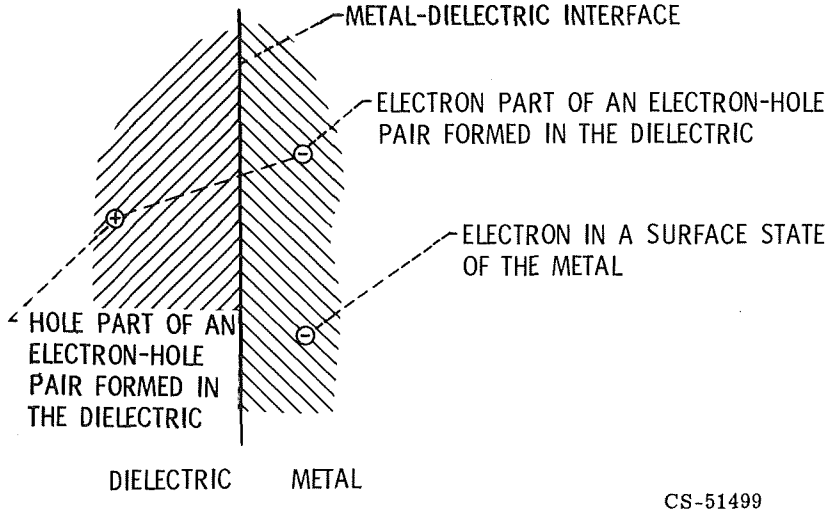


Figure V-37. - Excitonic superconductor.

# VI. SOLID-STATE PHYSICS IN INTENSE MAGNETIC FIELDS

John A. Woollam

The Lewis Research Center has developed a number of very large magnets. These magnets are large, not only in available volume for experiments but also in magnetic field strength. This makes these magnets unique for solid-state physics experiments. Certain experiments, such as thermomagnetic effects, are easier to perform in large working volumes. Other experiments, such as extreme quantum limit studies and spin-orbit interaction studies, are possible only in high magnetic fields. Many of the solid-state experiments which are performed are devoted to understanding the physical nature of solids in fields and to searching for fundamentally new phenomena. Yet some of the experiments have practical purposes, such as determining how transistors perform in fields and how thermometers are affected by fields. This paper describes some of the physics experiments and some of the results which have engineering application. These include transport experiments, transistors in magnetic fields, magnetocaloric experiments, and a technique for plotting magnetic field lines in plasma containment magnets.

## THE MAGNETS

Figure VI-1 shows a 4.0-tesla magnet (ref. 1) which produces a horizontal field with vertical probe access. It consists of superconducting wire wound on a 4-inch-diameter iron core. This produces a field directed out of the figure. The outside dimensions are 1 by 1 by 1 foot. The gap between pole faces is 1 inch. The dewar and magnet are precooled to 78 K by the surrounding liquid nitrogen dewar. Iron specific heat below 78 K is low enough that very little liquid helium is evaporated in cooling the magnet to 4 K and covering it with liquid. The solid to be studied is attached to a long probe and inserted from above. The magnet and sample are then at bath temperature which can be lowered from 4.2 to 1.2 K by pumping on the helium with a large vacuum pump. The sample can be rotated from above, changing the angle between the field and the crystal axis by a motor attached to the drive gear. Angles are recorded by an infinite-resolution, high-linearity potentiometer attached to the drive gear, and field strengths are measured by integrating the

voltage induced in a coil placed near the center of the field. This method of measuring field strength is accurate and independent of bath temperature, whereas, a magnetoresistor calibration depends on bath temperature. Integrator output is calibrated against nuclear magnetic proton resonances (NMR). Integrator drift is the biggest source of error for this method. The magnet takes 100 liquid liters of helium for about 10 hours of running at 4 K or about 6 hours at 1.2 K. The major advantages of this magnet for solid-state research are threefold. (1) The transverse field permits changing the angle between the field and the sample by rotating the probe from above. (In an axial access solenoid a gearing mechanism must be used.) (2) Helium consumption is low so that little time is spent transferring. (3) At low fields the iron core provides a highly homogeneous field. The superconducting coils provide a maximum field of about twice the field of a conventional electromagnet.

Figure VI-2 shows a 10.5-tesla superconducting solenoid. It has an insert dewar and sample probe as shown. The field is vertical and parallel to the access holes, so any rotation of the sample is done with gearing. Helium at 4.2 K covers the magnet, and an insert dewar pumpable to 1 K is large enough to take a 2-inch-diameter probe. This large dimension, plus high maximum field, gives the magnet advantages over the 4-tesla transverse magnet just described. The field strength in the 10.5-tesla magnet is measured with a copper magnetoresistor calibrated against NMR resonances at 4 K. Major disadvantages of this magnet are threefold. (1) After the magnet has been driven to 10 tesla, a field of about 0.4 tesla remains trapped with zero magnet current. (2) Because shorting strips are used for stabilization, the magnet sweeps at a maximum rate of 10 tesla per half hour. (3) At this fast sweep rate, helium must be retransferred every 3 to 4 hours.

The third magnet system, shown in figure VI-3, is a 20-tesla neon-cooled cryomagnet (ref. 1). The most obvious advantage of this magnet is the high magnetic field it produces. The 20-tesla system is nearly vibration free since cooling is by neon evaporation. The 2-inch-diameter working volume allows for a large experiment. Temperatures down to 1.3 K are possible. However, the insert dewar is long and narrow, so pumping to 1.3 K takes several hours. There are several other advantages of this magnet over the two described earlier. Rapid sweep rates are possible, which permits getting much information from the experiment in a short time. The field direction is easily reversed, and exact zero fields are available because remnant magnetizations are not present, as they sometimes are in superconducting solenoids. The field is highly homogeneous over large volumes. The major disadvantage of this magnet is that at slow sweep rates, only one run per day to maximum field is possible.

# EXPERIMENTS INVOLVING TRANSPORT OF HEAT AND ELECTRICAL CURRENTS

Transport measurements provide a check on theoretical assumptions about the nature of solids and thus promote our understanding of these materials. They also provide a method of studying electron collisions. Coefficients such as the Hall effect are measured frequently to characterize the solid for its use in devices such as solid-state electronic elements. Figure VI-4 shows how a few of these coefficients are measured (ref. 2). On the left voltages $V_1$, $V_2$, and $V_3$ are the galvanomagnetic voltages developed when a current flows into the sample (where $V_1$ is the Hall voltage, $V_2$ is the transverse even voltage, and $V_3$ is the magnetoresistance voltage, all with a horizontal field, as shown). The measurement of thermomagnetic effects is described on the right side of figure VI-4. Heat flow is provided by a heater shown at the bottom of the sample. At the other end a heat sink is at the bath temperature. Because of the heat flow, voltages are produced in the sample. For constant heat currents, coefficient $V_1$ is proportional to the adiabatic Nernst-Ettingshausen coefficient, $V_2$ to the adiabatic thermal transverse even coefficient, and $V_3$ to the adiabatic thermoelectric coefficient, again, for the horizontal field, as shown.

As discussed earlier, experiments done in a superconducting solenoid with an axial field must have a gearing mechanism (fig. VI-5) in order to rotate the sample relative to the direction of the field (ref. 3). Two drive rods (fig. VI-5) are driven from above with synchronous motors. If the drive rods rotate in opposite directions, the apparatus tilts the sample, but does not rotate it about its cylinder axis. If the drive rods turn in the same direction, the sample will not tilt, but will rotate about its cylinder axis. This apparatus thus provides a rotation drive with two independent degrees of rotational freedom. This permits measuring transport coefficients in a solenoid for any angle between the field and the sample. Typical data runs consist of continuously monitoring the transport coefficient against field at a fixed angle, or against angle at a fixed field. The parts of the probes which move in fields are made of poor conducting materials to reduce eddy currents.

An example of a rotation at a fixed field of 10 tesla is shown in figure VI-6 for a crystal of tin at 4.2 K (ref. 4). As can be seen, the electrical resistivity is highly anisotropic with respect to the angle between the crystal axis and field direction. At a symmetry direction which is at an angle marked zero in the figure, the resistivity in a field of 10 teslas drops to nearly the zero field value. At $10^{\circ}$ on either side of this minimum, the resistivity is approximately $10^5$ times as large as the zero field resistivity. The half width of this particular notch is $4^{\circ}$. For

comparison, the output of a Hall probe is shown, and, as is well known, the half width of the output of a Hall probe is $120^{\circ}$. This high anisotropy of the resistance could be used as a very sensitive device for plotting the direction and magnitude of the magnetic field in magnetic bottles used for plasma confinement. The angle of the minimum in the resistivity gives the direction, and the value of the resistance just outside the minimum gives the magnitude of the field. This could be used to plot point by point the field and its direction throughout the volume of the magnet. Samples with all dimensions less than 1/8 inch could be used.

## Further Results in Tin

Results of some thermomagnetic experiments in tin are shown in figure VI-7 (refs. 2 and 4). The sample is in a field of 3.3 teslas and at a temperature of 1.2 K. As can be seen, the thermal transverse even coefficient is very small and is within experimental error of being zero for all fields and all angles. However, the Nernst-Ettingshausen coefficient is very large and highly anisotropic with respect to the angle between the field and the crystalline axes. The field dependence of this coefficient has been studied, and, for example, at an angle of $-60^{\circ}$ (as shown in the fig. VI-7), the Nernst-Ettingshausen coefficient has both cubic and quadratic dependencies on field. This large field dependence demonstrates the importance of this coefficient in possible thermoelectric power devices.

One of the most exciting discoveries in tin was large oscillations in the thermoelectric voltage as a function of field strength (ref. 5). Figure VI-8 shows the thermoelectric power as a function of field from 1.4 to 2 teslas for a sample of tin at 1.2 K. The thermopower is oscillatory in field, and the oscillations grow in amplitude with field strength. Each peak was assigned an integer, and the value of the field was measured at each peak. Figure VI-9 shows that plotting these integers as a function of the reciprocal of the magnetic field corresponding to each integer results in a straight line. These oscillations are periodic in inverse field, and they result from a quantization of electron orbits in momentum space. A strong magnetic field causes the charged electrons to spiral in a circular motion in a plane perpendicular to the direction of the field. The radius of these circles, or the area encompassed by these paths must have quantized values. This is shown by the following equation:

$$A_N = \frac{2\pi eH}{ch} (N + \gamma) \qquad (1)$$

where $A_N$ is the area in momentum space for an electron trajectory perpendicular to the magnetic field direction. The area $A_N$ depends linearly on field strength H, and for a fixed field there are N quantized areas. The quantization is only in the plane perpendicular to the direction of the magnetic field. Parallel to the magnetic field there is no quantization. Thus, the equation showing the quantization for $A_N$, results in a series of concentric cylinders. If the thermopower is calculated knowing that the areas in momentum space must be quantized when high magnetic fields are present, the following expression for the thermopower S results (ref. 6):

$$S \propto \cos\left(\frac{2\pi F}{H} - \frac{\pi}{4}\right) \tag{2}$$

The thermopower with a frequency of F is oscillatory as a cosine function and periodic in 1/H. The frequency F is proportional to A, the extremeal cross sectional area of the Fermi surface. Figure VI-10 shows the Fermi surface for a case of free electrons. For free electrons, the Fermi surface is a sphere. The cylinders which were described are inside the Fermi surface and are parallel to the direction of the magnetic field (ref. 7). The radius or cross sectional areas of the cylinders are proportional to field strength. Thus, as the field increases, the cylinders radii increase also. As the outermost cylinder passes through the Fermi energy, the electrons on it redistribute onto other cylinders. Since thermopower, as well as other transport coefficients, depend on the density of electron states at the Fermi surface, this redistribution of electrons on the outer cylinder, as it passes through the Fermi energy, causes the oscillations which are observed. In real metals, such as tin, the Fermi surface is not a simple sphere; it can be broken up into many different parts and can be very complicated. This can cause superimposed oscillations, all periodic in 1/H, but having different frequency values.

Figure VI-11 shows an example of two heating frequencies in tin at 1.2 K. The magnetization of this sample is plotted as a function of the strength of the magnetic field. Oscillations in the magnetization are the deHaas-vanAlphen effect. Tin has a large number of deHaas-vanAlphen frequencies, all dependent on the angle between the field and the crystalline axes, as shown in figure VI-12 (ref. 8). Here, the deHaas-vanAlphen frequencies are plotted as the function of angle between the field and the crystal axes. For the field along the [001] axis, for example, there are 10 superimposed frequencies. These frequencies can be accurately measured (with an error of 0.1 percent or less). This essentially gives the energy band structure at the Fermi energy. Energy bands, of course, occur at all energies,

not just the Fermi energy. But these measurements give an accurate method of determining the band structure at particular points. This allows the band structure theorist to match his calculation to the highly accurate experimental values at the Fermi energy. It is the band structure at energies other than the Fermi energy which result in the optical properties, for example, of solids.

Very unusual effects occur in tin because of magnetic breakdown as shown in figure VI-13 (refs. 5 and 9). In this figure the thermoelectric power is plotted as a function of magnetic field for two different angles between the field and the crystalline axis. At $52.95^{\circ}$ large oscillations in the thermopower are seen, but, less than $2^{\circ}$ away, at $51.23^{\circ}$ the oscillations are barely visible. An extensive study of the amplitude of the oscillations as a function of the angle between the field and the crystalline axes has been made. Figure VI-14 shows the amplitude of the oscillations plotted against angle in the (110) rotation plane (ref. 5). As seen, there are several giant resonances in the amplitude. The two peaks near the [001] axis (at about $\pm 4^{\circ}$) are due to a linear chain of orbits which are opened and closed by magnetic breakdown. The resonances at A and A' are due to a coupling between two linear chains of orbits opened by magnetic breakdown. The exact mechanisms for the resonances B and B' and C and C' are not known, but they are believed also to be due to magnetic breakdown. The linear chain responsible for the resonances at $\pm 4^{\circ}$ are shown in figure VI-15. The large orbits $4a\zeta$ and the small orbits $3\delta$ are not connected at zero field or very low field. At high fields magnetic breakdown probability increases, and the orbits $3\delta$ and $4a\zeta$ can be connected. The probability for breakdown increases exponentially with the strength of the magnetic field, and the giant resonances in the amplitude of the thermopower oscillations are due to the opening and closing of orbits along the [110] direction, which is formed by a linear chain of the $4a\zeta$ and $3\delta$ orbits (ref. 10).

The quantum phenomena described yield accurate information on the energy band structure of the solid. This gives the band structure at the Fermi energy and allows the theorist to construct an accurate band structure picture at all energies. Quantum phenomena also yield information about the effective masses of electrons, electron energies, and scattering mechanisms. Magnetic breakdown is seen especially well in the quantum phenomena in the galvanomagnetic and thermomagnetic effects.

## Results in Graphite

In crystalline form, graphite is a highly anisotropic material. It is a semimetal, but, with alkali metals dissolved in it, it becomes a superconductor. In

one direction the crystal can be pulled apart with a piece of tape, and in the other, it has a tensile strength of over 100 000 psi. Fiber mats are now being made with this material; the mats are extremely strong and light and have been used in such things as airplane wings. Good synthetic crystals have only been available recently, so little is known about their transport properties in extremely high magnetic fields. One of these properties is the electrical magnetoresistance. In figure VI-16 we show the magnetoresistance of two different crystals of graphite as a function of field. The plots were made for two different temperatures for each crystal. These crystals are made by pressure annealing pyrolytic graphite at temperatures above 3300 K. Sample PG3 was annealed at a lower temperature and with less pressure than sample PG5. Thus, the crystallites are more highly oriented in sample PG5 than they are for PG3.

We've been studying the field and temperature dependence of various samples of pressure-annealed pyrolytic graphite in the extreme quantum limit. By "extreme quantum limit," we mean that there is only one Landau level beneath the Fermi energy for fields above approximately 8 teslas. As shown in figure VI-16, below 8 teslas the quantum resonances in the magnetoresistance are apparent and are stronger for the more highly oriented crystalline material. We've also been studying quantum resonances in the thermoelectric power as shown in figure VI-17 where the adiabatic thermoelectric power is plotted as a function of magnetic field from zero to about 3.8 teslas. At low fields there are sinusoidal oscillations due to quantization as was described earlier; however, at higher fields (above approx. 0.7 tesla) resonances result as each Landau level cylinder passes through the Fermi surface. With the sign of the resonances and their deHaas-vanAlphen frequency known, the position of the Fermi surface in the Brillouin zone, from which they originate, was determined.

## Transistors in Fields

Of practical importance, is the study which we have been making of transistor performance in high magnetic fields. Table VI-1 lists several different materials of different constructions and their performance in a magnetic field (ref. 11). "Performance" is defined as the ratio of the gain of the transistor in the field, to the gain in zero field. The high field data listed were taken at 7 teslas, and the effects are very large. For example, in the npn-germanium alloy transistor, gain has been reduced to 27 percent of its value in zero field. The conclusions from this work are that planar diffused silicon transistors are best for use in magnetic fields. It is

also best to have the magnetic field oriented parallel to the carrier motion. Transistor performance is independent of whether the transistor is a pnp or an npn type.

## MAGNETOCALORIC EXPERIMENTS

A second major class of experiments is magnetocaloric experiments. A schematic of the apparatus and the measuring electronics is shown in figure VI-18. The sample is thermally isolated by a carbon support rod. The sample sits in a vacuum, and the vacuum can is surrounded by liquid helium. Thus, the sample comes to an equilibrium temperature with the surrounding bath. The bath temperature varies from 4 to 1.0 K in most cases. The temperature of the sample is monitored with a carbon thermometer using an alternating-current Wheatstone bridge. The bridge consist of an oscillator driving the bridge, and off-balance is detected with the output of a phase sensitive detector, which is tuned to the oscillator frequency. Using this method, changes in the temperature of the sample on the order of $10^{-6}$ K can be detected. An example of this type of experiment is shown in figure VI-19, where the temperature of the sample is monitored as a function of field strength for a crystal of tin at 1.0 K and for fields between 2.3 and 5 teslas. Temperature changes are on the order of a few times $10^{-5}$ K, and the oscillations are a result of the quantization of electron orbits as was described earlier. These experiments yield information about the electron energy bands of the solid. The advantage of this method is that the samples need not be shaped. This method for studying quantum effects in solids is sensitive to spin-orbit coupling in the material. Measurements of the spin-orbit coupling in bismuth and antimony have been made by other observers (ref. 12). Preparations are underway to use this method on samples of lead telluride. The magnetocaloric method has been used in a preliminary test to study flux jumping in type II superconductors.

A third example of this type of experiment is the magnetic phases of cesium-manganese-chloride. Figure VI-20 shows the phase diagram for cesium-manganese-chloride material (ref. 13). The magnetic field strength is plotted as a function of the temperature of the sample. Above 5 K the sample is in a paramagnetic state. Below 5 K, in low fields, the sample orders antiferromagnetically. On raising the field at temperatures below 5 K, the spins of the sample flop $90^{o}$. This figure was made for the field along one particular axis of the crystal. Studies of the magnetic phases of this crystal for other orientations at low field were made by other researchers. Other experimental methods, such as nuclear magnetic resonance were also used. In a sample of cesium-copper-chloride, the phase boundary between the antiferromagnetic region and the paramagnetic region becomes

pendent of temperature at a field of 6.2 teslas. The sample, starting at 1.2 K, cooled rapidly in an increasing field in the antiferromagnetic region and passed through the antiferromagnetic boundary into the paramagnetic region at a temperature of about 0.8 K and at a field of 6.2 teslas. On increasing the field in the paramagnetic state, the sample warms very rapidly. From the value of the field at which rapid cooling of the sample changed to rapid heating of the sample, we are able to detect the upper antiferromagnetic - paramagnetic boundary. Low temperatures have traditionally been achieved by adiabatically demagnetizing a paramagnetic material. The rapid cooling which occurs in the antiferromagnetic region in an increasing field for cesium-copper-chloride, for example, opens the possibility for experiments at low temperatures in increasing fields.

Other experiments being performed at Lewis are, for example, magnetostriction experiments in bismuth, lead telluride, and copper (ref. 14); flux flow and flux pinning experiments in thin film superconductors (ref. 15); and studies of the critical field, critical current, and critical temperature for superconducting alloys that are used for constructing superconducting magnets (ref. 16). These experiments are continuing.

## REFERENCES


1. Laurence, James C.: High-Field Electromagnets at NASA Lewis Research Center. NASA TN D-4910, 1968.

2. Woollam, John A.: Galvanomagnetic and Thermomagnetic Effects in White Tin in Fields to 3.3 Tesla and at Temperatures between 1.2 and 4.2 K. NASA TN D-5227, 1969.

3. Brennert, G. F.; Reed, W. A.; and Fawcett, E.: Low Temperature Sample Holder Providing Two Degrees of Freedom in a Solenoid. Rev. Sci. Instr., vol. 36, no. 8, Aug. 1965, pp. 1267-1269.

4. Woollam, John A.: Thermomagnetic Effects and Fermi Surface Topology: Results in Metallic Tin at Low Temperatures. Presented at the Am. Phys. Soc. Winter Meeting, San Diego, Calif., Dec. 18-20, 1968.

5. Woollam, John A.; and Schroeder, P. A.: Magnetic Breakdown and Thermoelectricity in Metallic Tin. Phys. Rev. Letters, vol. 21, no. 2, July 8, 1968, pp. 81-82.

6. Guseva, G. I.; and Zyryanov, P. S.: Quantum Theory of Thermomagnetic Phenomena in Metals and Semiconductors. Phys. Stat. Solidi, vol. 8, 1965, pp. 759-772.

7. Chambers, R. G.: Our Knowledge of the Fermi Surface. Can. J. Phys., vol. 34, no. 12A, Dec. 1956, pp. 1395-1423.

8. Craven, J. E.; and Stark, R. W.: de Haas-van Alphen Effect and Fermi Surface of White Tin. Phys. Rev., vol. 168, no. 3, Apr. 15, 1968, pp. 849-858.

9. Woollam, J. A.: Anomalous Shubnikov-de Haas Amplitudes in White Tin. Phys. Letters, vol. 27A, no. 4, July 1, 1968, pp. 246-247.

10. Young, R. C.: Magnetoresistance and Coupled Orbits in Tin. Phys. Rev., vol. 152, no. 2, Dec. 9, 1966, pp. 659-660.

11. Hudson, Wayne R.; Meyn, Erwin H.; and Schultz, Clarence W.: Transistor Performance in Intense Magnetic Fields. NASA TN D-5428, 1969.

12. McCombe, B.; and Seidel, G.: Magnetothermal Oscillations and Spin Splitting in Bismuth and Antimony. Phys. Rev., vol. 155, no. 3, Mar. 15, 1967, pp. 633-641.

13. Butterworth, G. J.; and Woollam, J. A.: Magnetic Phase Diagram of $CsMnCl_3 \cdot 2H_2O$. Phys. Letters, vol. 29A, no. 5, May 19, 1969, pp. 259-260.

14. Aron, P. R.; and Chandrasekhar, B. S.: Oscillatory Magnetostriction and Deformation Potentials in Bismuth. Phys. Letters, vol. 30A, no. 2, Sept. 22, 1969, pp. 86-87.

15. Hudson, Wayne R.; and Jirberg, Russell J.: Nonlinear Flux Flow in Single Crystal Niobium. NASA TN D-5198, 1969.

16. Aron, P. R.; and Ahlgren, G. W.: Critical Surfaces for Commercial $Nb_3Sn$ Ribbon and Nb - 25% Zr Wire. Advances in Cryogenic Engineering. Vol. 13. K. D. Timmerhaus, ed., Plenum Press, 1968, pp. 21-29.

TABLE VI-1. - TRANSISTOR PERFORMANCE IN MAGNETIC FIELD

| Material | Material type | Construction | Relative performance at 7.0 T (70 kG) |
|---|---|---|---|
| Silicon | pnp | Alloy | 0.83 |
| Germanium | npn | Alloy | .31 |
| Silicon | ↓ | Planar diffused | .96 |
| Germanium | | Alloy | .27 |
| Silicon | | Planar diffused | .94 |
| Silicon | pnp | Planar diffused | .94 |
| Germanium | pnp | Planar diffused | .67 |

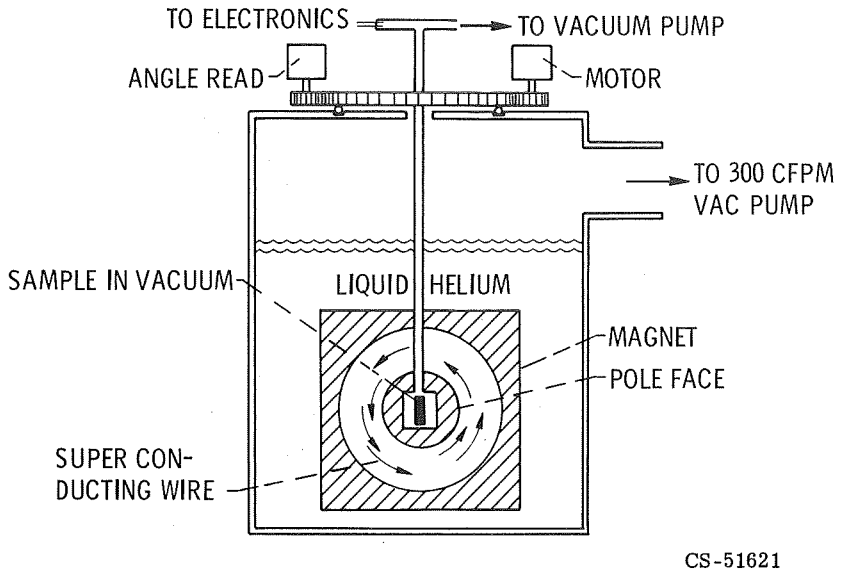


Figure VI-1. - 4.0-Tesla transverse field magnet.

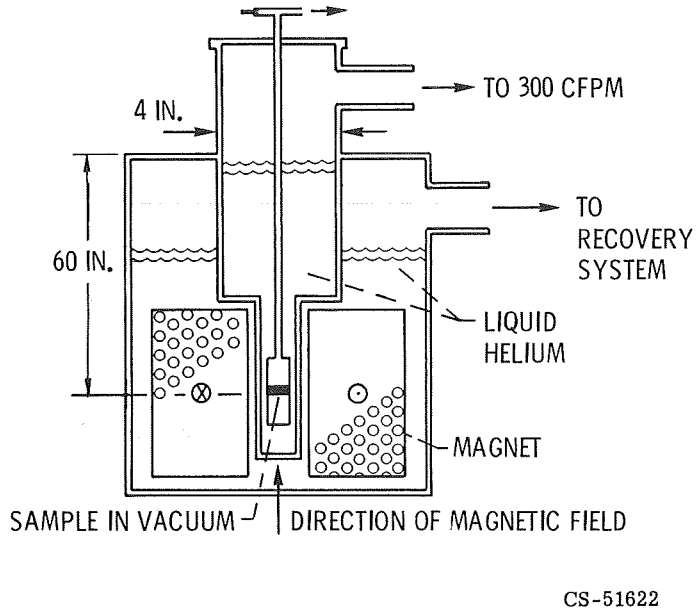


Figure VI-2. - 10.5-Tesla superconducting solenoid.

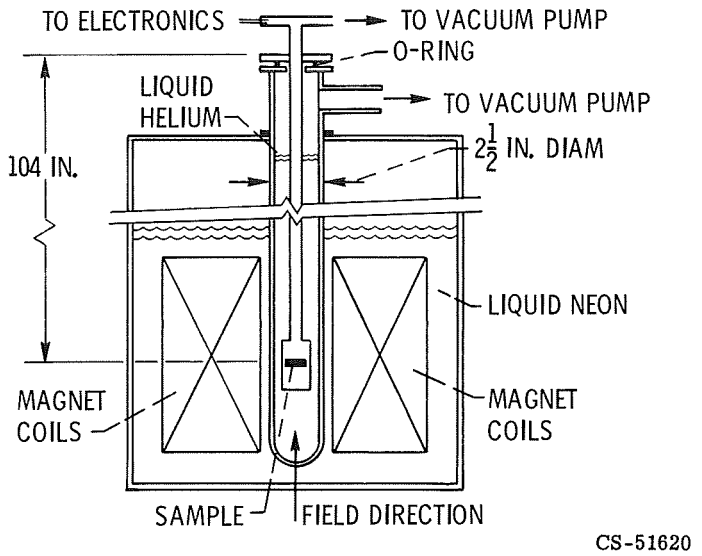


Figure VI-3. - 20-Tesla neon-cooled cryomagnet.

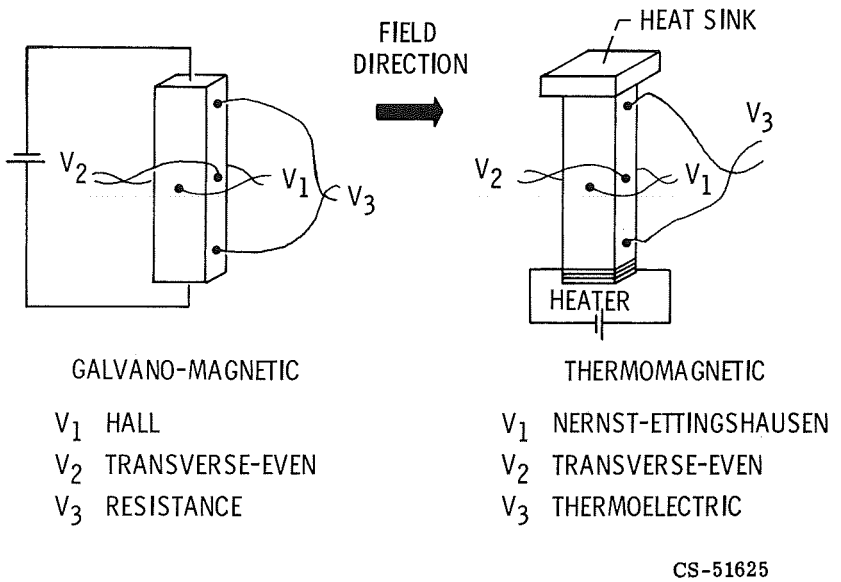


Figure VI-4. - Transport coefficients.

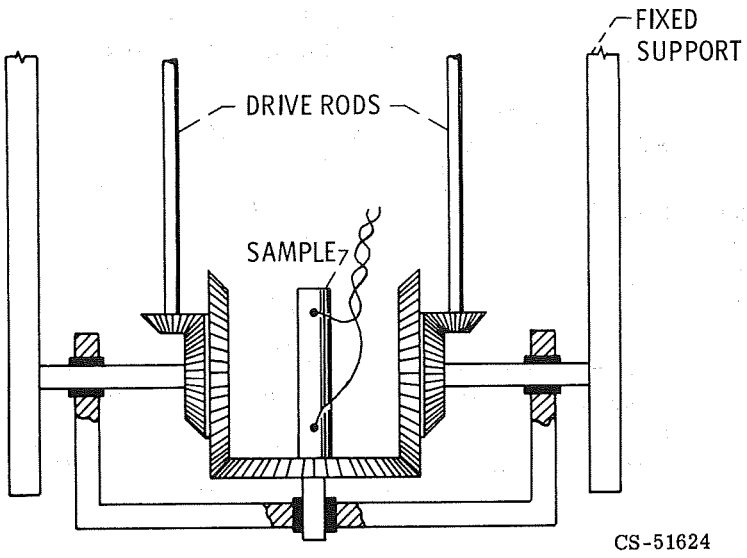


Figure VI-5. - Superconducting solenoid gearing mechanism for rotating or tilting the sample.

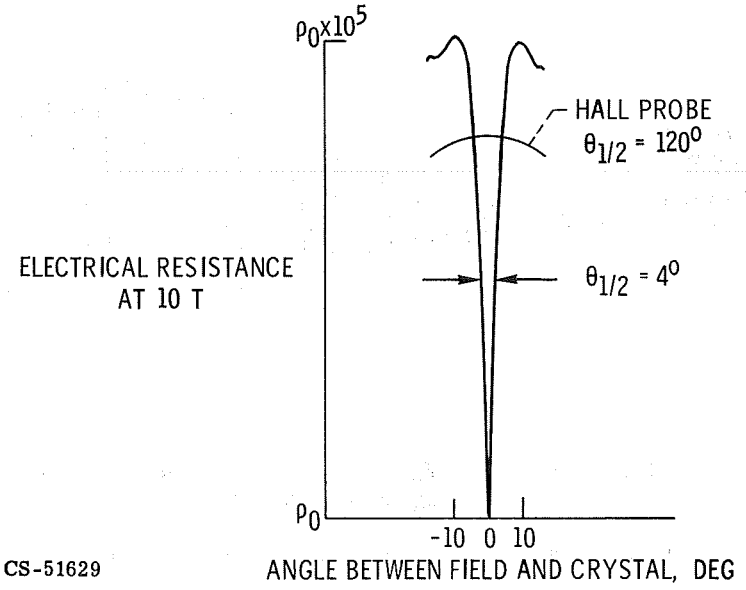


Figure VI-6. - Tin at 4.2 K.

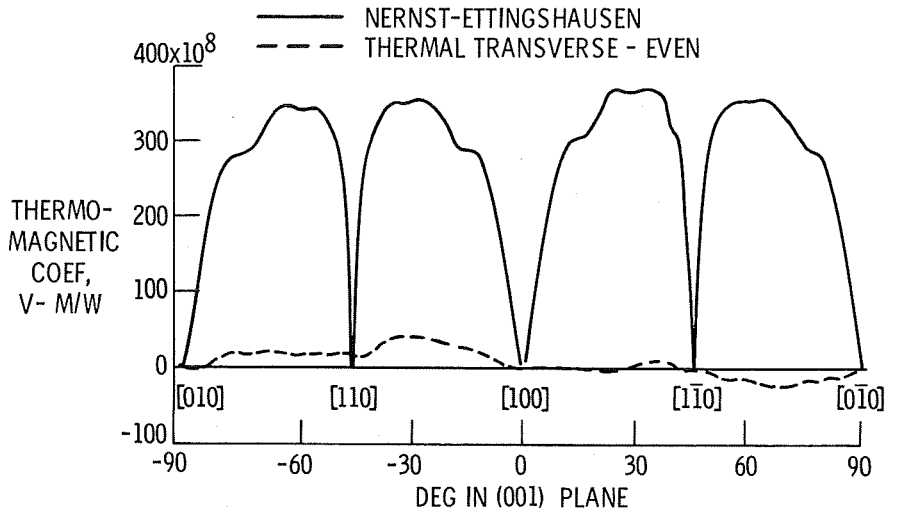


Figure VI-7. - Tin; field, 3.3 teslas; temperature, 1.2 K.

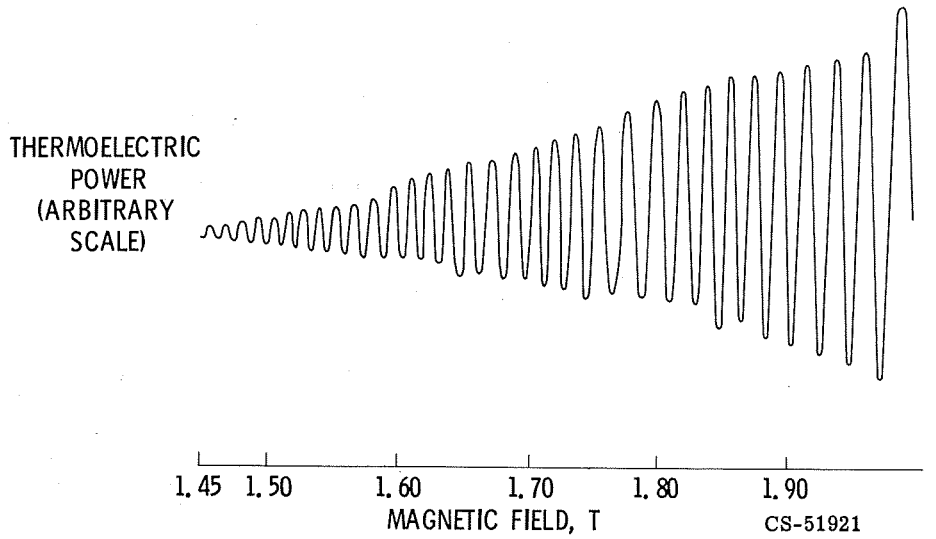


Figure VI-8. - Thermoelectric quantum effects in tin at 1.2 K.

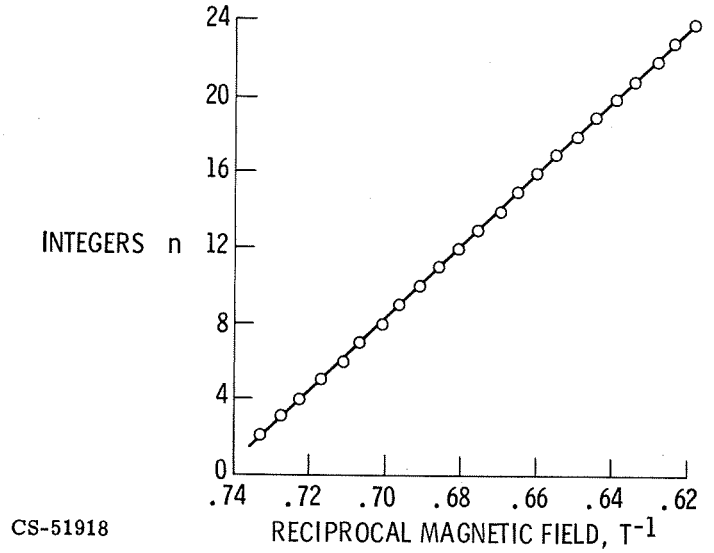


Figure VI-9. - Demonstration of periodicity in inverse field.

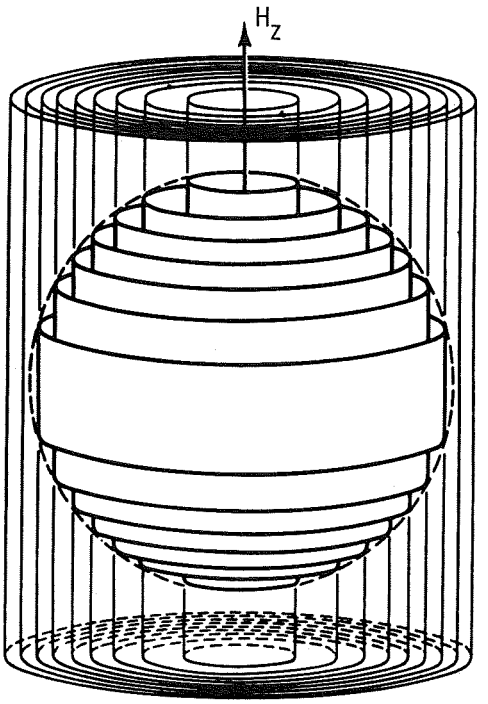


Figure VI-10. - Quantization of energy spectrum in x-y plane into discrete cylindrical surfaces in k-space under influence of applied magnetic field $H_z$ (after Chambers, 1956).

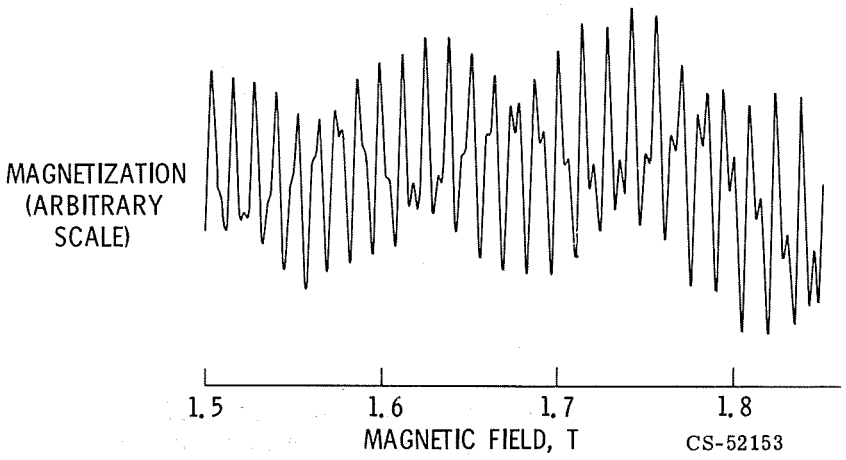


Figure VI-11. - deHaas-vanAlphen effect in tin at 1.2 K. Two beating frequencies shown.

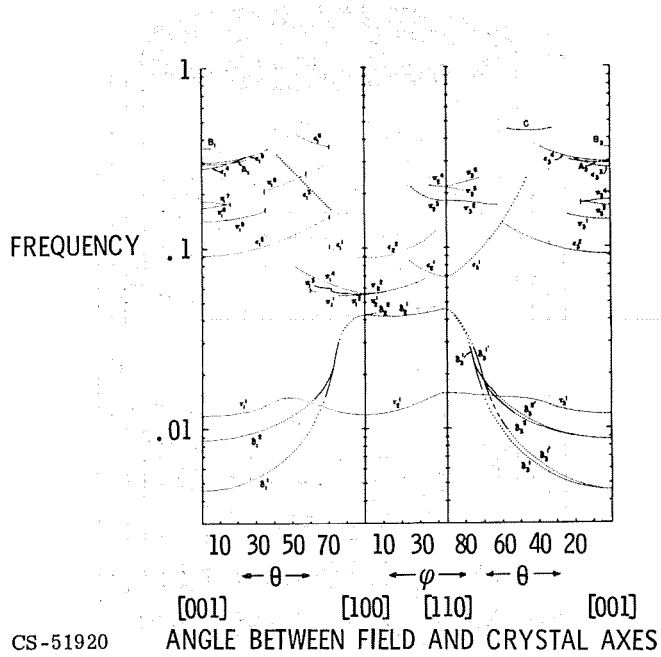


Figure VI-12. - deHaas-vanAlphen frequencies for tin (after Craven and Stark).

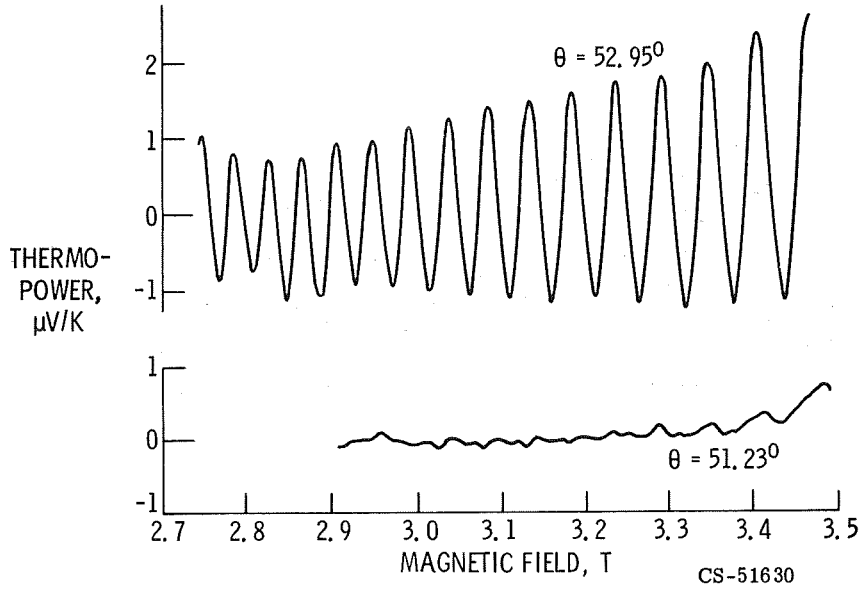


Figure VI-13. - Tin magnetic breakdown at 4.2 K.

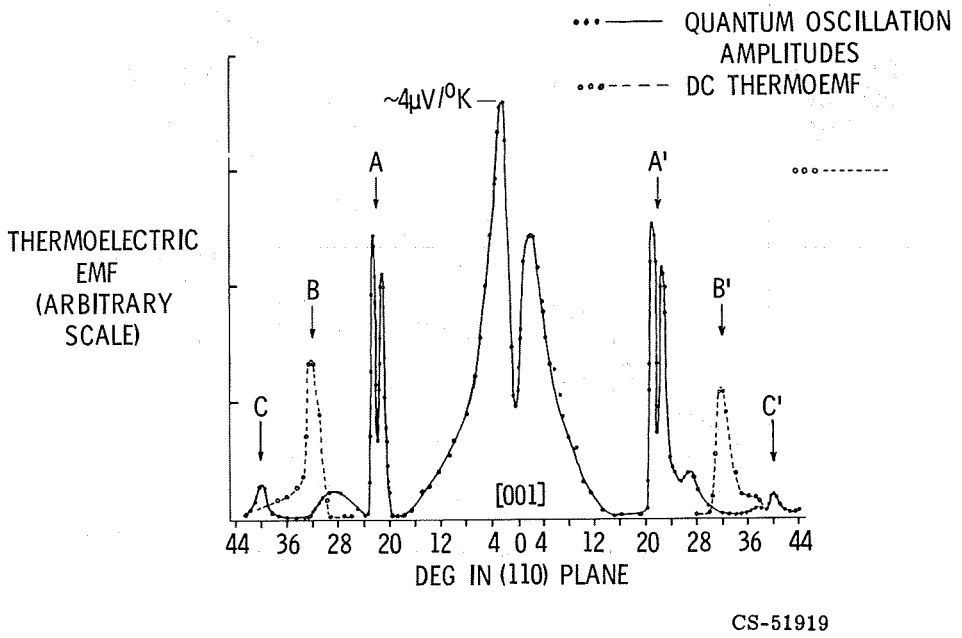


Figure VI-14. - Magnetic breakdown in tin; field strength, 3.3 teslas; temperature, 1.2 K.

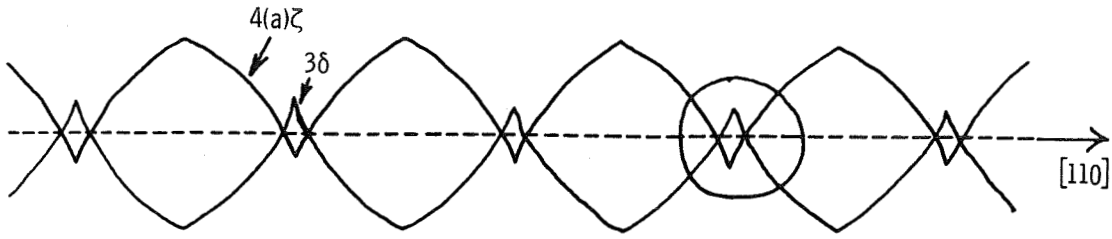


Figure VI-15. - Linear chain of orbits connected by magnetic breakdown.

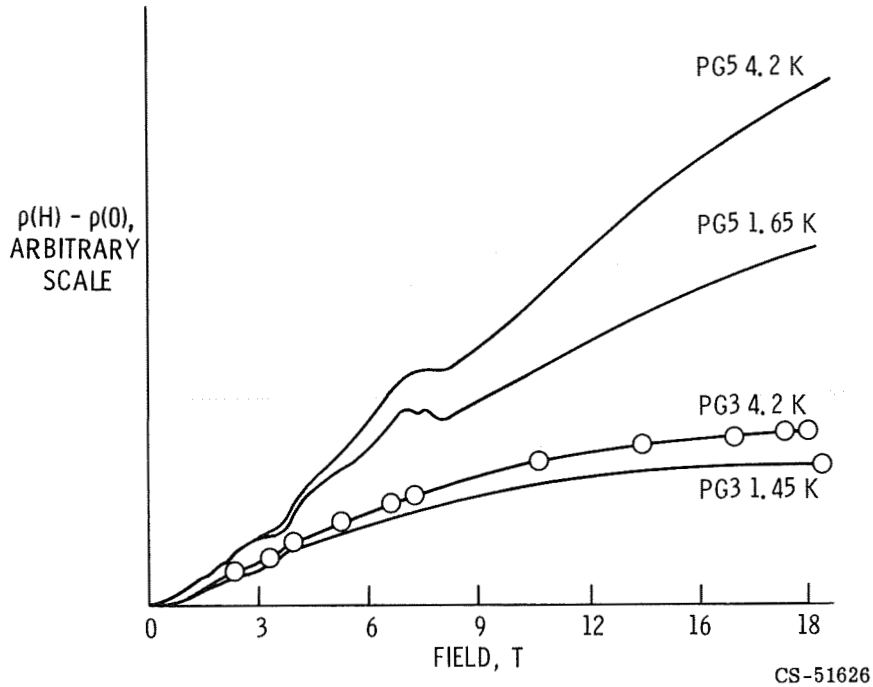


Figure VI-16. - Magnetoresistance of graphite.

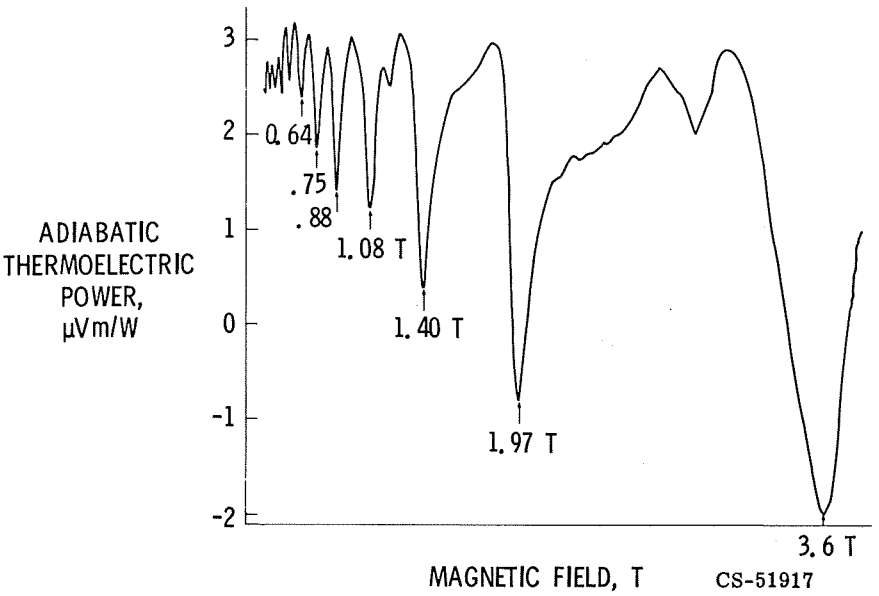


Figure VI-17. - Graphite quantum resonances at 1.1 K.

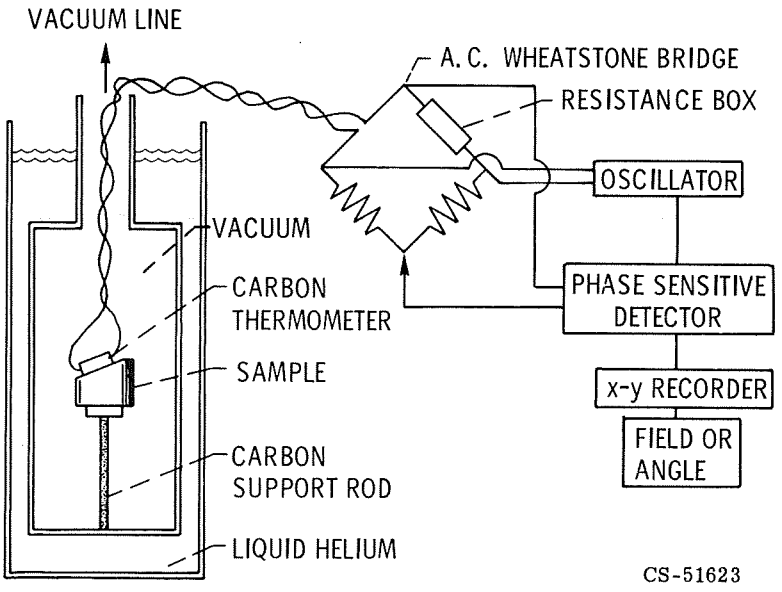


Figure VI-18. - Magnetocaloric experiments.

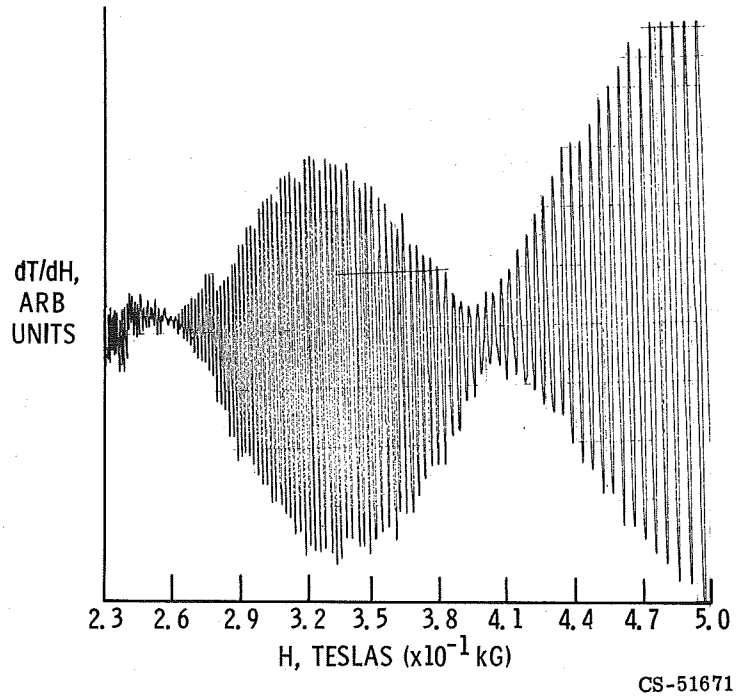


Figure VI-19. - Tin at 1.0 K.

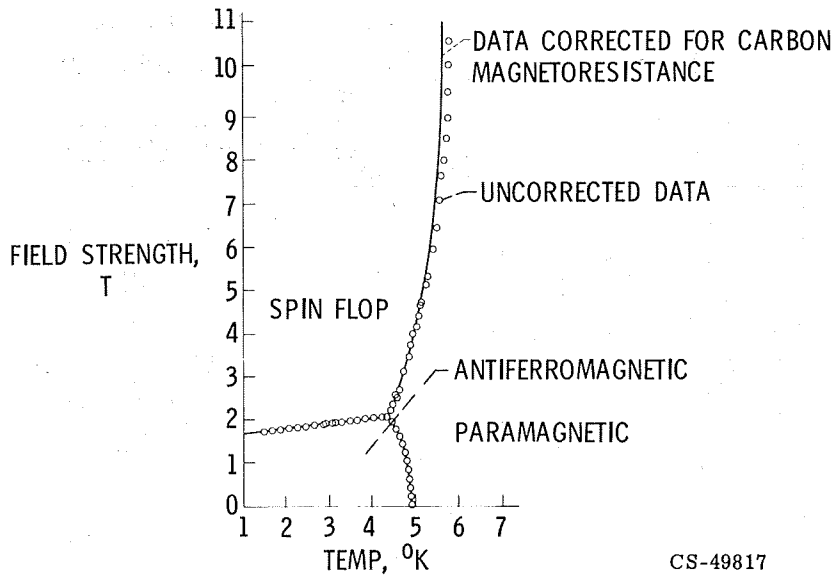


Figure VI-20. - Magnetic phases of $CsMnCl_3 \cdot 2H_2O$.

# VII. SIMULATION OF SOLAR-WIND - EARTH-MAGNETOSPHERE INTERACTION

Donald L. Chubb

Research on solar-wind - Earth-magnetosphere interaction at the Lewis Research Center was a natural outgrowth of research on magnetoplasmadynamic (MPD) arc thrusters. These thrusters were discussed in the paper by Seikel et al. Figure VII-1 shows the flow obtained in the initial exploratory experiments. The highly ionized high-velocity hydrogen exhaust of the water-cooled MPD arc on the right is used to represent the solar-wind flow. A dipole electromagnet in the insulated globe simulates the Earth's magnetic field.

Although these preliminary experiments were encouraging, significant improvements are required to obtain an adequate simulation of solar-wind - Earth-magnetosphere interaction. This paper describes the progress being made toward that goal.

## CHARACTERISTICS OF SOLAR-WIND - EARTH-MAGNETOSPHERE INTERACTION

A complete discussion of the solar-wind - Earth-magnetosphere interaction is given by Hess (ref. 1). Figure VII-2 shows the pertinent details of the interaction. The solar wind, which has a density of ~3 particles per cubic centimeter, is made up of electrons, protons, and some helium nuclei and is therefore a plasma. It flows radially from the Sun with a velocity of $\sim 4\times10^5$ meters per second and a temperature of $\sim 10^5$ K. Imbedded in this plasma flow is a magnetic field of $\sim 4\times10^{-9}$ tesla that originates at the Sun. It should be emphasized that these solar-wind properties increase by factors of 2 or 3 during periods of solar activity. The properties of the wind are such that the flow is supersonic. (For a plasma flow to be supersonic, the square of the velocity must be greater than the sum of the squares of the sound speed and the Alfven speed.) Therefore, just as in the case of an aircraft flying supersonically in the atmosphere, a shock wave forms when the

solar wind impinges on the Earth's magnetic field. The Earth's magnetic field acts like a solid body deflecting the solar-wind flow. The shock wave is about $13R_E$ from the Earth ($R_E$ = Earth radius = $6.37 \times 10^6$ m) on the line connecting the Earth and Sun and has a thickness of $\sim 0.001R_E$. One of the most interesting details about this bow shock wave is that it is "collisionless," which means that the average distance a particle travels before colliding with another particle (mean free path) is large compared to some characteristic dimension. For the bow shock, the characteristic dimension is the thickness of the shock. In a conventional gas dynamic shock wave, it is the dissipation that results from particle collisions that accounts for the shock structure. However, for a plasma collisionless shock wave, it is the interaction of the charged particles and the electric and magnetic fields in the plasma that produces the dissipation.

As a result of passing through the shock wave, the solar wind is decelerated and compressed. The embedded magnetic field is also compressed. After passing through the shock the flow enters a region called the magnetosheath where the plasma properties show rapid fluctuations. Forming the boundary between the magnetosheath and the region where the Earth's magnetic field is confined is the magnetopause. The region where the Earth's magnetic field is confined is called the magnetosphere. Within the magnetopause electrical currents must flow in order to allow the transistion between the solar-wind magnetic field and the Earth's magnetic field. In figure VII-2 the solar-wind magnetic field and the Earth's magnetic field are not shown connected. Whether the magnetic field lines join or do not join is a question that has not been resolved as yet. If the field lines do connect, the magnetosphere is called open; if they do not connect, the magnetosphere is called closed. Figure VII-2 also shows the solar magnetic field at some angle to the solar-wind flow. This angle changes as the Earth rotates about the Sun.

Within the magnetosphere are the belts of trapped high energy electrons and protons usually called the Van Allen belts. These charged particles spiral about the Earth's magnetic field lines and are reflected back and forth between the North and South Poles. The radiation belts begin at about $1.5R_E$ and extend to about $8R_E$. From $1.5R_E$ to $2R_E$ many protons have energies greater than 30 MeV. This is usually called the inner radiation belt. In the region $3R_E$ to $4.5R_E$, which is called the outer belt, many electrons have energies greater than 1.6 MeV.

Trailing behind the Earth is the region called the geomagnetic tail. This tail is caused by the solar wind dragging the Earth's magnetic field along with it. Figure VII-2 shows the tail only out to $40R_E$. It is actually much longer and has been observed at distances beyond the Moon ($60R_E$). Within the geomagnetic tail is a region, called the neutral sheet, where the magnetic field is nearly zero. The

magnetic field changes direction across the neutral sheet. Associated with the geomagnetic tail is a band of keV energy charged particles denoted in figure VII-1 as the plasma sheet, which has a thickness of about $10R_E$.

## SIMULATION CRITERIA

Now that a brief description has been given of the main features of the solar-wind - Earth interaction, a way to simulate the entire interaction in the laboratory is considered. The following discussion was first presented in reference 2. First of all, there must be a theoretical understanding of the phenomenon in order to know what conditions must be satisfied for its simulation. In the case of the solar-wind - Earth interaction there are very few completely accepted explanations for the various features of the interaction. Therefore, simulation is dependent on the criteria considered most important. We assume the following conditions (see fig. VII-3) must be satisfied for a proper simulation:

(1) Collisionless flow, $\lambda > \ell$

(2) Hypersonic flow, $M_s^2 >> 1$, $M_a^2 >> 1$

(3) Bow shock thin compared to standoff distance, $\delta < \Delta$

(4) Geometrical similarity, $a = 10R$

(5) Plasma beam diameter greater than interaction size, $d > 4a$

The terms introduced in these expressions are defined as follows: collisional mean free paths, $\lambda$; characteristic dimension of the experiment, $\ell$; shock thickness, $\delta$; shock standoff distance, $\Delta$; distance from the center of the dipole to the edge of the magnetosphere, a; diameter of the dipole, R; diameter of the plasma beam, d; acoustic Mach number, $M_s$; and Alfven number, $M_a$.

In the following discussion each one of these conditions is considered. The simulation criteria resulting from these conditions are written in terms of the velocity $u_1$, the number density $n_1$ upstream of the shock, and the parameter a.

## HYPERSONIC FLOW AND SHOCK CRITERIA

From satellite data it is known that both $M_s$ and $M_a$ are about 8. The acoustic Mach number is defined as

$$M_s^2 \equiv \frac{u_1^2}{C_1^2} \tag{1}$$

where

$$C_1^2 = \frac{5}{3}\frac{kT_1}{m_i} \tag{2}$$

is the upstream acoustic speed. The Alfven number $M_a$ is defined as

$$M_a^2 \equiv \frac{u_1^2}{V_{a_1}^2} \tag{3}$$

where

$$V_{a_1}^2 = \frac{B_1^2}{m_i n_1 \mu_0} \tag{4}$$

is the upstream Alfven number. Other terms appearing in equations (1) to (4) are the velocity $u_1$, the temperature $T_1$, the magnetic field $B_1$, the number density $n_1$, the Boltzmann constant k, the ion mass $m_i$, and the magnetic permeability $\mu_0$ (= $1.2556\times10^{-6}$ H/m). The subscript 1 refers to conditions upstream of the shock (fig. VII-3).

The Mach number of the flow is defined as (ref. 8)

$$M_1^2 \equiv \frac{u_1^2}{C_1^2 + V_{a_1}^2} \equiv \frac{M_a^2 M_s^2}{M_a^2 + M_s^2} \tag{5}$$

Since $M_a$ and $M_s$ are both approximately 8, equation (5) yields $M_1 \approx 6$. In a simulation experiment it is difficult to achieve such large Mach numbers. However, to a first approximation the flow is required to be hypersonic. For hypersonic flow, $M_s^2 >> 1$ and $M_a^2 >> 1$. Thus equations (1) and (3) yield the following:

$$C_1^2 = \frac{5}{3}\frac{kT_1}{m_i} << u_1^2 \tag{6a}$$

$$V_{a_1}^2 = \frac{B_1^2}{m_i n_i \mu_0} << u_1^2 \tag{6b}$$

From satellite data it is known that the shock thickness is of the order of $10^4$ meters and that it stands off from the magnetosphere a distance $\Delta \approx 0.3a$. There are several theoretical treatments of the bow shock structure (ref. 1, pp. 361 to 364). However, the shock thickness predicted by Tidman (refs. 3 and 4) shows the best agreement with satellite results. Tidman gives the shock thickness $\delta$ as

$$\delta = \frac{2\sqrt{\frac{kT_2}{m_2}}}{\frac{qB_1}{m_e}} \tag{7}$$

where $\delta$ is the order of the electron cyclotron radius, $T_2$ the temperature downstream of the shock, $m_e$ the electron mass, and $q$ the magnitude of the electron charge. Since the shock has a standoff distance $\Delta \sim 0.3a$ and $\Delta > \delta$, the shock thickness simulation criterion is

$$0.3a > \frac{2\sqrt{\frac{kT_2}{m_e}}}{\frac{qB_1}{m_e}} \tag{8}$$

## GEOMETRY CRITERIA

From satellite data we know that $a = 10R_E$, where $R_E$ is the radius of the Earth. Maintaining this geometrical similarity in a simulation experiment leads to a simulation criterion for the magnetic field. Using satellite information about the size of the interaction and also experimental data on the divergence angle of the MPD leads to a relation for the characteristic dimension of the experiment.

Several investigators have considered the shape of the boundary between a streaming plasma and a dipole field (i.e., the magnetosphere). These results are summarized in reference 1 (pp. 293 to 300). One of the results used to arrive at the simulation criterion is the following. The tangential magnetic field strength just inside the magnetopause is twice the strength of the field that would exist for an un-

disturbed dipole. For an undisturbed dipole the magnetic field along the Earth-Sun line is

$$B = B_E\left(\frac{R_E}{r}\right)^3 \tag{9}$$

where $r$ is the distance from the center of the Earth and $B_E$ is the magnetic field at the surface of the Earth. Therefore, for the case with flow, at the position $a$ (fig. VII-3) the magnetic field is

$$B_a = 2B_E\left(\frac{R_E}{a}\right)^3 \tag{10}$$

Using the geometrical similarity result $a = 10R_E$ gives equation (10) as

$$B_a = 2\times10^{-3}\, B_E \tag{11}$$

It is more convenient to use the magnetic field strength on the axis of the dipole, which is denoted by $B_P$ in figure VII-3. For a dipole, $B_P = 2B_E$. Therefore, equation (11) can be written as

$$B_a = 10^{-3}\, B_P \tag{12}$$

From satellite data it is known that the magnetosphere has a width of approximately 4a (fig. VII-3). Therefore, the plasma beam must satisfy the requirement

$$\text{Beam diameter} = d \geq 4a \tag{13}$$

Also, from experimental results it is known that the divergence angle of the MPD arc beam is approximately $\tan\theta \approx 1/4$ (fig. VII-3). Therefore, in order to satisfy the beam diameter requirement,

$$L \geq 8a \tag{14}$$

where $L$ is the distance between the arc and the forward stagnation point located a distance $a$ from the center of the dipole. A characteristic length for the experiment can now be established. Since the neutral sheet is to be investigated, it is necessary to maintain a collisionless flow downstream of the dipole. Based on satellite information, the distance $4a$ from the front of the magnetosphere is

chosen as a minimum distance for maintaining a collisionless flow. Therefore, referring to figure VII-2, the characteristic dimension of the experiment is

$$l \geq L + 4a = 12a \tag{15}$$

## COLLISIONLESS CRITERIA

In the case of the solar wind, the only collisional mean free path to consider is the electron-ion. However, in a laboratory experiment where neutral atoms are present the electron-atom and ion-atom collisions must also be considered. For hydrogen, which is the gas most likely to be used in a simulation experiment, the electron-atom mean free path is larger than the other mean free paths. Therefore, if the restrictions on the electron-ion and ion-atom mean free paths are satisfied, the electron-atom mean free path is automatically larger than the dimensions of the experiment. First consider the electron-ion mean free path. If Spitzer's (ref. 6) deflection time $t_D$ is used, the electron-ion mean free path is defined as follows:

$$\lambda_{ie} = u_1 t_D = \left(\frac{q^2}{4\pi\epsilon_0 m_i}\right)^{-2} \frac{u_1^4}{8\pi n_1 \ln \Lambda f(x)} \tag{16}$$

where $\epsilon_0$ is the permittivity of free space. The function $\Lambda$ is defined as

$$\Lambda = 1.55\times10^{13}\left(\frac{kT_1}{q}\right)^{3/2} n_1^{-1/2} \tag{17}$$

and since

$$x = u_1\left(\frac{2kT_1}{m_e}\right)^{-1/2} << 1 \tag{18}$$

the function f(x) can be approximated as

$$f(x) \approx \frac{4}{3\sqrt{\pi}}\, x \tag{19}$$

Substituting equation (19) into equation (16) yields the following simulation criterion:

$$l < \lambda_{ie} = 1.625\times10^{6}\, A_w^2 \left(\frac{kT_1}{q}\right)^{1/2} \frac{u_1^3}{n_1 \ln \Lambda} \tag{20}$$

where $A_w$ is the atomic weight of the ion.

Now consider the ion-atom mean free path. Since the atom number density is controlled by the pumping rate of the vacuum facility, the ion-atom mean free path can be related to the pumping rate. If it is assumed that the plasma beam is fully ionized, then in steady-state operation the conservation of the heavy particles requires that

$$An_1u_1 = n_a\dot{V} \tag{21}$$

where $A$ is the cross-sectional area of the beam, $n_a$ the atom number density, and $\dot{V}$ the tank pumping speed. If the definition of the ion-atom mean free path

$$\lambda_{io} = \frac{1}{n_a\sigma_{io}} \tag{22}$$

is used, where $\sigma_{io}$ is the ion-atom collision cross section, equation (21) yields the following simulation criterion:

$$l < \lambda_{io} = \frac{\dot{V}}{\sigma_{io}n_1u_1A} \tag{23}$$

There are several ion-atom cross sections (i.e., elastic and ionization). However, the largest of these is the charge-exchange cross section. Since $\lambda_{io}$ is inversely proportional to $\sigma_{io}$, using the charge-exchange cross section is the most conservative way of requiring that $\lambda_{io} > l$. Values for $\sigma_{io}$ as a function of ion velocity are given in reference 6.

## DENSITY AND VELOCITY REQUIREMENTS

Table VII-1 lists the simulation criteria that must be satisfied. These conditions can all be expressed in terms of the upstream density $n_1$, the velocity $u_1$, and the parameter a.

If continuum one-dimensional flow expressions and the shock "jump" conditions are used, the shock thickness criteria can be reduced to an expression for $n_1$ as a function of a. The equation of motion for a one-dimensional plasma flow where the magnetic field is perpendicular to the flow direction is

$$m_i n u^2 + p + \frac{B^2}{2\mu_0} = \text{Constant} \tag{24}$$

This states that the sum of the momentum flux $m_i n u^2$, kinetic pressure p, and magnetic pressure $B^2/2\mu_0$ is a constant. At the stagnation point located at position a, $m_i n u^2 \to 0$ and $p \to 0$. Therefore, applying equation (24) to the flow along the stagnation line gives

$$m_i n_1 u_1^2 + p_1 + \frac{B_1^2}{2\mu_0} = m_i n_2 u_2^2 + p_2 + \frac{B_2^2}{2\mu_0} = \frac{B_a^2}{2\mu_0} \tag{25}$$

where the subscript 2 denotes conditions just downstream of the shock and subscript a denotes conditions at the stagnation point. The pressure is

$$p = nkT \tag{26}$$

Since both the acoustic Mach number and the Alfven number are much greater than 1 (eq. (6)), p and $B^2/2\mu_0$ can be neglected compared to $m_i n_1 u_1^2$. Therefore,

$$m_i n_1 u_1^2 \approx m_i n_2 u_2^2 + n_2 k T_2 + \frac{B_2^2}{2\mu_0} = \frac{B_a^2}{2\mu_0} \tag{27}$$

Also, for high Mach numbers the shock "jump" conditions of Tidman (refs. 3 and 4) are the following:

$$n_2 \approx 4 n_1 \tag{28a}$$

$$u_2 \approx \frac{1}{4} u_1 \tag{28b}$$

$$\frac{kT_2}{m_i} \approx \frac{3}{32} u_1^2 \tag{28c}$$

$$B_2 \approx 4B_1 \tag{28d}$$

Using equations (12) and (28) in equation (27) gives

$$B_P^2 = 2\mu_0 m_i n_1 u_1^2 \times 10^6 \tag{29}$$

and

$$B_1^2 = \frac{3}{64} \mu_0 m_i n_1 u_1^2 \tag{30}$$

If equations (28c) and (30) are now used in equation (8), the shock thickness criterion becomes

$$n_1 > \frac{25\times10^{14}}{a^2} m^{-3} \tag{31}$$

Equation (31) gives the minimum value of the density that satisfies the shock thickness criterion.

The mean free path requirements (eqs. (20) and (23)) can be reduced to relations between $n_1$ and $u_1$. First consider the electron-ion mean free path (eq. (20)). The high acoustic Mach number requirement sets the limit on $T_1$. For our purposes assume that $M_s \geq 4$. Therefore, from equation (1),

$$kT_1 \leq \frac{1}{16}\left(\frac{3}{5} m_i u_1^2\right) \tag{32}$$

Substituting equation (32) and $\ell = 12a$ into equation (20) yields

$$n_1 < \frac{10.7}{4 \ln \Lambda} A_w^{5/2} \frac{u_1^4}{a} \tag{33}$$

Now $\ln \Lambda$ is a slowly varying function of $T_1$ and $n_1$. For the densities and temperatures to be considered $\ln \Lambda \sim 10$. Therefore, for our purposes $(10.7/\ln \Lambda) \sim 1$, so that

$$n_1 < \frac{A_w^{5/2}}{4} \frac{u_1^4}{a} \tag{34}$$

Equation (34) determines the maximum density that will satisfy $\lambda_{ie} > \ell$.

The ion-atom mean free path requirement (eq. (23)) can be simplified by substituting $\ell = 12a$ and $A = 4\pi a^2$. Therefore, equation (23) gives

$$n_1 < \frac{1}{48\pi} \frac{\dot{V}}{a^3 \sigma_{io} u_1} \tag{35}$$

which sets another maximum limit on the number density.

Figure VII-4 shows the results obtained from equations (31) and (33) to (35) for $a = 0.2$. Results for two pumping speeds ($\dot{V}$) are shown. For $\dot{V} = 10^3$ cubic meters per second, which is the pumping speed of the present Lewis 15-foot-diameter vacuum tank, all the simulation requirements cannot be satisfied. However, at $\dot{V} = 5 \times 10^3$ cubic meters per second the shaded area in figure VII-4 is a region of $u_1$ and $n_1$ values that will satisfy all the requirements. Near-future modifications to the 15-foot vacuum tank should increase its pumping speed to $5 \times 10^3$ cubic meters per second to permit operation of an experiment in the shaded area of figure VII-4. The polar magnetic fields associated with these conditions are of the order of 1 tesla, which is a large field for a 4-centimeter-diameter magnet. If the value of $a$ is increased, then the magnetic field requirement is reduced. At the same time, however, the region of acceptable $u_1$ and $n_1$ values is reduced. With a value of $a = 0.4$ meter there will still be a small range of acceptable velocities and densities for a pumping speed of $\dot{V} = 5 \times 10^3$ cubic meters per second. The polar magnetic field required will be of the order of 0.5 tesla. This size field should be no problem for an 8-centimeter-diameter magnet.

## INITIAL EXPERIMENTAL RESULTS

As figure VII-4 shows, it is not possible to satisfy all the simulation criteria with the present experiment. However, conditions can be simulated for a collisionless stagnation flow. As a result, the initial investigation was in the stagnation region of the flow where a collisionless shock was expected to exist. Figure VII-5 shows the experiment in operation. The view is at an angle of approximately $45^\circ$ from slightly behind the MPD arc. Measurements of the plasma potential and the magnetic field in the Z-direction were made in the region about half way between the thruster and the dipole (ref. 7). Table VII-2 compares the plasma properties of the

flow from the MPD arc with those of the solar wind. It is the ion-atom mean free path, which is approximately 1 meter, that limits the collisionless flow regime. This is the reason the investigation has been confined to the stagnation region close to the arc.

The first results obtained from the experiment indicated that the existence of a shock wave is unlikely. The Mach number of the flow is approximately 0.95. Since $M_1$ must be greater than 1 for a shock to form, it is concluded from these results that no shock can exist. Further evidence against the existence of a shock resulted from the plasma potential and magnetic field measurements.

The plasma potential $V_p$ is shown in figure VII-6 as a function of distance from the dipole x. In figure VII-7, the magnetic field in the Z-direction $B_z$ is presented as a function of x. To show where the magnetic field and plasma potential profiles are with respect to the light emitted, the results of figures VII-6 and VII-7 are superimposed on the results of figure VII-5. These results are shown in figure VII-8. Two different profiles of $V_p$ appear in figure VII-6. The only major difference between the two is that the region of rapid increase moves back about 4 centimeters for the case where the dipole current is 495 amperes. This is as expected, since the stagnation magnetic field will be closer to the dipole for the lower current.

Both potential profiles show a rise of about 12 volts in the initial discontinuity. This rising potential region corresponds to a change in velocity given by

$$\frac{1}{2} m_i \left(u_1^2 - u_2^2\right) = q \, \Delta V_p \tag{36}$$

where $\Delta V_p$ is the change in potential, $u_1$ the upstream velocity, and $u_2$ the downstream velocity. If $\Delta V_p = 12$ volts and $u_1 = 5 \times 10^4$ meters per second, then for hydrogen ions equation (36) yields

$$u_2 = 4.5 \times 10^3 \text{ m/sec}$$

and

$$\frac{u_1}{u_2} = 11$$

The limiting velocity ratio for a shock is 4 (ref. 8). Therefore, this potential jump cannot represent a shock. However, it is very nearly the potential change that is required to stagnate hydrogen ions with a velocity of $5 \times 10^4$ meters per

second. To stagnate ions with $u_1 = 5\times10^4$ meters per second requires 13.1 volts.

Figure VII-7 shows that when the thruster is not operating the magnetic field has the usual $1/x^3$ dependence of a dipole field. When the thruster is operating, the magnetic field shows a change occurring in the same location as the rapid rise in the plasma potential. If the region of change is considered as lying between $x \sim 71$ and 59 centimeters, then

$$\frac{B_2}{B_1} \sim \frac{8\times10^{-4}}{3\times10^{-4}} = 2.7$$

If the change in magnetic field is assumed to occur across a shock, then from shock relations (ref. 8) this corresponds to $M_1 \sim 2.7$, which is higher than expected. Thus the magnitude of the magnetic field change also supports the contention that this region of change is not a shock.

When the measured plasma properties of equation (25) are used, the magnitude of the stagnation magnetic field can be calculated:

$$m_i n_1 u_1^2 + \frac{B_1^2}{2\mu_0} + n_1 k T_1 = \frac{B_a^2}{2\mu_0}$$

Using the values given in table VII-2 gives

$$B_a \sim 7\times10^{-4}\ \mathrm{T}$$

Referring to figure VII-7 shows that the $7\times10^{-4}$ tesla point occurs at the end of the magnetic field change. This further substantiates the fact that the region of change in magnetic field and plasma potential is a stagnation flow rather than a shock wave. A more detailed study of the structure of the collisionless stagnation flow is certainly of interest. It may be useful in understanding the flow in the neighborhood of the magnetopause.

Besides investigating the stagnation region in our initial experiments, we have also visually observed regions of intense light in locations where we might expect to find radiation belts. However, no diagnostics of these regions have been made since in the present experiment some collisional processes are occurring.

## FUTURE EXPERIMENTS

At the present time we are in the process of modifying the experiment to satisfy the simulation criteria previously outlined for the solar-wind - Earth interaction. The two things that must be done are to increase the pumping rate of the vacuum tank and to produce a higher Mach number flow. As has already been stated, the pumping rate of the vacuum tank is being increased to $5\times10^3$ cubic meters per second. This can be accomplished by adding a liquid helium cryopump to the tank. Two approaches are being investigated to produce a higher Mach number flow. First, the MPD arc will be modified to produce higher velocity flows. Second, the increased pumping rate will permit the dipole to be located further downstream. This should allow the thruster flow to expand to lower temperature and thus higher sonic Mach number. Once all the modifications are finished, a complete simulation may be possible.

## REFERENCES


1. Hess, Wilmot N.: The Radiation Belt and Magnetosphere. Blaisdell Publishing Co., 1967.
2. Seikel, George R.; and Chubb, Donald L.: Simulation of Solar-Wind Magnetosphere Interactions. Bull. Am. Phys. Soc., series II, vol. 13, no. 7, July 1968, p. 959.
3. Tidman, D. A.: Turbulent Shock Waves in Plasmas. Physics of Fluids, vol. 10, no. 3, March 1967, pp. 547-564.
4. Tidman, D. A.: The Earth's Bow Shock Wave. J. Geophys. Res., vol. 72, no. 7, April 1, 1967, pp. 1799-1808.
5. Spitzer, Lyman: Physics of Fully Ionized Gases, 2nd edition, Wiley-Interscience Publishers, Inc., 1962.
6. McDaniel, Earl W.: Collision Phenomena in Ionized Gases, John Wiley & Sons, Inc., 1964, pp. 252-253.
7. Chubb, Donald L.: Laboratory Simulation of Solar Wind - Earth Interaction. NASA TM X-1738, 1969.
8. Ferraro, V. C. A.; and Plumpton, C.: An Introduction to Magneto-Fluid Mechanics. Oxford University Press, 1961, pp. 90-94.

TABLE VII-1. - SIMULATION CRITERIA

| Simulation criteria | Analytical result |
|---|---|
| Shock thickness $\delta$ less than shock standoff distance $\Delta = 0.3a$ | $0.3a > 2\sqrt{\frac{kT_2}{m_e}}\Big/\left(\frac{qB_1}{m_e}\right)$ |
| Tangential magnetic field at magnetopause is twice the strength of field that would exist for an undisturbed dipole | $B_a = 10^{-3} B_p$ |
| Electron-ion mean free path $\lambda_{ie}$ greater than characteristic dimension of experiment $\ell = 12a$ | $12a < 1.625\times10^6 A_w^2\left(\frac{kT_1}{q}\right)^{1/2} \frac{u_1^3}{n_1 \ln \Lambda}$ |
| Ion-atom mean free path $\lambda_{io}$ greater than characteristic dimension of experiment | $12a < \frac{\dot{V}}{\sigma_{io} n_1 u_1 A}$ |
| Acoustic Mach number much greater than 1 | $\frac{5}{3}\frac{kT_1}{q} << u_1^2$ |
| Alfven number much greater than 1 | $\frac{B_1^2}{m_i \mu_0 n_1} << u_1^2$ |

TABLE VII-2. - PROPERTIES OF PLASMA FLOW

| Plasma property | Solar-wind experiment | Solar wind |
|---|---|---|
| Flow velocity, $u_1$, m/sec | $5\times10^4$ | $4\times10^5$ |
| Electron number density, $n_1$, $cm^{-3}$ | $2.6\times10^{10}$ | 3 |
| Electron temperature, V | 7 | 15 |
| Upstream magnetic field, $B_1$, T | $3\times10^{-4}$ | $4\times10^{-9}$ |
| $\beta = n_1 kT_1 \Big/ \left(B_1^2/2\mu_0\right)$ | 0.8 | 1 |
| Upstream acoustic Mach number, $M_s$ | 1.5 | 8 |
| Upstream Alfven number, $M_a$ | 1.2 | 8 |
| Electron-ion mean free path, m | 10 | $10^5$ |
| Electron-neutral mean free path, m | 10 | --- |
| Ion-neutral mean free path, m | 1 | --- |
| Debye length, m | $10^{-5}$ | 10 |

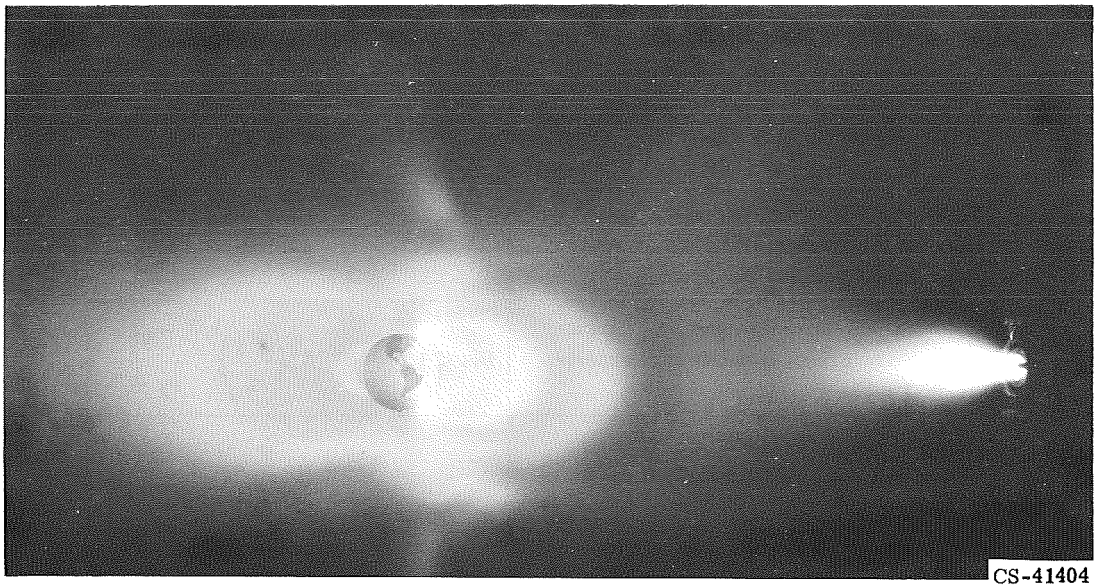


Figure VII-1. - Simulation experiment.

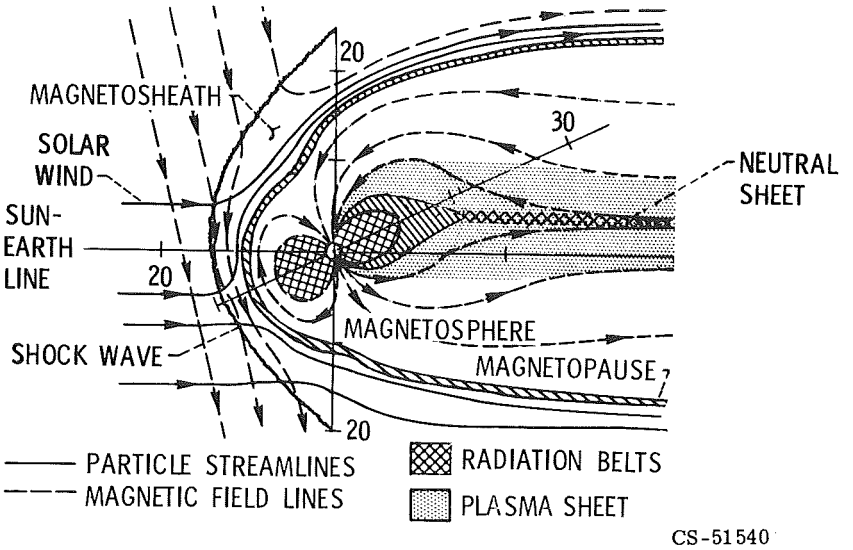


Figure VII-2. - Interaction of solar wind and Earth's field. Dimensionless distances are in terms of Earth radii, $R_E$.

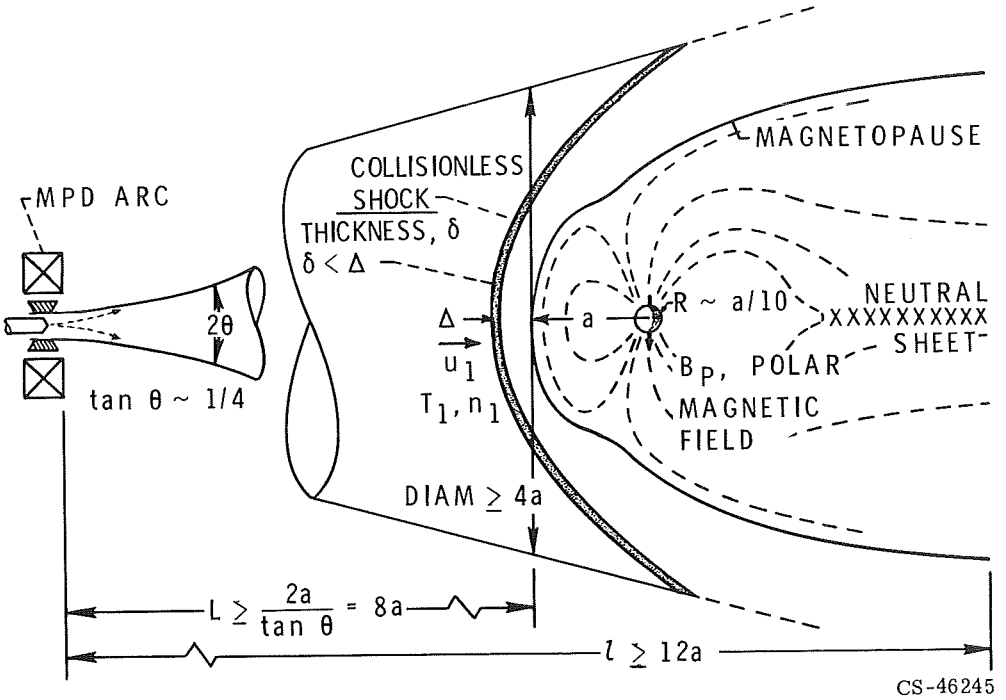


Figure VII-3. - Simulation of solar-wind - Earth interaction. Mean free paths $>> l$; $M_s >> 1$; $M_a >> 1$; $\delta < \Delta \sim 0.3$ a.

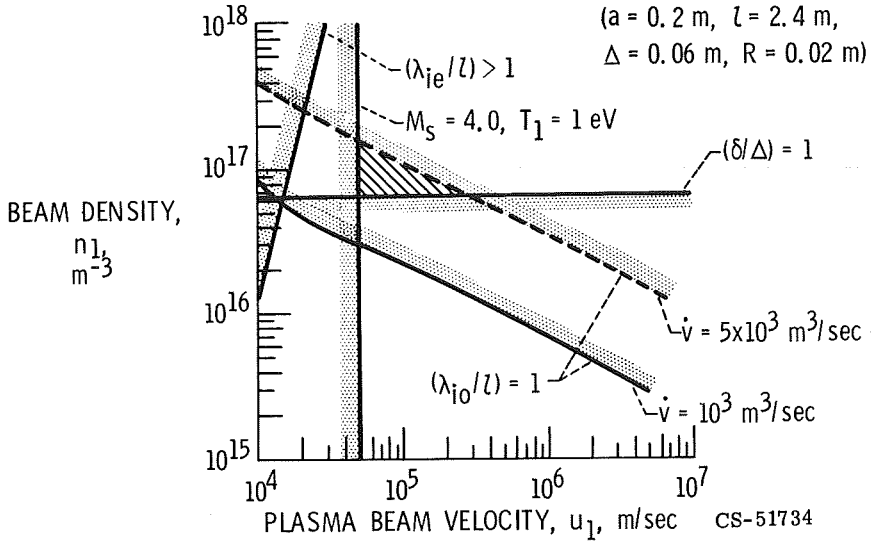


Figure VII-4. - Simulation criteria for stagnation point at 0.2 meter from magnet. (a = 0.2 m; $l$ = 2.4 m; Δ = 0.06 m; R = 0.02 m.)

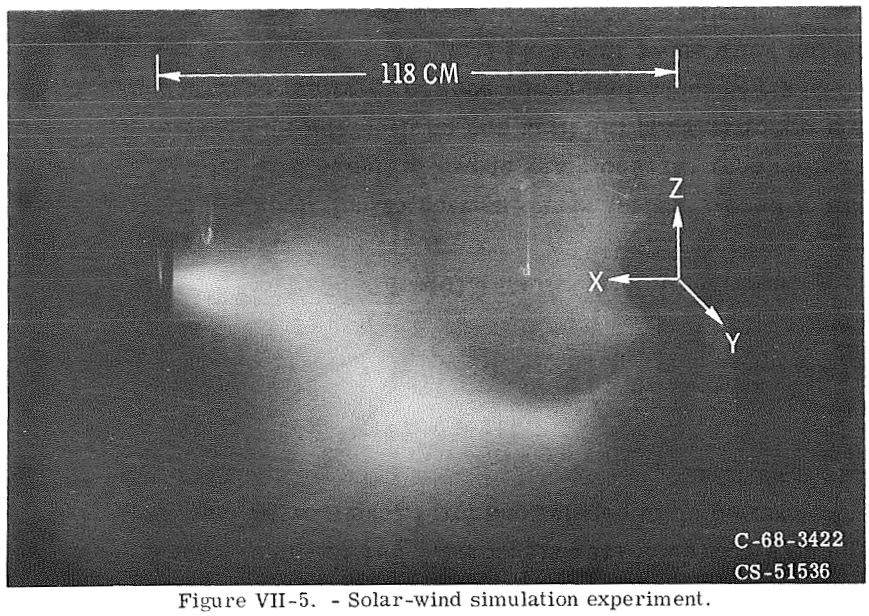


Figure VII-5. - Solar-wind simulation experiment.

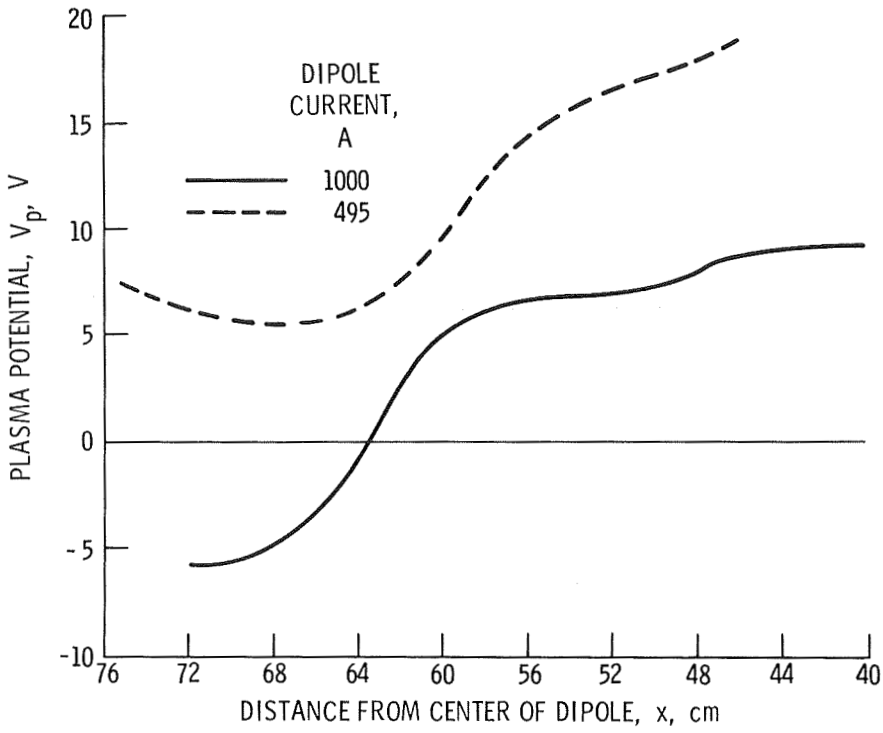


Figure VII-6. - Plasma potential profiles in stagnation region.

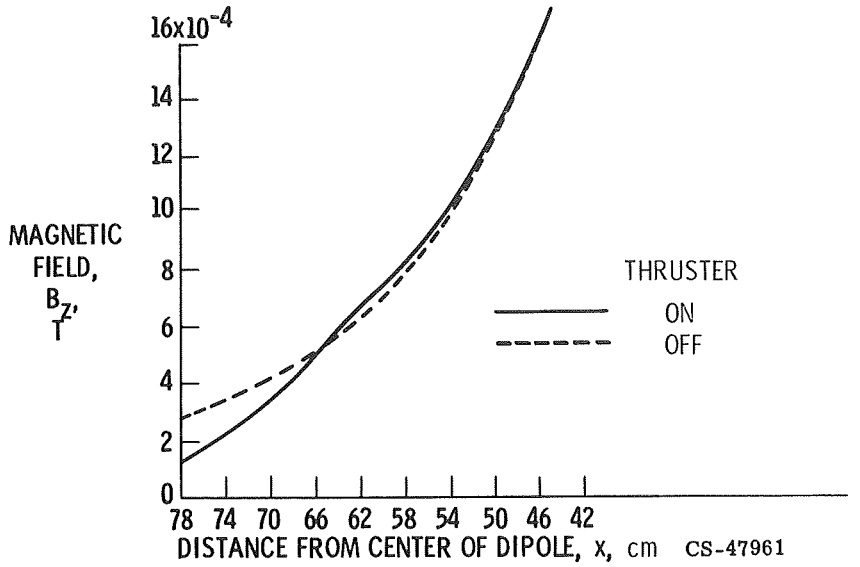


Figure VII-7. - Magnetic field profile in stagnation region. Dipole current, 1000 amperes.

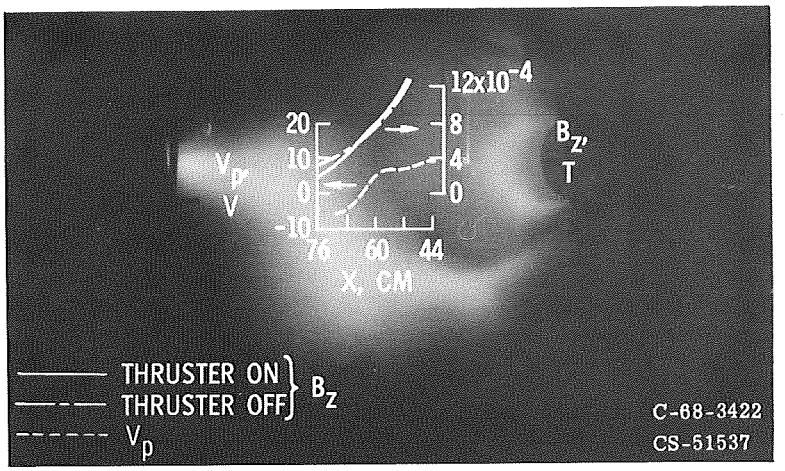


Figure VII-8. - Comparison of $B_z$ and $V_p$ profiles with emitted light.

# VIII. PLASMA CHEMISTRY AND ION-MOLECULE INTERACTIONS

John V. Dugan, Jr.

## PLASMA CHEMISTRY AND COLLISIONS

This discussion is concerned with the computation of cross sections for electron and heavy-particle collisions as well as with their plasma applications. These plasma collisions determine plasma chemistry. Electron-atom collisions and impacts of ions on molecules are of interest for plasma rate calculations. An outline of approaches and results is shown in figure VIII-1. The microscopic cross sections for such processes are required to calculate their relative probabilities. For a fixed temperature, the rate constant (or collision coefficient) is a very useful kinetic quantity. It is the Maxwell averaged product of cross section and velocity denoted by $\langle Qv \rangle$. These coefficients are used in both plasma continuity and energy equations to determine species number densities and temperatures.

Inelastic electron-atom cross sections are of particular interest since the energy transfer $\Delta E$ in these collisions is relatively large. The $\Delta E$ values range from 10 to $10^4$ times the average energy loss per elastic collision. Ion-molecule collisions have large capture cross sections at thermal energies which correspond to relatively rapid chemical reactions. These reactions may be of the rearrangement type or simple charge-exchange. Both electron-atom or molecule and ion-molecule collisions control energy exchange and govern heavy particle chemistry in flowing ionized gases. Examples of such systems are an expanding hypersonic air stream and continuously operating lasers.

## ELECTRON-ATOM COLLISIONS

Inelastic electron-atom collisions are important in both low ($<10^{-2}$ torr) and high pressure nonequilibrium plasmas. Elastic collisions are important only in high pressure discharges. In many cases the inelastic electron-atom cross sections have been computed using the classical Gryzinski theory. This theory is applied semiclassically with recognition of quantum structure and atomic transition

rules. Details of quantum structure are approximated in the selection of a model atom. These semiclassical cross sections have been used to calculate volume ion production costs in low pressure discharges (refs. 1 and 2). Satisfactory results of this method have been mentioned by Sovie for sustained helium plasmas. Although strictly applicable to optically thin plasmas, this approach works well for plasmas partially thick to resonance radiation. Such plasmas are found in ion engine discharges (ref. 3), radiofrequency plasma sources (ref. 4), and cathode sheaths (ref. 5).

One high pressure application of semiclassical cross sections has been in the calculation of three-body ($e^-$ - $e^-$ - ion) recombination rates. These rates have been computed for cesium-seeded argon (MHD application) and agree well with the experimental values (refs. 6 and 7). The semiclassical electron-atom cross sections have also been used in more elaborate plasma calculations. They are employed in calculating electronic state populations and in evaluating collision terms for the Boltzmann equation (ref. 8). This integro-differential equation is solved iteratively for the free electron distribution function $f_e(u)$, which is then used self-consistently in the rate equations for bound state populations and free electron number density $N_e$ (ref. 9).

## ION-MOLECULE COLLISIONS

Both types of ion-molecule collisions are of interest in astrophysics, astronomy, gas discharges (including masers), radiation chemistry, and molecular energetics. The early theory of Langevin considers the ion-molecule collision in terms of an ion-induced dipole interaction. This theory has been used to set upper limits to reaction cross sections for ion-molecule capture collisions. Collisions involving polar targets (i.e., molecules with permanent dipoles) cannot be treated so simply. Mass spectrometry experiments indicate that these collisions have capture cross sections larger than Langevin. Numerical capture cross sections have been calculated for these collisions (refs. 10 and 11). The shape of the ion trajectories has also been studied by means of computer-plotter techniques (refs. 12 to 14). The nature of the ion orbits raises the question of collision time so the latter was computed. Computer-plotter techniques have been recently applied to making motion pictures of ion-molecule collisions to predict chemical reactions (ref. 15).

## MODEL ATOMS

Both low and high pressure rate calculations require a judicious choice of model atoms - that is, the number of discrete electronic levels considered. Two-level model atoms are satisfactory to account for excitation and ionization energy losses in volume ion production. Schematic diagrams of cesium and argon atoms are shown in figure VIII-2. It is useful to classify atoms (for eV $ion^{-1}$ calculations) by the ratio of first excitation potential $U_{ex}$ to ionization potential $U_I$ (ref. 2):

$$y = \frac{U_{ex}}{U_I}$$

This parameter is equal to 0.36 for cesium (relatively easily excited low ionization potential) and 0.72 for argon (high ionization potential but easily ionized once excited). Energy losses by means of excitation to levels above the first excited state are allowed for by assigning a mean energy loss $\Delta E = (U_{ex} + U_I)/2$.

The low pressure plasmas of interest have relatively high electron temperatures from $T_e \simeq 1$ to 50 electron volts. The most detailed analyses include only ground state and metastable (long-lived) excited state populations in the rate equations. The process of stepwise excitation through upper levels leading to ionization is neglected as a source of free electrons. For the high pressure MHD plasmas, however, the excited state populations for 5 levels or so must be solved from the steady-state equations.

## RESULTS

### $e^-$-Atom Cross Sections

Results of semiclassical cross-section calculations for cesium excitation and argon ionization near threshold are shown in figure VIII-3. The cesium predictions are within a factor of 2 for the first and total excitation cross sections at maximum (ref. 2). The argon ionization cross section is within several percent of experiment for 10 electron volts above threshold (ref. 2).

## Electrical Conductivity

Solutions of the Boltzmann and rate equations for the free electron distribution function and state populations have been done for cesium (ref. 8). The atomic model consisted of 5 energy levels with 2- and 3-level models for comparison. The results were used to calculate electrical conductivity in cesium-seeded argon. The calculated conductivity is plotted against current density and compared with experiment in figure VII-4 (ref. 8). Comparison with elastic results (using Saha $N_e$ values) indicates that the inclusion of the inelastic collision terms improve agreement with experiment. Results for $T_e < 2100$ K are dashed because of numerical convergence difficulties. All of the converged distribution functions are near-Maxwellian; the $N_e$ values are with 10 percent of Maxwellian but somewhat below Saha.

Maxwellian results of ionization fraction ($f = N_e/N_0$) where $N_0$ is the neutral density, for 2-, 3-, and 5-level cesium model atoms are compared with detailed 26-level results in figure VIII-5. It is assumed that the plasma is optically thick to resonance radiation. The 5-level results are within factors of 2 to 5 of the 26-level results for $T_e = 0.2$ electron volt (2321 K) (ref. 9). The 5-level optically thin argon results for $T_e = 1$ electron volt (11 605 K) in figure VIII-5 show large departures of the ionization fraction from Saha. The results are also very sensitive to details of the model. This can be seen by comparison of the 2- and 3-level results with 5-level results. Plots of free electron source terms show that a step-wise ionization mechanism operates for $T_e < 2000$ K for cesium and at $T_e$ values from 8000 K to 1 electron volt for argon.

## Capture Cross Sections

Numerical solutions of the Lagrangian equations of motion have been done for capture cross sections in ion-polar molecule collisions. The coordinate system used is shown in figure VIII-6. The angle $\gamma$ defines the orientation of the dipole with respect to the ion-molecule vector. The classical interaction potential has been used; it consists of ion-permanent dipole ($\mu e \cos \gamma / r^2$) and ion-induced dipole ($\alpha e^2 / 2r^4$) terms. The quantity $\mu$ is the dipole moment and $\alpha$ is the polarizability. Capture in Langevin collisions occurs only for impact parameters less than a critical value which is a function of $\alpha$ and the translational energy. Because of the dipole, the ion-polar molecule collisions are not all-or-nothing captures such as the Langevin captures. Thus, the cross section must be computed from the capture ratio $C_R$. This ratio is the fraction of collisions in which ion and molecule approach

within a prescribed separation for the fixed impact parameter. The variation of $C_R$ with $b^2$ is shown for a typical $CH_3CN$-parent ion capture collision in figure VIII-7 (ref. 11). The maximum value $b_m^2$ for these cross sections occurs when the dipole adjusts adiabatically to the ion.

The Langevin capture ratio is also indicated in figure VIII-7. The maximum capture ratio is a step function at 425 $Å^2$. It is clear that although the dipole increases the cross section considerably above the Langevin value it does not guarantee an adiabatic collision.

The comparison of numerical and experimental cross sections as functions of maximum ion energy (corresponding to an experimental voltage setting) is made in figure VIII-8 (ref. 11). The agreement between theory and experiment is within 10 percent at all values of ion energy. Both cross sections are below the maximum.

## Ion-Dipole Collision Orbits

Computer plotting techniques have been applied to the study of ion orbits in dipole collisions. The ion is reflected at separations of 1 to 3 Å to simulate the repulsive electron cores of ion and molecule. It has been proposed that long collision times due to spiraling imply large charge exchange cross sections in certain ion-molecule systems. Plots of the ion orbit for Langevin collisions demonstrate that spiraling does not occur at separations greater than 1 Å (refs. 13 and 14). However, a permanent dipole does introduce multiple reflection behavior, which leads to the formation of long-lived ion-molecule collision complexes. The multiple reflections are caused by a raising of the potential barrier due to dipole rotation. This is shown schematically in figure VIII-9.

The particles approach with relative translational energy $\epsilon$. In the Langevin case they pass over the effective potential barrier at $r = r^*$. After reflection (at $r = r_c$), the ion simply passes out over the barrier since the maximum is fixed. In a representative ion-dipole collision the pre-reflection barrier is located at $r = r'$; however, rotation of the dipole during reflection may shift the maximum to $r = r''$ and raise it. Thus, the ion and polar molecule will reflect with efficient energy exchange until the barrier is once again lowered.

The probability of multiple reflections at impact parameters from 3 to 15 Å generally increases going from HCl to CO and $CH_3CN$ (ref. 13). It appears that HCl has few multiple reflection collisions because of its small moment of inertia. Some $CH_3CN$ multiple reflection cases have turning points at separations as large as 23 Å. A typical ion-orbit is shown in figure VIII-10 for a 10 reflection $CH_3CN^+ + CH_3CN$ capture collision.

The numerical cross section $\sigma_c$ is independent of collision time in all cases. The values of $\sigma_c$ range from Langevin ($\approx 10^2$ Å$^2$) for CO to $10^3$ Å$^2$ for $CH_3CN$ (ref. 10).

Nonpolar targets should behave like polar molecules to a greater or lesser degree. This is because their intermolecular potentials have angular dependent interaction terms. There is much evidence for long-lived complexes in such systems; for example, $N_4^+$ formed from impact of $N_2^+$ on $N_2$.

## Computer-Made Motion Pictures

From a chemical aspect one is interested in whether the rotation of the polar molecule is hindered by the incident ion. It has been suggested that hindering will favor a specific chemical reaction. The plot of ion-dipole orientation angle as a function of ion-molecule separation is shown in figure VIII-11. These results are for a $CH_3CN$ collision. It is clear from the $\gamma$ plot (abruptly decreasing envelope) that the dipole becomes hindered at separations less than 10 Å.

Computer-made motion pictures of ion-dipole collisions allow for the simultaneous study of ion (translational) and dipole (rotational) motion (refs. 14 and 15). The sample movie frame shown in figure VIII-12 consists of ion and polar molecule models. The sum of the radii is the reflection distance $r_c$. There is a clock in the upper right corner consisting of a diamond moving about an asterisk. The clock speeds up and slows down since a variable step-size integration routine is used.

Movie evidence for hindered rotation in a representative collision is shown by the seven frames of figure VIII-13. Similar motion pictures of ion-dipole collisions were shown at the conference. The main features of those collisions are summarized as follows.

The first collision was a multiple reflection movie for a CO target. Three reflections occurred and the rotator was heated. The polar rotator was only slightly hindered since the $\mu$ value was relatively low (0.1 debye unit). However, the dipole played a significant enough role to cause multiple reflections.

The second collision was a HCl single reflection in which a relatively hot rotator ($E_R = 2\ kT_R$) was heated. This was an example of relatively strong interaction (dipole moment $\mu = 1.08$ debye units). The single reflection behavior was typical of HCl targets. The dipole was hindered and precessed before reflection, but rotated rather freely afterwards.

A 10 reflection $CH_3CN$ collision was the third movie shown. The ion hindered the polar rotator so drastically that it actually became still at several different separations. In these instances the ion and polar molecule rotated about each

other to conserve total angular momentum. The $CH_3CN$ molecule had a dipole moment of 3.92 debye units. This high $\mu$ value corresponded to an ion-dipole interaction of 3 electron volts at a typical reflection distance. This energy was about 100 times the sum of the thermal translational and rotational energies.

## FUTURE PLANS

Plasma chemistry plans consist of numerical solution of the quasi-equilibrium flow of high temperature air. The ranges of temperature and pressure of interest are from thermal to 50,000 K and $P/P_o$ from $10^{-4}$ to 10 (where $P_o$ is atmospheric pressure). These values cover an interesting range for hypersonic conditions. The equilibration times for electron energy relaxation and heavy particle chemistry must be calculated to check the assumption of local thermodynamic equilibrium. Preliminary work will be done with a nitrogen model consisting of $N_2$, N, $N_2^+$, $N^+$, and $N^{++}$ and $e^-$. Similar calculations will be done with model atoms on flowing laser systems.

A classical harmonic oscillator has been added to the ion-molecule collision model for future calculations. These ion-dipole studies will consist of computing collision lifetimes as a function of vibrational degrees of freedom. Reaction cross sections for experimental pairs will be computed from capture cross sections and hindering probabilities ($\gamma$ plots).

## REFERENCES


1. Sovie, Ronald J.; and Dugan, John V., Jr.: Effects of Metastable Atoms on Volume Ion Production in a Tenuous Helium Plasma. NASA TN D-3121, 1965.

2. Dugan, John V., Jr.; and Sovie, Ronald J.: Volume Ion Production Costs in Tenuous Plasmas: A General Atom Theory and Detailed Results for Helium, Argon, and Cesium. NASA TN D-4150, 1967.

3. Masek, T. D.: Plasma Properties and Performance of Mercury Ion Thrusters. Paper 69-256, AIAA, Mar. 1969.

4. Sovie, Ronald J.; and Seikel, George R.: Radio-Frequency Induction Heating of Low-Pressure Plasmas. NASA TN D-4206, 1967.

5. Nichols, L. D.; and Mantenieks, M.: Analytical and Experimental Studies of MHD Generator Cathodes Emitting in an "Spot" Mode. NASA TN D-5414 (also presented at the Annual Winter Meeting of American Society of Mechanical Engineers, Los Angeles, Calif., Nov. 16-21, 1969). Paper 69-WA/HT-51, ASME, Nov. 1969.

6. Dugan, John V., Jr.: Three-Body Collisional Recombination of Cesium Seed Ions and Electrons in High-Density Plasmas with Argon Carrier Gas. NASA TN D-2004, 1964.

7. Dugan, John V., Jr.: Calculation of Three-Body Collisional Recombination Coefficients for Cesium and Argon Atomic Ions with an Assessment of the Gryzinski Cross Sections. J. Appl. Phys., vol. 37, no. 13, Dec. 1966, pp. 5011-5012.

8. Dugan, J. V., Jr.; Lyman, F. A.; and Albers, L. U.: Solution of the Boltzmann and Rate Equations for the Electron Distribution Function and State Populations in Non-Equilibrium MHD Plasmas. Electricity from MHD. Vol. 2. International Atomic Energy Agency, 1966, pp. 85-100.

9. Dugan, John V., Jr.: The Selection of Simple Model Atoms for Calculations of Electron Density in Nonequilibrium, Low Temperature Cs Plasmas. Presented at the 27th Annual Conference for Physical Electronics, Massachusetts Inst. Tech., Cambridge, Mass., Mar. 20-22, 1967.

10. Dugan, John V., Jr.; and Magee, John L.: Capture Collisions Between Ions and Polar Molecules. J. Chem. Phys., vol. 47, no. 9, Nov. 1, 1967, pp. 3103-3113.

11. Dugan, John V., Jr.; Rice, James H.; and Magee, John L.: Calculation of Capture Cross Sections for Ion-Polar-Molecule Collisions Involving Methyl Cyanide. NASA TM X-1586, 1968.

12. Dugan, J. V., Jr.; Rice, J. H.; and Magee, J. L.: On the Nature of Ion-Molecule Collisions. Chem. Phys. Letters, vol. 2, no. 4, Aug. 1968, pp. 219-222.

13. Dugan, J. V., Jr.; Rice, J. H.; and Magee, J. L.: Evidence for Long-Lived Ion-Molecule Collision Complexes from Numerical Studies. Chem. Phys. Letters, vol. 3, no. 5, May 1969, pp. 323-326.

14. Dugan, John V., Jr.; and Rice, James H.: A Computer Plotting Description of Ion-Molecule Collisions with Long-Lived Capture Complexes. NASA TN D-5407, 1969.

15. Dugan, John V., Jr.: Canright, R. Bruce, Jr.; Palmer, Raymond W.; and Magee, John L.: Computer-Made Movies and Plotting Descriptions of Ion-Molecule Collisions with Polar Targets. Presented at Sixth International Conference on the Physics of Electronic and Atomic Collisions, Cambridge, Mass., July 28-Aug. 2, 1969.

# BIBLIOGRAPHY

This bibiography comprises publications authored by the members of the NASA Lewis Research Center Staff.


Dugan, John V., Jr.: Some Theoretical Bases for Selection of Molecular Ion Propellants and a Survey of Molecular Plasma Collisions Processes. NASA TN D-1185, 1964.

Dugan, John V., Jr.: Three-Body Recombination of Cesium Ions and Electrons in an Optically Thin Plasma. Bull. Am. Phys. Soc., vol. 9, no. 3, 1964, p. 342.

Dugan, John V., Jr.: Effect of Model Atom Assumptions Upon Calculation of Electron Density in Nonequilibrium, Low-Temperature Cs Plasmas. Bull. Am. Phys. Soc., vol. 12, no. 6, Aug. 1967, p. 986.

Dugan, J. V., Jr.; and Magee, J. L.: Theory of Collisions Between Ions and Polar Molecules. Bull. Am. Phys. Soc., vol. 10, no. 2, 1965, pp. 190-191.

Dugan, John V., Jr.; and Magee, John L.: Semiclassical Approach to Capture Collisions Between Ions and Polar Molecules. NASA TN D-3229, 1966.

Dugan, John V., Jr.; and Magee, John L.: Capture Collisions between Ions and Polar Molecules. J. Chem. Phys., vol. 47, no. 9, Nov. 1, 1967, pp. 3103-3112.

Dugan, John V., Jr.; Rice, James H.; and Magee, John L.: Calculations of Capture Cross Sections for Ion-Polar Molecule Capture Collisions with $CH_3CN$ Targets. Bull. Am. Phys. Soc., vol. 13, no. 1, Jan. 1968, p. 68.

Dugan, J. V., Jr.; Rice, J. H.; and Magee, J. L.: On the Nature of Ion-Molecule Collisions. Chem. Phys. Letters, vol. 2, no. 4, Aug. 1968, pp. 219-222.

Sheldon, John W.; and Dugan, John V., Jr.: Semiclassical Calculation of Inelastic Cross Sections for Electron-Cesium Atomic Collisions. J. Appl. Phys., vol. 36, no. 2, Feb. 1965, pp. 650-651.

Sovie, Ronald J.; and Dugan, John V., Jr.: Effects of Metastable Atoms on Volume Ion Production in a Tenuous Helium Plasma. NASA TN D-3121, 1965. Also Bull. Am. Phys. Soc., vol. 11, no. 4, 1966, p. 502.

Sovie, Ronald J.; and Dugan, John V., Jr.: Energy Required for Ion Production by Electron Bombardment in Helium, Argon, and Cesium. Bull. Am. Phys. Soc., vol. 10, no. 2, 1965, p. 179.

Sovie, R. J.; and Dugan, J. V., Jr.: Volume Ion Production Costs in Tenuous Plasma. Bull. Am. Phys. Soc., vol. 12, no. 2, Feb. 1967, p. 239.

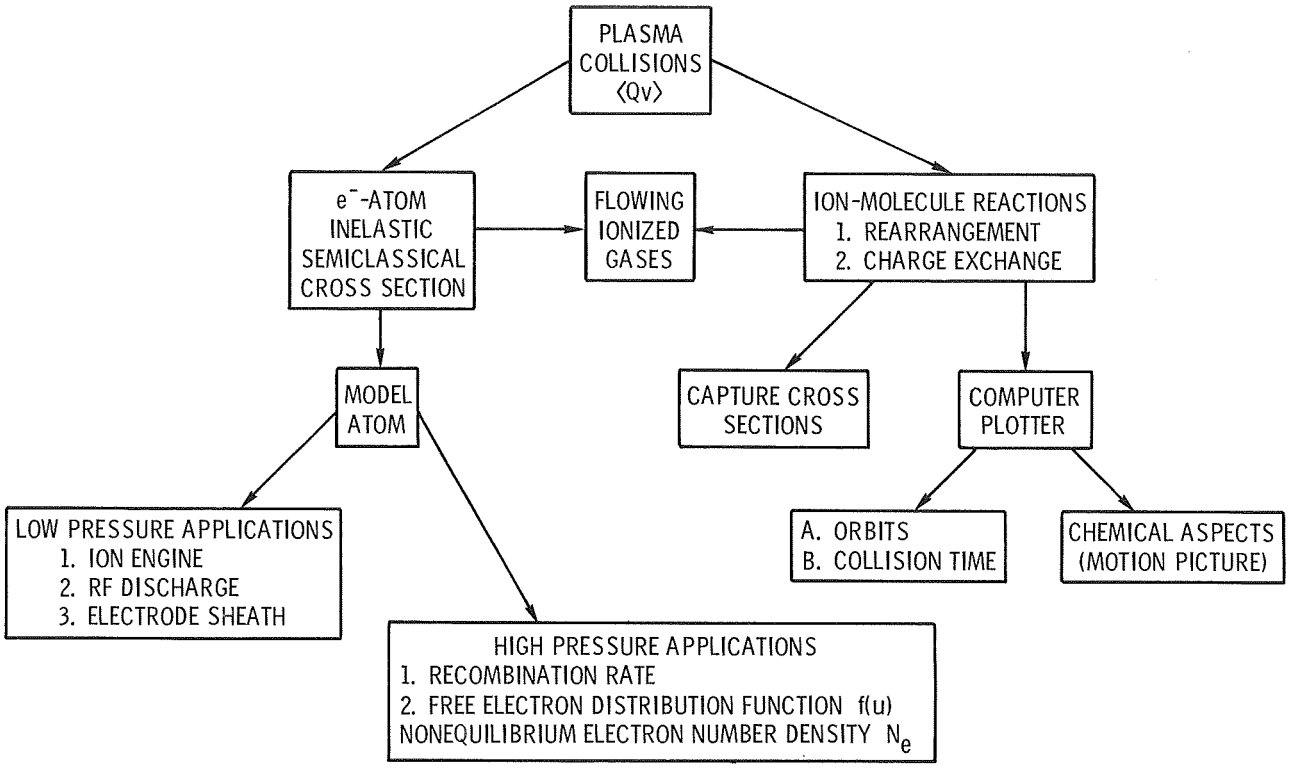


Figure VIII-1. - Outline of problems studied and approaches used in plasma chemistry and ion-molecule collisions.

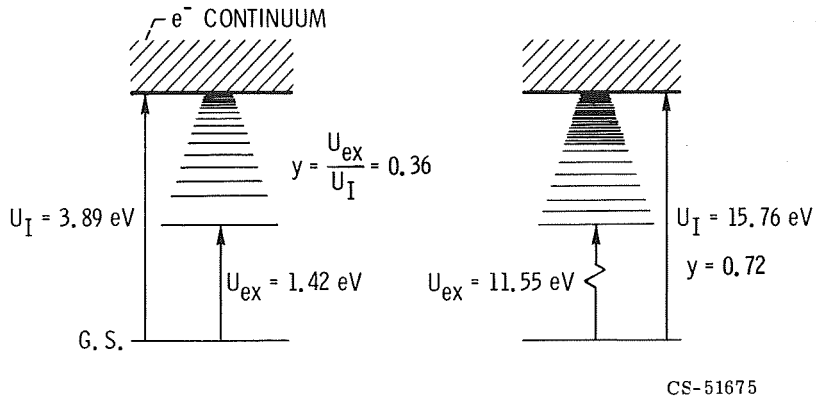


Figure VIII-2. - Schematic model atoms of cesium and argon with first excitation and ionization potentials indicated.

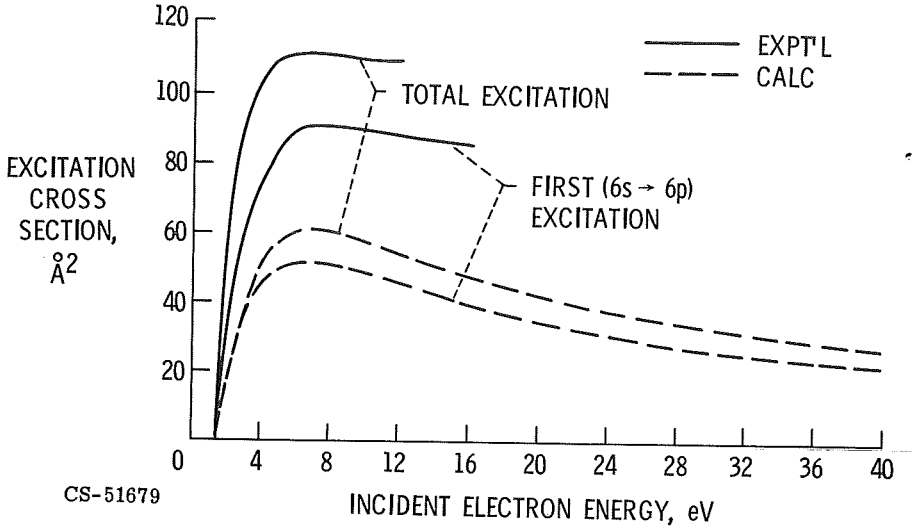


(a) Cesium excitation cross sections.

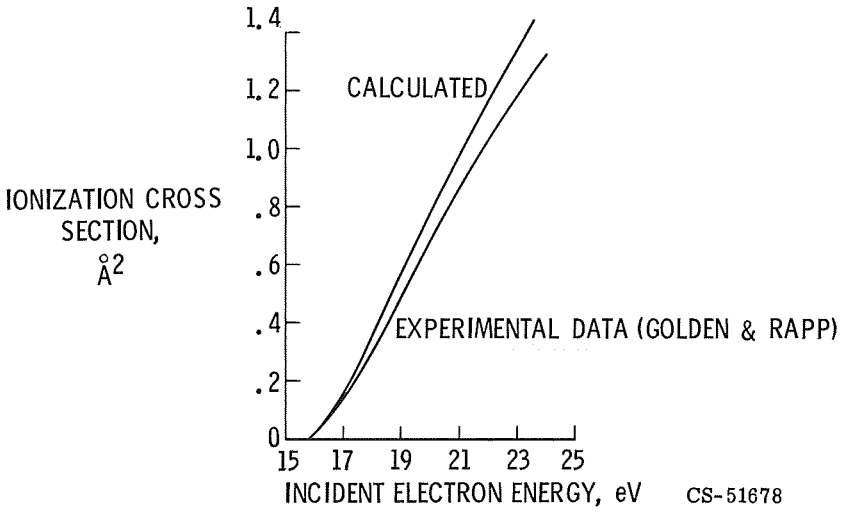


(b) Argon ionization cross section.

Figure VIII-3. - Comparison of experimental and theoretical inelastic electron-atom cross sections plotted against incident electron energy.

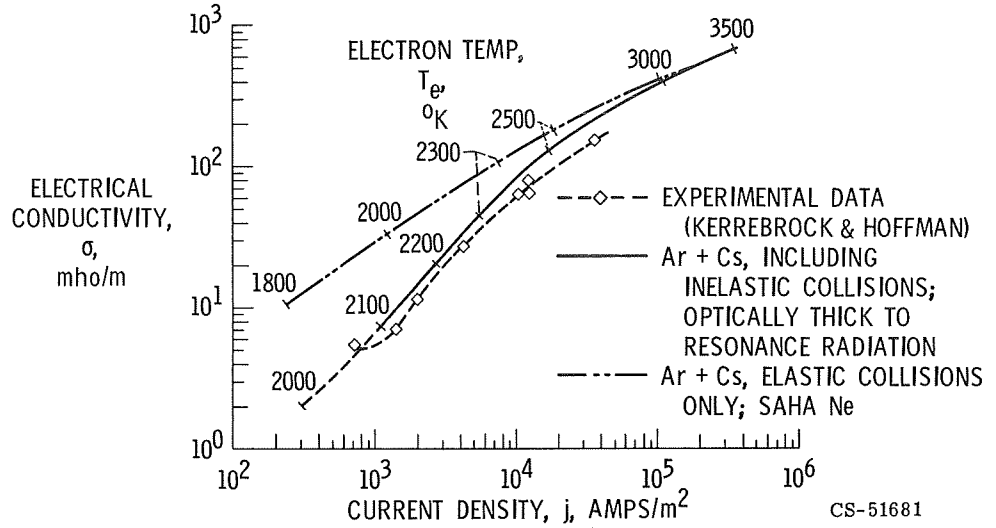


Figure VIII-4. - Comparison of experimental electrical conductivity with two sets of theoretical values for alkali-seeded argon discharges as function of current density. Atmospheric pressure; gas temperature, 1500 K; seed fraction, 0.0015.

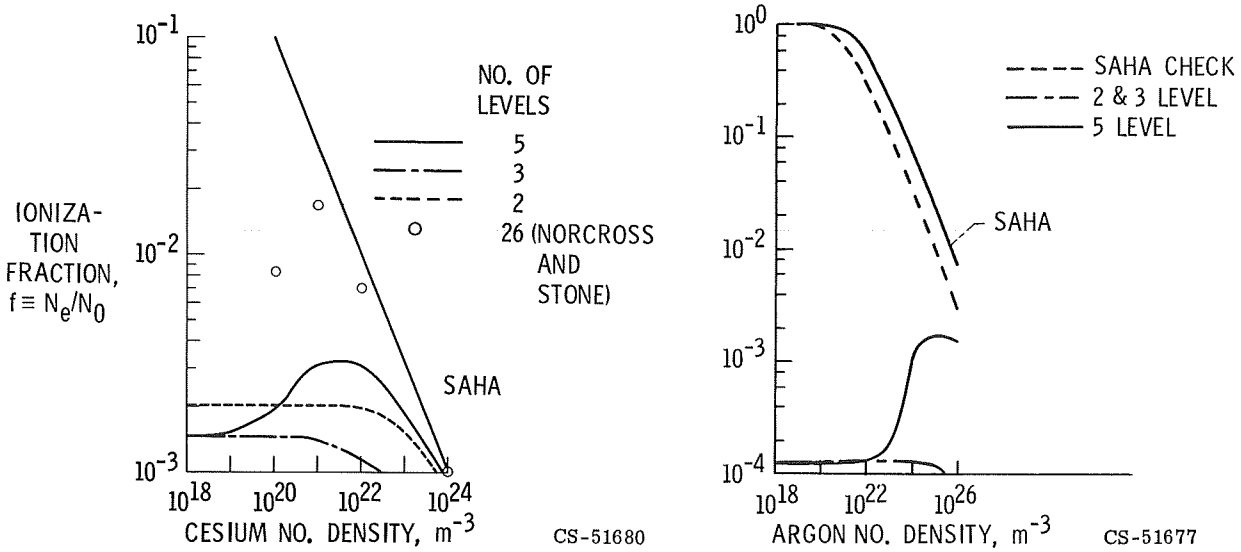


(a) Cesium. Optically thick; $T_e$ = 2321 K (0.2 eV).

(b) Argon. Optically thin; $T_e$ = 11 605 K (1 eV).

Figure VIII-5. - Plots of ionization fraction as function of neutral density for various model atoms.

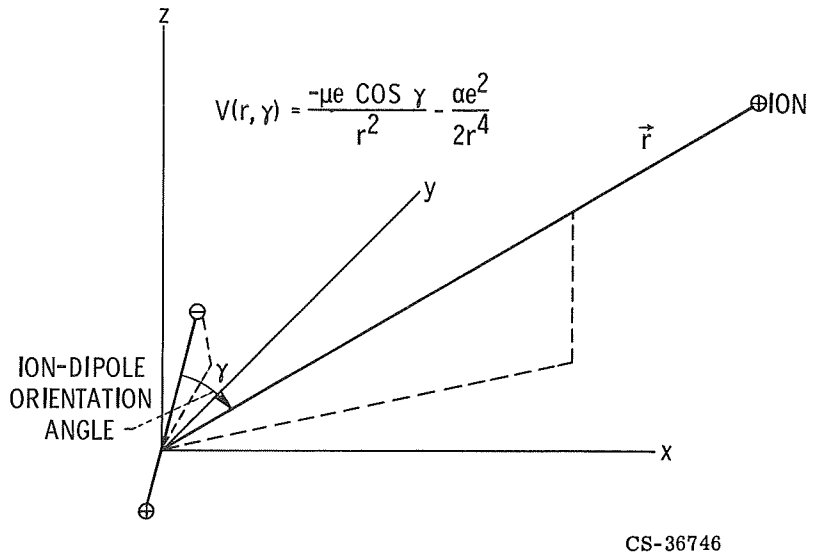


Figure VIII-6. - Coordinate system for three-dimensional interaction ion-linear molecule collision.

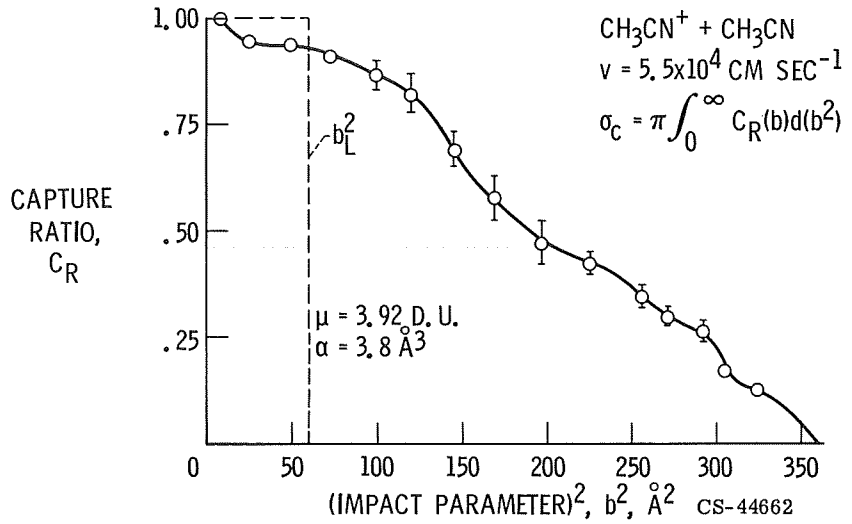


Figure VIII-7. - Variation of capture ratio (fraction of collisions for which ion and molecule approach to within 2 Å) with ion impact parameter for $CH_3CN$-parent ion collisions. Step-function behavior of Langevin ratio is plotted for comparison.

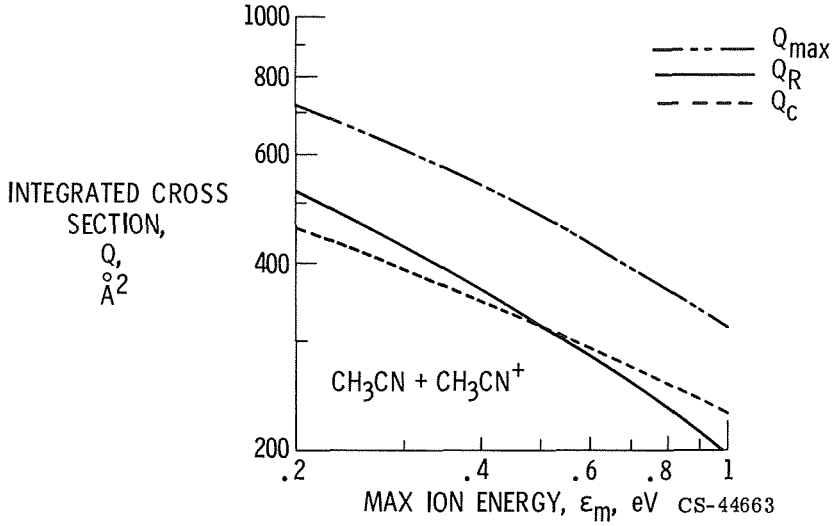


Figure VIII-8. - Maximum $Q_{max}$, experimental $Q_R$, and numerical (capture) $Q_c$ reaction cross sections plotted against experimental voltage setting.

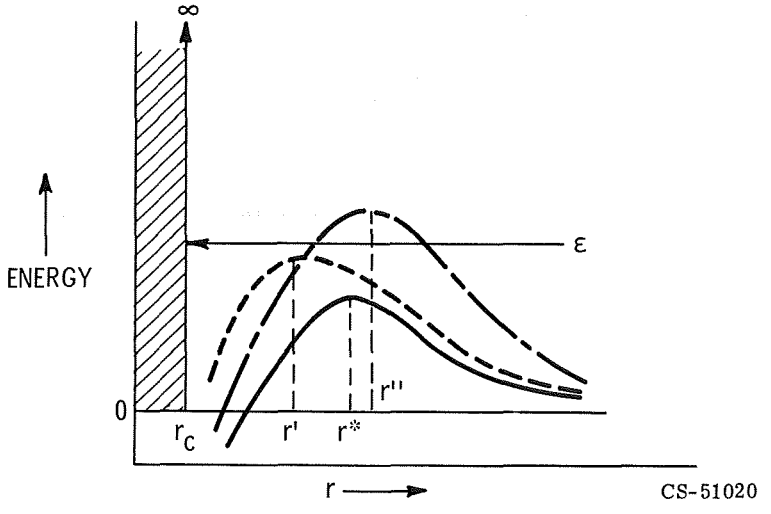


Figure VIII-9. - Schematic diagrams illustrating mechanism of multiple reflection phenomena in ion-dipole collisions with plots of effective potentials for Langevin and permanent dipole collision systems against ion-molecule separation. Ion-polar molecule interaction potential, $V_{eff}(r) = (L^2/2mr^2) + V(r)$.

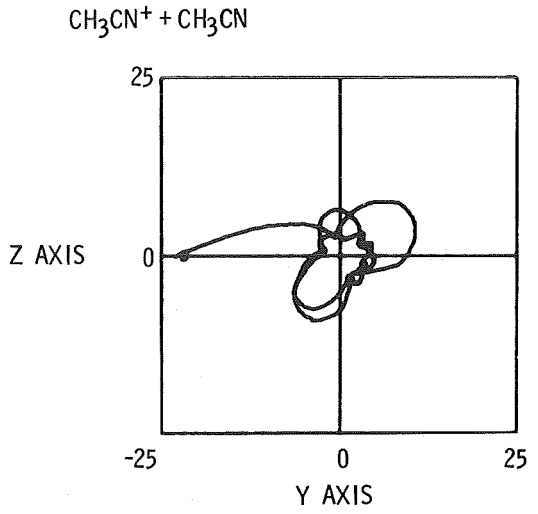


CS-51676

Figure VIII-10. - Trace of ion projection in Y-Z plane for 10 reflection $CH_3CN$-parent ion capture collision.

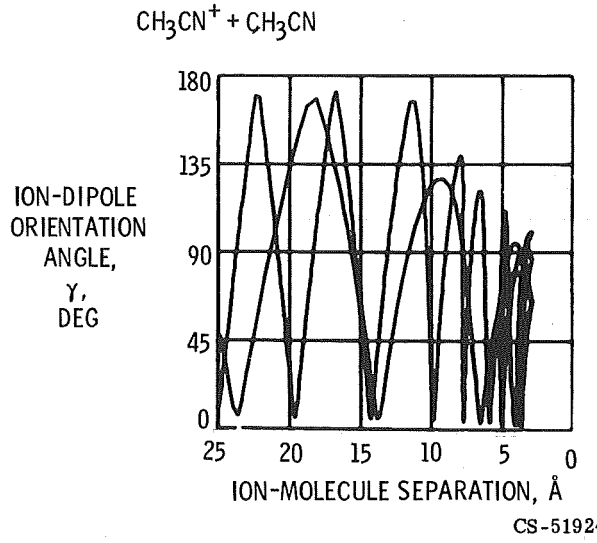


CS-51924

Figure VIII-11. Variation of ion-dipole orientation angle during $CH_3CN$-parent ion capture collision indicating hindering of the rotating dipole.

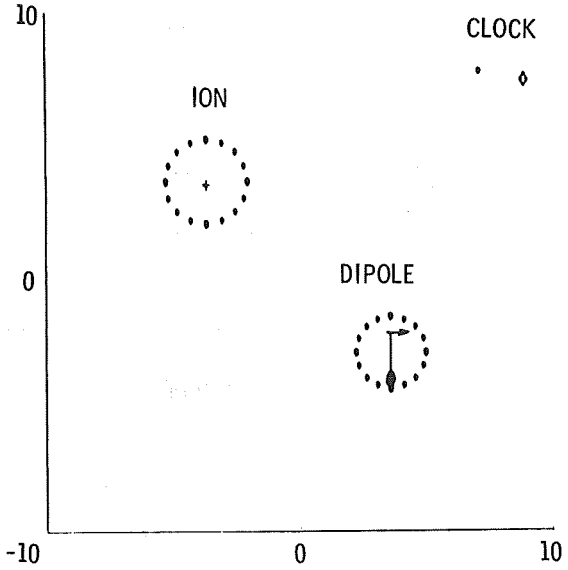


CS-51925

Figure VIII-12. - Sample motion-picture frame for $CH_3CN$ collision.

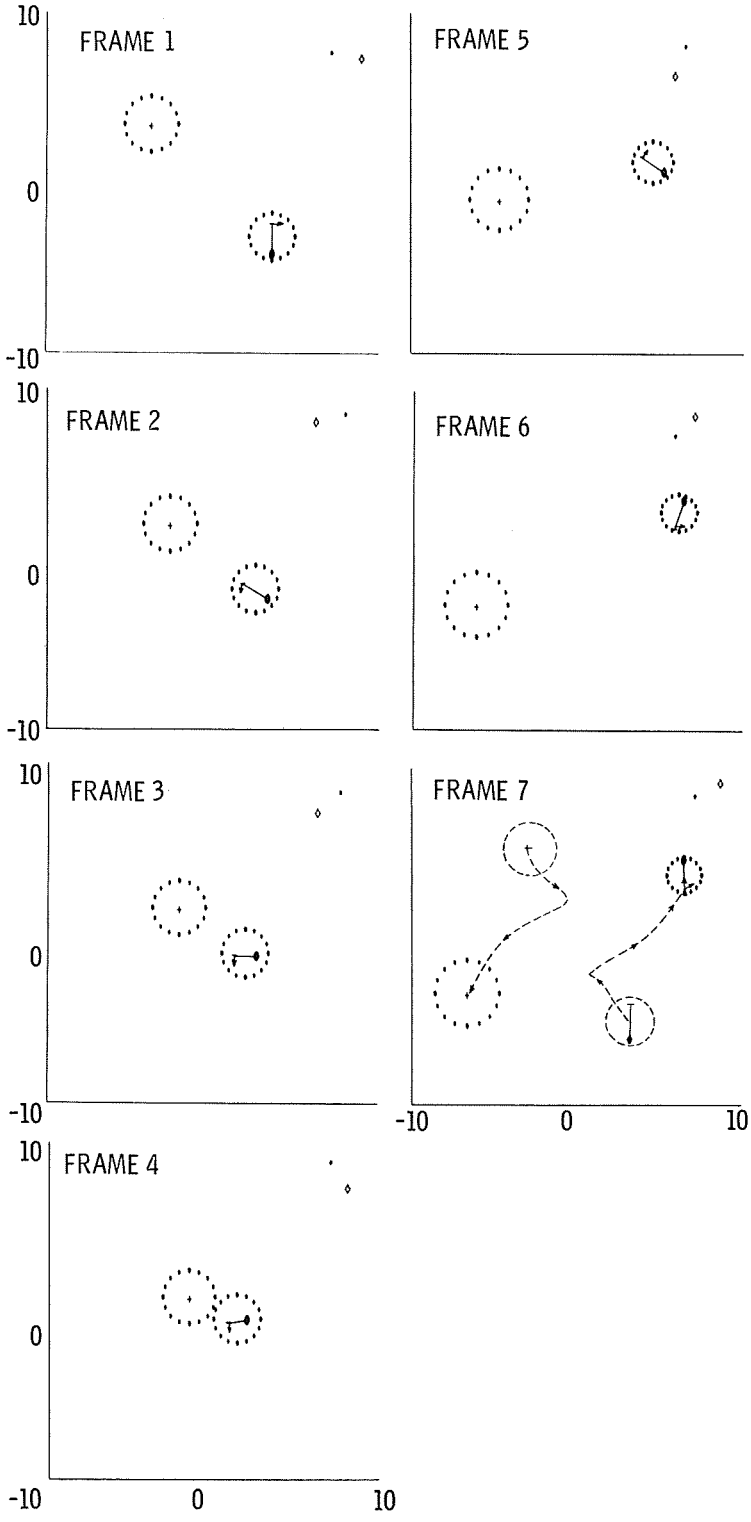


Figure VIII-13. - Motion picture evidence for hindered rotation in frames 1 to 7 for $CH_3CN^+$ + $CH_3CN$ single reflection collision.

NATIONAL AERONAUTICS AND SPACE ADMINISTRATION
WASHINGTON, D. C. 20546

OFFICIAL BUSINESS

FIRST CLASS MAIL

POSTAGE AND FEES PAID
NATIONAL AERONAUTICS AN
SPACE ADMINISTRATION

02U 001 50 51 3DS 69363 00903
AIR FORCE WEAPONS LABORATORY /WLOL/
KIRTLAND AFB, NEW MEXICO 87117

ATT E. LOU BOWMAN, CHIEF,TECH. LIBRARY

POSTMASTER: If Undeliverable (Section 158 Postal Manual) Do Not Retur

*"The aeronautical and space activities of the United States shall be conducted so as to contribute . . . to the expansion of human knowledge of phenomena in the atmosphere and space. The Administration shall provide for the widest practicable and appropriate dissemination of information concerning its activities and the results thereof."*

— NATIONAL AERONAUTICS AND SPACE ACT OF 1958

# NASA SCIENTIFIC AND TECHNICAL PUBLICATIONS

TECHNICAL REPORTS: Scientific and technical information considered important, complete, and a lasting contribution to existing knowledge.

TECHNICAL NOTES: Information less broad in scope but nevertheless of importance as a contribution to existing knowledge.

TECHNICAL MEMORANDUMS: Information receiving limited distribution because of preliminary data, security classification, or other reasons.

CONTRACTOR REPORTS: Scientific and technical information generated under a NASA contract or grant and considered an important contribution to existing knowledge.

TECHNICAL TRANSLATIONS: Information published in a foreign language considered to merit NASA distribution in English.

SPECIAL PUBLICATIONS: Information derived from or of value to NASA activities. Publications include conference proceedings, monographs, data compilations, handbooks, sourcebooks, and special bibliographies.

TECHNOLOGY UTILIZATION PUBLICATIONS: Information on technology used by NASA that may be of particular interest in commercial and other non-aerospace applications. Publications include Tech Briefs, Technology Utilization Reports and Technology Surveys.

*Details on the availability of these publications may be obtained from:*

SCIENTIFIC AND TECHNICAL INFORMATION DIVISION
NATIONAL AERONAUTICS AND SPACE ADMINISTRATION
Washington, D.C. 20546